



University
of Glasgow

Samarelli, Antonio (2011) *Micro ring resonators in silicon-on-insulator*.
PhD thesis.

<http://theses.gla.ac.uk/2327/>

Copyright and moral rights for this thesis are retained by the author

A copy can be downloaded for personal non-commercial research or
study, without prior permission or charge

This thesis cannot be reproduced or quoted extensively from without first
obtaining permission in writing from the Author

The content must not be changed in any way or sold commercially in any
format or medium without the formal permission of the Author

When referring to this work, full bibliographic details including the
author, title, awarding institution and date of the thesis must be given



Micro Ring Resonators in Silicon-on-Insulator

Antonio Samarelli

January 2011

A thesis submitted for the degree of
Doctor of Philosophy (Ph.D.)

in the

Faculty of Engineering

Department of Electronics and Electrical Engineering

©Antonio Samarelli 2010

Declaration of Authorship

I, Antonio Samarelli, declare that this thesis titled, *Micro Ring Resonators in Silicon-on-Insulator* and the work presented in it are my own. I confirm that:

- This work was done wholly or mainly while in candidature for a research degree at this University.
- Where any part of this thesis has previously been submitted for a degree or any other qualification at this University or any other institution, this has been clearly stated.
- Where I have consulted the published work of others, this is always clearly attributed.
- Where I have quoted from the work of others, the source is always given. With the exception of such quotations, this thesis is entirely my own work.
- I have acknowledged all main sources of help.
- Where the thesis is based on work done by myself jointly with others, I have made clear exactly what was done by others and what I have contributed myself.

Signed:

Date:

*"Some people listen to themselves,
rather than listen to what others say.
These people don't come along very often.
But when they do
They remind us
that once you set out on a path
even though critics may doubt you,
it's OK to believe...
that there is no can't, won't or impossible.
They remind us that it's ok to believe ..
Impossible is nothing."*

Adidas - The long Run

Keep Rolling!

Abstract

by Antonio Samarelli

Silicon as a platform for photonics has recently seen a very large increase in interest because of its potential to overcome the bandwidth limitations of microprocessor interconnects and the low manufacturing cost given by the high compatibility with the already established micro-electronics industry. There has therefore been a significant push in silicon photonics research to develop all silicon based optical components for telecoms applications. The work reported in this Thesis is concerned with the design, fabrication and characterisation of coupled ring resonators on silicon-on-insulator (SOI) material. The final objective of this work is to provide a robust and reliable technology for the demonstration of optical buffers and delay-lines operating at signal bandwidths up to 100 *GHz* and in the wavelength region around 1550 *nm*. The core of the activity focused on the optimisation of the fabrication technology and device geometry to ensure the required device performance for the fabrication of long chains of ring resonators. The final process has been optimised to obtain both intra-chip and chip-to-chip reproducibility with a variability of the process controlled at the nanometre scale. This was made possible by careful control of all the variables involved in the fabrication process, reduction of the fabrication complexity, close feature-size repeatability, line-edge roughness reduction, nearly vertical sidewall profiles and high uniformity in the ebeam patterning. The best optical propagation losses of the realized waveguides reduced down to 1 *dB/cm* for $480 \times 220 \text{ nm}^2$ rectangular cross-section photonic wires and were consistently kept at typical values of around 1.5 *dB/cm*. Control of the coupling coefficients between resonators had a standard deviation of less than 4 % for different realizations and resonance dispersion between resonators was below 50 *GHz*. All these figures represent the state-of-the-art in SOI photonics technology. Considerable effort has also been devoted to the development of efficient thermal electrodes (52 $\mu\text{W/GHz}$) to obtain a reconfigurable behaviour of the structure and polymer inverse tapers to improve the off-chip coupling (insertion losses $< 2 \text{ dB}$). Phase-preserving and error-free transmission up to 100 *Gbit/s* with continuously tunable optical delay up to 200 *ps* has been demonstrated on the final integrated systems, proving the compatibility of these devices with advanced modulation formats and high bit-rate transmission systems.

Publications

Publications arising from this work

Journal papers

A. Melloni, A. Canciamilla, F. Morichetti, C. Ferrari, M. Martinelli, L. O'Faolain, T. F. Krauss, R. De La Rue, A. Samarelli, M. Sorel, "*Tunable delay lines in silicon photonics: coupled resonators and photonic crystals, a comparison*", IEEE photonics, Vol 2, pp. 181-194, April 2010.

A. Canciamilla, C. Ferrari, M. Torregiani, F. Morichetti, A. Melloni, R. De La Rue, A. Samarelli, M. Sorel, "*Silicon coupled ring resonators structures for slow light applications: potential, impairments and ultimate limits*", submitted to Journal of Optics, Slow Light special issue, Feb 2010.

T. F. Krauss, L. O'Faolain, S. Schulz, D. M. Beggs, Francesco Morichetti, Antonio Canciamilla M. Torregiani, A. Melloni, P. Lalanne, A. Samarelli, M. Sorel, R. De La Rue, "*Understanding the rich physics of light propagation in slow photonic crystal waveguides*", Proceedings of SPIE - The International Society for Optical Engineering, Integrated Optics: Devices, Materials, and Technologies XIII, Proc. SPIE, Vol. 7612, 76120L (2010).

F. Morichetti, A. Canciamilla, C. Ferrari, M. Torregiani, M. Ferrario, R. Siano, P. Boffi, L. Marazzi, P. Martelli, P. Parolari, A. Samarelli, M. Sorel, R. M. De La Rue, L. O'Faolain, D. M. Beggs, A. Melloni, T. F. Krauss, and M. Martinelli, "*Silicon Photonics for 100 Gb/s systems*", to be submitted.

F. Morichetti, A. Melloni, A. Canciamilla, A. Samarelli, M. Sorel, R.M. De La Rue and M. Martinelli, "*Coherent backscattering in optical microring resonators*", Applied Physics Letters, Feb 2010

A. Samarelli, D. S. Macintyre, M. J. Strain and R. M. De La Rue, M. Sorel, S. Thoms, "*Optical characterisation of an HSQ lithography process*", Journal of Vacuum Science and Technology B (JVST B), Nov/Dec 2008.

Conferences

F. Morichetti, A. Canciamilla, C. Ferrari, M. Torregiani, M. Ferrario, R. Siano, P. Boffi, L. Marazzi, P. Martelli, P. Parolari, M. Martinelli, A. Samarelli, M. Sorel, R.

M. De La Rue, L. O'Faolain, D. M. Beggs, T. F. Krauss, and A. Melloni, "*Controlling the delay of 100 Gb/s polarization division multiplexed signals through silicon photonics delay lines*", submitted to 36 European Conference and Exhibition On Optical Communication, ECOC 2010, September 19-23, 2010 Torino, Italy, 2010

A. Melloni, A. Canciamilla, G. Morea, F. Morichetti, A. Samarelli, M. Sorel, "*Design kits and circuit simulation in integrated optics*", submitted to IPR (Integrated Photonic Research, Silicon and Nano Photonics), July 25-29, 2010, Monterey, California, USA, 2010

A. Melloni, F. Morichetti, A. Canciamilla, C. Ferrari, and M. Martinelli, G. Morea, M. Sorel, A. Samarelli, R. De La Rue, "*Advances in Filters and Delay Lines in Silicon Photonics*", 15th European Conference of Integrated Optics (ECIO'10), 7-9 April 2010, Cambridge, United Kingdom, 2010.

F. Morichetti, A. Canciamilla, M. Torregiani, A. Melloni, L. O'Faolain, D. M. Beggs, T. F. Krauss, A. Samarelli, M. Sorel, and R. M. De La Rue, "*Backscattering in Slow Light Waveguides*", Integrated Photonics and Nanophotonics Research and Applications, OSA Technical Digest, Optical Society of America, Honolulu, Hawaii, USA, July 12-17, 2009.

F. Morichetti, C. Ferrari, A. Canciamilla, M. Torregiani, A. Melloni, A. Samarelli, R. De La Rue, and M. Sorel, "*Processing Light in Coupled Ring Resonators*", Slow and Fast Light, OSA Technical Digest, Optical Society of America, Honolulu, Hawaii, USA, July 12-17, 2009.

L. O'Faolain, Sebastian Schulz, D. M. Beggs, T. P. White, T. F. Krauss, A. Samarelli, M. Sorel and R. De La Rue, F. Morichetti, A. Canciamilla and A. Melloni, "*Low Loss Dispersion Engineered photonic crystal for optical delay lines*", 6th International Conference on Group IV Photonics 9-11 September 2009, San Francisco, California, 2009.

Francesco Morichetti, Andrea Melloni, Antonio Canciamilla, Carlo Ferrari, Matteo Torregiani, Antonio Samarelli, Richard M. De La Rue, Marc Sorel, "*Phase Preserving Wavelength Conversion over 6 THz in a Silicon Coupled Resonator Optical Waveguide*", 2009 OFC/NFOEC.

A. Melloni, P. Boffi, A. Canciamilla, C. Ferrari, M. Ferrario, L. Marazzi, M. Martinelli, F. Morichetti, M. Torregiani, A. Samarelli, M. Sorel, R. M. De La Rue, L.

O'Faolain, D.M. Beggs, and T.F. Krauss, "100G Silicon Photonics", to be submitted
F. Morichetti, A. Canciamilla, M. Torregiani, A. Melloni, L. O'Faolain, D.M. Beggs, T.F. Krauss, A. Samarelli, M. Sorel, R.M. De La Rue, "*Backscattering in slow light waveguides*", Integrated Photonics and Nanophotonics Research and Applications (IPNRA), July 12-17, 2009, Honolulu, Hawaii, USA, 2009.

A. Samarelli, R. M. De La Rue, M. Sorel, A. Canciamilla, F. Morichetti, A. Melloni, "*Precise fabrication of coupled ring-resonator structures*", presented at CLEO EUROPE 2009, Conference on Laser and Electro-Optics, June 14-19 2009, Munich International Congress Centre, Munich, 2009.

A. Canciamilla, C. Ferrari, A. Melloni, M. Torregiani, F. Morichetti, A. Samarelli, M. Sorel, and R. De La Rue, "*Reconfigurable CROW Delay Lines on a Silicon Platform*", CLEO EUROPE 2009, Conference on Laser and Electro-Optics, June 14-19 2009, Munich International Congress Centre, Munich, 2009.

L. O'Faolain, S. Schulz, T. P. White, D. Beggs, A. Samarelli, M. Sorel, R. De La Rue, T. F. Krauss, "*Losses in engineered slow light photonic crystal waveguides* ", CLEO EUROPE 2009, Conference on Laser and Electro-Optics, June 14-19 2009, Munich International Congress Centre, Munich, 2009.

A. Canciamilla, M. Torregiani, C. Ferrari, F. Morichetti, A. Melloni, M. Martinelli, A. Samarelli, R. De La Rue and M. Sorel, "*Optical Processing in Reconfigurable Slow-Light CROW*", Fotonica 2009, Pisa, 27-29 May 2009.

L. O'Faolain, S. Schulz, T. P. White, D. Beggs, A. Samarelli, M. Sorel, R. De La Rue, T. F. Krauss, "*Losses in engineered slow light photonic crystal waveguides* ", PECS VIII, The 8th International Photonic & Electromagnetic Crystal Structures Meeting, April 5-9 2009, Cockle Bay Wharf, Sydney Australia, 2009.

A. Samarelli, M. Gnan, R. M. De La Rue, M. Sorel, "*Low propagation loss photonic wire and ring resonator devices in silicon-on insulator using hydrogen silsesquioxane electron-beam resist*", presented at 14th European Conference of Integrated Optics (ECIO'08), June 11-13 2008, Eindhoven, The Netherlands, 2008.

S. Thoms, M. Gnan, D. S. Macintyre, A. Samarelli, M. Sorel, M. Strain and R. M. De La Rue, "*Optical characterisation of an HSQ lithography process*", Conference on Electron, Ion, and Photon Beam Technology and Nanofabrication (EIPBN), May 27 - 30 2008, Portland, Oregon, 2008.

Other

Journal papers C. E. de Nobriga, G. D. Hobbs, W. J. Wadsworth, J. C. Knight, D. V. Skryabin, A. Samarelli, M. Sorel, and R. M. De La Rue, "*Supermode Dispersion and Waveguide-to-Slot Mode Transition in Silicon-on-Insulator Waveguide Arrays*", submitted to Optics Letters, May 2010.

A. V. Gorbach, W. Ding, O. K. Staines, C. E. de Nobriga, G. D. Hobbs, W. J. Wadsworth, J. C. Knight, D. V. Skryabin, A. Samarelli, M. Sorel, and R. M. De La Rue, "*Solitonic supermodes and resonant radiation in arrays of silicon photonic wires*", submitted to Physical Review Letter, May 2010.

Conferences P. Orlandi, M. Gnan, A. Samarelli, G. Bellanca, A. Melloni, R. M. De La Rue, M. Sorel, P. Bassi, "*Accoppiatori Assistiti da Reticolo Associati a Risuonatori ad Anello*", XVIII Riunione Nazionale di Elettromagnetismo, Benevento, Italy, September 6-10, 2010

P.Orlandi, M.Gnan, A. Samarelli, G.Bellanca, A.Melloni, R.M.De La Rue, M.Sorel, P.Bassi, "*Modeling of Racetrack Resonator with Grating Assisted Coupling*", Workshop on Optical Waveguide Theory and Numerical Modelling (OWTNM), April 9-10, 2010, Cambridge, UK, 2010.

W. Ding, C. De Nobriga, G. Hobbs, J.C. Knight, A. V. Gorbach, O. Stains, and D. V. Skryabin, A. Samarelli, M. Sorel, and R. De La Rue, "*Spectral signatures of spatio-temporal solitons in arrays of silicon-on-insulator photonic wires*", Non-linear Photonics (NP) Topical Meeting and Tabletop Exhibit, June 21-24, 2010, Karlsruhe, Germany, 2010

C.E. de Nobriga, G.D. Hobbs, W. Ding, A.V. Gorbach, W.J. Wadsworth, J.C. Knight, D.V. Skryabin, A. Samarelli, M. Sorel, R.M. De La Rue, "*Supermode Dispersion and Mode Transitions in Silicon-on-Insulator Waveguide Arrays*", Non-linear Photonics (NP) Topical Meeting and Tabletop Exhibit, June 21-24, 2010, Karlsruhe, Germany, 2010

A. Samarelli, M. Sorel, R.M. De La Rue, A. Melloni, P. Orlandi, M. Gnan, P.Bassi, "*Grating Assisted Coupling in Microring Resonators*", 15th European Conference of Integrated Optics (ECIO'10), 7- 9 April 2010, Cambridge, United Kingdom, 2010.

C.E. de Nobriga, W. J. Wadsworth, A. Gorbach, D.V. Skryabin, J. C. Knight, A. Samarelli, M. Sorel, R.M. De La Rue, " *Supermode Dispersion of Strongly Coupled Silicon-on-Insulator Waveguides*", CLEO 16-21 May 2010, San Jose, California, 2010

Lu-Min Tsai, F. Causa, J. Sarma, A. Samarelli, M. Sorel, " *Novel Optical Multiplexers based on the Double Grating Frustrated Coupler*", CLEO EUROPE 2009, Conference on Laser and Electro-Optics, June 14-19 2009, Munich International Congress Centre, Munich, 2009.

R. De La Rue, A. Khokhar, R. Dylewicz, M. Strain, N. Johnson, M. Sorel, F. Rahman, B. Lahiri, A. Samarelli, A. Md Zain and M. Gnan, " *Strongly confined guided-wave photonic structures with nano-scale control for linear and non-linear functionality*" 17th International Laser Physics Workshop (LPHYS'08) June 30 - July 4 2008, Trondheim, Norway, 2008.

A. Samarelli, A. Md Zain, M. Gnan, H.M.H. Chong, M. Sorel, R.M. De La Rue, P. Frascella, C. Ciminelli and M.N. Armenise, " *Single Row SOI-based Photonic Crystal/Photonic Wire Micro-cavities with Medium Q-factor and High Transmission*", IPNRA, 8-11 July 2007 Salt Lake City Utah, USA, 2007.

A. Md Zain, A. Samarelli, M. Gnan, M. Sorel, M.N. Armenise, C. Ciminelli, R.M. De La Rue, " *Photonic crystal microcavity filters embedded in silicon on insulator photonic wire waveguides*", Microtechnologies for the New Millennium 2007, 2-4 May 2007, Gran Canaria, Spain, 2007.

Acknowledgements

First and foremost, I would like to thank my supervisors, Dr. Marc Sorel and Prof. Richard de La Rue, for having made this PhD possible. Their continuous suggestions, advices, and psychological support during these 3 years constituted an immeasurable value for me. Both of them helped me mature from a scientific point of view. Thanks a lot.

Thanks to the European project SPLASH for funding my scholarship and to all the project partners for the fruitful scientific discussions (Prof. T. Krauss, Prof. P. Lalanne, Prof. Andrea Melloni, Dr. Francesco Morichetti and Dr. Antonio Canciamilla). Antonio and I were *tuned* at the same wavelength, always collaborating, joking, arguing and exchanging ideas. Most of the work developed during the course of this thesis originated from the excellent friendship grown between the two of us during the SPLASH project. Thanks guys.

Dr. Marco Gnan has been a model for me. I still remember the first time he took me to the clean room, the first time he gave me the tweezers and the first waveguide alignment. Although he left Glasgow several years ago, he is still a great friend who has clarified most of my doubts over the course of my thesis. Thanks Marco.

Thanks to my office mates, especially Gabor and Steven and the Italians: Giuseppe, Giangi, Carla, Oberdan, Francesca and Piero (my flatmate and new colleague in Silicon Photonics). Cheers guys.

Thanks Dr. Michael Strain and Dr. Philippe Velha for the fruitful discussions, to Prof. Douglas Paul for giving me good advices, to Dr. Stephen Thoms and Dr. Douglas Macintyre for having made the JWNC a place where good science can be made and to the staff of the JWNC for the competence and availability. Thanks a lot.

Thanks to my mother and my father to the continuous support in every moment of my life. For everything you do, for all the suggestions and love. You are special! The last but most important thank is for you Cinzia, the only person able to radically change my life. Thanks for psychologically supporting me in the bad moments when everything seemed so difficult, I can always see your hand dragging me out from there and pushing me to get better. Thanks love.

Contents

Declaration of Authorship	i
Abstract	iii
Acknowledgements	ix
List of Figures	xiii
List of Tables	xx
1 Introduction	1
1.1 Slow Light features and motivation	1
1.2 Slow light approaches	3
1.3 Integrated Slow Light Structures	5
1.4 The Potential of Photonics	6
1.4.1 Index-contrast and materials	7
1.4.2 Silicon On Insulator platform	11
1.5 Aims of the Thesis	12
2 Fabrication Techniques	15
2.1 The Material	15
2.2 Process Steps	17
2.3 Patterning using Electron Beam Lithography (EBL)	19
2.4 Process with Hydrogen Silsesquioxane resist	22
2.4.1 Literature Review on HSQ resist	24
2.4.2 HSQ process details	25
2.5 Etching techniques	26
2.5.1 Silicon Etching in RIE	28
2.5.2 Silicon Etching in ICP	29
2.6 Silica Deposition	33
2.7 Buffer Layer	34
2.8 Metal deposition and Lift off techniques	34
2.9 Conclusions	37

3	Basic Building Block Design and Characterization	39
3.1	Experimental Set up	39
3.2	Waveguide design	41
3.2.1	Deeply etched waveguides	43
3.2.2	Shallow etch waveguides	44
3.3	Transmission Loss Estimation	47
3.4	Input and Output Coupling losses	48
3.4.1	Anti-reflection coatings	49
3.4.2	Inverse Tapers	50
3.5	Directional Couplers	56
3.6	Microring Resonators	62
3.6.1	Ring Resonator Phase Shifter	64
3.6.2	Ring Resonator Filter	74
3.7	Conclusions	78
4	Thermal tuning of Silicon on Insulator Ring Resonators	79
4.1	Introduction	79
4.2	Thermo-optic effect in Silicon	80
4.3	Heater Configuration	81
4.3.1	Buffer Layer Design	82
4.3.2	Heating element geometry	83
4.4	Single Ring Tuning	87
4.4.1	Thermal Cross Talk	88
4.4.2	Tuning Speed	89
4.5	Conclusions	90
5	Variability, Uniformity and Consistency in the Fabrication of Ring Resonator cavities	91
5.1	HSQ Process Variability	92
5.1.1	Pattern Variation results for Phase Shifter Ring Resonator Structures	94
5.1.2	Pattern Variation results for Coupled Ring Resonator Structures	96
5.2	Conclusions	98
6	Silicon On Insulator Coupled Microring Resonator Optical Waveguides	99
6.1	Introduction	99
6.2	Slow Light Structures	100
6.3	Coupled Optical Resonator Waveguides	102
6.4	Design of a Delay line with N resonators	105
6.5	Measurement of a Delay line with N resonators	106
6.5.1	Static Behaviour	106
6.5.2	Reconfigurable Behaviour	108
6.6	Conclusions	112

7	Conclusions and Future Work	113
A	Transfer Matrix Method (TMM)	116
A.1	Transfer Matrix Method	116
A.1.1	Waveguide	116
A.1.2	Coupler	117
A.1.3	Ring Resonator Filter	117
A.2	Coupled Optical Resonators	119
A.3	Conclusions	122
B	Origin and Extraction of the propagation losses	123
B.1	The origin of propagation losses	123
B.2	The extraction of the propagation losses	126
B.2.1	The properties of the sample cavity	126
B.2.2	Fabry-Perot measurements using Fringe Contrast	127
B.2.3	Fourier Analysis of Transmission Losses	130
C	Thermal Model	132
C.1	Thermal Model	132
C.1.1	Heat transfer equation	133
C.1.2	Joule Heating	135
D	CROW structures	137
D.1	Reconfigurable Slow Light Delay Lines Architectures	137
D.1.1	Digital Delay	138
D.1.2	Analogue Delay	140
D.2	CROW impairments	142
D.2.1	Dispersion limits	142
D.2.2	Limits on propagation losses, disorder and backscattering	143
D.2.3	Apodisation of the structure	145
D.2.4	Back scattering in CROW structures	147
E	System measurements for CROW structures	150
E.1	Time domain characterization	150
E.1.1	10 Gbit/s OOK transmission	150
E.1.2	Phase modulation formats	152
E.1.3	1 Byte delay at 100 Gbit/s OOK	153
E.2	Comparison with the-State-of-Art	155
	Bibliography	158

List of Figures

1.1	Spatial compression and intensity enhancement of optical pulses propagating into a slow-light medium.	2
1.2	Scanning electron microscope pictures of several configurations of slow light structures fabricated in the course of this work in the James Watt Nanofabrication Centre (JWNC).	5
1.3	Dependence on the index contrast Δn of the Free Spectral Range and of the minimum allowed bending radius that guarantee a figure for the radiation losses of 0.1 dB/rad . For a defined index contrast, values of radii below the green line produce an higher value of the radiation losses.	8
2.1	Schematic of the Smart Cut process for the production of Silicon on Insulator wafers.	16
2.2	Sequential schematic of the process steps for the definition of the chip structure.	18
2.3	Graphical view of the effect of the choice of the BSS and SS, from the top left to top right the BSS is linearly increased, there is a point after that the line edge roughness become a problem as shown in the bottom picture (courtesy of Dr. S. Thoms, EBL notes).	20
2.4	Stitching error on a coupled optical waveguide system.	21
2.5	Schematic of the process steps for the definition of the guiding layer structures. On the left the process with PMMA or ZEP which require an intermediate hard mask of SiO_2 , on the right the process with HSQ, etching resistant e-beam resist. The process with HSQ results in a better quality of the devices and a reduced complexity of the process.	23
2.6	HSQ chemical structure and reaction under e-beam radiation.	24
2.7	Schematic of an etching process. In the chamber there is first the formation of active species by electron collisional dissociation and ionization, diffusion to the wafer surface with subsequent absorption and reaction to etch the material both physically and chemically.	27
2.8	Scanning electron microscope pictures of Waveguide Cross Section etched with a RIE tool.	29
2.9	Scanning electron microscope of a waveguide cross section Waveguide Cross Section	30
2.10	Scanning electron micrograph of the <i>RIE – lag</i> phenomenon for 100 seconds of etching	31

2.11	Dependence of the etching depth vs gap dimension in the HSQ resist mask.	32
2.12	Scanning electron microscope of an array of 3 waveguide spaced 50 nm and etch for 140 seconds. Such small gaps are deeply etched and only 40 nm of material is still present at the bottom of the gaps.	32
2.13	Development in the passivation of the structure to obtain an upper cladding with good gap filling and mechanically and chemically robust.	35
2.14	Figures of bonding processes: a) poor adhesion of the NiChrome layer resulted in not capability to realize the bonding of the devices, b) optimized process with the wires bonded on the sample (optical microscope picture acquired in Milano).	37
3.1	Schematic diagram of the experimental set-up used for the end-fire characterization of the fabricated devices.	40
3.2	Typical power characteristics for TE and TM polarizations at the output of the tunable laser. The power level for TE and TM are dependent from the input fiber and any alignment and optimization for the desired polarisation is necessary prior to each measurement. Both characteristics present a flat behavior across the wavelength range of interest.	41
3.3	Schematic of the Cross section for the waveguide configurations modeled and realized in the course of this work.	42
3.4	Deep etched waveguides: effective refractive index n_{eff} for TE modes as a function of the waveguide width w , the fundamental mode in blue and the first order mode in black. The power flux distribution and the sensitivity $\delta n_{eff}/\delta w$, are shown for $w = 480$ nm – at a wavelength of $\lambda = 1.550$ μm	43
3.5	Shallow etched waveguides: bending losses as a function of bending radius R for different values of w and t : $w = 450$ and $w = 600$ nm (red and black lines respectively); $t = 70$ -80-90 nm (dotted, dashed and solid lines respectively) (courtesy of Prof. A. Melloni, Politecnico di Milano).	44
3.6	Shallow etched waveguides: effective refractive index n_{eff} for TE modes as a function of the waveguide width w , for an etching depth of 90 nm; the fundamental mode in blue and the first order mode in black; the power flux distribution and the sensitivity $\delta n_{eff}/\delta w$, are shown for $w = 650$ nm – at a wavelength of $\lambda = 1.550$ μm	45
3.7	Shallow etched waveguides with a width $w = 650$ nm: the fundamental TE-mode effective refractive index n_{eff} variation, as a function of the etching depth t – and the sensitivity, $\delta n_{eff}/\delta t$, for an etching depth of 90 nm is $3 \cdot 10^{-4}$ nm ⁻¹	46
3.8	Loss estimation using a) the fringe contrast method (at the University of Glasgow) and b) using the Fourier Transform (measurements performed at Politecnico di Milano).	48

3.9	Transmission spectra of the same device structure with (red) and without Anti-Reflection Coatings (black). The difference in the power level is due to optimization in the alignment process.	50
3.10	Schematic representation of a mode adapter structure. The silicon wire waveguide is depicted in blue and is tapered down to a narrow tip. The yellow waveguide is a low index waveguide $n = 1.52$ (SU8). The entire structure is covered with SiO_2	51
3.11	Simulation performed with a Rsoft Beam Prop of a typical device. The top represent a top view of the transformation of the optical beam and, at the bottom, a side view is shown.	52
3.12	Optical and SEM micrograph of some fabricated tapers.	53
3.13	Intensity and cross-polarization coupling measurements for tapers with different length.	54
3.14	Normalized transmission characteristics for a $400 \mu m$ long taper with a final aperture of $20 nm$. The TE-TE transmission is shown in black while the TE-TM transmission is shown in red.	55
3.15	Simulated transmission losses for taper with different length for a linear variation along the propagation direction (black circular dots) and an exponential variation (blue squares).	56
3.16	SEM picture of the polymer waveguide a) and the cross section of a cleaved sample ready for measurements b).	56
3.17	Schematic and SEM picture of a Coupler.	58
3.18	Transition length simulations for different radii of the bent waveguides of a coupler.	59
3.19	Dependence of the coupling coefficient with the gap dimensions for several values of coupler length.	59
3.20	Measurements of the output transmission characteristics for a directional coupler. From this graphs it is possible to calculate the value of K	60
3.21	Simulated behavior of the power coupling coefficient as a function of the gap: $K = 0.5$, $\epsilon_K = 10 \%$ can be obtained by controlling the gap dimension G with a precision $< \pm 7 nm$	61
3.22	Measurements of the power coupling coefficient K for the directional coupler with a fixed gap ($200 nm$) and different coupler lengths. The outputs at the DROP and the BAR ports are obtained by exciting the device at both input ports, in sub-sequential measurements. The fitted data obtained from the average power level for each measurement are in good agreement with the design values and within the mean value error of 25%	63
3.23	Schematic and SEM image of Ring Resonator Phase Shifter.	64

3.24	a) Transmission ($ H_{12} ^2$), b) slowing ratio (S), c) phase (H_{12}) and d) pole zero diagram of a Ring Resonator Phase-shifter (FSR = 250 GHz) with $r = 0.8$ ($K = 36\%$) for increasing round-trip loss γ : lossless phase-shifter with $\gamma = 1$ (black line), maximum-phase response $\gamma = 0.9$ (blue line), critical coupling $\gamma = r = 0.8$ (red line) and minimum phase response $\gamma = 0.6$ and 0.4 (green and pink lines respectively).	65
3.25	Q factor for a fixed value of ring length ($L_c = 130 \mu m$) and different values of Losses and cross coupling power coefficient (K).	67
3.26	Q factor for a fixed value of Losses ($2 dB/cm$) and different values of ring length (L_c) and cross coupling power coefficient (K).	67
3.27	Transmission spectra of a Ring Resonator Phase Shifter with $K = 10\%$ for TE (black line) and TM (red line) polarizations.	68
3.28	Transmission spectra of a Ring Resonator Phase Shifter for several values of the coupling coefficient K : 5% (Black), 10% (Red) and 20% (Blue). The higher transmission and small level of FP oscillation, if compared to 3.27, are greatly reduced by inverse tapers described in section 3.4.2.	69
3.29	Transmission characteristic of two nominally identical devices, the peak position is slightly shifted due to the process variability. The difference in the peak depths is due to the random nature of the backscattering which influence similar devices in a different way.	72
3.30	Transmission characteristic of ring resonator phase shifter with point coupler and different ring radii.	73
3.31	Schematic and SEM picture of Ring Resonator Filter.	74
3.32	a) Transmission ($ H_{13} ^2$), b) slowing ratio (S), c) phase (H_{13}) and d) pole zero diagram of a Ring Resonator Filter (FSR = 250 GHz) at the drop port in the lossless (solid line, $\gamma = 1$) and lossy $\gamma = 0.7$ cases, for different coupling coefficients: $r = 0.6$ (red lines), 0.8 (blue lines), 0.9 (green lines)	75
3.33	Normalized intensity at the bar (black line) and the drop port (red line) of a ring resonator filter with $K_1 = K_2 = 5\%$	76
3.34	Normalized intensity at the bar (black line), the drop port (red line) and the reflection port (blue line) of a ring resonator filter with $K = 10\%$	76
3.35	Normalized intensity at the bar (black line), the drop port (red line) and the reflection port (blue line) of a ring resonator filter with $K = 20\%$	77
4.1	Schematic cross-section of a general device structure where the thermo-optic effect is analyzed.	80
4.2	Schematic Top view a) and cross section b) of the heaters. The Heating elements are realized after the fabrication of the photonic wires and the passivation of the structure.	82
4.3	Losses for different values of the buffer layer thickness (a) and temperature values at the core of the waveguide (b).	82

4.4	Temperature profile for two different width dimensions of the heater w_t ((a) 500 nm and (b) 2 μm) and corresponding tuning efficiency dependence on the w_h and t_h	84
4.5	Temperature dependence for different values of heater thickness (a), and heater width (b). In blue the corresponding values imposed, by technological issues, on the thickness and the relative limits on the waveguide width to prevent melting of the device.	85
4.6	Optical Microscope Image of the micro heater. In red colour are indicated the high resistivity areas where the heat is generated by the Joule heating effect.	86
4.7	Tuning of the resonance peak for different values of the voltage applied and correspondent Wavelength - Voltage characteristic.	87
4.8	Schematic of the measurements and results for the evaluation of the Thermal Cross Talk of adjacent rings with metal conductor spaced 7 μm	88
4.9	a) Sketch of the measurement; b) Time traces of a driving electrical square wave at 10 KHz (red line) and the corresponding optical power (blue line) at the output port of an all pass filter; c) Detail of the optical power transient.	89
5.1	Calculated variation of waveguide width for several realization of fabricated devices using a Single dilution of HSQ. The inset shows the length of the ring resonator, B (bottom) and T (top) represent the position of the structure on the sample with size $1 \times 1 \text{ cm}^2$	94
5.2	Calculated variation of waveguide width for several realization of fabricated devices using a Fresh dilution of HSQ. The inset shows the length of the ring resonator, B (bottom) and T (top) represent the position of the structure on the sample.	95
5.3	Intensity spectral response at drop port of Coupled Ring Resonators realized in two different fabrication runs (Chip A and Chip B) (measurements performed in Milano.)	96
5.4	Measurement of the band broadening of a chain of 64 ring resonators in APF configuration.	97
6.1	Ring-resonator-based slow light architectures realized in (a) all pass filters (APF), (b) coupled resonator optical waveguides (CROW) in Reflection configuration and (c) coupled resonator optical waveguides (CROW) in Transmission configuration.	100
6.2	Spectral response for an increasing number N of resonators. Dotted lines show the theoretical response of the infinitely long Slow Light structure (courtesy of Prof. A. Melloni, Politecnico di Milano).	103
6.3	Inverse of the Slowing Ratio S for different value of the cross-coupling field coefficient t	104
6.4	Measurements of a CROW structure with 6 rings and $F = 4$ in Transmission configuration	107
6.5	Fine tuning and phase disorder adjustment for a CROW with 4 Rings, a Bandwidth of 28 GHz and a Finesse $F = 16$	109

6.6	Experimental intensity spectra of a CROW with $M = 20$: by controlling the resonance of two ring resonators (red rings in (c)), the length of the delay line (green rings in (c)) was discretely changed from $N = 2$ to $N = 9$	110
6.7	Intensity measurements and delay of a CROW structure with $M = 20$, for N varying from 2 to 6.	111
A.1	Graphical representation of the coupler with the amplitudes of the fields at the four ports.	117
A.2	Graphical representation of a ring resonator structure coupled to two bus waveguides, with the complex amplitudes of the fields in the different sections of the ring.	118
A.3	Schematic representation of an APF system. Starting from a basic level, it is possible to analyze systems with an increasing complexity where the Ring cell (green square) is obtained as a combination (matrix product) of sub-building blocks (couplers and waveguides - red and blue, respectively) and the cascade is a product of the matrix of each ring resonator multiplied by the waveguide phase shift matrix (orange).	120
A.4	Schematic representation of a CROW system. Starting from a basic level, with the consideration of fields (left) it is possible to analyze systems with an increasing complexity (right), where a basic building block (ring - green square) is obtained as combination (matrices product) of sub building blocks (couplers and waveguides - red and blue, respectively).	121
B.1	Schematic of Fabry Perot Cavity	127
B.2	Transmission spectra of a waveguide under consideration.	128
B.3	Waveguide Configuration for the estimation of the losses.	128
B.4	Fourier Transform of the transmission spectra of the device shown in Figure B.2. The oscillations in the transmission spectra are clearly visible from the presence of the the peaks in the FT. For a good estimation of the Transmission losses, it is necessary to have a FT with clearly isolated peaks.	130
C.1	Schematic of the Thermal Resistance. The difference in temperature on the two surface will produce an heat flow proportional to the Thermal resistance of the layer.	132
D.1	Scheme of a continuously tunable Ring based delay line: the coupled-resonator Slow light structure S1 provides a digital tunable delay and the all-pass ring S2 gives an additional analog tunable delay. . .	138
D.2	Time domain simulations for a Gaussian pulse traveling inside the coupled ring resonator structures while varying the number of on-resonance ring resonators [1].	139
D.3	Fine tuning of the delay by slightly changing the resonance wavelength of the last resonator (number 4 in the Figure) [1].	141

- D.4 a) Intensity transfer function in the Transmission (drop port: solid lines) and Reflection (through port: dashed lines). b) Group delay of a CROW structure with $N = 8$ rings and finesse $F = 4$ for apodized (blue lines) and non-apodized (red lines) structures. . . . 147
- D.5 Measured transmission ($|H_T|^2$) and backreflection ($|H_R|^2$) spectra of a reconfigurable coupled optical resonator structure with $N = 4$ (black solid curves), $N = 6$ (blue dotted curves) and $N = 8$ (red dashed curve) on-resonance Ring Resonators. Experimental data are averaged over 16 *FSRs* (1520 nm - 1580 nm wavelength range). (b) Backscattering of SOI (averaged over 87 GHz bandwidth of the device), versus the number N of coupled Ring Resonators. 148
- E.1 Time-domain measurements at 10 Gbits/s of the tunable delay of a Slow Wave Delay line with bandwidth $B = 50$ GHz. (a) 100-ps-long Gaussian probe pulses with carrier λ_r are employed. (b) Reference trace (black) corresponding to propagation in the bus waveguide only ($N = 0$); delay of 39 ps (red) 69 ps (blue) and 90 ps (green) with negligible pulse distortion are obtained when 3, 5 and 7 Ring Resonators are tuned at resonance, respectively. (c) Experimental eye diagram for 10 Gbits/s NRZ transmission: input optical signal (upper image) and output optical signal delayed by 50 ps (lower image) 151
- E.2 Transmission of 10 Gbits/s DPSK - NRZ data stream through a reconfigurable Slow Wave Delay line with bandwidth $B = 50$ GHz: (a) setup scheme; (b) eye diagrams of the input DPSK signal (left side) and of the DPSK signal transmitted through the device with a delay of 50 ps (right side). 153
- E.3 Schematic of the time-domain characterization principle, exploiting 10 ps long Gaussian probe pulses, equivalent to 100 Gbit/s OOK-NRZ transmission; b) measured optical pulses at the output port of SOI Delay Line with bandwidth $B = 87$ GHz, $F = 5.17$ and $M = 20$: delay and attenuation is observed when 0 (black), 4 (red), 8 (green) and 12 (blue) Ring Resonators are tuned at resonance; only a slight broadening and distortion of the pulse is noticeable for highest delay. 154

List of Tables

2.1	Electron Beam Parameters for the definition of the pattern.	20
2.2	Electron Beam Parameters for the definition of the pattern in HSQ.	23
2.3	Silicon Etching Parameters in BP80 RIE.	29
2.4	Silicon Etching Parameters in STS ICP	30
2.5	Silica Deposition Parameters	33
3.1	Deep Etched vs Shallow etched waveguides: main comparison parameter summary	46
3.2	Comparison between design specifications (K_D) and experimental results (K_M) for several fabricated couplers.	62
3.3	Comparison between design specifications (K_D and Q_D) and estimated value (K_E) of the coupling coefficient through the extraction of the the real coupling coefficient from the measured Q -factor (Q_M).	70
3.4	Comparison between the Q -factor of Ring Resonator Phase Shifter (Q_{PS}) and Ring Resonator Filters (Q_D) for different value of K	75
4.1	Thermo-optic coefficients for Silicon and Silica, a difference of one order of magnitude is present between the two coefficients.	81
6.1	Comparison between design specifications and measured parameters for three different configurations of Coupled Optical Resonators.	108
C.1	Thermal conductivity and electrical resistivity of the materials under interest.	135
D.1	Apodization of 20 rings coupled ring resonator in Reflection configuration with Finesse values of 4 and 8: the values of the coupling coefficients required and the corresponding values of the gap dimension (G).	148
E.1	Figures of merit for the state-of-the-art integrated ring resonators delay lines.	156

To my father and my mother

*and to Cinzia, the love of my life:
the present and the future.*

Chapter 1

Introduction

1.1 Slow Light features and motivation

The high frequency of light allows for great information carrying capacity (potentially up to several tens of *Tbit/s*). Efficient data transmission over long distances in optical fibres or in a single chip in integrated optics is achievable in low attenuation systems – due to the small interaction (reduced absorption) of photons with the matter. This advantageous feature, however, also makes the control of optical signals more difficult, especially in the time domain. The slowing of light can be used to increase the strength of the light-matter interaction and for delaying optical signals. In this perspective, a key role could be played by photonics in providing functionalities for the time-domain control of optical pulses: delaying, data synchronization, buffering and storage.

To access this functionality, the control of the group velocity v_g of a propagating light pulse is required. The group velocity is defined [2] as:

$$v_g = \frac{c}{n + \omega \partial n / \partial \omega} \quad (1.1)$$

where c is the velocity of light in the vacuum, ω is the optical angular frequency and n is the refractive index of the medium. The group velocity not only depends on the refractive index (as defined with respect to the phase velocity $v_p = c/n$), but also on the dispersion (i.e., $\omega \partial n / \partial \omega$). In the slow-light regime, v_g is typically reduced by the large dispersion arising from an optical resonance within the material or

the structure. The group velocity reduction is the fundamental figure of merit in slow light phenomena and is generally referred to as the slow down factors, defined as:

$$S = \frac{v_p}{v_g} = \frac{\tau_g}{\tau_p} \quad (1.2)$$

where τ_g and τ_p are the group and the phase delay associated with the pulse propagation. The slower the optical propagation, the higher is the introduced delay and the higher is the slow-down factor. As shown in Figure 1.1, when an optical pulse propagates through a slow-light medium, it experiences spatial compression due to the velocity slowing-down. Consequently, in order to provide the conservation of the total energy flow, the local intensity increases.

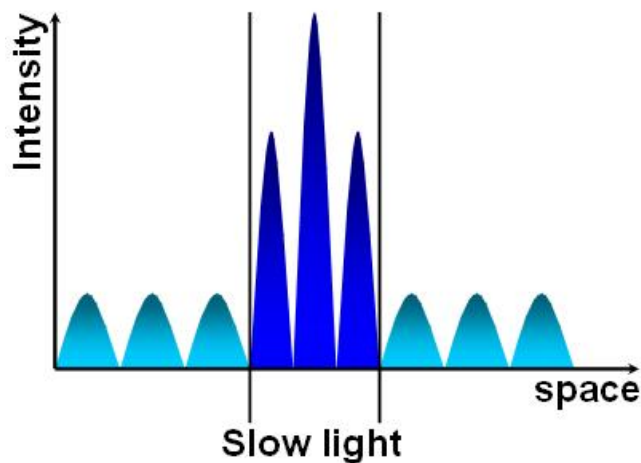


FIGURE 1.1: Spatial compression and intensity enhancement of optical pulses propagating into a slow-light medium.

In the linear regime, slow light produces a spatial compression by a factor S of the optical pulse. This means that the light interacts with the medium for S times longer and all the linear effects are consequently enhanced by a factor S . In a slow-light medium of length L , absorption, gain, phase shift and delay behave exactly as in a medium of length SL , allowing significant reduction of the dimensions of several optical devices. This property can be exploited in any application based on optical phase modulation, whether the physical phenomenon that induces the phase shift is thermo-optical, elasto-optical or electro-optical [1].

Slow light can be employed to match the velocities of the optical and electrical waves, or to reduce the interaction length between them, in both cases improving

bandwidth and efficiency of the modulation [3, 4]. In the same way, since the phase shifting is enhanced by slow light, it can usefully be exploited in optical switching devices [5]. The most important application in the linear regime is the ability to control the time-delay of an optical pulse. By slowing down the velocity of the light, remarkable delays, that otherwise would require several tens of centimetres of fiber optic or several millimetre of integrated optical waveguides, can be provided in sub-millimeter slow-light devices.

In non-linear propagation, besides the spatial compression by a factor S , intensity considerations have to be taken into account. In the slow light regime the mean power P_m is increased with respect to the input mean power P_{in} , due to the resonance of the material or of the structure. The enhancement factor P_m/P_{in} is, as a result, once more equal to the slowing ratio S . The non-linear effective phase shift experienced by an optical pulse is therefore enhanced by a factor S^2 for non linear effects, like self-phase modulation (SPM), cross-phase-modulation (XPM), Raman and two photon absorption (TPA), while in four wave mixing (FWM), where four waves interact, it is proportional to S^4 [4–6].

Research into slow light promises therefore to bring a wealth of applications, in particular in the field of telecommunications and optical data processing. The aim of the present work is the realization of efficient and large bandwidth photonic devices for slow-light applications.

1.2 Slow light approaches

In some early studies on slow light, researchers used the large normal dispersion associated with electronic resonances in atomic systems. Processes such as electromagnetically induced transparency (EIT) and coherent population oscillations (CPO) were used to generate narrow transparency windows within absorption resonances. The smallest group velocities ever observed (17 *m/s*) were obtained in this way [7, 8], yet requiring impractical low temperatures and exhibiting narrow spectral bandwidths. Larger bandwidths have been achieved by exploiting two closely spaced absorption resonances in atomic systems [9].

Stimulated scattering processes, commonly found in room-temperature telecom optical fibers, such as stimulated Brillouin scattering (SBS) and stimulated Raman scattering (SRS), have also been exploited to produce slow-light effects. These

techniques make use of the rapid variation of the refractive index that occurs in the vicinity of the Brillouin or Raman gain feature. The group velocity of a probe pulse can be calculated by using the susceptibility formalism in [10]. The wavelength at which the induced delay occurs (ω) is tunable by controlling the wavelength position of the laser pumping process (ω_p). Depending on the process involved, the resulting tuned wavelengths are $\omega = \omega_p - \Omega_R$ and $\omega = \omega_p - \Omega_B$, where Ω_R and Ω_B represent the angular frequency shift of the Raman and Brillouin process, respectively.

First SBS-based works demonstrated delays of 63-ns-long pulses by 25 ns (fractional delay 2.5) with no distortion and delays of 15-ns-long pulses by 20 ns (fractional delay 1.3) with some pulse broadening [11]. In more recent work, multiple SBS gain lines were exploited either to increase pulse delay [12] or to broaden the SBS gain spectrum far above the GHz.

Larger bandwidths are offered by SRS processes, ranging into the THz scale for typical fibers, yet not providing significant improvements in terms of fractional delay with respect to SBS-based slow-light [13]. Demonstration of SRS-based slow-light in integrated devices has been also reported. Tunable delays of up to 4 ps for 3-ps-long pulses have been achieved in a compact (8 mm) silicon-on-insulator (SOI) planar waveguide [14]. Alternative fiber-based approaches exploit the wavelength conversion of an incoming pulse, which is then supplied to a strongly dispersive medium and, finally, reconverted to the original wavelength [15, 16]. In these schemes, tunable delay is obtained as a function of a wavelength conversion due to the Raman or Brillouin frequency shift.

To date, possibly the best results have been achieved by combining a periodically poled lithium-niobate waveguide, as a rapidly tunable converter, and a dispersion compensating fiber, to introduce a continuous delay: this scheme was demonstrated to provide up to 44 ns delay on a 10 Gbits/s NRZ data stream [17].

Although very large delays can be obtained, these approaches require a variety of optical sources (for an efficient wavelength conversion) and many km of dispersion compensating fiber – therefore they cannot be integrated on chip-scale and are not cost-effective.

1.3 Integrated Slow Light Structures

Large group delays can be achieved by taking advantage of the dispersion properties of waveguide-based resonant photonic systems. The idea is to *trap* the light inside an optical resonators for a time which is proportional factor Q -factor (or alternatively, the Finesse F) of the resonator [6].

Different topologies of resonators can be used as building blocks for slow light structures. These include structures such as micro-disks [18] or micro-toroids [19], Bragg cavities [20, 21], nanowire cavities [22–24], coupled ring-resonators [25, 26], or photonic crystal (PhC) waveguides [27, 28].

Figure 1.2 are shown scanning electron microscope (SEM) images of some of the fabricated resonators.

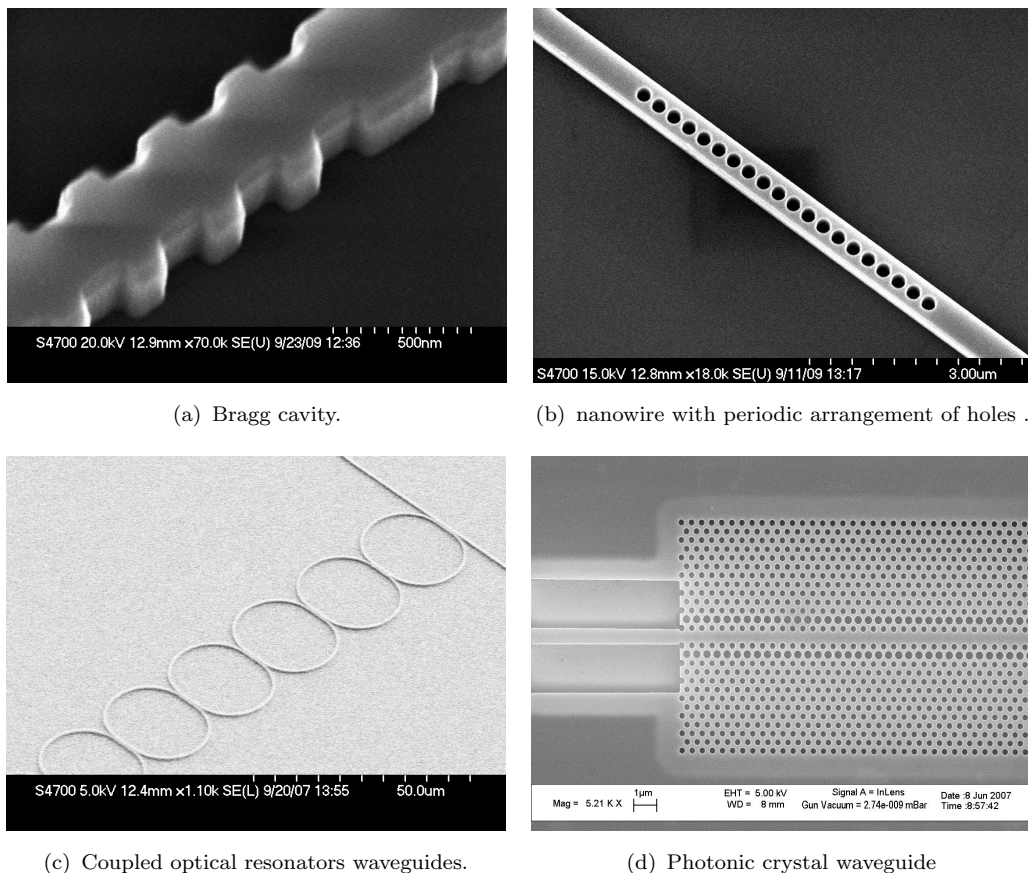


FIGURE 1.2: Scanning electron microscope pictures of several configurations of slow light structures fabricated in the course of this work in the James Watt Nanofabrication Centre (JWNC).

Although, theoretically, these geometries may be regarded as having a measure of equivalence, each one is characterized by distinct critical features, from a practical

and technological point of view. Compact Bragg devices, for example, are difficult to obtain with low-index contrast technologies, while high technological accuracy is required when higher index contrast technologies are employed. PhC devices can be engineered to produce large group velocity reduction (as much as 300 times smaller than the vacuum light speed) and fast activation speed [27]. However they are very sensitive to fabrication tolerances. Better results have been demonstrated by exploiting ring resonators based on structures made from glass [29], polymer [30] and silicon [31] waveguides.

Despite the fact that PhC and ring resonator based structures have shown comparable performance in the slow light regime [32], it was decided to focus the present work on ring resonator approach. The reasons for this choice were related to the better device parameter control – and the availability of an easier tuning scheme. Ring resonator structures are a relatively mature and reliable option in the slow light scenario – being able to provide the combination of a large bandwidth and large fractional delays in integrable and relatively small footprint devices.

1.4 The Potential of Photonics

The ambition of photonics is to become a pervasive technology, able to address the emerging limitations of microelectronics. The continuous growing of the traffic and the increasing bandwidth demand require the development of electronic devices with increasing speed. The miniaturization of integrated transistors, with faster switching time, also results in an increase of the parasitic RC factor of electrical interconnections [33, 34]. This will lead to a situation in which the total signal latency is dominated by the interconnection delay. Integrated optics promises also to be able to address power consumption and heat dissipation issues [35], which are becoming a major limitation in micro-electronics – as instance by the fact that a 2 billion transistor processor [36] dissipates more than 100 W/cm^2 .

Optical links have been initially introduced for longer distance communications and are becoming increasingly relevant for shorter distance communications [37]. In the short term, the signal conversion from electrical to optical processing and vice versa would be required at the chip level, because of bandwidth requirements –

and for the possibility to harvesting the heat [35]. Optical waveguides for interconnection and routing functions will possibly be able to overcome the *interconnection bottleneck* of electronics [38].

The mission of integrated photonics should be therefore to develop large bandwidth, low-power, cost effective and chip-level integration optical circuits. Moreover the development of processes that are compatible and cost comparable with electronic manufacturing is required.

It is in this perspective that slow-light could become an appealing feature for application – in which the control of the group velocity would make achievable applications such as: dynamical delay and synchronization of the signals.

The present-day photonics industry is characterized by exploitation of a variety of different materials and technologies, each one optimized for a defined functionality: *InP* and in general III - V compounds for optical sources, *LiNbO₃* for modulators, silica-on-silicon for passive DWDM filters.

A deeper analysis and a comparison between them is therefore required in order to identify the best technology for our purposes.

1.4.1 Index-contrast and materials

The refractive index contrast Δn has a strong impact on the device dimensions, fabrication tolerances and device performance. The definition $\Delta n = (n_{wg} - n_{cl})/n_{cl}$ is used, where n_{wg} and n_{cl} represent the waveguide and cladding refractive index, respectively – and the higher is Δn , the stronger is the light confinement.

As shown in Figure 1.3 higher light confinement enables the use of a smaller waveguide bending radius. In the development of ring-resonator based architectures, R_{min} allows a corresponding decrease of the device footprint. R_{min} is also inversely proportional to the maximum achievable *FSR* – and hence to the possibility of providing large bandwidths [39].

The strength of the light confinement also sets the maximum size of the optical waveguide, if single mode operation has to be guaranteed. Smaller waveguide cross-sections are more sensitive to fabrication tolerances – so accurate control of the fabrication and high resolution lithographic tools are required.

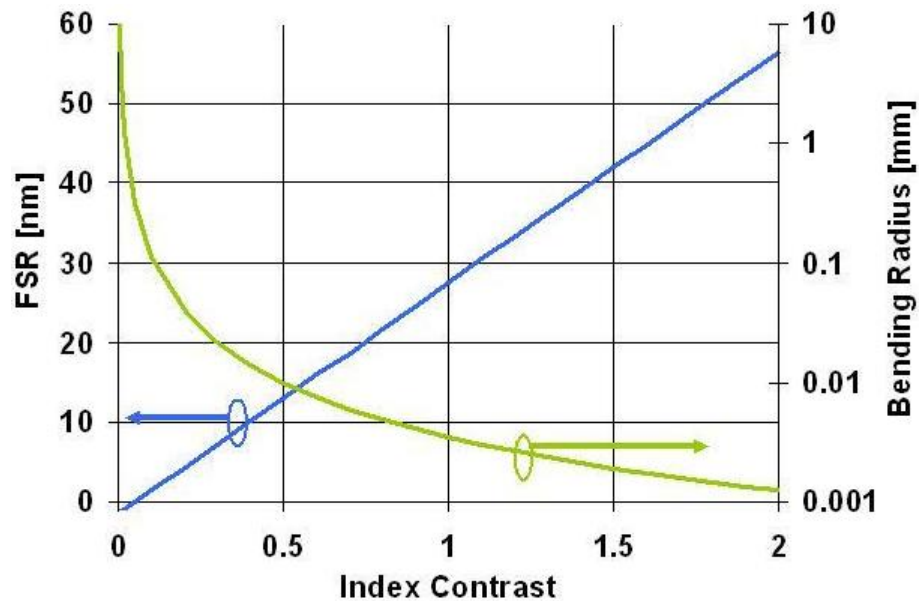


FIGURE 1.3: Dependence on the index contrast Δn of the Free Spectral Range and of the minimum allowed bending radius that guarantee a figure for the radiation losses of 0.1 dB/rad . For a defined index contrast, values of radii below the green line produce an higher value of the radiation losses.

For sub-micrometre dimension devices, a waveguide dimension perturbation of the order of a few nanometers is enough to cause a non-negligible alteration of the behaviour of the propagating mode. Scattering processes due to sidewall roughness become a critical issue.

Furthermore, the reduced dimensions of the optical waveguides and the high index contrast reduce the fibre-to-waveguide coupling efficiency – because of both the index and the mode mismatch at the interface, producing backreflection and radiation losses. Higher reflectivity in the facets of the sample, and the reduction of the mode field diameter (MFD) of the waveguide, reduce, in turn, the percentage of power coupled into the system.

A further implication of the magnitude of the index-contrast concerns the polarization state of the propagating field. When the index-contrast increases, the continuity conditions at the dielectric interfaces of the waveguide generate field components in both the longitudinal direction and the minor transverse direction – in particular, close to the waveguide corners. The guided modes are no longer largely transverse polarized, but show a significant degree of hybridity. Hybrid modes can be responsible for polarization mismatch when the waveguide mode has to be coupled with to fibre mode. A further implication concerns polarization

rotation effects that may arise in association with waveguide bending and sidewall roughness.

Looking at the scenario of present-day photonics materials, low index contrast silica-on-silicon technologies ($\Delta n < 0.01$), exploiting *Ge*, *P* or *B* doped SiO_2 layers on silicon wafers, enable very low losses (below 0.05 dB/cm), low birefringence and a high degree of repeatability and reliability. Several micrometre cross-section waveguides (typically $w = 5 \mu m$) provide, moreover, large modal areas that allow efficient coupling with standard fibers, having $MFD = 10 \mu m$ [40].

A low Δn value of 0.01 fixes the minimum achievable bending radius at about 5 mm – so, the maximum *FSR* of a waveguide ring resonator is below 10 GHz. The low index contrast prevents the possibility of increasing the bandwidth of the devices. The circuit dimension is on the order of several square centimeters.

The silicon oxynitride (SiO_xN_y) platform offers a tunable refractive index in the range from 1.45 up to 2.0, by changing the nitrogen concentration between the two opposite limits: silica (SiO_2) and silicon nitride (SiN). Devices fabricated with this technology [41] have a typical Δn of about 0.05, which translates into a minimum achievable bending radius of about $R_{min} = 400 \mu m$ and a maximum *FSR* below 100 GHz. The propagation losses associated to this technology are of the order of 0.3 dB/cm [42] at 1550 nm. Small core fibers with *MFD* between 3 μm and 4 μm are required for efficient coupling. The main drawback of SiON technology is an absorption peak in the wavelength range between 1500 nm and 1510 nm [43] – which, being as much pronounced as the *SiON* index is high, limits once again the possibility of increasing bandwidth and integration scale.

To further increase the index contrasts, only a limited number of available materials can be found. Si_3N_4 provides a refractive index about 2 at 1550 nm and so a Δn of about 0.4 [44]. Bending radii down to 25 μm and maximum achievable *FSRs* up to 1 THz [45] have been reported – and so the realization of very compact and large bandwidth devices is possible. The main drawback is an increase of losses (about 1 dB/cm [46]), sidewall-roughness induced backscattering, fabrication tolerance sensitivity and polarization issues [47]. Tapered and lensed fibers to reduce the spot sizes down to 1 to 2 μm , as well as mode adapters to enlarge the waveguide mode dimension, are required.

Finally, the maximum index contrast in optics can be obtained exploiting semiconductor materials. III - V compounds, like indium-phosphide (*InP*) and gallium-arsenide *GaAs*, provide a refractive index about 3 ($\Delta n = 1$), while silicon (*Si*) provides a refractive index of 3.5 ($\Delta n = 1.4$). For these technologies, the same considerations given for *SiN* hold: bending radii can be as small as few microns (about $1.5 \mu m$ for Silicon) and maximum *FSR* achievable increases to more than $7 THz$. However a waveguide dimensions of only few hundreds of nanometres, make side-wall roughness-induced backscattering the dominant contribution to losses, that increase to about $2 dB/cm$, while fabrication tolerances sensitivity, fiber to waveguide coupling and polarization issues, become very challenging issues to address.

In the choice of a platform for integrated photonic devices, however, not only the refractive index contrast has to be taken into account. A key role is played by the technological maturity and the potential improvement of the process, the costs, the capability to realize on the same platform a wide set of functionalities, the potential for further integration with other platforms and with the present micro-electronic technology.

Semiconductor materials, despite the described drawbacks, are the most promising technologies: besides enabling the highest down scaling of optical components, they are also the best candidates to realize monolithic or hybrid integration on-chip of all the optical functionalities.

III - V compounds show the best performances for active devices: efficient sources and modulators suitable for DWDM applications up to $40 Gbit/s$ [48] and high-efficiency photo-detectors operating up to $160 Gbit/s$ [49] have been in the market place for long time. Integration between III - V active devices with microelectronic driver circuits, as well as with passive silicon photonic devices has been demonstrated.

Silicon on Insulators (SOI) shows, instead, the best performances for passive devices, promising ultra-small footprint and high speed add/drop and multiplexer/demultiplexer filters and interconnection networks [50], but the great advantage of silicon-based photonics lies in its intrinsic compatibility with microelectronic CMOS technology [51]. This not only give the possibility of a natural and complete integration between optic and electronic devices and functionalities, but suggests also that the exploitation of the same process baselines, fabrication tools, packaging solutions and standards of microelectronics manufactures, could give

a substantial boost to the development of photonic devices, at effective cost and suitable for mass-market applications [52].

1.4.2 Silicon On Insulator platform

Silicon on Insulator was chosen as the best solution to fit our purposes, for the considerations that follow.

The transparency range of Silicon extends from $1.1 \mu\text{m}$ to the far infrared region (absorption of the bulk material at 1520 nm is only 0.004 dB/cm), covering therefore both the second and third windows of optical communications [53].

The refractive index contrast between Silicon ($n_{Si} = 3.5$) and Silica ($n_{SiO_2} = 1.46$) is $\Delta n = 1.4$. Due to the high confinement of the optical field, typical waveguide cross sections are $220 \times 500 \text{ nm}^2$ [51, 54] and the minimum permissible bending radius is only about $R_{min} = 1.5 \mu\text{m}$. Sharp bends have two advantageous effects: a dramatic scaling of the device footprint that enables high density integration on a single chip – and a very broad maximum achievable free spectral range, $FSR_{max} = 7 \text{ THz}$, that enables the realization of filters with both large bandwidth and high selectivity.

Silicon photonics has attracted a lot of interest in the last years for its compatibility with the CMOS industry. The fabrication process can be carried out in established industrial machines – exploiting consequent economy of scale to effective cost production. The eventual integration with microelectronics and monolithic photonic integration with other platform would make it possible to realize, on the same substrate, all the optical functionalities and use it in a vision of optical interconnection.

A key limitation for Silicon is the scattering process due to sidewall roughness that becomes the dominant contribution to losses [55, 56]. A few nanometer amplitude scale of roughness is enough to produce significant values of propagation losses (for instance, 5 nm standard deviation roughness results in 10 dB/cm losses). At the beginning of the work, the state-of-the-art loss figure for silicon waveguides was $1.7 \pm 0.1 \text{ dB/cm}$ [31]. A considerable effort in process optimization at Glasgow University has decrease this figure to a value of $0.92 \pm 0.14 \text{ dB/cm}$ [57] which still represents the best reported loss value for deeply etched SOI waveguides. Further

improvements require the use of a different fabrication approach (0.3 ± 0.02 dB/cm [58]) or waveguide geometry.

Moreover, strong confinement of the optical field makes the component more sensitive to fabrication tolerances, because small inaccuracies cause non-negligible alteration of the propagating mode. Very high accuracy and high resolution lithographical tools are therefore required. This suggests also the need to evaluate carefully tolerance effects on component transfer functions, in order to make their design more robust and to develop suitable techniques and efficient algorithms for tuning of the devices.

The coupling loss is typically about 10 dB/facet – so mode adapters, such as inverse tapers [59] or out-of-plane gratings couplers [60], are required at the chip-edge in order to enlarge locally the waveguide mode size, with the goal of improving the coupling efficiency and maximizing the coupling tolerances to fiber misalignments.

An advantage of SOI compared to planar silica waveguide technology is related to the efficiency of the thermo-optical effect, which can be used for phase adjustments and active control of the optical elements by thermally tuning the local refractive index. The higher thermo-optical coefficient (one order of magnitude greater than silica) and the lower thickness of the silica cladding layer between heaters and waveguides, make the power consumption of silicon devices more than two orders of magnitude lower than their silica counterpart, as well as the time response more than one order of magnitude faster.

1.5 Aims of the Thesis

The role of this Thesis work in this scenario is to develop ring resonator based tunable slow light structure on Silicon Photonics. Although slow light is a research topic that has existed for some time, it has been in practice limited to the narrow-bandwidth available. The perspective of the present Thesis is to realize reliable devices for high-bit rate optical signal processing.

For these reasons, the interest in slow light has grown remarkably in the last three to five years. This is confirmed by the increasing number of publications in the field (including a special issue of Nature Photonics in 2008), by the space dedicated to this topic in the most important conferences of optics and photonics,

and by the capital investments in slow light research from both public and private institutions.

Leading academic institutions around the world have research groups engaged in this theme. The most important microelectronics companies, like Intel, IBM [31] and NTT [28] have active *R&D* groups working on slow-light. To this aim, much effort has been put in to developing advanced components in SOI technology, as is proved by the 'exponentially' increasing number of scientific publications in the last ten years. Potential merits motivated from the most important majors of microelectronics, like Intel [61] and IBM [62], planned detailed and challenging road maps to boost SOI market.

Major challenges mainly related to the high index contrast, such as propagation losses, backscattering, variability control and coupling losses, together with an efficient tuning scheme have been analyzed and solved in this work.

Looking now at the organization of the thesis:

Chapter 2 describes the fabrication tools and techniques employed in the fabrication of the devices. The chapter starts with the introduction of the properties of the material used within this work, Silicon-on- Insulator (SOI), followed by the process step sequence employed for the fabrication of the devices is introduced and explained.

Chapter 3 describes the techniques and tools employed for the characterization of the fabricated devices. The reduction of the Fabry Perot oscillation of the cleaved facet is obtained with both anti-reflection coatings and inverse taper coupler structures. In the perspective of realizing coupled structure geometries, the design of basic building blocks is investigated – highlighting the limitations imposed by the technology and the solutions adopted.

Chapter 4 describes the technique adopted for the tuning of the structures and for compensation of the phase disorder. The thermo-optic effect is used to vary locally the refractive index. Thermo-controlled ring resonators have been fabricated and the power requirement per wavelength shift, the response speed and the thermal cross talk have all been evaluated.

Chapter 5 is focused on the repeatability of the fabrication process and the control over the variability of the device dimensions. This is a remarkable issue that needs to be addressed in order to obtain devices with a required working behaviour –

since, in the high index contrast case, even a nanometre variation may translate into an unacceptable variation of the device characteristic.

Chapter 6 presents the most common configurations of coupled cavities used to access slow light functionality. The advantages and disadvantages of each configuration are presented. The realization of the slow light structure is the best compromise that arises from considerations related to the the fabrication processes, the optimization of the single cells, the device control and tuning scheme. Interesting experiments in both static and dynamic regimes and in real communication systems, performed from project partners at Politecnico di Milano, are presented – in order to demonstrate the high quality of fabricated devices and their feasibility for practical applications.

Finally, in Chapter 7, conclusions about the results achieved in the present work are merged together with considerations on future activity that could follow from the present research.

Chapter 2

Fabrication Techniques

In this chapter, the fabrication techniques used for the realization of the structure under examination are described. Process limitations and further improvements are reported later in the course of this Thesis. The chapter starts with the introduction of the properties of the material used within this work, Silicon-on-Insulator (SOI), then the process step sequence employed for the fabrication of the devices is explained. Each section includes firstly a brief description of the standard micro-electronics type process, followed by a more detailed description of the particular process used for the realization of the photonic structure. Dedicated optimization of the processes developed is also introduced within the Thesis when required.

2.1 The Material

The substrate used within this project is a Silicon-On-Insulator (SOI) UNIBOND wafer produced by the Smart-Cut technique from SOITEC [63]. This technique is based on hydrogen ion implantation (i.e. protons) and bonding of two wafers to create a UNIBOND SOI wafer. A detailed description of the process can be found in [64]. A schematic view of this process is shown in Figure 2.1 – and it basically comprises the following steps [65]:

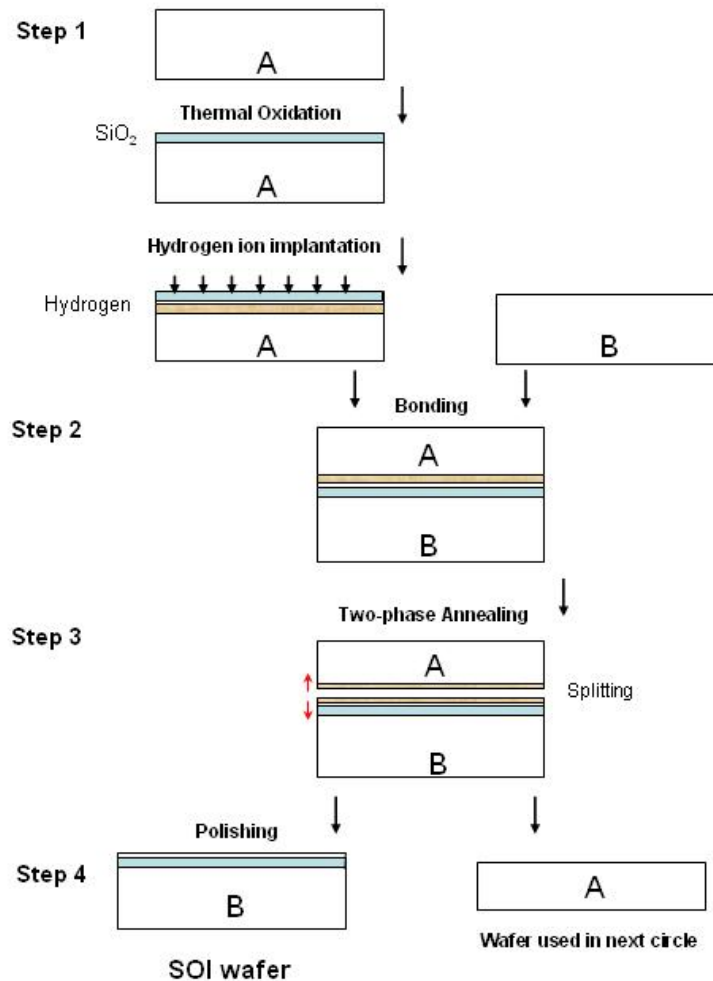


FIGURE 2.1: Schematic of the Smart Cut process for the production of Silicon on Insulator wafers.

- A wafer A capped with a dielectric layer (e.g., thermally-grown SiO_2) is exposed to hydrogen implantation at room-temperature in order to introduce a thin buried layer with hydrogen ions of sufficiently high density.
- The second step consists of chemical cleaning and hydrophilic bonding at room temperature of wafer A to a handle wafer B, by Van der Waals forces. The handle wafer serves as a stiffener and provides the bulk silicon beneath the buried SiO_2 in the final SOI structure.
- The third step consists of splitting and annealing of the two bonded wafers, including two stages of heating, a medium-temperature annealing stage (400-600 °C) and a high-temperature stage (about 1100 °C). During the first stage, a thin highly damaged layer appears at the depth of the maximum hydrogen ion concentration in the implanted wafer A, which splits into two parts –

yielding an SOI structure and the remainder of wafer A. The subsequent high-temperature thermal treatment removes radiation defects in the silicon layer and strengthens the chemical bonds between the two wafers.

- The top silicon layer is polished by a chemical-mechanical method to obtain a high-quality surface. Thus, as a result of the process, an SOI wafer and a residual wafer A are obtained, and the latter can be used again as a handle wafer.

The final SOI wafer, which is commercially available on the market, is composed of three layers: a top layer of Silicon with a nominal thickness of 220 *nm*, for the present work. This layer is the guiding core of the optical devices. Below the core layer there is a silica layer (BOX) with a nominal thickness of 2000 *nm*, which forms the lower cladding of the optical waveguides. The interface between the top layer and the BOX layer is very sharp with a very small level of roughness [64]. The silicon layer is typically lightly acceptor (Boron) doped, with a value of conductivity of 20 Ωcm , corresponding to a doping concentration of approximately $10^{15} cm^{-3}$ [66]. The optical losses induced by this doping value can be considered negligible. Finally, the substrate layer is made of bulk silicon 750 μm thick, which confers a mechanical robustness on the wafer.

2.2 Process Steps

The basic principle that is behind the propagation in a photonic structure is the the creation of two dimensional confinement for the light. The vertical dimension of the waveguide is defined by the core thickness (220 *nm* in the substrate under consideration) while the lateral direction is defined by means of lithography and etching techniques. Considerations relating to the waveguide width design are reported in section 3.2. The conceptual fabrication sequence is shown schematically in Figure 2.2. Each step and its optimization are discussed in detail in the following sections. In each each process the improvements are aimed at obtaining devices with an ideal rectangular cross section (i.e. small sidewall angle), with a small level of sidewall roughness – while trying to minimize, at the same time, the exposure time required.

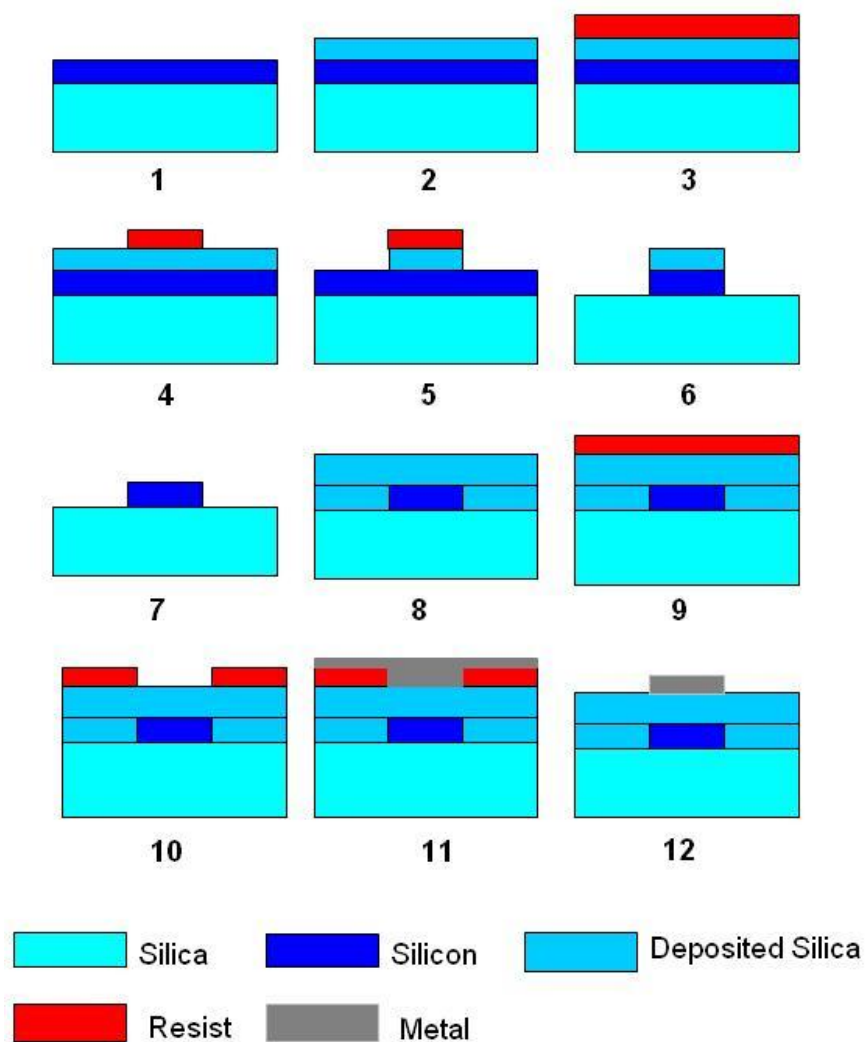


FIGURE 2.2: Sequential schematic of the process steps for the definition of the chip structure.

With reference to Figure 2.2 the steps for the fabrication of the complete structure can be summarized as follow:

- Marker: definition of a suitable structure for the alignment of different layers.
- Photonic Structure definition: Deposition of Silica (2), spinning of the resist (3), resist exposure and development (4), dry-etching of the Silica Hard mask (5), etching into the silicon core (6).
- Deposition of a Buffer layer of SiO_2 (8).
- Metal electrodes definition: Spinning of the resist (9), resist exposure and development (10), metal deposition (11) and lift off of the metal (12).

2.3 Patterning using Electron Beam Lithography (EBL)

Lithography is the transfer of a desired pattern into a material. The pattern is defined by exposing a radiation sensitive polymer or a sensitized resin which is spun on the surface of the sample.

The wavelength used in the exposure defines the minimum feature size achievable with a particular lithographic tool. Nowadays there are several techniques for the pattern definition and, in each field, researchers are trying to boost each technology to achieve smaller resolutions. Developments in Optical lithography, mainly supported by CMOS industry have proved to be able to scale down the gate dimension of CMOS transistors below 30 *nm* [67]. This pattern transfer approach consists in a single exposure, through a mask, of a large area of the wafer, for this reason this technique is fast and cheap. On the other hand, electron beam lithography (EBL) is characterized by an extremely high resolution – of the order of nanometer. It consists in a raster scan of a collimated beam on the surface of the wafer to define the structure – and is more flexible in terms of pattern definition (no mask preparation is required). So it is suitable for research where the pattern needs to be changed several times and the total area to be written is small.

Due to the small dimension of the devices required in this work, a Vistec VB6-UHR-EWF e-beam tool, which is a state-of-the-art in electron beam lithography machine, has been used for the pattern definition of the structures investigated. The Optical Lithography available in our facilities was limited to a resolution comparable with the wavelength used, 365 *nm* (i-line).

In the EBL control software, it is necessary to preset several parameters that dramatically influence the final quality of the patterned structure. After the definition of the pattern using a layout generation software, the pattern is processed with a software that fractures each region to be exposed in small areas (trapezia), which correspond to each position of exposure of the electron beam. The Trapezia are positioned over a square lattice grid – and the minimum distance between its points is called the *Resolution*. Row by row, the beam scans the grid horizontally, exposing only dots separated by a fixed gap: the *Beam Step Size* (which is therefore an integer multiple of the Resolution). The beam has a finite width that is

defined by the *Spot Size* parameter and it depends on the diameter of the aperture and on the beam current. The pattern is therefore a discrete set of exposed pixels.

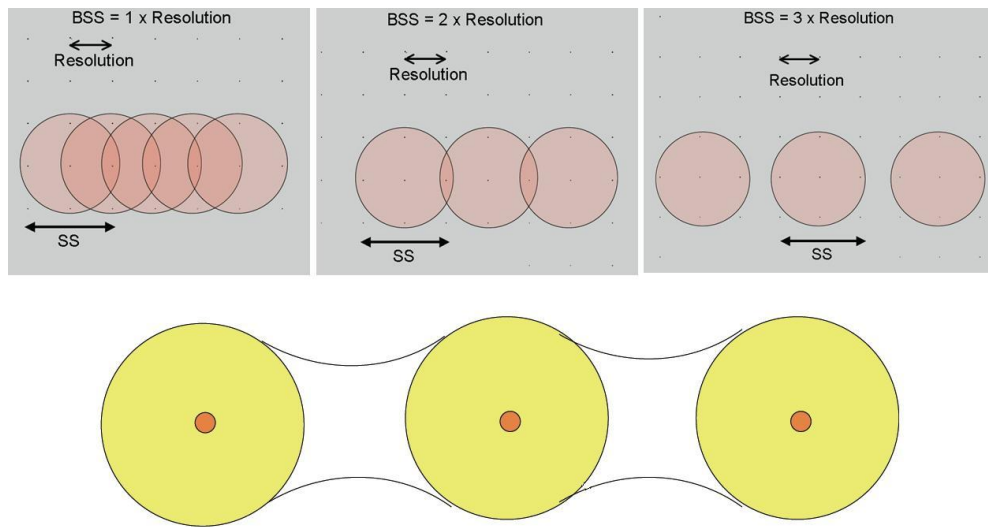


FIGURE 2.3: Graphical view of the effect of the choice of the BSS and SS, from the top left to top right the BSS is linearly increased, there is a point after that the line edge roughness become a problem as shown in the bottom picture (courtesy of Dr. S. Thoms, EBL notes).

The Beam Step Size (BSS) should be a fraction of the Minimum Feature Size (MFS), guide lines suggest to choose $BSS = MFS/5$. Figure 2.3 shows a graphical view of the effects associated with the choice of the BSS and SS. Clearly there is a point where the BSS starts to affect the integrity of a single pixel line. In this situation line-edge roughness becomes a problem. In the present work the SS has been always chosen to be around 2 times bigger than the BSS. Both were the best combination in terms of small line edge roughness (Small SS and BSS) and minimum beam time (Large SS and BSS). Further reduction of the Beam time is made possible by writing uncritical devices (i.e. broad-stripe waveguides) with bigger spots – and in the case of isolated patterns, this choice does not affect the final result.

Parameter	High Resolution	Low Resolution
Electron acceleration (keV)	100	100
Resolution (nm)	1	1
Spot Size (nm)	4/6/9/12	19/24/33/45
Beam Step Size (nm)	2/3/4/5	8/12/16/22

TABLE 2.1: Electron Beam Parameters for the definition of the pattern.

Table 2.1 shows the combination of values in terms of Beam Step Size and Beam Spot Size needed to obtain a device with minimal line-edge roughness.

The electron beam has a characteristic wavelength so small that diffraction no longer defines the lithographic resolution. Resolution is mainly limited by the scattering of electrons in the resist and underlying substrate. These electron scattering effects, often referred to as the proximity effect, cause exposure of regions surrounding the area where the electron beam was incident. Any pattern written can suffer significant variation from the intended size because of proximity effects. The EBL tool used within this work has a proximity correction that reduces the proximity effect by modulating the exposure dose according to the density of the pattern to be defined – and thus eliminating the extra exposure caused by the finite size of the electron beam. The resulting effect of the proximity is a smoothing of the dotted pixelated line.

The EBL tools have a finite writing field since the electrons cannot be deflected more than a certain amount without distortion. The complete pattern is divided into blocks which have to be stitched together by movements of the stage. Stage misalignment causes stitching errors when a pattern exceeds the boundaries of one field. The accuracy of stage positioning is a critical parameter that characterizes EBL tools. For this reason, during the design and the fracturing process, it is important to avoid situations where critical structures are on the boundaries of the fields. A value of misalignment of up to 30 *nm* could be present at each field boundary. The total field area for the e-beam is 1048.576 x 1048.576 μm^2 . Figure 2.4 shows an example of stitching error.

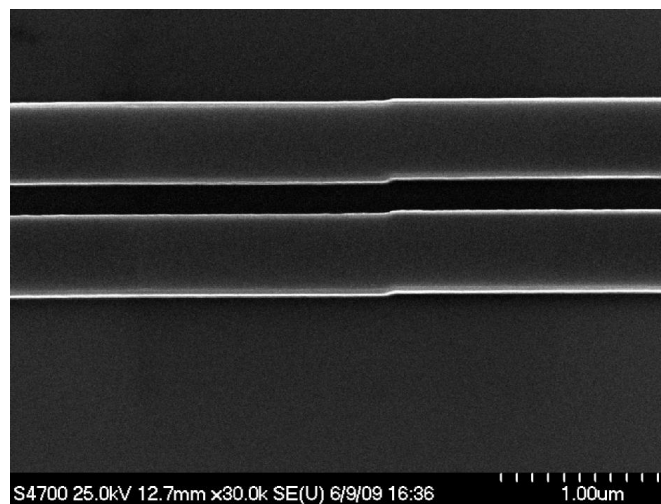


FIGURE 2.4: Stitching error on a coupled optical waveguide system.

All the patterns were realized in L-edit (Mask Editor Software), saved in a GDSII-type file to be processed in CATS (Computer Aided Transcription) for the fracturing and the proximity correction. After this process they were processed in Belle to define the beam parameters (desired dose, beam spot size and step size) and then transferred to the e-beam tool.

2.4 Process with Hydrogen Silsesquioxane resist

Resists are radiation sensitive compounds. During the exposure, they change their chemical structure – and become soluble in the development solution. Depending on how they respond to the electron exposure they can be classified as:

- Positive: the exposed regions become more soluble. The net result is that the pattern formed is the reverse of the mask.
- Negative: the exposed regions become less soluble – and the pattern formed is the same as in the mask.

Two important parameters define the resist structure:

- *Sensitivity*: For Negative resists is defined as the energy required to retain 100 % of the thickness of exposed region after development. The resist has a finite solubility in its developer even without exposure to radiation.
- *Contrast*: correspond to the selectivity between exposed and unexposed regions

An ideal EBL resist would have a high contrast, in order to allow vertical profiles after the development and a high sensitivity, which allow together the possibility of a low writing dose and a faster exposure process.

The characteristics of the resist available in our department are summarized in Table 2.2.

The fabrication process for the photonic structures changes, depending on the particular resist used. In most work to date, positive electron-beam resists such as PMMA and ZEP have been used to transfer the required device pattern into the

Resist	Tone	Contrast	Sensitivity	Etching Resistance
PMMA	Positive	Low	High	Poor
ZEP	Positive	Low	High	Poor
NEB	Negative	High	Low	Medium
HSQ	Negative	High	Medium	Good

TABLE 2.2: Electron Beam Parameters for the definition of the pattern in HSQ.

substrate (Figure 2.5). Their poor etching resistance (generally 1:1 of selectivity between mask and material to be etched) requires the use of a transfer mask layer of silica or silicon nitride. Any imperfection in the mask is amplified from the double step process.

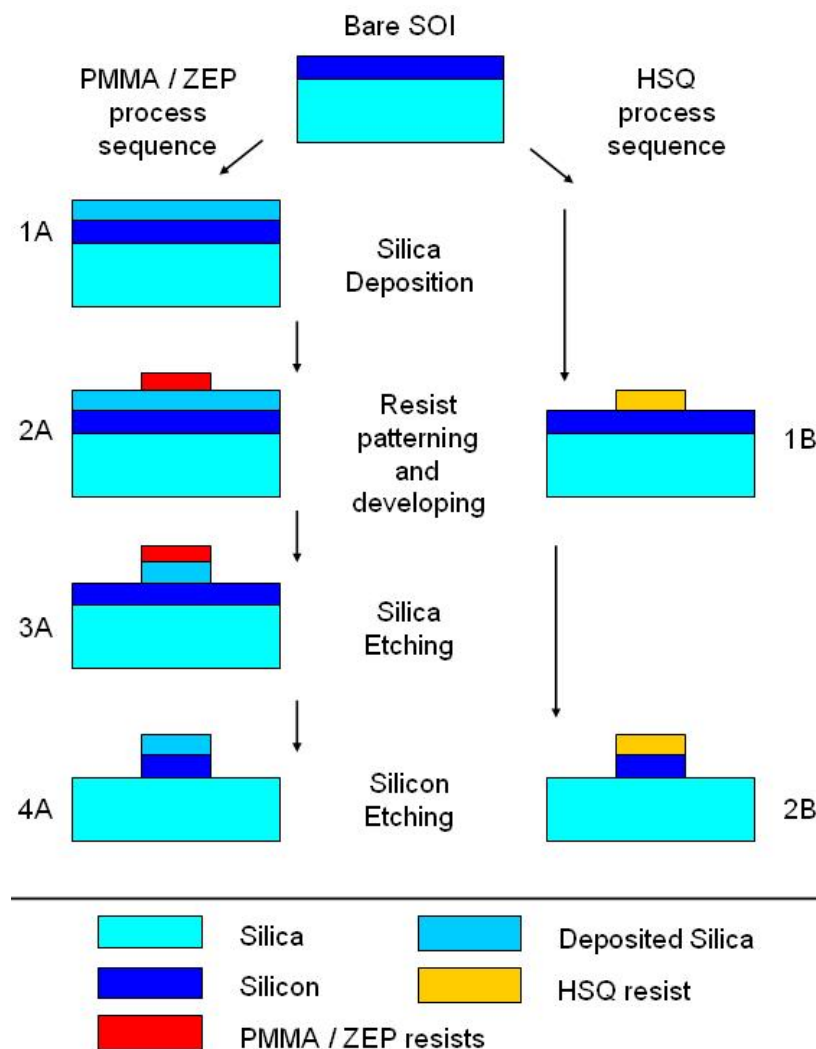
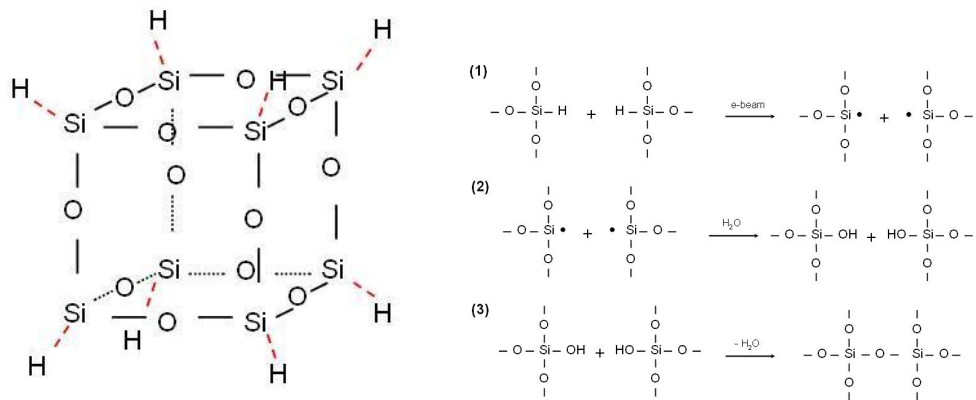


FIGURE 2.5: Schematic of the process steps for the definition of the guiding layer structures. On the left the process with PMMA or ZEP which require an intermediate hard mask of SiO_2 , on the right the process with HSQ, etching resistant e-beam resist. The process with HSQ results in a better quality of the devices and a reduced complexity of the process.

In recent years Hydrogen Silsesquioxane (HSQ), has proven to be a promising electron-beam resist because it combines high resolution at a moderate sensitivity with minimal line edge roughness, together with a substantial level of etch resistance [68, 69]. The fabrication process used in this work for the definition of the guiding structure was based on HSQ resist and consists of two main steps after resist coating: patterning (by electron-beam lithography) and development – and then silicon etching. The limited number of steps is made possible by the elimination of the transfer silica layer (Figure 2.5), with the net result of a reduced process complexity – resulting in a better quality and reproducibility. Even if the HSQ has a lower sensitivity when compared to many positive resists, the area to be written is substantially reduced, due to the writing of only the waveguide structures instead of their negative, making this parameter only marginally important in the choice of the best resist when compared to other figures such as the etching resistance and the contrast.

2.4.1 Literature Review on HSQ resist

The chemical structure of HSQ [70] is shown in the Figure 2.6. It consists of silicon, oxygen and hydrogen atoms that are initially disposed in a three-dimensional cage fashion [70]. When energy is applied (e.g. via an electron beam), the SiH bonds, which are weaker than SiO bonds, are displaced to form a three-dimensional network structure more similar to that of silica (Figure 2.6(a)) [69–71]. Details on the reactions that occur during the writing process can be found in [72] – and are shown in the Figure 2.6(b) for completeness.



(a) Structural formula of HSQ negative tone e-beam resist. (b) Typical reaction in the e-beam lithography for HSQ resist.

FIGURE 2.6: HSQ chemical structure and reaction under e-beam radiation.

The exposed region has a different level of reactivity with TMAH (Tetra-Methyl-Ammonium Hydroxide) [69], which is used as developer. The choice of the optimum thickness (dependent on concentration of the resist and spin speed), pre-baking (time and temperature), dose and development process (concentration, time and temperature) have different influences on the final quality of the mask for the etching. Ideally, this should be thick enough to protect the guiding layer and contain the minimum level of roughness that could be directly transferred to the guiding core during the etching process. In the following, the main attributes of HSQ are reported – and arise from comparisons of contrast curves for different baking and development conditions that are available in the literature [71, 73]

- by increasing the developer concentration, the contrast and reproducibility of the process increase – while the sensitivity reduces.
- Increasing the baking temperature also increases the sensitivity, but reduces the contrast: the effect of thermal curing is to start bond division and recombination, thereby favouring the transition to a network structure and reducing the cage/network ratio [71]. Baking can be considered as a sort of pre-exposure, which enhances the sensitivity but reduces the contrast.

Another important aspect that must be taken into account is the surface roughness, which depends on the baking temperature and is a function of the concentration of the developer (smaller for larger concentration) [73].

Since the aim is to achieve high contrast with a reasonably high sensitivity, maximizing repeatability and reducing roughness, it was concluded that the HSQ process should include:

- Low temperature bake,
- Minimum delay between bake and exposure,
- Use of high concentration developer.

2.4.2 HSQ process details

Taking into account all the considerations on the physics of the resist it is possible to choose a defined set of values that correspond to the best working point in

terms of performance of the resist. The baking temperature was fixed at 90 °C as in [71].

The developer used was TMAH (TetraMethyl Ammonium Hydroxide) at 25% concentration in water.

A nominal 200 nm film thickness process with a 2 minute bake at 90 °C was chosen as giving the best combination of conditions. This nominal thickness is obtained by using a 1:1 dilution of HSQ in MIBK (Methyl Isobutyl Ketone), spun at 3000 r.p.m. for 60 seconds. The best dose was found to be 1700 $\mu\text{C}/\text{cm}^2$: this value has been controlled for each batch of resist, presenting small fluctuations around the nominal dose value.

The unexposed resist was removed during the development in TMAH at 22 °C. The development is typically 30 seconds and no post exposure bake is necessary. This temperature is a critical aspect of the process and its value was controlled accurately by a digital thermometer (with a precision of $\pm 0.1^\circ\text{C}$). A subsequent rinse in De-ionized Water (DI) for 60 seconds (or more generally 30 seconds in each beaker) was used to remove the development from the surface of the sample. A final rinse with IPA (15 seconds) is useful for high aspect-ratio features because IPA has a lower surface tension than water: it does not self-dry and it is more easily extracted from the resist while drying, thus maintaining a low roughness level and allowing a more uniform drying with a nitrogen gun.

2.5 Etching techniques

The last fundamental step for the definition of the waveguide structures is the transfer of the pattern from the sample surface into the core layer, which is achieved by means of etching techniques, i.e. in the selective removal of unmasked material areas by a physico-chemical attack. Dry Etching techniques have been used because of requirements on anisotropy (i.e. vertical sidewalls), uniformity and etching time control.

A general dry etching process can be divided into the following four steps [74], shown schematically in Figure 2.7:

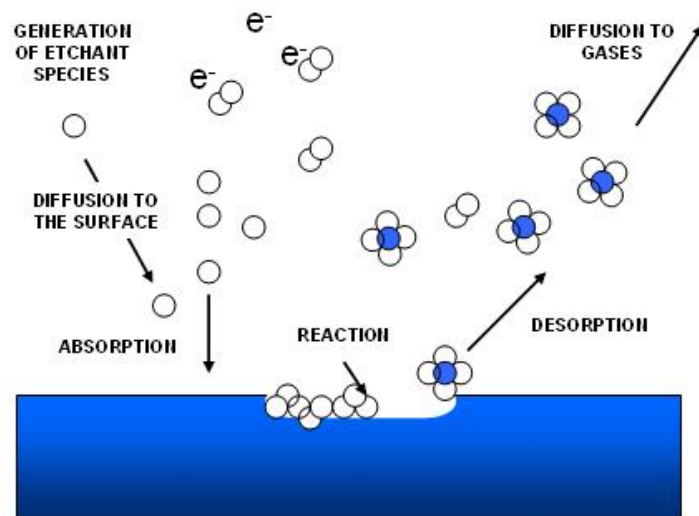


FIGURE 2.7: Schematic of an etching process. In the chamber there is first the formation of active species by electron collisional dissociation and ionization, diffusion to the wafer surface with subsequent absorption and reaction to etch the material both physically and chemically.

- 1 Production of active gas species by RF discharge of the reactive gases pumped into the chamber. This process is accomplished by electron collisional dissociation and ionization reaction.
- 2 Transport of the active species by diffusion from the bulk plasma of the discharge onto the surface of wafer.
- 3 Reaction steps:
 - Absorption of the radicals on the surface and concurrent ion bombardment.
 - Chemical reaction between the adsorbed reactive species and the materials to be etched.
- 4 Pump-out of volatile chemical byproducts.

The two main classes of dry etching available in our facilities are:

- RIE (Reactive Ion Etching): is a technique that remove the undesired material through the combined effect of chemical and physical interaction with accelerated ions. In particular conditions, RIE can produce both strongly anisotropic profiles and good selectivity between the mask layer and the material to be etched. RF power applied to two parallel plates is used to

control both plasma generation and ion acceleration; the etching rate directly depends on the plasma density. The increase of the RF power has the effect of increasing the self-biasing voltage on the cathode where the sample is located. The consequence is an increase in the ion bombardment energy – and hence a deterioration of the etching selectivity and increased sample damage.

- ICP: The plasma generation is separated from the etching chamber and there are two different RF power generators coupled to the plasma to control ion energy and ion density independently. An inductively coupled RF generator control the density of the plasma through the chamber walls and, in addition, capacitively coupled RF supply is used to vary the ion acceleration towards the material. ICP can produce a very high plasma density as well as low ion bombardment energy [74, 75]. The separate process for ions generation and acceleration make it possible to choose a well balanced set of operating parameters, in order to produce the etch profiles required.

During the course of this work, both the BP80-RIE machine from Oxford Plasma Instruments [76] and STS-ICP from Surface Technology Systems [77] were used for the etching of the Silicon layer.

2.5.1 Silicon Etching in RIE

In the RIE etching process, SF_6 chemistry was used. The isotropic nature of the process, together with the low selectivity, results in a thin mask with a high level of roughness (shown in Figure 2.8(a)), due to a too aggressive physical process – and undercutting as a result of an aggressive chemical processes.

To overcome this problem several experiments have been carried out by diluting the SF_6 with other gases such as O_2 . In the absence of O_2 , the etching is entirely isotropic – since it depends exclusively on the chemical reaction between the F^* ions and the exposed silicon [78].

The presence of O_2 has the effect of reducing the plasma density (preventing the recombination reaction of fluorine radicals with sulphur) and passivation (as a result of the reaction of fluorine radicals with oxygen and silicon with the growth of $Si_xO_yF_z$) [79]. The presence of the oxygen, however, has the effect of reducing

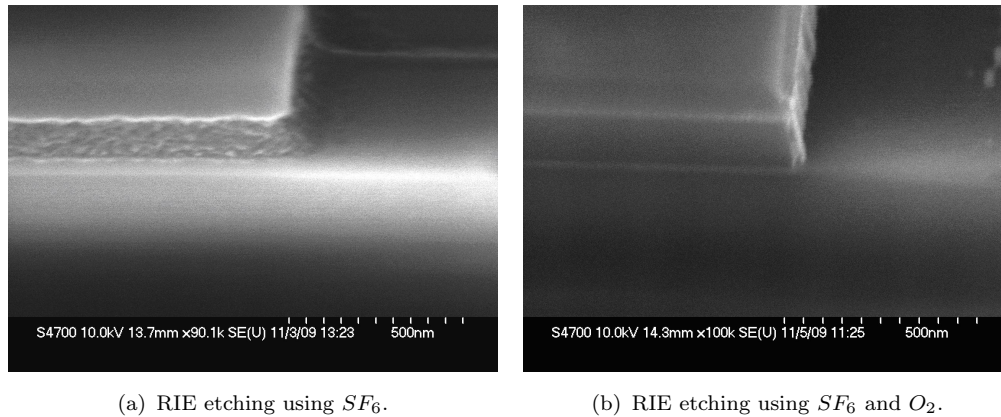


FIGURE 2.8: Scanning electron microscope pictures of Waveguide Cross Section etched with a RIE tool.

the etch rate due to the reduced power density. It is possible to increase the platen power, in order to increase the incident power density of the ions – and increase the speed of the process that limits the chemical reaction with the etched sidewalls. The best working conditions obtained by varying the pressure and the power are summarized in Table 2.3 and shown in Figure 2.8(b), which constitutes an example of an improved etching process for an RIE tool.

Parameter	Value
Gas	SF_6 O_2
Flow (SCCM)	10 15
Platen Power (W)	15
Bias (V)	-390
Pressure (mT)	15
Etch Rate (nm/s)	0.6

TABLE 2.3: Silicon Etching Parameters in BP80 RIE.

2.5.2 Silicon Etching in ICP

The silicon etching process using ICP-RIE was performed with $SF_6 - C_4F_8$ chemistry, with the parameters given in Table 2.4.

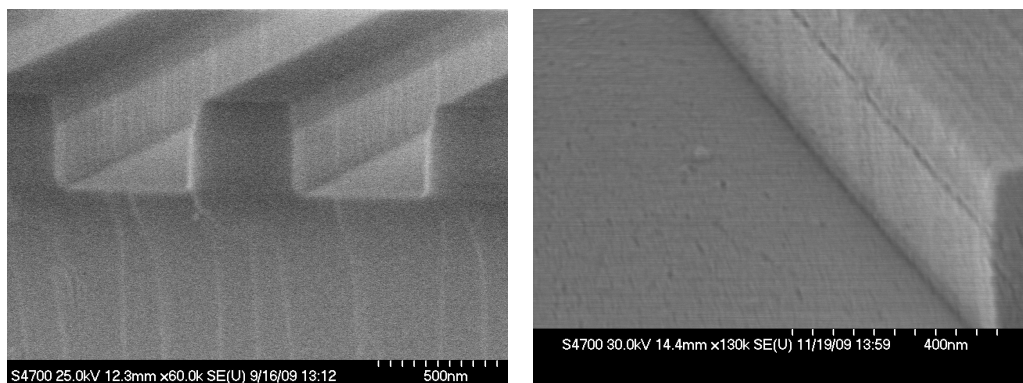
For this process, the vertical etching is assisted by deposition on the sidewalls: this technique is based on the idea that the vertical side-wall etching is protected by a deposited non-reactive film, but the horizontal surface is bare – and is open to etching [74]. In order to stop or weaken lateral etching, the sidewalls can be coated

Parameter	Value
Gas	SF_6 C_4F_8
Flow (SCCM)	30 80
Platen Power (W)	12
Coil Power (W)	600
Pressure (mT)	10
Etch Rate (nm/s)	2.2

TABLE 2.4: Silicon Etching Parameters in STS ICP

with a layer of etch resistant film. In the chamber, a repeated etching passivation process is obtained by introducing alternating gases.

The etching gas is SF_6 and the passivation gas is C_4F_8 . C_4F_8 in the plasma can form a fluorine-carbon compound which once deposited on the silicon surface, can prevent F^+ from further reacting with the silicon. Etching and passivation are switched every 5 seconds during the cycle. Although pure SF_6 gas reacting with Silicon results in isotropic etching, the etched surface is soon passivated by C_4F_8 . In the next round SF_6 , ion bombardment in the depth direction removes the deposited film to allow SF_6 to react further with the fresh silicon surface, whereas the ions cannot sputter-etch the sidewalls. The etching process is very fast, but at the same time slight: the Si etch rate is around 2 nm/s with a Si/SiO_2 selectivity of $\simeq 10$. Figure 2.9 shows an SEM micrograph of a typical fabricated waveguide.

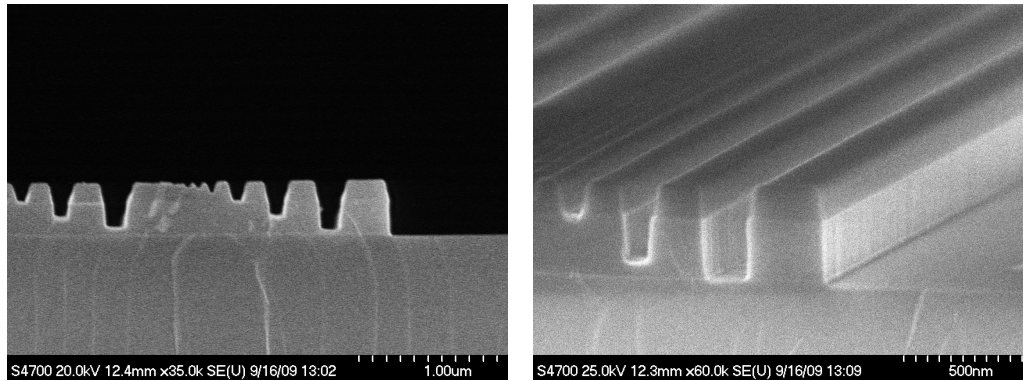


(a) The sidewall angle can be estimated to be 88° . (b) The sidewall roughness has a mean value of around 1 nm .

FIGURE 2.9: Scanning electron microscope of a waveguide cross section Waveguide Cross Section

The resulting sidewall angle was about 88° – and the roughness associated with this process was around 1 nm .

Maximum care was taken in the realization of a dense pattern with small gap dimensions. In this case, the RIE-Lag phenomena influences the patterned layout in terms of etching depth, which is reduced accordingly to the gap dimension. This phenomenon and its limitation is particularly imperative in devices such as coupled-waveguides, arrays and holes. In Figures 2.10(a) and 2.10(b) are shown, as an example of this phenomena, two SEM images of a waveguides cross section and an angled view at 45° .



(a) Cross Section of the test device, the etching depth is reduced accordingly to the gap size, due to RIE-lag phenomena.

(b) Angled view of the device under consideration.

FIGURE 2.10: Scanning electron micrograph of the *RIE – lag* phenomenon for 100 seconds of etching .

Several tests have been carried out for different etching times. Starting from the basic etching time (100 seconds) used for isolated waveguides and wide gaps, increasing etching times (110, 120, 140 seconds) have been investigated – and the results are summarized in Figure 2.11.

As expected, an increase in the etching time corresponds to an increase in the etch depth reached. For the shortest time (100 seconds), gaps as small as 50 nm are only etched 30 nm deep due to difficulties for the ion species in penetrating the gaps. Moreover, such small gaps are not fully cleared out after development – residual resist is still present at the bottom of the gaps, part of the etching process is spent by the chemical to clear out the resist, than start the actual etching process. For the longest process (140 seconds) the etching recipe proved to be able to etch fully gaps as small as 100 nm , while for 50 nm gaps a step of unetched material of 40 nm depth was still present at the bottom of the trench, as shown in Figure 2.12. The granular surface over the waveguide in the picture is due sputtering of a gold layer prior to the image acquisition, in order to reduce the SEM charging effect and improve the image quality.

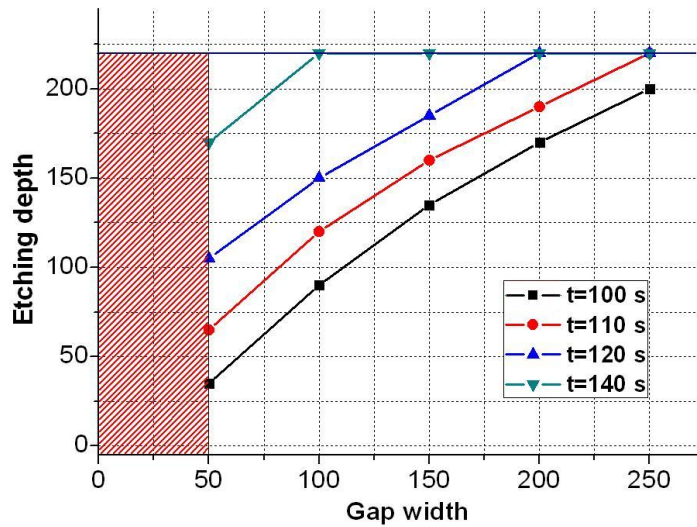


FIGURE 2.11: Dependence of the etching depth vs gap dimension in the HSQ resist mask.

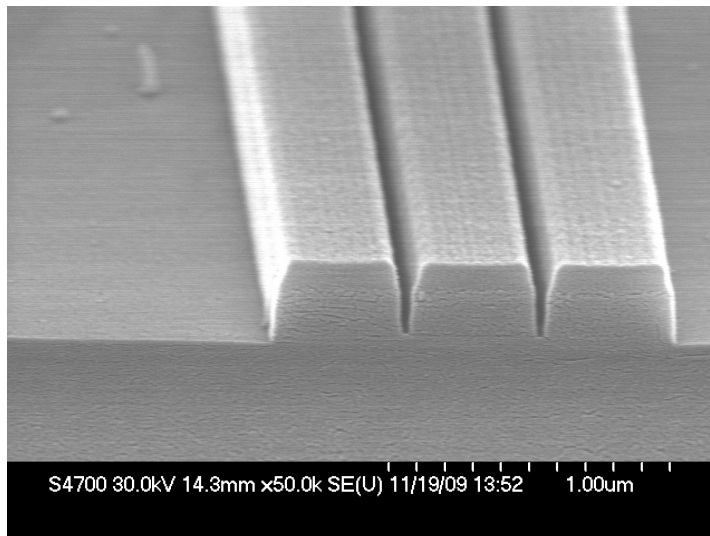


FIGURE 2.12: Scanning electron microscope of an array of 3 waveguide spaced 50 nm and etch for 140 seconds. Such small gaps are deeply etched and only 40 nm of material is still present at the bottom of the gaps.

It is important to notice that an etch of 140 seconds is at the limit of the mask quality – and any further time increase will result in damage to the mask edges and changes in the dimension of the fabricated waveguide. Solutions to this problem could consist in an increase in the HSQ mask thickness, at the cost of a readjustment of the dose and the etching parameters.

2.6 Silica Deposition

During the fabrication process, deposition of a silica film is required. Its purpose is to provide a buffer layer between the guiding structures and the metal electrodes – in order to minimize the absorption losses due to the interaction of the optical beam with the metal, or simply to protect the structure from the outside environment (i.e. dust that produces scattering centers). Preliminary studies have been carried out using PECVD (Plasma Enhanced Chemical Vapor Deposition) silica film.

PECVD is a low temperature (around 300 °C) method of deposition where the energy to dissociate the reactants is provided by RF, microwave and photon excitation [80]. In general, gas phase precursors are delivered into the deposition chamber, where free electrons are accelerated by the electric field to create a plasma. The excited atoms are accelerated out from the plasma region towards the deposition substrate, thereby helping to grow a silica coating. The desired stable film is produced as a results of the reaction with adsorbed species on the surface that form the chemical bonds. The nature of the deposition is governed by two main factors:

- 1 the plasma initiates chemical reactions that create radicals and ions
- 2 the energy with which these reactive species reach the substrate.

Different variables must be taken into account: RF power, temperature and the relative proportions of the input precursor. Each of these variables affects the reactions that occur in the plasma and the interaction that occur at the substrate interface. We used a standard recipe, which is summarized in Table 2.5.

Parameter	Value		
Gas	SiH_4	N_2O	N_2
Flow (SCCM)	9	710	171
Power (W)	10		
Pressure (mT)	1010		
Temperature (°C)	300		

TABLE 2.5: Silica Deposition Parameters

The deposited silica film thickness was found to slightly diverge from the nominal value about $\pm 5\%$. A refractive index equal to ($n_{SiO_2} = 1.461$) has been measured

by ellipsometry. The quality of this silica layer was also found to be characterized by a granular surface, as in Figure 2.13(a). The main problem encountered was the poor gap penetration capability of the plasma. The penetration is a fundamental requirement without which the working behavior of the devices under consideration would vary uncontrollably.

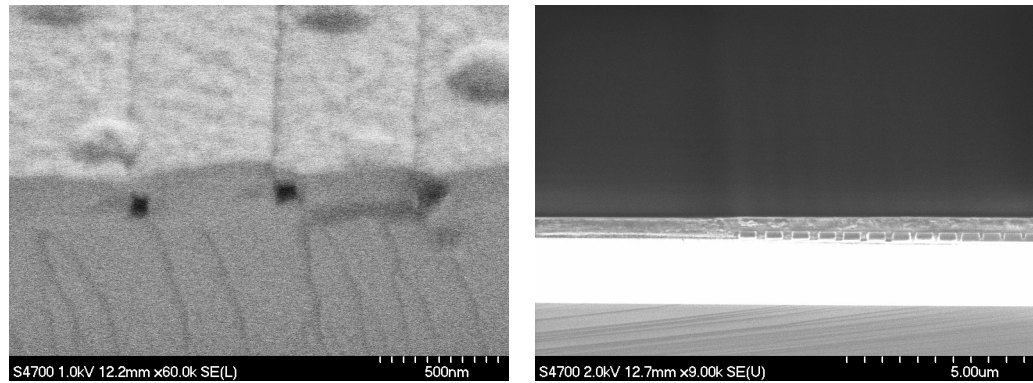
2.7 Buffer Layer

To overcome the silica coating problems, an alternative spin-on glass upper cladding layer has been developed for the passivation of the structure. Direct spinning of undiluted HSQ at 3000 rpm for 60 seconds has been shown to be a very good solution, since the liquid state makes this material more suitable for penetrating very small gaps. A subsequent thermal curing stage, of around 12 hours at 180 °C, was used to stabilize the film. A structure very similar to silica was obtained after the baking process, with filling of gaps as small as 50 nm being evident in Figure 2.13(b).

This technique is very useful for passivation, but starts to suffer if the sample is post-processed with solvents such as Acetone or methyl isobutyl ketone (MIBK). These liquids are used in the processing for the lift-off technique and as developer for PMMA (poly methyl meta acrylate) in the fabrication of metal electrodes. Different baking temperatures and times have been tested, aiming to increase the robustness of the film, but without any interesting results: they were not able to confer the required mechanical stability onto the material (Figure 2.13(c)). A final solution (Figure 2.13(d)) that met both the requirements of good gap filling and chemical and mechanical stability was obtained by combining the silica and HSQ. A first layer of HSQ was spun and then baked and a subsequent final layer of Silica is then deposited by PECVD and used to embed the structure and ensure better mechanical resistance - and as a further protection during additional chemical processes.

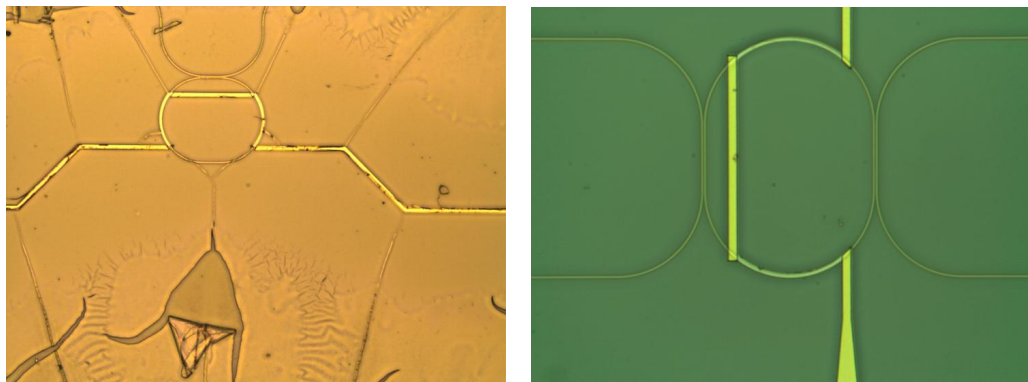
2.8 Metal deposition and Lift off techniques

The PMMA resist was used for lift-off processes when metallisation was required. This process was used when electrodes were needed as part of a photonic device,



(a) SEM picture of the gap filling, the Silica is not able to penetrate inside the small gaps, moreover it is characterized by a granular surface.

(b) SEM picture of HSQ overcladding, the problem of poor gap filling is solved since the liquid state of this material makes it more suitable for penetrating small gaps.



(c) Optical microscope picture of the structures under examination with an overcladding of only HSQ. Even if cured it has not the mechanical and chemical robustness to Acetone and MIBK treatment.

(d) Optical microscope picture showing that a better mechanical and chemical robustness is conferred to the buffer layer using a layer of PECVD Silica deposited after the HSQ.

FIGURE 2.13: Development in the passivation of the structure to obtain an upper cladding with good gap filling and mechanically and chemically robust.

such as a thermo-optically tunable microcavity. Moreover the definition of marker structures is necessary, prior to the patterning of the core layer, for the alignment of all the different layers (i.e. guiding structures, Polymer structures and metal electrodes).

The deposition of the metals was carried out using a Plassys (MEB 400s) e-beam evaporator [81]. In the evaporation process, an electron beam is used to heat the source material to be deposited – to the point where it starts to boil and evaporate. The process takes place inside a vacuum chamber, enabling the molecules to evaporate freely in the chamber until they reach the substrate material, where they condensate.

The marker and electrode deposition consisted in the following steps:

- 1) Resist Spinning and baking [82]:
 - a) First layer of PMMA resist: 15% 2010 Elvacite TM ($\approx 1200 \text{ nm}$ at 3000 rpm), baking for 30 minutes at 180 °C.
 - b) Second layer of PMMA resist: 4% 2041 Elvacite TM ($\approx 150 \text{ nm}$ at 3000 rpm), baking for 1.5 hours at 180 °C.
- 2) E-beam exposure with a dose of $550 \mu\text{C}/\text{cm}^2$.
- 3) Development: 1:1 dilution of isopropyl alcohol (IPA) and methyl isobutyl ketone (MIBK) for 30 seconds – and then two subsequent rinses in IPA for 30 seconds each.
- 4) Metal layer evaporation onto the sample.

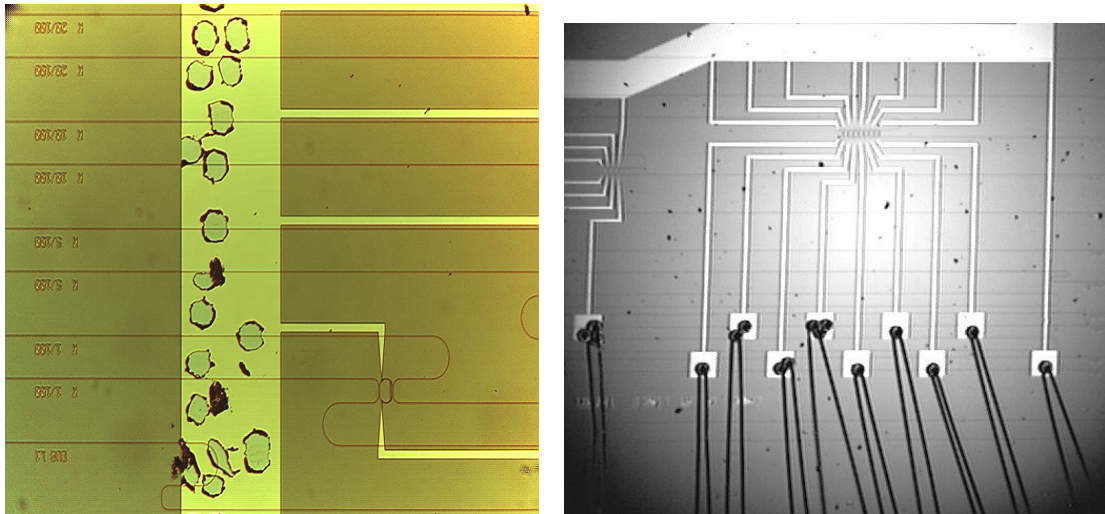
The two different sensitivities of the PMMA resist layers allow the realization of undercutting of the mask – and as result the metal layer deposited has a step between the top surface of the resist and the patterned area on the sample, allowing easier removal of the undesired metal and giving sharp edges. A subsequent lift-off step in acetone for a time around of 3-4 hours was sufficient to remove the unwanted metal from the sample surface.

For the definition of the markers and the metal electrodes, two different recipes were used.

The marker structure consisted in a single deposition of *Ti/Pt/Au* (20 nm, 30 nm, 200 nm). The titanium was employed to guarantee good adhesion onto the silicon surface and the top layer of gold (Au) due to its brightness under e-beam radiation, yielding an excellent contrast in comparison with the silicon substrate allowing a precision in the alignment on the order of few nanometers.

The metals used for thermo-optic device electrodes were 50 nm layers nichrome followed by 200 nm of gold. These layers were deposited in two separate deposition processes, with two different patterns, in order to obtain two layers with different resistivity. The Gold was removed where high resistivity areas were required.

A preliminary bonding test on the electrode showed poor adhesion of the metal on the surface of the sample (Figure 2.14(a)). The top layer of gold was completely teared in correspondence of the bonding wire tip.



(a) Optical microscope picture showing bites in the top layer of gold produced during the bonding process, due to a poor adhesion on the NiChrome layer.

(b) Optical microscope picture showing the final bonded device, the introduction of a Titanium intermediate layer solved the adhesion problem.

FIGURE 2.14: Figures of bonding processes: a) poor adhesion of the NiChrome layer resulted in not capability to realize the bonding of the devices, b) optimized process with the wires bonded on the sample (optical microscope picture acquired in Milano).

This removal suggested that a major problem was occurring at the *NiCr/Au* interface due to the formation of an oxide layer on top of the *NiCr* layer, making the adhesion of gold more difficult. To solve this problem the process was reversed, via the deposition of a first layer of gold that does not oxidize when removed from the vacuum chamber and then the deposition of the *NiCr* layer. Moreover, due to the well known poor adhesion properties of gold on silicon, an additional layer of titanium has been introduced in correspondence with the bonding pads. The electrical characteristics of the devices were preserved, even with the introduction of this layer – with the result of excellent mechanical robustness in the bonding process, as shown in Figure 2.14(b).

2.9 Conclusions

All the fabrication tools and techniques involved in this work have been presented. Further targeted process development will be introduced in due course when required for fulfillment of device development or to address the process variability and stability on the sample and consistency over the time (see chapter 5). Considerable time and effort were devoted to the optimization of almost all the critical

process steps. The high quality of the fabrication reached allowed the development of several building blocks which are novel devices for Silicon Photonics – or if already present in literature, represent the-state-of-the-art in terms of performance. With these basic tools and their stable and reproducible behavior it become possible to develop more complex structures aimed at meeting the desired system requirements. In the following Chapters, the devices developed will be analyzed both theoretically and practically.

Chapter 3

Basic Building Block Design and Characterization

In this chapter, the measurement set-up and characterization techniques are first introduced. Building blocks with an increasing complexity are then designed and analyzed. Simulated and measured behavior are compared and the impact of the fabrication limitations on the device performance are discussed.

3.1 Experimental Set up

A layout of the measurement setup is shown in Figure 3.1. An external cavity tunable laser source emitting in the range 1475 - 1580 *nm* is coupled into a single mode fiber; the output beam of the fiber is collimated with a 20X lens and modulated by a chopper at a frequency of 317 *Hz*. A pair of 40X lenses controlled by micro-positioners is used to couple the beam into and out of the device chip. Two polarizers are used in the measurement setup: the first one, inserted between the chopper and the input lens, is used to select the desired injected polarization; the second one, between the output lens and the photo-detector, is used to evaluate the presence of any polarization conversion. The transmitted power is detected by a Germanium photo-diode through a lock-in amplifier. The system is controlled by a PC which synchronizes the laser source with the lock-in amplifier via GPIB ports and performs the data acquisition. Prior to each measurement a camera is used to optimize the alignment of the single device by varying its relative position with respect to the lenses.

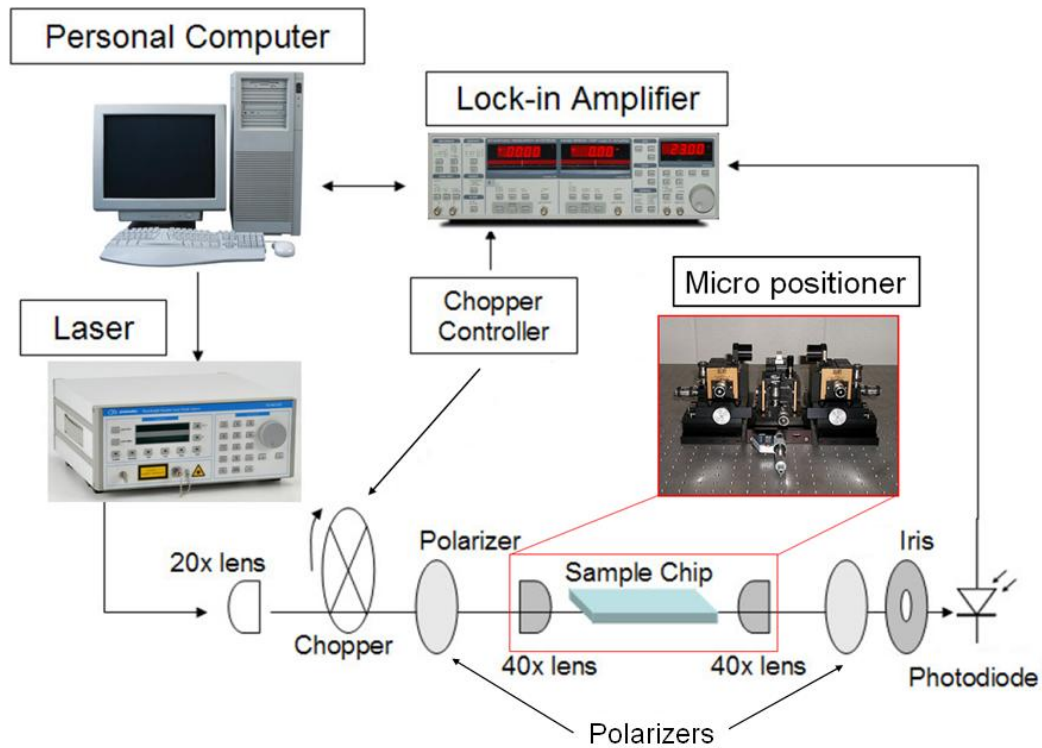


FIGURE 3.1: Schematic diagram of the experimental set-up used for the end-fire characterization of the fabricated devices.

The input power was usually set to be 1 mW and the wavelength range generally used was between $1510\text{--}1560\text{ nm}$. Some instabilities in the source power level were present when the wavelength was approaching the boundaries of the laser tuning range. However a flat and uniform signal was available for both polarizations in the range used in our measurements. A typical input power characteristic of the system, measured in absence of the sample for both TE and TM polarizations is shown in Figure 3.2.

The signals show a slow 5% variation across the whole spectrum for both polarizations. The value of power for the TM polarization is 40% smaller than for the TE polarization but this is strongly dependent on the input fiber and optimization prior to the measurement can be executed to increase the power level in the desired polarization. For each experiment, characterization of the input power level, similar to the one shown in Figure 3.2, was performed to control the absolute power level for each polarization – and for the subsequent normalization of the transfer function of each device. The measurement setup is very stable and able to keep its alignment for several hours.

The *end-fire* technique has the advantage of being very simple, because it provides

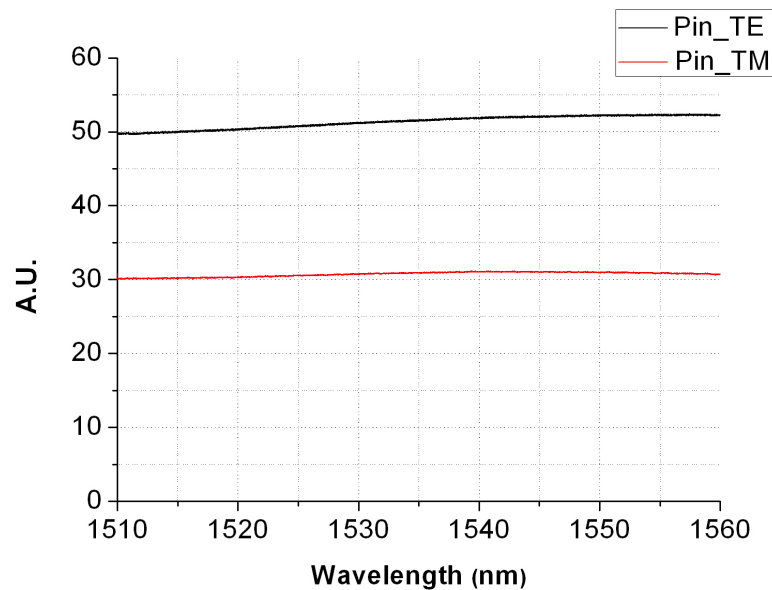


FIGURE 3.2: Typical power characteristics for TE and TM polarizations at the output of the tunable laser. The power level for TE and TM are dependent from the input fiber and any alignment and optimization for the desired polarisation is necessary prior to each measurement. Both characteristics present a flat behavior across the wavelength range of interest.

and collects power in the plane of the sample. However, the disadvantage is that the coupling into the device is dependent on the focusing conditions (i.e. on the relative position between the lenses and the sample, and the changes with wavelength), thus affecting the reproducibility.

3.2 Waveguide design

An optical waveguide produces bi-dimensional confinement for light. This is the basic element for the realization of any optical circuit. The main requirement for this basic building block is to support single-transverse-mode propagation and to allow a small bending radius, without introducing significant radiation losses. The substrate for the fabrication of the considered waveguide is reported in section 2.1.

Several configurations with different geometries and light-guiding mechanisms may be found in literature, such as stripe waveguides [55], slots [83] and photonic crystal waveguides [84]. The most common configurations, to realize ring resonator structures, are deep etched or shallow etched waveguides.

Figure 3.3 shows a schematic representation of the cross section of the two configurations of possible interest:

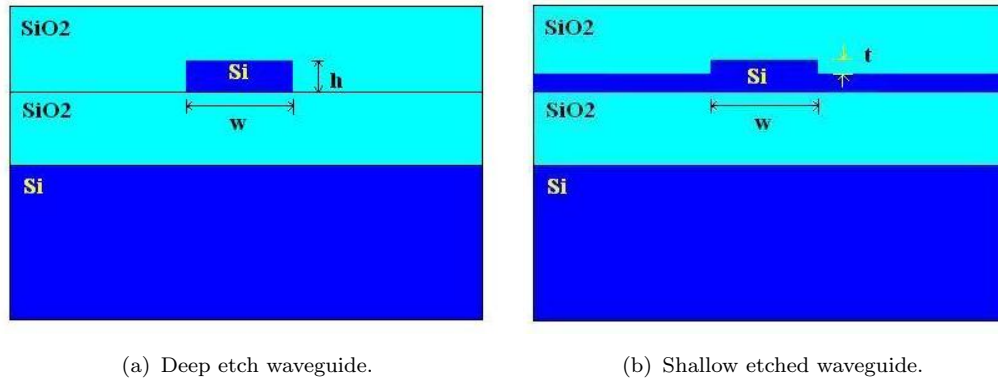


FIGURE 3.3: Schematic of the Cross section for the waveguide configurations modeled and realized in the course of this work.

- The deep etched waveguides (photonic wires) are obtained by a complete etch of the silicon guiding layer, as shown in Figure 3.3(a): the resulting structure has a rectangular cross-section, completely surrounded by cladding regions, the height h is fixed by the wafer specifications ($h = 220 \text{ nm}$), while the width w can be suitably varied;
- The Shallow Etched waveguides, as in Figure 3.3(b), are obtained by a partial etch of the guiding layer: both the width, w , and the etching depth, t , are free parameters that define the core geometry and the optical properties of the waveguide.

A commercial numerical simulator (FIMMWAVE), based on the Film Mode Matching method [85], was employed for an analysis of advantages and disadvantages of the two approaches, in order to choose the one that is more suitable for the realization of our structures. In the software the refractive index of Silicon was set to $n_{Si} = 3.5$ and the refractive index of Silica to $n_{SiO_2} = 1.46$.

3.2.1 Deeply etched waveguides

The trend for the effective index versus the waveguide width for deep etched waveguide is shown in Figure 3.4.

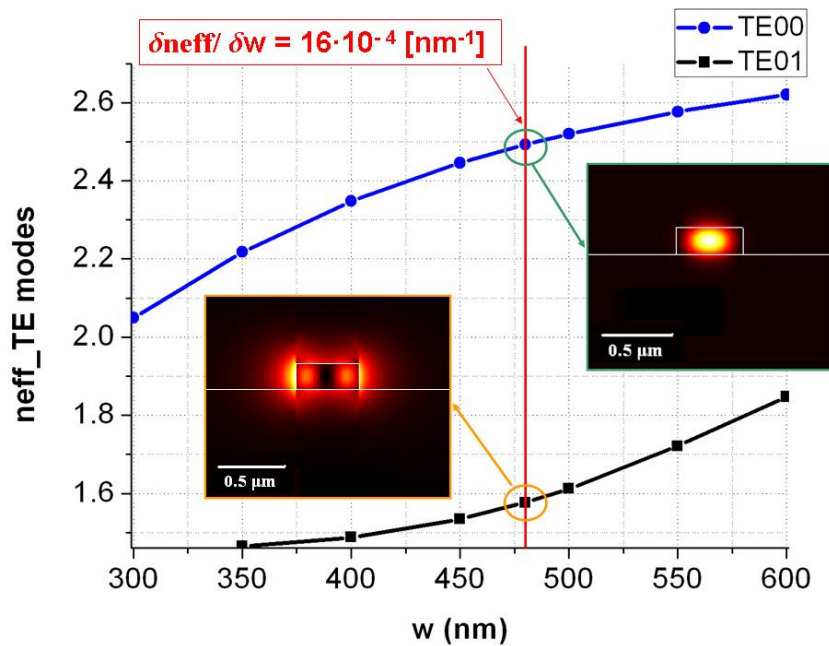


FIGURE 3.4: Deep etched waveguides: effective refractive index n_{eff} for TE modes as a function of the waveguide width w , the fundamental mode in blue and the first order mode in black. The power flux distribution and the sensitivity $\delta n_{eff}/\delta w$, are shown for $w = 480 \text{ nm}$ – at a wavelength of $\lambda = 1.550 \mu\text{m}$.

A $w = 480 \text{ nm}$ wide deep-etched waveguide supports a quasi-TE fundamental mode with an effective refractive index of $n_{effTE00} = 2.4925$ at $\lambda = 1.55 \mu\text{m}$. The first higher-order mode is also above cut-off, the effective index is $n_{effTE01} = 1.5770$ at the same wavelength. The fundamental mode is strongly confined in the core while the higher order mode has less power in the core and more overlap with the side-wall, suggesting very high propagation and bending losses. Moreover the structure supports a quasi-TM mode with $n_{effTM00} = 1.8688$.

The sensitivity of the waveguide to technological tolerances has been estimated as the n_{eff} variation as a function of the width w variation. For $w = 480 \text{ nm}$ the sensitivity is $\delta n_{eff}/\delta w = 16 \cdot 10^{-4} \text{ nm}^{-1}$ for the fundamental mode TE_{00} . A deeper analysis on the control of the patterned dimensions and on sensitivity control will be analyzed in the Chapter 5.

3.2.2 Shallow etch waveguides

For Shallow etched waveguides, it is necessary to optimize two free design parameters: the width w and etching depth t . Because of the lower lateral confinement, the mode is more affected by bending losses. Numerical calculations of the trend of the bending losses as a function of bending radius R for different values of w and t are shown in Figure 3.5. Two different waveguide dimensions and three different etching depths are analyzed.

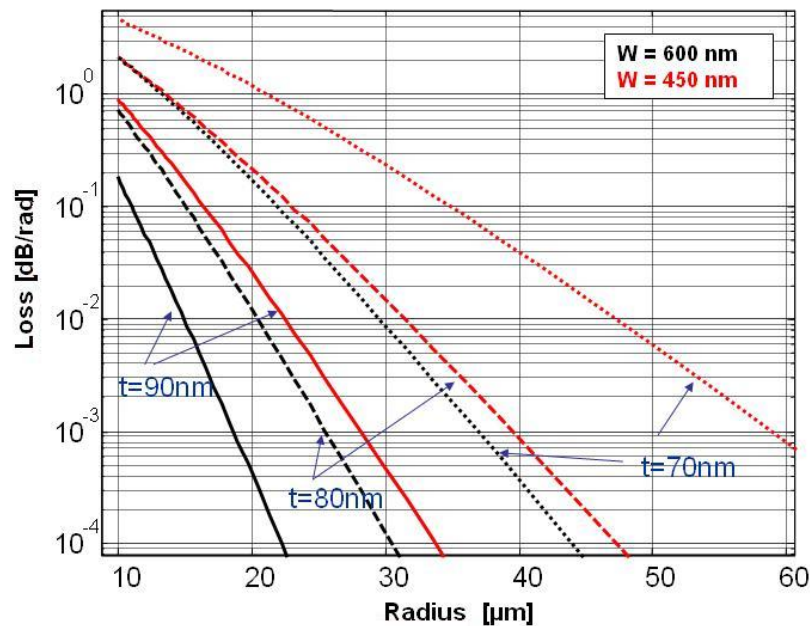


FIGURE 3.5: Shallow etched waveguides: bending losses as a function of bending radius R for different values of w and t : $w = 450$ and $w = 600$ nm (red and black lines respectively); $t = 70$ - 80 - 90 nm (dotted, dashed and solid lines respectively) (courtesy of Prof. A. Melloni, Politecnico di Milano).

As the etching depth t increases, the mode is more confined in the Silicon core – thus ensuring smaller bending losses for a fixed radius. As the waveguide width w is reduced, the mode is less confined leading to an increase in the bending losses.

At a Fixed value of $t = 90$ nm, the simulated behavior of the effective refractive index n_{eff} , as a function of the waveguide width w , is shown in Figure 3.6.

A $w = 650$ nm wide waveguide has a fundamental quasi-TE mode with a refractive index equal to $n_{effTE_{00}} = 2.745$ at $\lambda = 1.55$ μm , while the first higher-order mode has an effective index of $n_{effTE_{01}} = 2.4712$. The power flux distribution for $w = 650$ nm, is shown in the inset: the maximum intensity of the mode is

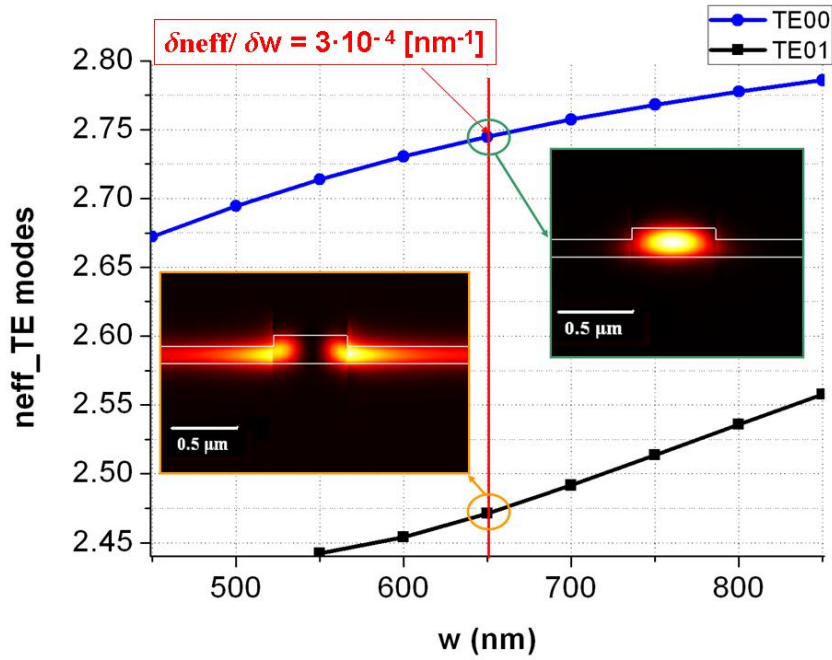


FIGURE 3.6: Shallow etched waveguides: effective refractive index n_{eff} for TE modes as a function of the waveguide width w , for an etching depth of 90 nm ; the fundamental mode in blue and the first order mode in black; the power flux distribution and the sensitivity $\delta n_{eff}/\delta w$, are shown for $w = 650\text{ nm}$ – at a wavelength of $\lambda = 1.550\text{ }\mu\text{m}$.

concentrated in a lower position when compared to the deep etched configuration, because the mode spreads more into the silicon slab.

For this configuration, the mode is less affected by the surface roughness of the waveguide – due to a smaller overlap with the sidewall. However, this structure is more sensitive to any asymmetry or bending. The first order mode, moreover, has most of the power concentrated near the side walls of the waveguide, suggesting once again higher propagation and bending losses. The fundamental and the first order TM mode have effective indexes of $n_{effTM00} = 1.9454$ and $n_{effTM01} = 1.5963$, respectively.

For $w = 650\text{ nm}$ and $t = 90\text{ nm}$ the fundamental mode TE_{00} has a value of $\delta n_{eff}/\delta w = 3 \cdot 10^{-4}\text{ nm}^{-1}$, about five times smaller than deep etched configuration, and $\delta n_{eff}/\delta t = 12 \cdot 10^{-4}\text{ nm}^{-1}$ (See Figure 3.7). If it is considered that the etching depth t is a parameter that is difficult to control with nanometric precision, $\delta n_{eff}/\delta t$ is a critical parameter. In fact, every second in the etching time (see Chapter 2) introduces a variation of $\delta t = 2.2\text{ nm}$ – and so a variation in the effective index of $\delta n_{eff} = 26 \cdot 10^{-4}$.

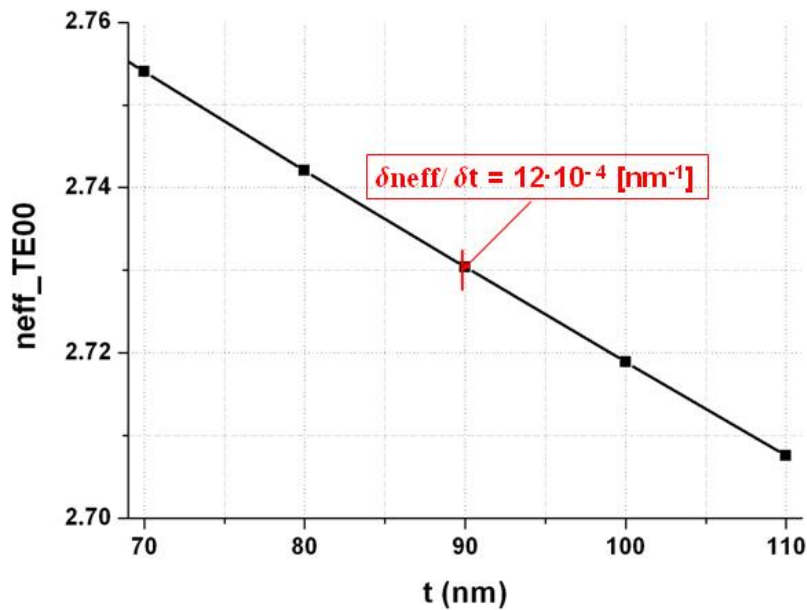


FIGURE 3.7: Shallow etched waveguides with a width $w = 650 \text{ nm}$: the fundamental TE-mode effective refractive index n_{eff} variation, as a function of the etching depth t – and the sensitivity, $\delta n_{eff}/\delta t$, for an etching depth of 90 nm is $3 \cdot 10^{-4} \text{ nm}^{-1}$

Table 3.1 summarizes the advantages and disadvantages of each configuration.

	Deep Etch	Shallow Etch
Single Mode WG width	Narrower	Wider
Sensitivity $\delta n_{eff}/\delta w$	High	Low
Sensitivity $\delta n_{eff}/\delta t$	Absent	Very High
Influence n_{upclad}	Strong	Weak
Propagation Losses	Higher	Lower
Bending Losses	Lower	Higher

TABLE 3.1: Deep Etched vs Shallow etched waveguides: main comparison parameter summary

Taking into account all the previous considerations, deep etched waveguides were chosen as the fundamental building block for this work. To ensure single-mode operation, but also the maximum confinement of the fundamental mode, a width of $w = 480 \text{ nm}$ turned out to be the best compromise. A higher order mode, even if excited, would be suppressed in a short distance, due to its poor confinement and the interaction with the surface roughness – which, in turn, will decrease its power in a short distance. An upper cladding of SiO_2 has always been employed, in order to realize thermo-optical tuning of the structures or simply to protect the devices from the external environment.

3.3 Transmission Loss Estimation

The waveguide losses originate from the complex nature of the refractive index $n' = n_{eff} + jn_i$. A field propagating inside the waveguide has the form:

$$E = E_0 e^{j(sz - \omega t)} = E_0 e^{j(k_0 n' z - \omega t)} = E_0 e^{j(k_0 n_{eff} z)} e^{(-k_0 n_i z)} e^{j\omega t} \quad (3.1)$$

where

$$\mathcal{A} = e^{-k_0 n_i z} = e^{-\alpha_{tot} z} \quad (3.2)$$

represent the loss and $k_0 n_i$ the loss coefficient α_{tot} . The propagation loss figure that is usually considered is:

$$\frac{\mathcal{A}_{dB}}{L_w} = 10 \frac{\log_{10}(e^{-2\alpha_{tot} L})}{L_w} = \frac{20}{\ln(10)} \alpha_{tot} \quad (3.3)$$

where the square in the exponential term is due to the fact that we are considering the power losses.

The Fringe-Contrast method a Fourier-Transform method, described more in detail in Appendix B, have been used in the course of this Thesis to analyze the transmission losses for different waveguide configurations. These methods have been used to control periodically the quality of the fabricated devices or to check a new batch of electron-beam resist and developer – or to analyze the losses for samples undergoing different thermal treatments, or with different over-cladding materials. Figure 3.8 shows Loss measurements for 480 x 220 nm² SOI waveguides analyzed using the two techniques. The two methods provide very similar results. The value of losses (in Figure 3.8) is the lowest ever obtained at Glasgow University [57]– and at the moment it is state-of-the-art for devices with similar technology and geometry.

A typical value of the propagation losses, measured in the present work, for a 480 nm-wide waveguide with silica upper cladding, is $\alpha = 1.5 \div 0.2$ dB/cm (best value: $\alpha = 1.0$ dB/cm) for the TE mode, and $\alpha = 0.8 \div 0.1$ dB/cm for the TM mode. This is due to the stronger interaction of the TE mode with the sidewall roughness that is the main source of loss.

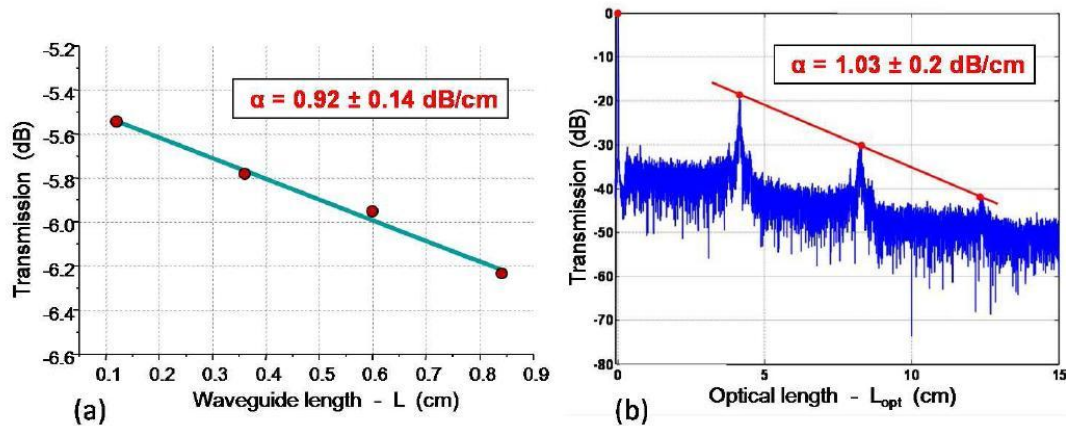


FIGURE 3.8: Loss estimation using a) the fringe contrast method (at the University of Glasgow) and b) using the Fourier Transform (measurements performed at Politecnico di Milano).

3.4 Input and Output Coupling losses

Beside the propagation losses, another major issue that limits the performance of the SOI platform is the high input-output coupling losses to fibres or lenses. The coupling losses, in many cases, can exceed a value of 20 dB per facet. The reasons for this large value arise from the differences in the size, the shape, and the velocity of the modes from lenses or fibres, in comparison with the ones propagating in a single-mode silicon waveguide.

In the early stages of the work, input/output sections 2 μm -wide were tapered down to 480 nm in a 300 μm -long section. Although the dimensions of the tapers, to join the large waveguide to the narrow one, were properly designed to guarantee an adiabatic transition, strong oscillations due to the reflections at the cleaved facets (Fabry-Perot oscillations) and multimode interference were a common source of contamination of the measured transmission spectra. Once the taper sections and the wide cross-section waveguides were eliminated from consideration, the main problem was still the presence of strong Fabry-Perot oscillations due to the reflectivity of the cleaved facets. Weak signals and small features in the transmission spectra were difficult to identify and post-processing of the signal was not always the best approach.

3.4.1 Anti-reflection coatings

A first attempt to reduce the Fabry-Perot oscillations was made by depositing anti-reflection (AR) coatings.

A perfect single layer AR coating is a quarter wavelength thick material ($d = \lambda_0/4n_f$) with a refractive index of $n_f = \sqrt{n_0n_s}$, where n_0 and n_s are the refractive index of air and the guiding layer. For a guided-wave geometry, the value of n_s represents the effective refractive index of the guided mode [86, 87].

Therefore a suitable material would require a refractive index close to 1.579 (equal to $\sqrt{n_{effTE0}}$) at a wavelength of 1550 nm. Silica (SiO_2) with $n_f = 1.46$ has been chosen as the best candidate among the limited number of readily available dielectric materials (TiO_2 : $n_f = 2.460$ and ZrO : $n_f = 2.1$). A multilayer approach was theoretically investigated to understand if a combination of two materials could compensate for the index difference mismatch.

For a multilayer stack composed of two dielectric layers, n_{f1} and n_{f2} , the reflectance can be expressed as:

$$r = \left(\frac{n_0 n_{f2}^2 - n_{eff} n_{f1}^2}{n_0 n_{f2}^2 + n_{eff} n_{f1}^2} \right)^2 \quad (3.4)$$

The thickness d_{tot} of the layer required would be

$$d_{tot} = d_1 + d_2 = \frac{\lambda_0}{4} \frac{n_{f1} + n_{f2}}{n_{f1} n_{f2}} \quad (3.5)$$

The zero reflectance condition can be obtained when $n_0 n_{f2}^2 = n_{eff} n_{f1}^2$ or

$$\frac{n_{f2}}{n_{f1}} = \sqrt{\frac{n_{eff}}{n_0}} \quad (3.6)$$

The conditions for zero reflectance are transferred to the thicknesses of the two dielectric layers. However, the non-availability of a dual-source sputtering system in our department, made this solution unpractical. For this reason, a single layer of silica with a thickness of around 200 nm was initially used to reduce the Fabry-Perot resonance effect.

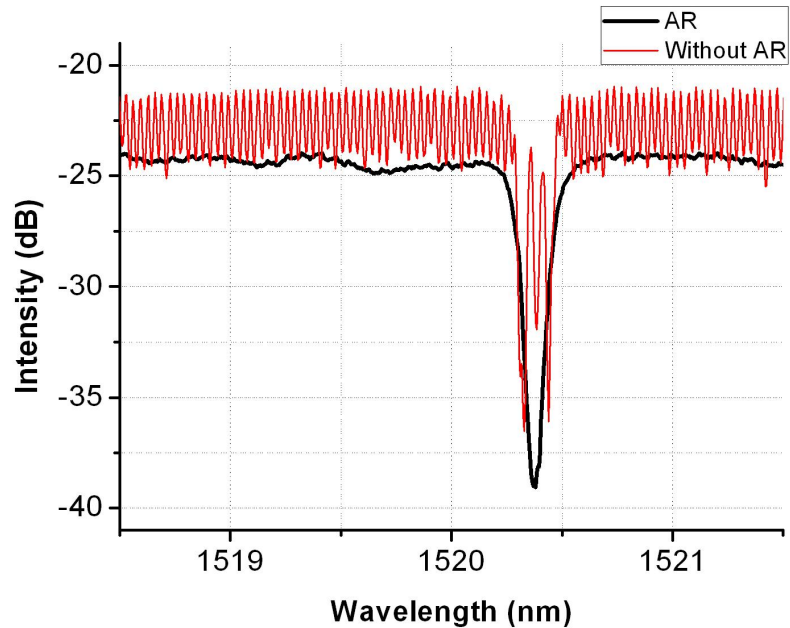


FIGURE 3.9: Transmission spectra of the same device structure with (red) and without Anti-Reflection Coatings (black). The difference in the power level is due to optimization in the alignment process.

Figure 3.9 shows the transmission spectrum of a ring resonator structure with (black) and without (red) anti-reflection coatings. An improvement in the quality of the acquired signal is clearly visible, with a reduction in the reflectivity to $R \cong 5\%$. Even if the Fabry Perot oscillation was partially eliminated, the coupling losses were still high, due to the modal mismatch between the guided mode and the focusing lens mode. In addition to the low coupled power, the use of anti-reflection coatings presented another drawback related to its poor stability and reproducibility – which was caused by the variable composition and thickness of the grown oxide layer associated to an insufficiently stable deposition process

3.4.2 Inverse Tapers

Several papers have shown different approaches as solution of the coupling problem. Grating couplers are good candidates. However they require a compromise between efficiency and optical bandwidth, making them unsuitable for some applications [60, 88]. Due to the planar geometry of the available characterization set-up, it was decided to explore other solutions, such as planar inverse tapers. This approach consists in the creation of a laterally tapered silicon waveguide [59] out-coupled via a polymer structure [89–91] in materials such as *SU8* resist [92].

A schematic of the structure under examination is shown in Figure 3.10.

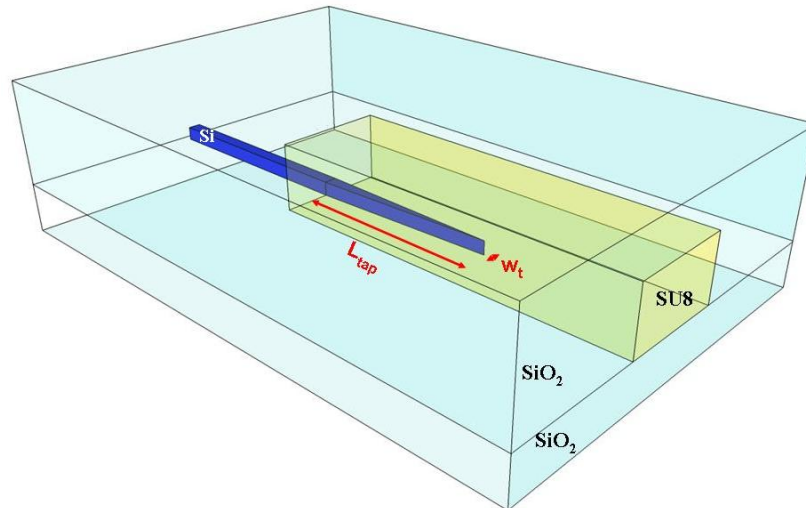


FIGURE 3.10: Schematic representation of a mode adapter structure. The silicon wire waveguide is depicted in blue and is tapered down to a narrow tip. The yellow waveguide is a low index waveguide $n = 1.52$ (SU8). The entire structure is covered with SiO_2 .

The silicon waveguide is embedded inside a low-index-difference waveguide (SU8) with relatively large cross-sectional area. The high-index-difference waveguide (silicon wire) is horizontally tapered to a narrow tip with a linear profile. The light from an optical fibre or a microscope lens is coupled into the large cross-section and low-index-difference polymer waveguide. In the silicon inverse taper the effective index gradually changes from that of a low-index waveguide to that of the high-index waveguide. Once full conversion into a high-index-difference waveguide occurs, a high-index-difference mode results. This design provides an efficient bi-directional mode transformation – and so the same geometry has been employed for both in and out-coupling.

A simulation of the mode transformation with RSoft Beam Prop is depicted in Figure 3.11. The top and the side views show the variation in the beam size and position. The main loss contribution arises from the technological limits on the tip dimension (w_t). Ideally, this should be zero, to minimize the mode conversion losses between the low-index waveguide and the high-index waveguide, but in practice values smaller than 20 nm are not reliably achievable, which is not related to electron-beam resolution but rather the surface of the resist mask. Figure 3.12 shows an optical microscope image (Figure 3.12(a)) of the first fabricated devices and an SEM micro-graph of the final fabricated taper (Figure 3.12(b)).

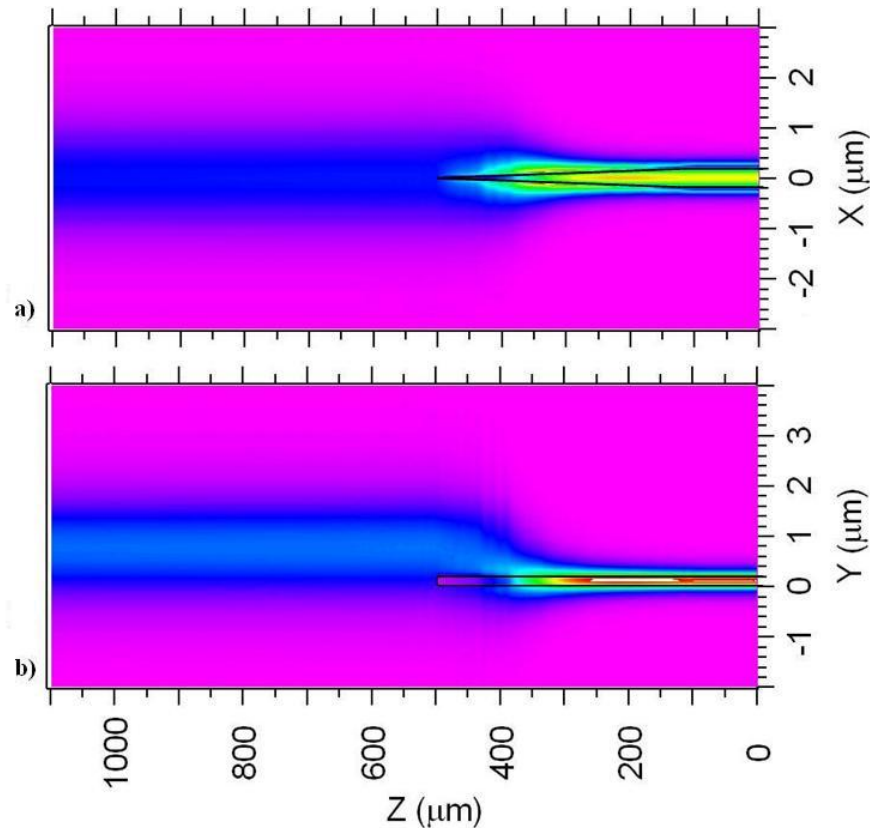


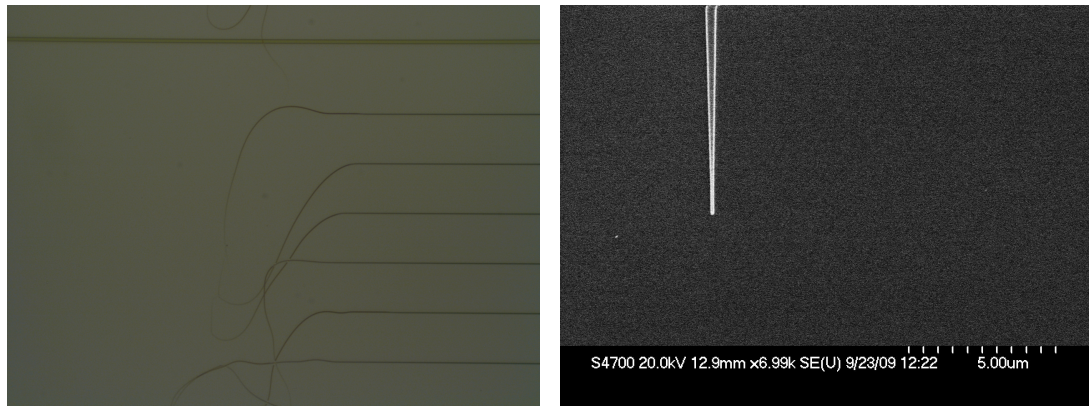
FIGURE 3.11: Simulation performed with a Rsoft Beam Prop of a typical device. The top represent a top view of the transformation of the optical beam and, at the bottom, a side view is shown.

Some problems were evident in the first fabrication run: as the dimensions of the taper were reduced the adhesion of the mask after the development became problematic. The difficulty was mainly related to the presence of moisture and solvent in the resist that were influencing the pattern for such small dimensions. Thermal curing and oxygen plasma ashing were introduced into the fabrication process as a supplementary step for improving the adhesion of the resist.

The final taper had a well shaped tip and a profile in good agreement with the designed one. To the best of my knowledge [89], this represents the taper with the smallest specified aperture ever realized limited ($w_t = 20 \text{ nm}$).

The length of the taper (L_{tap}) plays an important role in the efficient conversion of the optical mode from the low-index waveguide to the high index waveguide and vice versa.

If the characteristics of a tapered waveguide are such that the local modes do not change abruptly throughout the taper, adiabatic transformation of each local



(a) Optical Microscope picture of the first fabrications of the tapers. Adhesion problems are clearly visible from the bending of the tapered sections.

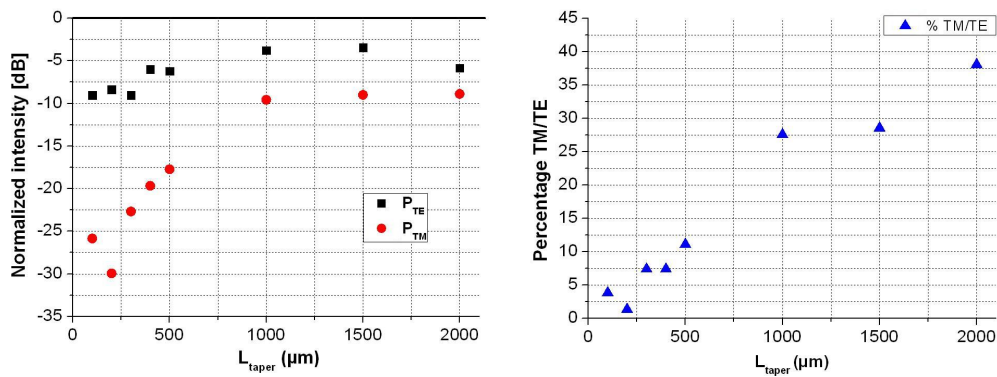
(b) SEM micrograph of the taper fabricated with the optimized process. The taper geometry is in agreement with the pattern dimension and the taper is well shaped.

FIGURE 3.12: Optical and SEM micrograph of some fabricated tapers.

mode is possible between the input and the output of the tapered waveguide. This theorem implies the well-known fact that either the medium variation should be gradual with respect to the propagation direction or the domain interfaces should be continuous functions in order that adiabatic mode transformation may be achieved as the taper length is increased [93].

From a theoretical point of view, the transformation losses are reduced as the length of the taper increases. In real devices where the scattering influences the mode propagation significantly, multi-modal behaviour and spurious modes due to TE-TM transformation can be excited [94]. This phenomenon is more likely to occur in a square waveguide geometry than in a more general rectangular waveguide. In the taper geometry, when the waveguide width is equal to the waveguide height ($w = h$) the square waveguide supports quasi-degenerate TE and TM modes – with the same propagation constant (same velocity) and the same mode profile, thus making polarization coupling efficiently phase-matched. In a short taper the length where the waveguide width and height are comparable is shorter, reducing the magnitude of this phenomenon.

Figure 3.13(a) shows the lens-to-lens measured losses (i.e. total insertion losses), normalized to the input power level for several tapers with an output width of $w_t = 20 \text{ nm}$ and different lengths varying from $100 \mu\text{m}$ to $2000 \mu\text{m}$. The TE-TE transmission is shown in black (squares), the TE-TM transmission is shown in red (circles). It can be extracted that for short tapers the power transfer from TE to TM, arising from spurious conversion, is small – the extinction ratio is as



(a) Normalized intensity for inverse tapers with the same aperture, 20 nm , and different lengths spanning from $100 \mu\text{m}$ to $2000 \mu\text{m}$. The TE transmission is shown in black (squares) when the light is polarized TE at the input; in red (dots) the spurious TM transmission obtained for a TE polarization at the input.

(b) Cross polarization coupling percentage obtained as ratio of TM to TE polarization for pure TE polarisation at the input for inverse tapers with a lengths varying from $100 \mu\text{m}$ to $2000 \mu\text{m}$. The polarization transformation has a stronger effect for longer tapers.

FIGURE 3.13: Intensity and cross-polarization coupling measurements for tapers with different length.

large as 15 dB . As the length of the taper increases there is a progressive decrease of the difference between the two power levels. In particular, a decrease of the transmission for the TE level and a constant increase in the spurious TM level suggest an increasing power transfer from the fundamental TE mode to the TM mode. For the longest taper realized ($2000 \mu\text{m}$), the length where the waveguide width and height can be assumed to be comparable is around $182 \mu\text{m}$, making this length non-negligible from the point of view of the polarization transformation: a value as high as 38% of the power TE is converted to the TM mode. Measurements of the conversion between the TE and TM modes are shown in 3.13(b).

The final configuration chosen for system integration consisted of a 20 nm aperture width and a 400 nm long taper, as the best compromise in terms of transformation losses and TE-TM conversion. Figure 3.14 shows a typical transmission spectrum for TE polarization at the input. The TE and TM power levels at the output have an extinction ratio of more than 10 dB and a cross polarization coupling from TE to TM as low as 7% . The characteristic oscillation in the spectrum, corresponding to the transfer of power between the TE and TM mode, have a periodicity of $\Delta\lambda_{\text{osc}} = 1.2 \text{ nm}$. The calculated [95] difference of the TE and TM mode refractive indices in the coupling regime is $4.449 \cdot 10^{-4}$.

The coupling efficiency of 6 dB represents the total contribution of coupling loss from the input to the output. Considering that the typical value of propagation

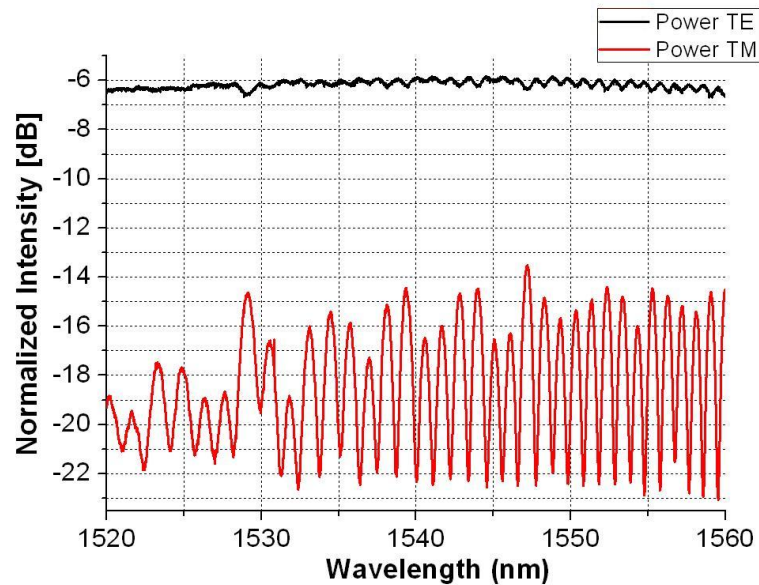


FIGURE 3.14: Normalized transmission characteristics for a $400 \mu\text{m}$ long taper with a final aperture of 20 nm . The TE-TE transmission is shown in black while the TE-TM transmission is shown in red.

losses is 1.5 dB/cm , the length of the guiding section ($480 \times 220 \text{ nm}^2$) is 1 cm and the polymer-to-fiber coupling loss is 0.6 dB (due to the difference in mode sizes and velocity between the polymer and the fiber, from simulation in R-soft), it is possible to estimate values of around 1.65 dB for each inverse taper coupler.

This value is in good agreement with simulated values shown in Figure 3.15 (in black) and with the most relevant work in this field – which adopts, in some cases, more complex structures and larger cross-section low-index waveguide structures.

Figure 3.15 also shows the behaviour of a taper with an exponential variation along the axial direction of the waveguide (similar to the one in [59] but out-coupled with a polymer block in the simulations). For this geometry an improvement in the efficiency for a longer taper is clearly visible due to a shorter length needed for the conversion (preserving the adiabatic condition). Moreover we expect that this configuration could partially or completely solve the problem of the spurious TE-TM conversion due to a more rapid transition into the square geometry configuration. This solution will be studied more in detail in the future.

The geometry of the polymer block used was $1.5 \times 1.5 \mu\text{m}^2$; the square geometry was chosen for a more efficient adaptation to the fiber mode. Tapers with a cross section of $2 \times 2 \mu\text{m}^2$ were also fabricated, but showed an improvement in the

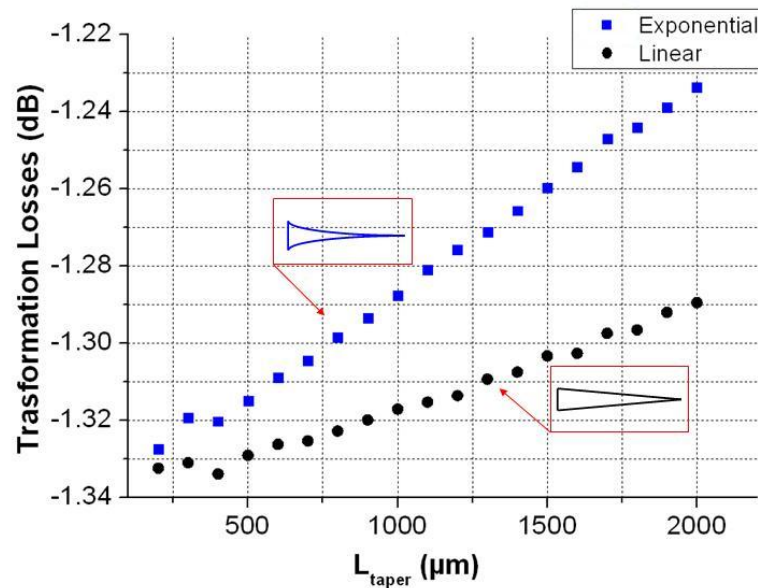
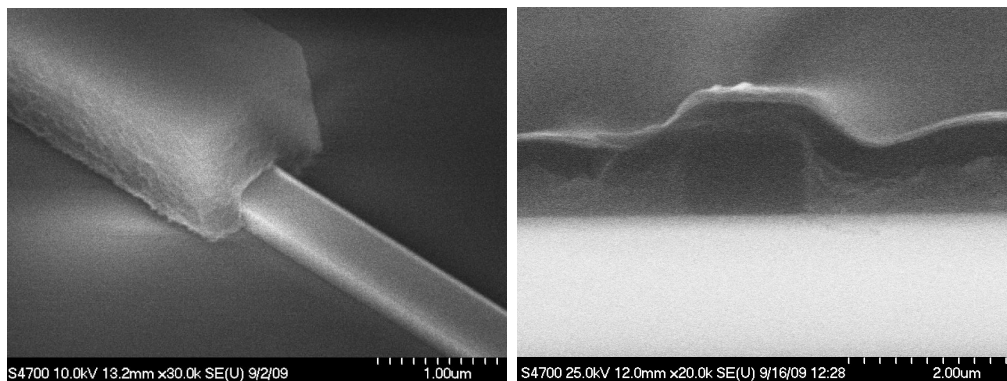


FIGURE 3.15: Simulated transmission losses for taper with different length for a linear variation along the propagation direction (black circular dots) and an exponential variation (blue squares).



(a) SEM picture of the polymer waveguide aligned with the Silicon waveguide

(b) SEM picture of the cross section of the polymer waveguide showing good planarity of the fabricated device.

FIGURE 3.16: SEM picture of the polymer waveguide a) and the cross section of a cleaved sample ready for measurements b).

transmission efficiency of only 0.25 dB/taper . SEM images of the final structures fabricated are shown in Figure 3.16.

3.5 Directional Couplers

Once the physical dimensions of the waveguide are optimised, more complex structures can be developed. One of the key building blocks to access more complex systems (Mach Zender interferometers, Micro-ring resonators and Coupled Optical

Waveguide) is the coupler. There are two main topologies of couplers, namely the directional coupler [96] and the Multi Mode Interference (MMI) coupler [97].

The need for coupling ratios other than 50-50%, and the requirement for tuning, ruled out the employment of MMI couplers. In this kind of coupler, in fact, a ratio different between 50-50% can only be achieved by changing the geometry of the MMI coupler, i.e. introducing a small etched gap in the MMI waveguide (with an etching precision within $\pm 5 \text{ nm}$ [98]), or introducing a small angle [99] or by using local refractive index variations [100] in the waveguide, in order to modify the interference pattern. Moreover, they may introduce spurious back-reflection if not well designed. An accurate apodization of the CROW structures, presented in Chapter 6, requires a large range of power coupling coefficients K , spanning from 4 % to 80 %. Although this objective involves some technological challenges, these figures are reproducible and controllable in directional couplers.

A directional coupler is simply made by placing in close proximity two parallel waveguides. In this condition, the optical modes of the original unperturbed waveguide are no longer independent, but are mutually coupled and interfere as a result of the interaction of the evanescent fields. Mathematically, the spatial dependence of the amplitude of each mode is affected by the existence of the other modes. The coupling coefficients between the two optical modes depend on the distance between the waveguides, G (the gap), and the coupling length, L_c .

The field self-coupling (r) and cross-coupling (t) coefficients of the coupler, shown schematically in Figure 3.17(a) are:

$$r = \cos(\kappa L_c) \quad (3.7)$$

$$t = -j \sin(\kappa L_c) \quad (3.8)$$

and the power fluxes are:

$$r^2 = 1 - \sin^2(\kappa z) \quad (3.9)$$

$$K = t^2 = \sin^2(\kappa z) \quad (3.10)$$

where κ is the coupling constant obtained from simulation of the coupled system equation.

Figure 3.17(a) shows a schematic of a directional coupler where G is the dimension of the Gap and L_c is the physical length of the coupler, i.e. the length of the

interaction between the two waveguides; Figure 3.17(b) shows a SEM micrograph of a typical fabricated directional coupler device.

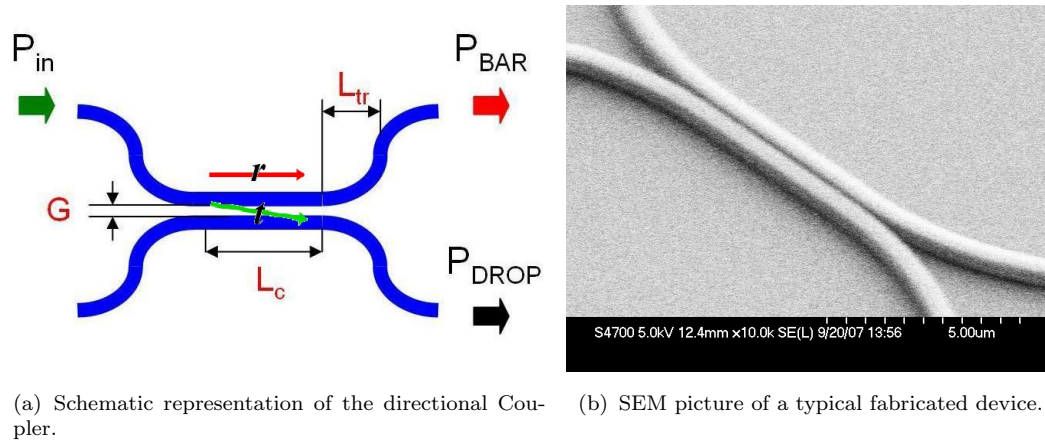


FIGURE 3.17: Schematic and SEM picture of a Coupler.

The region of interaction is not only limited to L_c but also includes two transition regions L_{tr} , in corresponding with the bending before and after the coupling regions, which constitute a non-negligible additional contribution [101] to the coupling coefficients. A precise evaluation of this contribution must be taken into account, both theoretically and experimentally.

The effective length of interaction is $L_{eff} = L_c + 2L_{tr}$, where the value of L_{tr} can be estimated considering an evanescent field with an exponential decay (ς) as in equation 3.11

$$L_{tr} = \int_0^{\infty} \exp(-\varsigma(d(z) - G)) dz = \frac{1}{2} \sqrt{\frac{\pi R}{\varsigma}} \quad (3.11)$$

where $d(z)$ represents the relative distance between the two waveguides at a particular section – G represents the gap width. The value of L_{tr} is dependent on the radius R of the bends before and after the straight section of the coupler: bigger radii have a longer interaction length.

The simulated values of L_{tr} , computed using equation 3.11, are shown in Figure 3.18 – these values are used for the correction of the coupling coefficients. For simplicity of notation in the course of this thesis we refer to L_c as the net coupling length, which includes both the physical coupler length and the contribution from the curved parts.

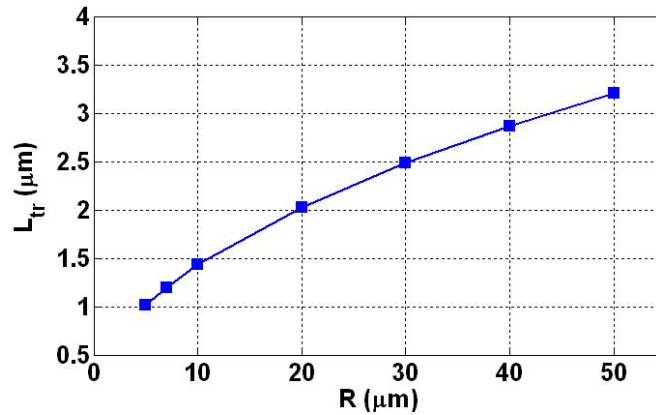


FIGURE 3.18: Transition length simulations for different radii of the bent waveguides of a coupler.

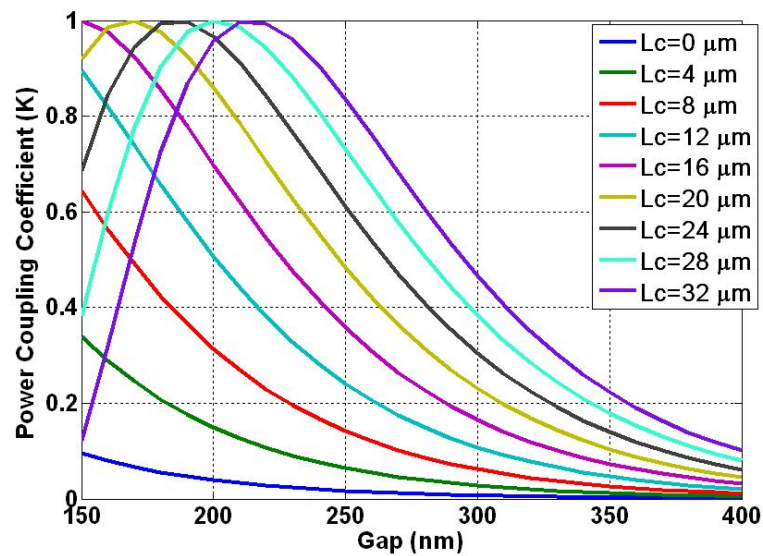


FIGURE 3.19: Dependence of the coupling coefficient with the gap dimensions for several values of coupler length.

Figure 3.19 shows the simulated variation of the power coupling coefficient versus the gap dimension for different values of length of the coupler L_c . To obtain a high coupling coefficient with an acceptable technological robustness, a value of coupling length higher than $16 \mu\text{m}$ is required. The reduction of the coupling length requires a reduction of the gap dimension – and values smaller than 100 nm are difficult to control. The analysis of the directional couplers has been one of the most central and critical subjects of the work.

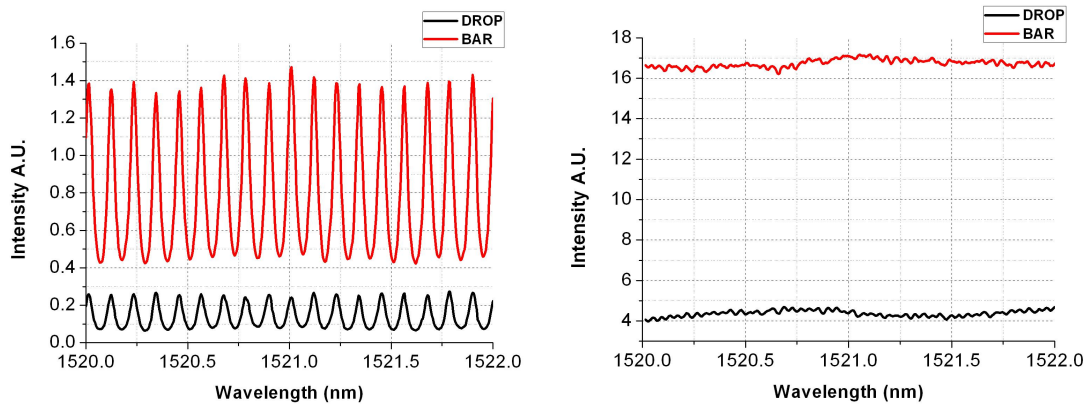
A large set of test devices, with different values of G , L_c and R , was designed and characterized, in order to evaluate the agreement between the physical devices and numerical simulations – and to identify the technological limitations, the accuracy and the reliability of the fabrication process. Measurements of the coupling factors

were carried out with the test rig described in section 3.1.

The coupling coefficient was extracted from the ratio of the percentage of the power intensities over the two waveguides as:

$$K = \frac{P_{DROD}}{P_{BAR} + P_{DROD}} \quad (3.12)$$

where P_{DROD} represent the power measured at the drop port and P_{BAR} the power in the Bar Port, shown in Figure 3.17(a). For this kind of measurement the ratio is independent of the power launched (since the coupler losses have been shown to be negligible) – and the output power levels at the two ports are measured with the same input alignment. An initial limitation to the precise estimation of the coupling ratio was the presence of the Fabry Perot oscillations, but the introduction of the inverse tapers improved the estimation accuracy.



(a) Measured power at the cross port (Red) and the Bar port (Black) for a device without mode adapters and a nominal power coupling coefficient of 20 %, using eq. 3.12 the value of K is equal to 12 %.

(b) Measured power at the cross port (Red) and the Bar port (Black) for a device with mode adapters and a nominal power coupling coefficient of 20 %, using eq. 3.12 the value of K is equal to 19 % in excellent agreement with the nominal value.

FIGURE 3.20: Measurements of the output transmission characteristics for a directional coupler. From this graphs it is possible to calculate the value of K .

Figure 3.20 shows, as an example, two measurements of a coupler with (b) and without (a) the inverse tapers. In the latter case, the value of K is easily derivable. In the former case, it is possible to estimate the value of the coupling factor as the ratio of the two transmission spectra for each wavelength. The maxima and the minima of the resonances are located at the same position, since these correspond to the interference pattern of a signal traveling in the same cavity. However, the measurements obtained without the tapers are not reliable, due to the interference of the backscattered power of the signal at the device edges.

The output characteristic in this case is the complex product (in the frequency domain) of the approximately sinusoidal response time of the cavity and the square sinusoidal response of the coupler. As the signal is reflected at the output facets it propagates back into the waveguide and it couples again at the coupler section – and this happens for each round trip, with the net result being a variation in the measured value from the designed one.

Initially, the directional couplers were only covered with a layer of PECVD silica and exhibited a great variability in the measured K values with a strong under-coupling (of about 50 %), suggesting major problems in the computation of the coupling coefficients or a serious problem in the fabrication process, such as the presence of air in the gaps. The variability was difficult to compensate due to its random nature and different behavior for nominally identical devices was measured. The hypothesis of poor gap filling was confirmed by an SEM inspection of the cross section of the gaps. To solve this problem a combined layer of a Spin on Glass (HSQ) and PECVD was always employed, giving a better reproducibility.

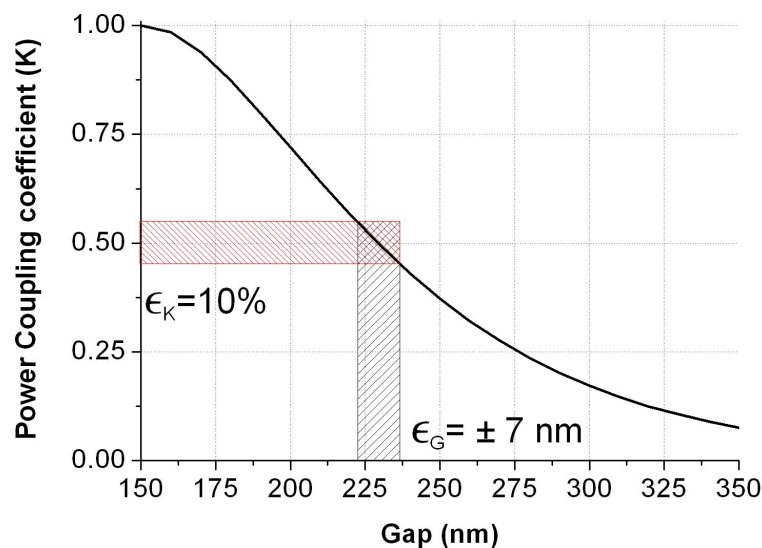


FIGURE 3.21: Simulated behavior of the power coupling coefficient as a function of the gap: $K = 0.5$, $\epsilon_K = 10\%$ can be obtained by controlling the gap dimension G with a precision $< \pm 7\text{ nm}$.

A change in the coupling coefficient could also derive from a small variation of the physical dimensions. A variation of $\pm 7\text{ nm}$, is enough to cause, for a value of $K = 0.5$, a modification of the coupling factor as large as 10%, which decreases as K becomes larger or smaller, as illustrated in Figure 3.21. In Chapter 5 the control on the physical dimensions of the fabricated structures is more deeply analyzed

and it will be shown that very small variation, on the order of nanometre, are achievable with an optimized technology.

Further measurements, summarized in Table 3.2 and Figure 3.22, without the inverse couplers, were still producing a residual level of under-coupling, with a mean value for the error of around 25 %. Measuring several realizations of nominally identical structures within the same chip and between different fabrication runs a high repeatability was observed. The standard deviation of the measured error over K is only $\epsilon_K = 4\%$, a value in agreement with the expected fabrication accuracy (about a few nanometres).

Sample/Device	K_D	K_M	$(K - K_M)/K$
2/A	0.08747	0.0705	0.1943
2/A	0.17780	0.1280	0.2801
2/A		0.3181	0.2952
1/A	0.45132	0.3317	0.2650
1/B		0.3248	0.2804
2/A	0.64770	0.5099	0.2127
Mean Value	-	-	0.2546
Std.Deviation	-	-	0.0411

TABLE 3.2: Comparison between design specifications (K_D) and experimental results (K_M) for several fabricated couplers.

The inverse coupler has reduced the error on the estimation of K to around 5 % (see Figure 3.20). The residual error is due to a small discrepancy between the value of the refractive index of the spinned HSQ used in the simulations and the actual value. The HSQ refractive index is dependent on the curing temperature and cannot be determined exactly if not in a bulk situation. The existing under-coupling, however, was not the major source of concern, since it was only responsible for a slight narrowing of the bandwidth of the CROW or microring resonators and can easily be compensated at the design stage.

3.6 Microring Resonators

The optical resonators developed in this work are racetrack resonators formed by two semi-circumferences having bending radius R – and two straight paths (L_c), as depicted in Figure 3.23(a). The straight section enables the design of a longer coupling region and relaxes the requirements on narrow gaps, reducing the problem

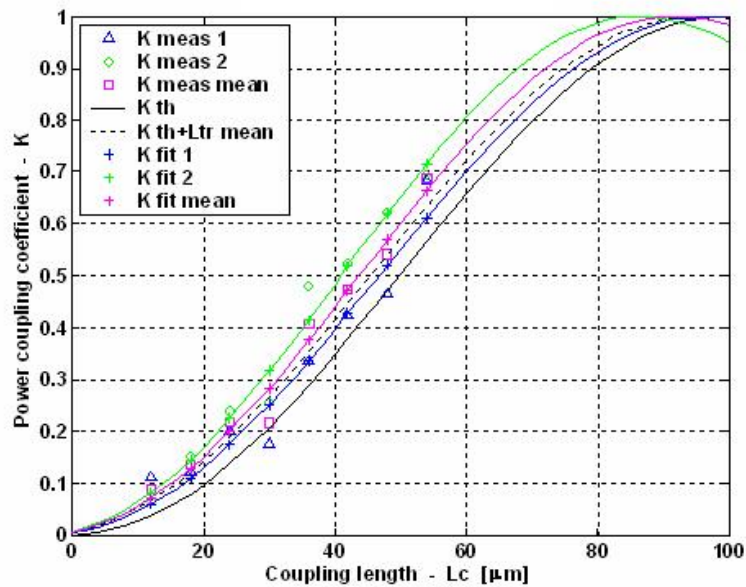


FIGURE 3.22: Measurements of the power coupling coefficient K for the directional coupler with a fixed gap (200 nm) and different coupler lengths. The outputs at the DROP and the BAR ports are obtained by exciting the device at both input ports, in sub-sequential measurements. The fitted data obtained from the average power level for each measurement are in good agreement with the design values and within the mean value error of 25 %.

related to the RIE Lag phenomenon. However, the increase in the coupling length causes an increase in the total optical length – and then a reduction of the FSR .

The configuration of the Ring Resonator most widely used in the course of this work had a $20 \mu\text{m}$ bending radius, with a variable coupler gap (G) and length (L_c). This choice was motivated by the following considerations:

- the value of R has to be chosen so as to guarantee negligible bending losses: a conservative value for both TE and TM polarizations is $R = 20 \mu\text{m}$;
- the power coupling coefficient K can be varied by changing either the gap G or the coupling length L_c . The first solution does not modify the shape of the ring resonator or the FSR , in the case of coupled cavities. The second one needs a more accurate technological control of the gap dimension G : for a fixed error on the gap dimension, it produces a bigger error in the coupling coefficient, as L_c increases (as may be deduced from Figure 3.19);
- The value of L_c must enable the realization of a large range of K , for a defined value of G ;

All the main properties of Ring based devices can be better understood by introducing two basic building blocks, namely the Ring Resonator Phase Shifter and the Ring Resonator Filter.

3.6.1 Ring Resonator Phase Shifter

Figure 3.23 is a schematic of a ring Resonator Phase Shifter structure (a) – and a SEM image of a fabricated device (b).

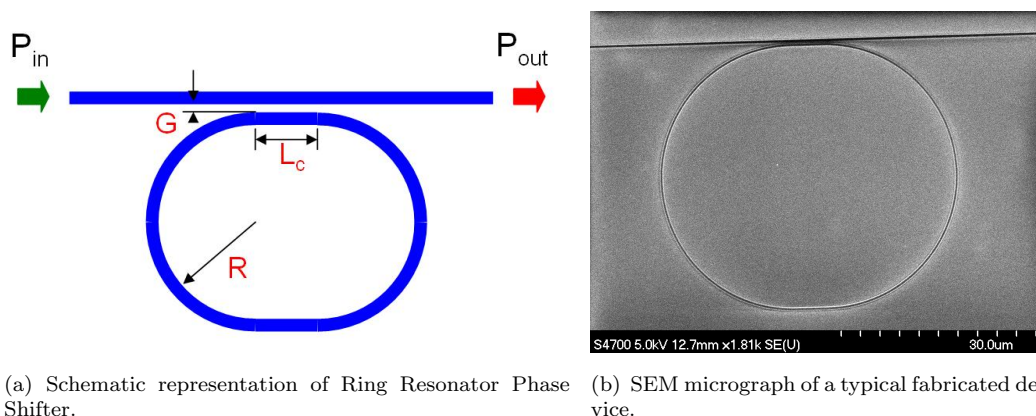


FIGURE 3.23: Schematic and SEM image of Ring Resonator Phase Shifter.

The ring has a radius R , a coupler length L_c (we consider the effective length in the analysis) and gap G that together determine the self-coupling field-coefficient r . The transfer function for this basic building block in the Z-transform domain, evaluated by using the Transfer Matrix formalism in Appendix A, is [102]:

$$H_{12}(z) = \frac{r - \gamma z^{-1}}{1 - r\gamma z^{-1}} \quad (3.13)$$

where $\gamma = \exp(-\alpha_r L_r/2)$ is the round trip field loss parameter, which takes into account all the possible losses of the components, including material absorption, scattering loss, radiation loss in the bend and the excess loss of the coupler – and $z^{-1} = \exp(-j\beta L_r)$.

The Phase Shifter transmission has one pole and one zero, at the positions $z_p = \gamma r$ and $z_z = \gamma/r$, respectively. While the pole always lies inside the unit circle (no amplification, $\gamma \leq 1$ always), the position of the zero depends on the round trip losses – and, in particular, on the ratio γ/r .

- If $r < \gamma$, the zero lies outside the unit circle and the phase shifter exhibits a maximum-phase response. In particular, with zero losses ($\gamma = 1$), the pole is a mirror image of the zero about the unit circle and the device behaves as a pure phase-shifter with unitary amplitude response, at any frequency.
- At the condition of $r = \gamma$, the zero lies on the unit circle and the transmission of the filter is identically zero, in correspondence with the Ring Resonator resonant frequency: this situation is usually referred to as *critical coupling*.
- If $r > \gamma$, the zero lies within the unit circle and the phase-shifter exhibits a minimum-phase response.

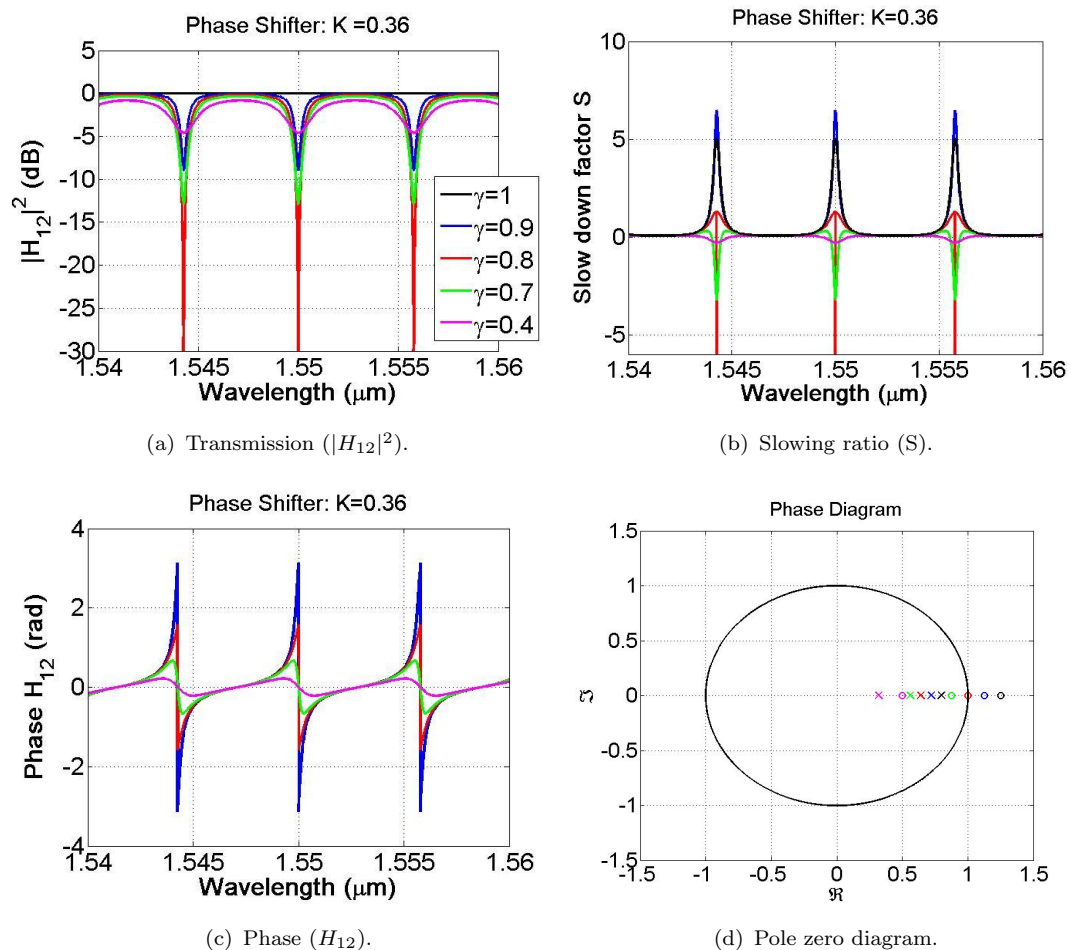


FIGURE 3.24: a) Transmission ($|H_{12}|^2$), b) slowing ratio (S), c) phase (H_{12}) and d) pole zero diagram of a Ring Resonator Phase-shifter ($\text{FSR} = 250 \text{ GHz}$) with $r = 0.8$ ($K = 36 \%$) for increasing round-trip loss γ : lossless phase-shifter with $\gamma = 1$ (black line), maximum-phase response $\gamma = 0.9$ (blue line), critical coupling $\gamma = r = 0.8$ (red line) and minimum phase response $\gamma = 0.6$ and 0.4 (green and pink lines respectively).

The intensity transmission $|H_{12}|^2$ and the slowing factor S of the Ring Resonator Phase-Shifter evaluated from equation 3.13 are shown in Figures 3.24(a) and 3.24(b), respectively. In the example shown, the power coupling coefficient between the Ring Resonator and the bus waveguide is fixed to be $K = 0.36$ and increasing values for the round-trip loss parameter γ are considered.

- Black lines show the frequency response of the lossless ($\gamma = 1$) phase-shifter, with unitary transmission.
- If $r < \gamma < 1$, the transfer function exhibits a notch corresponding with each resonance wavelength.
- At the critical coupling the $\gamma = r$ (red line) transmission drops to zero – and a singularity appears in the group delay ($\tau_g = \partial \angle H_{12}(\omega) / \partial \omega$) because the derivative of the phase response became infinite. The discontinuity in the Slow Down Factor ($S = \tau_g / \tau_r$) for this configuration can be calculated through the continuity condition at the left and right limits.
- If $\gamma < r$, the minimum-phase condition provides a negative delay due to the negative slope of the phase. The occurrence of negative delays (and so negative S) in Ring Resonator Phase Shifters is mathematically a valid solution and corresponds to an apparent negative group velocity v_g which arises as a consequence of strong attenuation and envelope reshaping effects [103].

The Q -factor of the cavity is defined as [104]:

$$Q = \frac{2\pi n_{eff}}{\lambda_0} \frac{L_r}{[-\ln(r_1 r_2) + \alpha_r L_r]} \quad (3.14)$$

It depends on the field coupling coefficients (r_1, r_2), the ring length (L_r) – and the value of the losses (α_r).

In the case of a ring that is side coupled to only one waveguide ($r_2 = 1$, so $t_2 = \sqrt{1 - r_2^2} = 0$), for a fixed value of the ring length, the Q -factor is inversely proportional to the losses – and proportional to the logarithm of r_1 (Figure 3.25). For small values of r_1 and α_r , the power coupled into the ring only slightly diminishes its value – due to the low propagation losses and the fact that only a small percentage of the power is extracted from the ring at each coupler section, leading

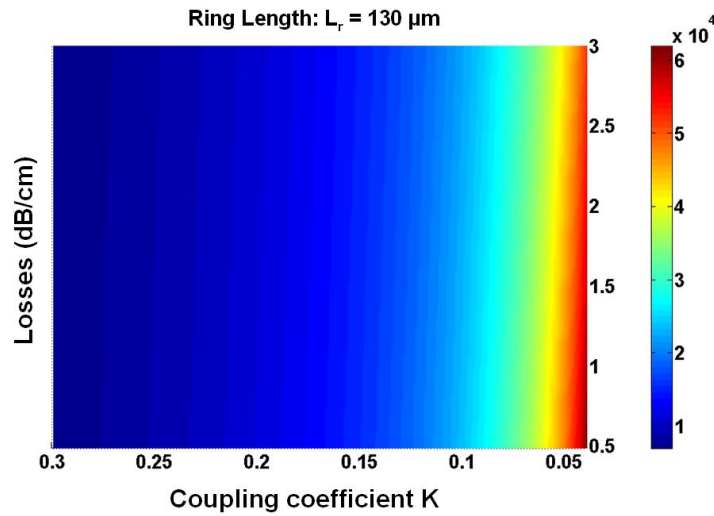


FIGURE 3.25: Q factor for a fixed value of ring length ($L_c = 130 \mu\text{m}$) and different values of Losses and cross coupling power coefficient (K).

to a large Q -factor. For the ring length ($L_r = 130 \mu\text{m}$) under consideration, the maximum achievable Q -factor (62000) is obtained for $\alpha_r = 0.434 \text{ dB/cm}$ and $K = 0.04$. While the condition on the coupling coefficient is easily achievable by a proper coupler design, the condition on the propagation losses is more difficult to obtain and is strongly related to the technology (Chapter 2): practically, values smaller than 1 dB/cm are difficult to accomplish (section 3.3).

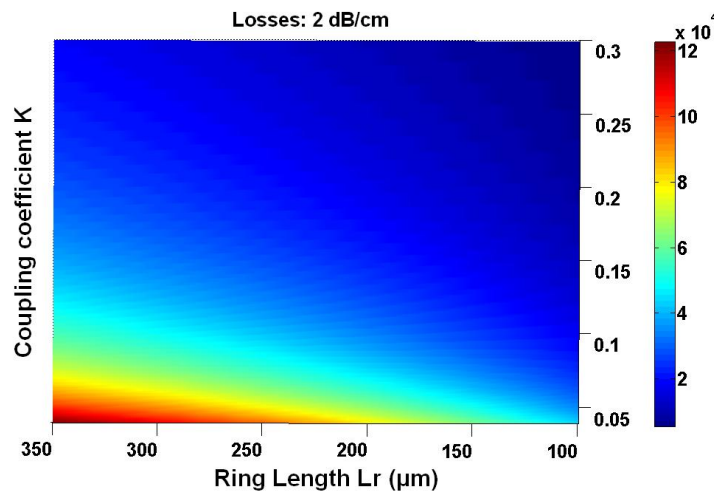


FIGURE 3.26: Q factor for a fixed value of Losses (2 dB/cm) and different values of ring length (L_c) and cross coupling power coefficient (K).

Figure 3.26 shows the behavior of the Q -factor in the case of losses equal to 2 dB/cm for different values of Ring length (L_r) and coupling coefficients (K). The value of the Q -factor increases rapidly with ring length, but at the cost of an increase in the footprint.

For small values of the field cross-coupling coefficient, the Q -factor is dominated by $\alpha_r L$ – the maximum Q -factor achievable [18] is:

$$Q_{limit} = \frac{2\pi n_{eff}}{\lambda_0} \frac{1}{\alpha_r} \quad (3.15)$$

Minimizing losses is of prime importance for the development of ultrahigh- Q [18]. The critical coupling, where complete throughput attenuation at resonance is achieved, is obtained when $r = \gamma$, in this case, $Q_{critical} = Q_{limit}/2$.

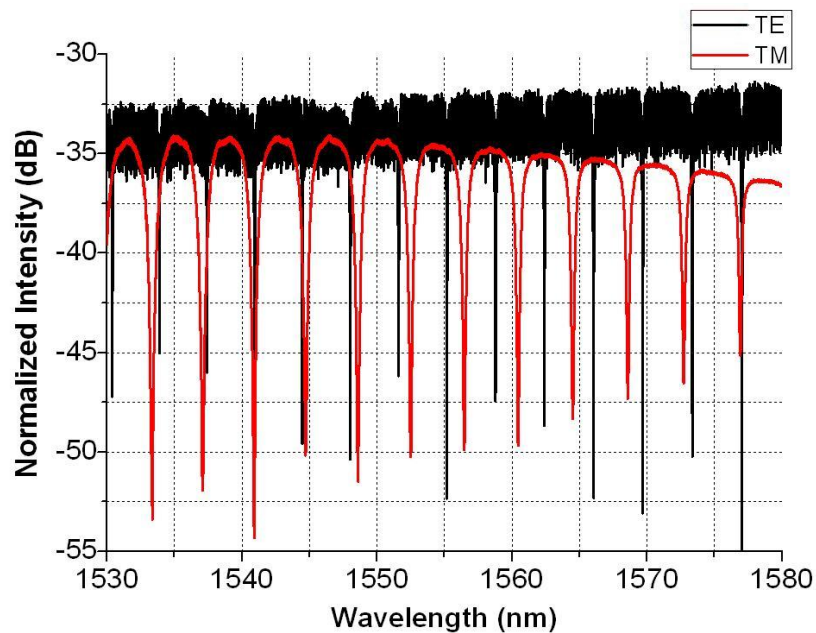


FIGURE 3.27: Transmission spectra of a Ring Resonator Phase Shifter with $K = 10\%$ for TE (black line) and TM (red line) polarizations.

Figure 3.27 shows a typical transfer function for a Ring Resonator phase shifter, for TE (Black) and TM (red) polarizations (in this device the inverse tapers are not present).

The characteristic behaviour of the Fabry-Perot fringes is clearly visible for TE (about 3-4 dB peak-to-peak modulation), while they are almost completely absent for TM polarization. These results arise from the fact that the TE mode experiences a higher reflectivity at the cleaved facets as compared to the TM mode.

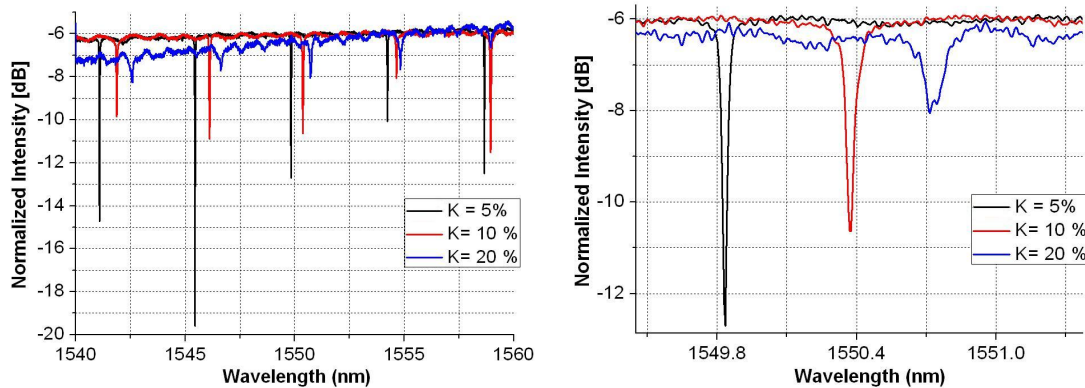
It can also be seen that TE and TM transfer functions have resonances at different wavelengths (due to their different values of n_{eff}) and a slightly different period (due to the different values of n_g).

Moreover, in the TE spectrum the depth of the notches exhibits a random variation with wavelength: as we shall see in the next section, this variation is due to the

random waveguide backscattering and it is less visible in TM spectrum because of its lower backscattering coefficient. In TM polarization, instead, a gradual increase in the losses can be observed as the wavelength increases – which is due to the leakage that increases with the wavelength (since the mode confinement diminishes).

Finally it can be also seen that the TE and TM experiences different values of K : while TE mode sees a coupling coefficient close to the designed one ($K = 10\%$), the TM mode sees a higher value of K , as indicated by the larger peaks.

The oscillations in the TE characteristics were eliminated by using the inverse taper described in section 3.4.2. The transfer functions of several different ring resonator phase shifters, with a radius $R = 20\ \mu\text{m}$ and different values of coupling coefficients K (5 %, 10 % and 20 %), are shown in Figure 3.28. The measured transmission spectra are characterized by a higher transmittivity and a smaller amount of Fabry Perot oscillation – making the extraction of the basic figures of merit of the devices easier, even for small values of the coupling coefficients.



(a) Normalized Intensity Spectra for 3 rings with different coupling coefficient obtained by changing the coupler length (L_c).

(b) Expanded section of the transmission spectra of the devices plotted on the left.

FIGURE 3.28: Transmission spectra of a Ring Resonator Phase Shifter for several values of the coupling coefficient K : 5 % (Black), 10 % (Red) and 20 % (Blue). The higher transmission and small level of FP oscillation, if compared to 3.27, are greatly reduced by inverse tapers described in section 3.4.2.

In the following, ring resonator phase shifters with different lengths are analyzed. To obtain the same error on the coupling coefficient, the ring resonators were designed with the same gap dimension – and, the different values of the coupling are obtained by changing the coupler length (L_c). An increase in the coupler length, has the effect of increasing the total length of the cavity, leading to a different value of FSR . The measured peak spacings in the wavelength domain

are 4.41 nm, 4.27 nm and 4.11 nm, corresponding to racetrack resonators with a total length of 129.14 μm , 133 μm and 138.78 μm , respectively. The value of the waveguide group index, extracted from the formula for the *FSR*, is $n_g = 4.22$, in agreement with the range of values found in [105, 106] for devices with a similar geometry.

The different coupler lengths result in an unequal amount of power being coupled into the ring structure from the bus waveguide. As a trend it is possible to identify that, as the power cross coupling coefficient (K) increases, the maximum depth of the peak decreases and its width increases. This corresponds to a decrease in the *Q-factor* and the corresponding on-resonance attenuation, as expected from the theory for maximum phase-response systems. The measured value of the *Q-factor*, summarized in Table 3.3, are in good agreement with the simulated devices shown in Figure 3.26.

Sample/Device	K_D	Q_D	Q_M	K_E	$(K - K_E)/K$
1/A	0.05	41300	43000	0.0475	0.05
2/A	0.05	41300	44288	0.046	0.08
1/B	0.1	22900	30000	0.0744	0.25
2/B	0.1	22900	22150	0.0985	0.015
1/C	0.2	11880	13470	0.1825	0.087
2/C	0.2	11880	12480	0.191	0.045
Mean Val	-	-	-	-	0.0875
Std.Dev	-	-	-	-	0.049

TABLE 3.3: Comparison between design specifications (K_D and Q_D) and estimated value (K_E) of the coupling coefficient through the extraction of the the real coupling coefficient from the measured *Q-factor* (Q_M).

From the formula of the *Q-factor*, for a given value of losses, it is possible to extract the value of the coupling coefficient, which is an easy way of confirming the values of K . A mean variation of about 10 % and a standard deviation of 5 % were extracted, in good agreement with the measurement of section 3.5.

The peak depth variation in the measurement of Figure 3.28(a) is due to the contribution of the backscattering phenomenon, which is frequency dependent. This effect is more evident in devices with sufficiently low values of K since it depends on the group index. In the off-resonance spectral regions, the back scattering effect almost disappears – and lead to has the same value as for straight waveguides [107]. Low coupling coefficients resonators exhibiting sharper notches with corresponding higher derivatives the phase and a higher group delay τ_g . The ring

resonator group index $n_g = \tau_g c / L_r$ is directly proportional to the group delay and inversely proportional to the L_r .

Since these two terms also determine the ring resonator *FSR*, the backscattering does not appear as a noise contribution in the transfer function – but there is a strong correlation with the ring length. It has been demonstrated that the backscattering increases with the square of the group index (n_g^2) [107]. This quadratic dependence results from the fact that backscattering produced at each round trip adds coherently to the power backscattered in the previous round trips and resonating in the ring resonator, with the coherent build-up mechanism being favorably phase matched by the periodic nature of the structure [108]. Ring resonators with a smaller K (bigger n_g) are more influenced by this phenomenon, due to a higher value of the group index. Moreover, the backscattering is a unique characteristic of a particular device i.e. different devices have different backscattering levels because of the variability in the waveguide roughness. Similar devices with the same physical geometry will experience the same total amount of backscattering but, since this process is stochastic, the random distribution of the imperfections will affect the overall spectra in different ways.

Figure 3.29 shows the transmission spectra of two rings with identical dimensions. The *FSRs* of the two devices are identical and the position of the peaks is slightly shifted due to the process variability (further discussed in Chapter 5). If we analyze the transmission notches, it is possible to distinguish the stochastic nature of the backscattering.

In practical applications, it is never convenient to choose a value of n_g too big. If the group delay has to be maximized, it is better to increase L_r , rather than n_g . In fact, large resonators with a small n_g exhibit less backscattering than small rings with a high n_g – the price to be paid for minimizing backscattering is the footprint increase and the free spectral range reduction [107].

Therefore, the effect of the backscattering, is a critical parameter in the realization of ring resonator structures, even for a state-of-the-art technology (sub-nanometre level of roughness). For sufficiently small values of K the amount of light that is back reflected could even exceed the level of power that is transmitted. This result was predicted theoretically [108], and recently, it has been measured by our collaborators in Politecnico of Milano. The other effect related to the backscattering which has been identified theoretically in high quality factor resonators such as

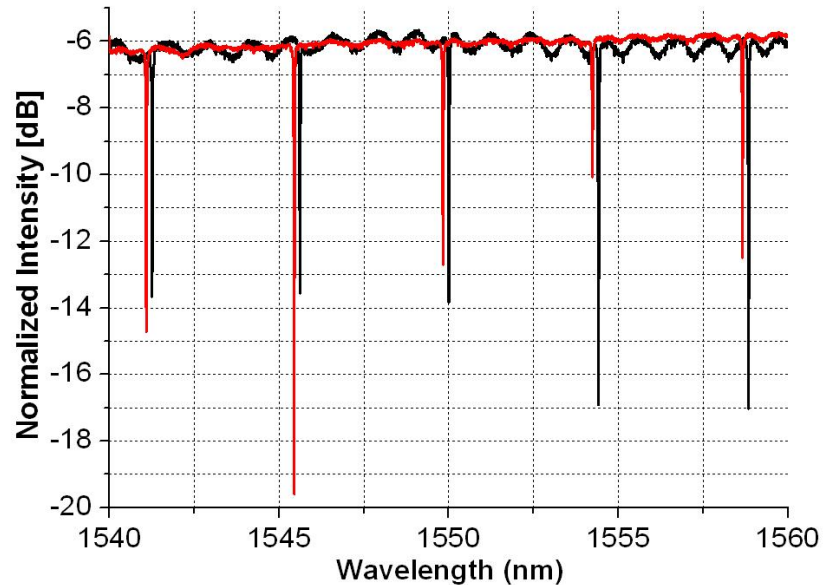


FIGURE 3.29: Transmission characteristic of two nominally identical devices, the peak position is slightly shifted due to the process variability. The difference in the peak depths is due to the random nature of the backscattering which influence similar devices in a different way.

micro-sphere [109] or micro-disk [110] is a peak splitting effect originated by the existence of a counter-directional propagating mode inside the ring structure.

Because of the periodic nature of the structure, forward and backward modes become naturally phase matched by any perturbation.

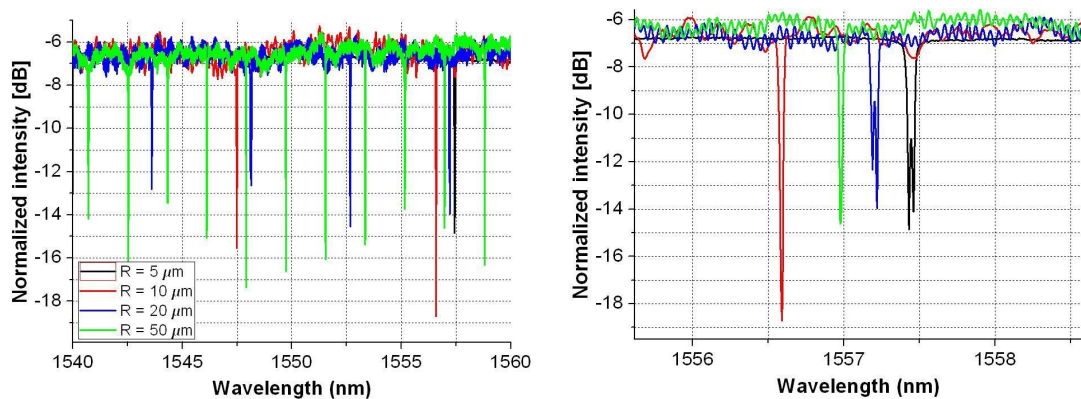
Such counter-directional coupling leads to two deleterious effects:

- It destroys the directionality of the traveling-wave resonator.
- It causes a split of the resonant peaks – since the coupling breaks the degeneracy of forward and backward modes.

From an intuitive point of view, the presence of surface roughness acts as a distributed partial reflector along the waveguide ring sidewalls. If this reflector was a lumped element, a resonance split would appear in correspondence of resonance peak and the effect would have the same intensity for all peaks [108]. Due to the stochastic nature of the sidewall roughness and the frequency dependence, the splitting does not occur at all the wavelengths with the same intensity.

Measurements of point coupler ring resonators with different radii (5, 10, 20, 50 μm) had shows this phenomenon. For point couplers, the total value of the coupling coefficient is related to the ring radius due to the not negligible contribution

of the curved part to the coupling coefficients. Figure 3.30(a) shows the transmission spectra of the devices under consideration. Firstly, the different number of peaks in the measured range of interest is due to different lengths of the cavities. The presence of backscattering affects all the structure almost in same way – this is due to the extremely low values of cross coupling coefficient realized ($K = 0.005$, 0.0068 , 0.019 and 0.0481 for $R = 5, 10, 20, 50 \mu m$, respectively) yield to large group indexes.



(a) Transmission characteristic of ring resonator with coupling coefficients of 0.005, 0.0068, 0.019 and 0.0481.

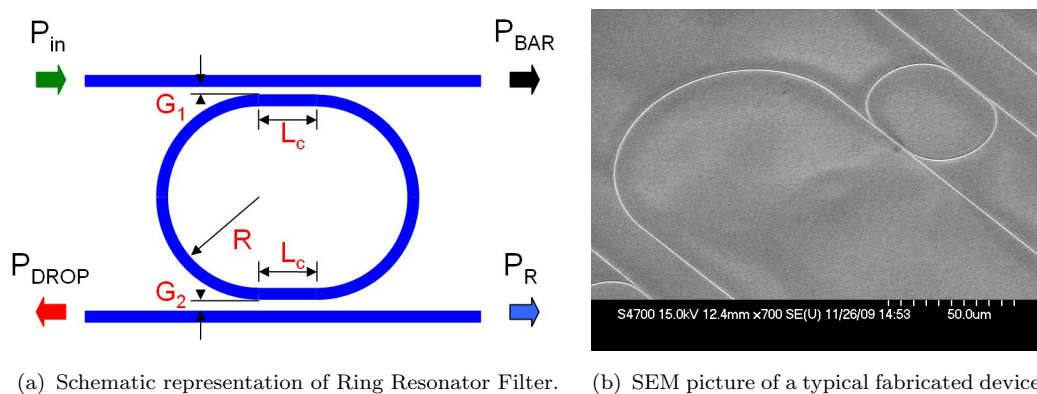
(b) Particular of the transmission for a randomly chosen range, showing as an example the peak splitting phenomena.

FIGURE 3.30: Transmission characteristic of ring resonator phase shifter with point coupler and different ring radii.

A deeper investigation of the transmission spectra around each peak shows that the splitting of the resonances has not the same effect on all the frequency range, suggesting once again the random nature of the backscattering. In fact, some peaks in the same device have a more pronounced effect while even neighborhood peaks do not show any splitting. The only visible trend is the one related to the maximum split distance which seems dependent on the value of the group index. Further devices are under investigation to quantify the splitting phenomenon and relate it to the phase and the group index. An important point to highlight is that extremely low coupling coefficients destroys the shape of the resonance peaks reducing consequently the value of the Q -factor. If high Q values are needed, it is convenient to increase the ring length at a cost of foot print or reducing the value of the losses.

3.6.2 Ring Resonator Filter

In the filter geometry the ring resonator is coupled to two bus waveguides. The ring-to-bus field coupling coefficients at the two ports are named jt_1 and jt_2 , respectively, with $t_i^2 = 1 - r_i^2$, with $i = 1, 2$. Figure 3.31(a) is a schematic representation of a Ring Resonator Filter, Figure 3.31(b) shows an SEM micrograph of a fabricated device – the drop port is curved for measurement purposes in order to have all output ports on the same side of the chip.



(a) Schematic representation of Ring Resonator Filter. (b) SEM picture of a typical fabricated device.

FIGURE 3.31: Schematic and SEM picture of Ring Resonator Filter.

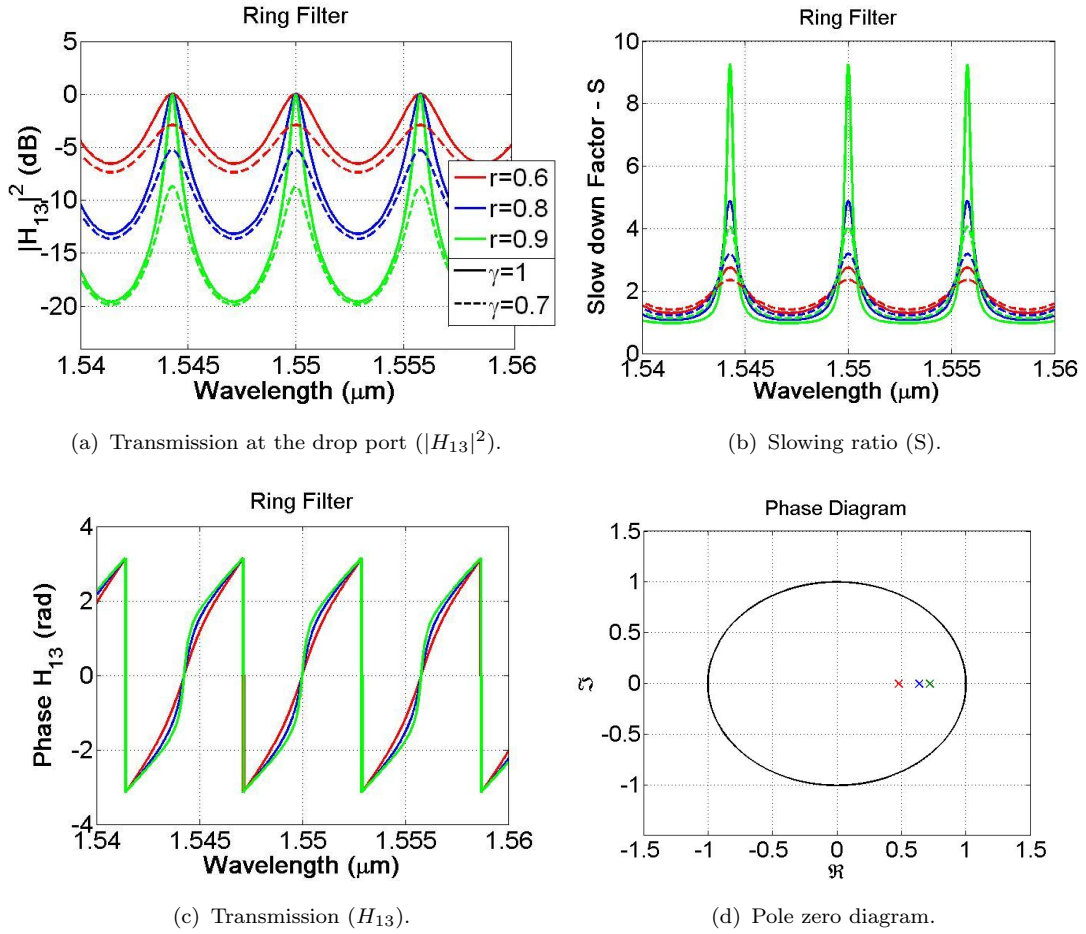
The transfer functions for this basic building block are [102]:

$$H_{12}(z) = \frac{P_{BAR}}{P_{in}} = \frac{r_1 - \gamma r_2 z^{-1}}{1 - \gamma r_1 r_2 z^{-1}} \quad (3.16)$$

$$H_{13}(z) = \frac{P_{DROP}}{P_{in}} = -\frac{t_1 t_2 \sqrt{\gamma} z^{-1}}{1 - \gamma r_1 r_2 z^{-1}} \quad (3.17)$$

The transmission and group delay at the bar port ($|H_{12}|^2$) of a ring resonator filter are qualitative the same as those of the ring resonator phase shifter shown in Figures 3.24(a) and (b), respectively.

The transmission H_{12} vanishes only if the zero of the transfer function, located at $z_z = \gamma r_2 / r_1$, lies exactly onto the unitary circle, that is if $\gamma = r_1 / r_2$. In a lossless ring resonator, this happens only if $r_1 = r_2$ and the frequency response is analogous to that of the phase-shifter operating at the critical coupling condition. If $\gamma < r_1 / r_2$ the bar port response exhibits a minimum phase response, whereas maximum-phase response requires $r_1 < \gamma r_2$. The transfer function H_{13} has the same pole as the through port, $z_p = \gamma r_1 r_2$ and one zero at infinity. The intensity transmission $|H_{13}|^2$ and the slowing factor S of the drop port of the ring resonator

(a) Transmission at the drop port ($|H_{13}|^2$).

(b) Slowing ratio (S).

(c) Transmission (H_{13}).

(d) Pole zero diagram.

FIGURE 3.32: a) Transmission ($|H_{13}|^2$), b) slowing ratio (S), c) phase (H_{13}) and d) pole zero diagram of a Ring Resonator Filter (FSR = 250 GHz) at the drop port in the lossless (solid line, $\gamma = 1$) and lossy $\gamma = 0.7$ cases, for different coupling coefficients: $r = 0.6$ (red lines), 0.8 (blue lines), 0.9 (green lines)

filter are shown in Figures 3.32(a) and 3.32(b), respectively. Solid lines refer to the case of zero losses, while dashed lines show an example of lossy filter with $\gamma = 0.7$. The coupling coefficients at the two ports are assumed equal with values of 0.6 (red lines), 0.8 (blue lines), 0.9 (green lines). When compared to the ring resonator phase shifter, the Q -factor of the cavity is reduced by the presence of the drop waveguide. In this case, there is an additional contribution ($\ln(r_2)$) to the cavity attenuation as shown in equation 3.14.

K	Q_{PS}	Q_F
5 %	41300	33670
10 %	22900	11850
20 %	13470	9950

TABLE 3.4: Comparison between the Q-factor of Ring Resonator Phase Shifter (Q_{PS}) and Ring Resonator Filters (Q_D) for different value of K .

Table 3.4 compares, the measured value of the Q – factor of ring resonator phase shifter (Q_{PS}) and ring resonator filters (Q_F) for different value of K . Figure 3.33 shows the normalized transmission spectrum at the bar-port (black line) and the drop port (red line) of a ring resonator filter with $K_1 = K_2 = 5\%$.

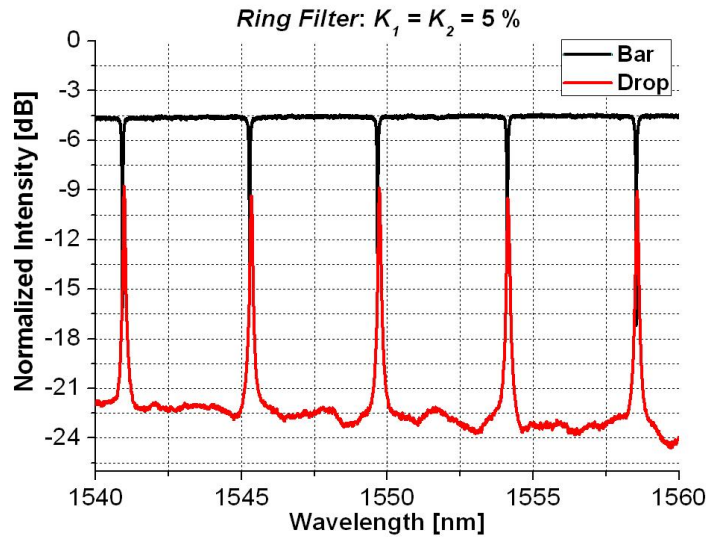


FIGURE 3.33: Normalized intensity at the bar (black line) and the drop port (red line) of a ring resonator filter with $K_1 = K_2 = 5\%$.

The transmission spectra corresponding to the value of $K = 10\%$ and 20% are shown in Figure 3.34 and Figure 3.35, respectively.

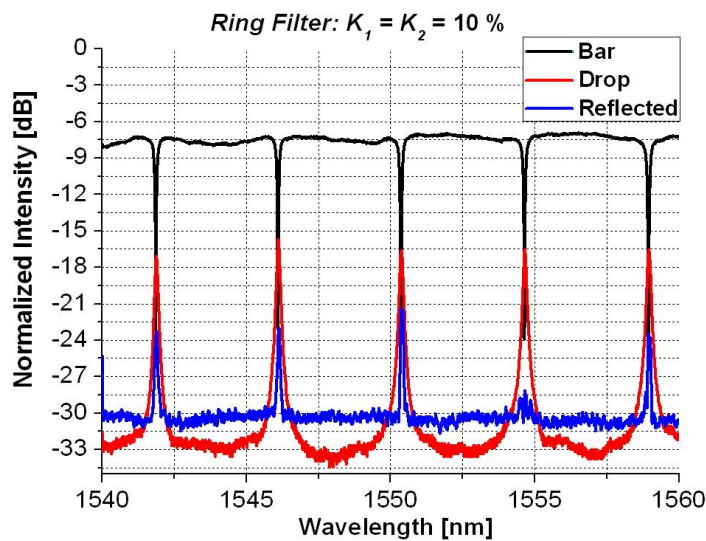


FIGURE 3.34: Normalized intensity at the bar (black line), the drop port (red line) and the reflection port (blue line) of a ring resonator filter with $K = 10\%$.

Consideration similar to the case of a single ring resonator can be made by examining the graph. One interesting result is constituted by the Blue curve, which

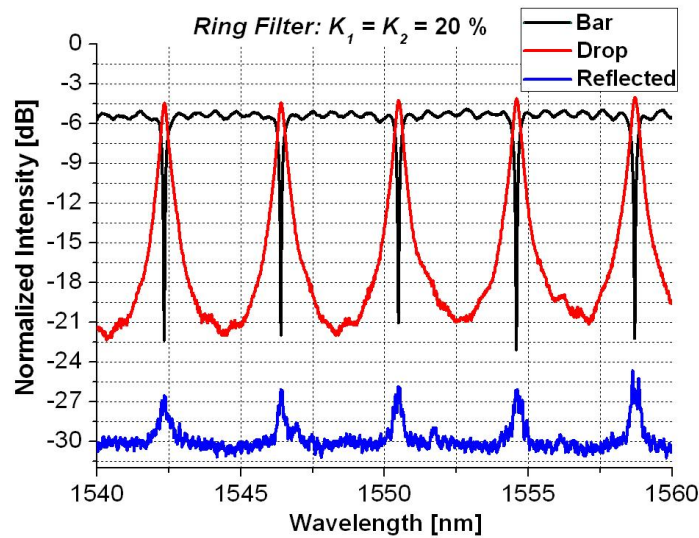


FIGURE 3.35: Normalized intensity at the bar (black line), the drop port (red line) and the reflection port (blue line) of a ring resonator filter with $K = 20\%$.

represent the output at the reflection port (P_R). In an ideal situation and in the absence of backscattering, the output at this port should be zero (the counter propagating mode is zero). The presence of roughness on the ring sidewalls induces a counter propagating mode which is reflected back to the input port and the reflection port. As the coupling coefficients are reduced, the intensity at the reflection port becomes larger confirming, once again the dependence of the backscattering with the group index (sharper peaks, more backscattering). It is important to underline that maximum care was taken during these measurements to optimize the alignment of the output lens in the resonance condition, where the maximum intensity was available at the drop and reflection port. Moreover, only the output lens was moved during the measurement of the single device, ensuring the same alignment precision and power level at the input for all three measurements.

For both the phase shifter and the ring resonator filter the pulse amplitude at the output of the system is dependent on the bandwidth, coupling coefficient and losses of the ring resonator. The presence of the losses do not affect the shape of the spectral response but simply induce an insertion loss usually higher at the drop port than at the through port. More important for dispersion consideration is the effect of the group delay characteristic. For the single ring systems the group delay has a bell-shaped characteristic centred at the resonance frequency. If the bandwidth of the filter is large enough when compared to the pulse bandwidth, small distortion will be present. The filter induced second-order dispersion vanishes at the center frequency whereas a third-order dispersion is always present.

For this reason the signal spectrum should be centred and well confined inside the filter bandwidth, otherwise the third-order dispersion produces an asymmetrical distortion of the pulses [111]. This impairment, however, can be eliminated by cascading an all-pass filter to equalize the group delay distortion as discussed in chapter 6 and appendix D.2.

3.7 Conclusions

Basic building blocks have been analyzed both theoretically and experimentally. Good agreement between the measurements and the simulations is shown. Propagation loss measurements constitute the state-of-the-art for silicon-on-insulator devices. The efficient power coupling scheme developed have results comparable with the best devices available in literature. Directional couplers and ring resonator devices were deeply investigated, presenting their limitation in terms of uniformity and backscattering. Chapter 5 is dedicated to the analysis of the variability over time. Further measurements on coupled cavities composed by a combination of the analyzed building block are presented in chapter 6

Chapter 4

Thermal tuning of Silicon on Insulator Ring Resonators

4.1 Introduction

One key requirement in the design of microring filters, resonators and delay lines is the capability to tune the position of the resonance of these devices over a certain range of wavelengths. The shift of the resonance peak is achieved by taking advantage of the ability to change the refractive index of the guiding layer via the temperature or the charge concentration (the thermo-optic effect and the electro-optic effect, respectively). In the delay lines discussed within this work, the tuning mechanism makes it possible not only to tune the position of the resonance of the device in order to compensate the fabrication variability but also to change the delay.

The SOI material is a crystallographically centro-symmetric material and therefore 2^{nd} order electro-optic effects such as Pockels are not present. The Kerr electrooptic effect may enable tuning of the refractive index. However, the coefficient for Silicon is very small – so this would require large voltage/field strength. A typical figure is an index change equal to $\Delta n \approx 10^{-4}$ for an electric field of $E = 10^6$ V/cm [112]. The refractive index can also be modulated by free carriers, resulting in a $\Delta n \approx 10^{-4}$ for a carrier injection level of $\Delta N \approx 10^{17}$ [112]. Exploitation of this tuning mechanism would require a major redesign of the waveguide geometry and the doping of the structure to define the *pin* junctions to be used in developing a simple tuning element.

The refractive index of optical materials such as crystals, semiconductors and glasses is not a constant parameter with the temperature [113] and this effect can be used to develop a simple tuning element.

Thermo-optic devices have been studied widely [114–117], especially in silicon on insulator based planar photonic integrated circuits such as Mach Zenders [118–121], photonic crystals [122–124] and microring resonators [125–127].

4.2 Thermo-optic effect in Silicon

The thermo-optic effect originates from the temperature dependence of the refractive index. An increase in the temperature (ΔT) has the effect of varying the refractive index by an amount Δn 4.1:

$$n' = n + \Delta n \quad (4.1)$$

Where n is the original refractive of the material and n' is the refractive index obtained as consequence of the variation. This variation induces a change in the transmission spectrum of the device, which experiences a red shift of the resonance peaks of the resonator:

$$\frac{\Delta \lambda}{\Delta T} = \frac{\lambda_0}{n_{eff}} \frac{\Delta n}{\Delta T} \quad (4.2)$$

A schematic cross-section of an SOI structure where the thermo-optic effect could be investigated is shown in Figure 4.1

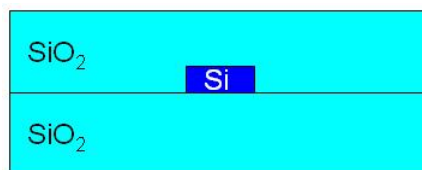


FIGURE 4.1: Schematic cross-section of a general device structure where the thermo-optic effect is analyzed.

Silicon has a large thermo-optic coefficient, $\Delta n/\Delta T = 1.86 \cdot 10^{-4} K^{-1}$, and a small thermal expansion coefficient $\alpha_{exp} = 4.6810^{-6} K^{-1}$ [128]. These figures make the

thermo-optic effect a very efficient mechanism for wavelength tuning. In Table 4.1 are shown the thermo-optic coefficients for *Si* and *SiO₂*.

Material	$\Delta n/\Delta T$ [K^{-1}]	α_{exp}
Si	$1.86 \cdot 10^{-4}$	$4.68 \cdot 10^{-6}$
SiO ₂	10^{-5}	$\approx 8.5 \cdot 10^{-6}$

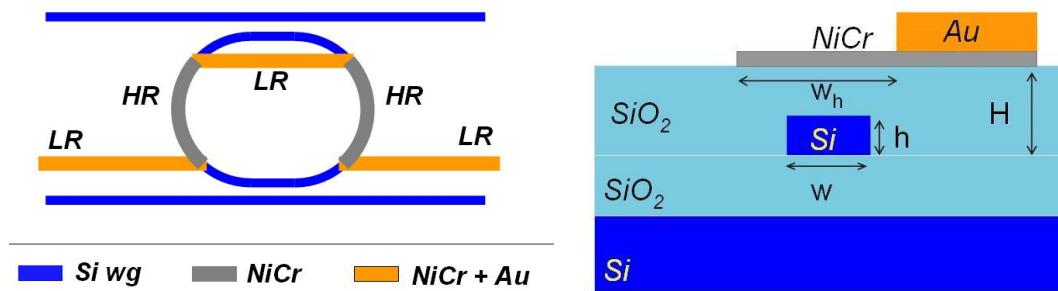
TABLE 4.1: Thermo-optic coefficients for Silicon and Silica, a difference of one order of magnitude is present between the two coefficients.

A Finite Element Method (FEM) based software, from Comsol, has been used for the analysis of the propagation of the heat and the temperature profile inside the structure, once the boundary and initial conditions were defined from considerations relating to the particular geometry. Simulations were performed for both the design and the analysis of measured results obtained on the fabricated devices.

4.3 Heater Configuration

In order to realize localized heating, it is convenient to use two different metals with different resistivities and adjust the thickness and the width of those materials in order to obtain different electrical resistances. The micro-heaters developed in this work consist of a metallic bi-layer of nichrome (*NiCr*) and titanium - gold (*Ti - Au*), having an electrical resistivity of $1.5 \cdot 10^{-6} \Omega m$ and $0.02 \cdot 10^{-6} \Omega m$ [129], respectively. These materials were the best candidates in terms of electrical resistivity difference. The high resistivity metal (*NiCr*) was patterned so as to cover only the tops of the waveguides and the regions where localized heat was required, thereby maximizing the power dissipation. In all the other regions, there was very little generation of heat due to the small value of resistance. A schematic of the photonic structure with the thermal heaters is shown in Figure 4.2.

The design of the heat flow geometry was focused on two separate parts. The first consisted in the determination of the optimum thickness of the cladding layer separating the heater film and the silicon core. This figure is a compromise between the maximum temperature transferred to the core and the absorption losses due to the interaction of the optical beam with the metal. The second step of the design consisted in the determination of the micro-heater geometrical dimensions (length, width and thickness); this part of the design was related to the analysis of the power consumption, the melting current density and the temperature distribution



(a) Schematic top view of the metals and guiding layer. *LR* and *HR* represent the low and high resistance regions, respectively.

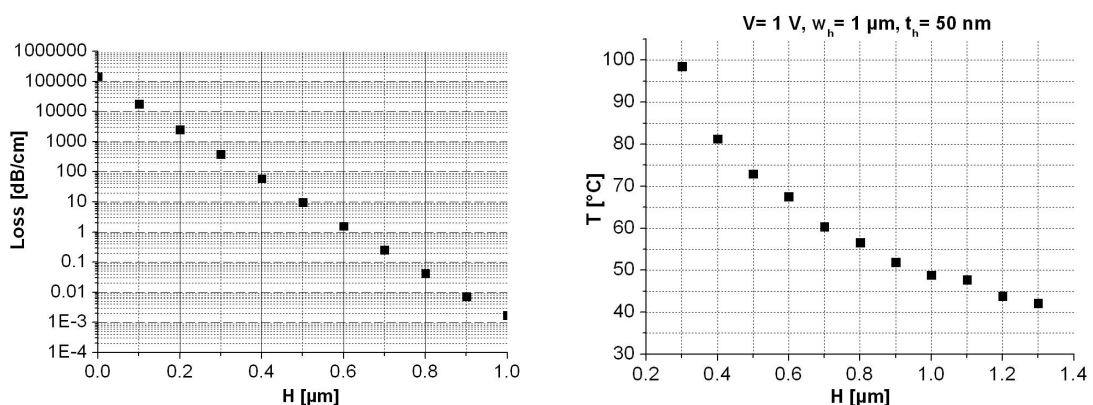
(b) Schematic Cross Section of the device.

FIGURE 4.2: Schematic Top view a) and cross section b) of the heaters. The Heating elements are realized after the fabrication of the photonic wires and the passivation of the structure.

inside the structure. Moreover, a change in the refractive index has the effect of changing the coupling factor between different rings and the bus waveguides. To avoid spurious tuning of the coupling factor, the metal wires were kept far enough from the coupling region.

4.3.1 Buffer Layer Design

In order to reduce the absorption losses due to the interaction of the optical beam with the electrodes, it is necessary to design a buffer layer of a proper thickness. This should ideally be as small as possible to maximize dn/dT but thick enough to ensure negligible losses.



(a) Losses for a different values of thickness of the buffer layer (H); a value of losses equal to 0.001 dB/cm is achievable with a buffer layer thickness of 900 nm .

(b) Temperature profile for different values of thickness of the buffer layer (H) when 1 V is applied to a metal wire $1 \mu\text{m}$ wide and 50 nm thick.

FIGURE 4.3: Losses for different values of the buffer layer thickness (a) and temperature values at the core of the waveguide (b).

Figure 4.3(a) shows results for simulation (in Rsoft Beam Propagation) of the absorption losses induced by the presence of the metal structure, for different values of thickness. An additional contribution of only 0.001 dB/cm is obtained with a buffer layer thickness of 900 nm . Figure 4.3(b) shows the temperature dependence, calculated using a Finite Element Method (in Comsol), at the silicon waveguide core for several values of the buffer layer thickness – when a Voltage of 1 V is applied to a *NiCr* metal wire that is 50 nm thick and $1 \mu\text{m}$ wide. The particular configuration of the heater analyzed, and the voltage applied, produce a temperature of 112°C on the metal surface – this figure has been extracted from simulation of the particular geometry with a Finite Element Method. The corresponding temperature at the waveguide core section is proportionally reduced due to an increase of the thermal resistance associated with a thicker buffer layer.

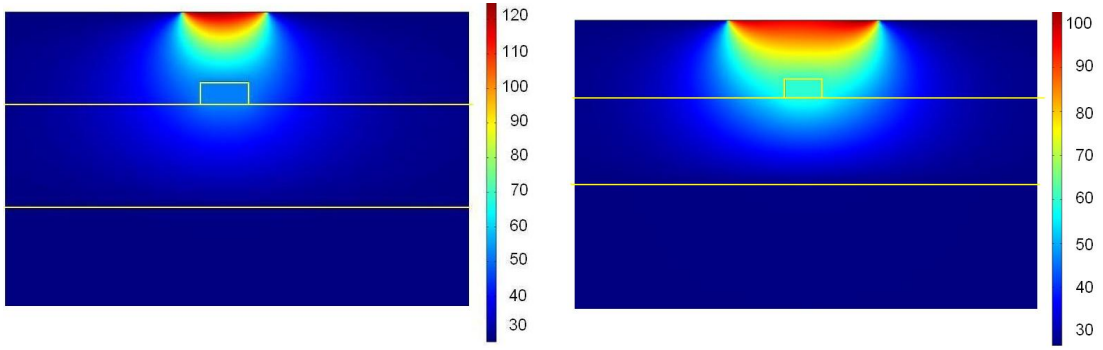
4.3.2 Heating element geometry

The length of the heater (L_h) is constrained by the structure dimensions i.e. by the length of the ring structure. To avoid spurious tuning of the coupler, the heater length was chosen to be equal to πR – half of the perimeter of the ring. To increase this length, and so the resistance, it is possible to use more complex heater configurations such as serpentine or inter-digited structures, as described in [115, 119, 126].

The electrical power dissipated at the heater can be expressed as

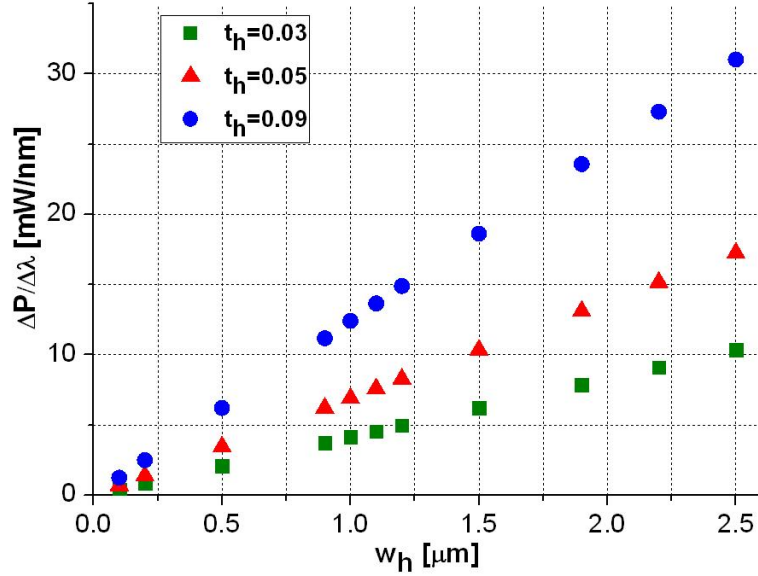
$$P = \frac{V^2}{R_h} = V w_h t_h \frac{V}{\rho_{NiCr} L_h} \quad (4.3)$$

Figure 4.4 shows the temperature profiles for two different widths of the heater: $w_t = 500 \text{ nm}$ (a) and $2 \mu\text{m}$ (b) simulated with a FEM (Finite Element Method) from Comsol Multiphysics and the dependence of the tuning efficiency on w_h and t_h (c). For the same applied voltage, a wider heater generates a higher temperature at the core of the waveguide, thus maximizing the thermo-optic effect; however, the increase in the dimensions also implies an increase in the total power, due to a decrease in the total Resistance (R_h). In order to obtain good efficiency of tuning, the value of $\Delta\lambda/\Delta P$ must be maximized – a small amount of power, for a high resonance wavelength shift. Maximizing the wavelength shift per unit of power is equivalent to minimize the quantity $\Delta P/\Delta\lambda$, which is analytically expressed as



(a) Temperature profile for the cross section of the device for a $w_t = 500 \text{ nm}$ wide and 50 nm thick heater when a voltage of 1 V is applied.

(b) Temperature profile for the cross section of the device for a $w_t = 2 \mu\text{m}$ wide and 50 nm thick heater when a voltage of 1 V is applied.



(c) Tuning efficiency expressed as ratio of $\Delta P/\Delta\lambda$ for waveguide width (w_h), ranging from $0.1 \mu\text{m}$ to $2.5 \mu\text{m}$, and different heaters thickness t_h . Narrow and thin heater allow to realize an efficient tuning i.e. the power required per nanometer shift is small.

FIGURE 4.4: Temperature profile for two different width dimensions of the heater w_t ((a) 500 nm and (b) $2 \mu\text{m}$) and corresponding tuning efficiency dependence on the w_h and t_h .

$$\frac{\Delta P}{\Delta\lambda} = \frac{\Delta V^2}{R_h \Delta\lambda} = \frac{w_h t_h}{\rho_{NiCr} L_h} \frac{\Delta V^2}{\Delta\lambda} \quad (4.4)$$

from equation 4.4 this is obtained when the product $w_h t_h$ is reduced. The value of $w_h t_h$ can not be reduced arbitrarily, since there is a lower limit related to the maximum current density in the metal wire before melting. The current density is

$$J = \frac{I}{w_h t_h} = \frac{V}{\rho_{NiCr} L_h} \quad (4.5)$$

The melting current density (J_m) has been measured with some destructive tests on heaters with different geometries – and a value equal to $J_m = 0.161 \text{ A}/\mu\text{m}^2$ has been found. The associated lower limit for the product $w_h t_h$ is $25 \cdot 10^{-3} \mu\text{m}^2$.

In the design process it is crucial to take into account this figure and the limitation of the fabrication process. Several simulations have been carried out to analyze the profile of the temperature at the waveguide core for different values of heater width and thickness, when a Voltage of 1 V is applied. The results are summarized in Figure 4.5.

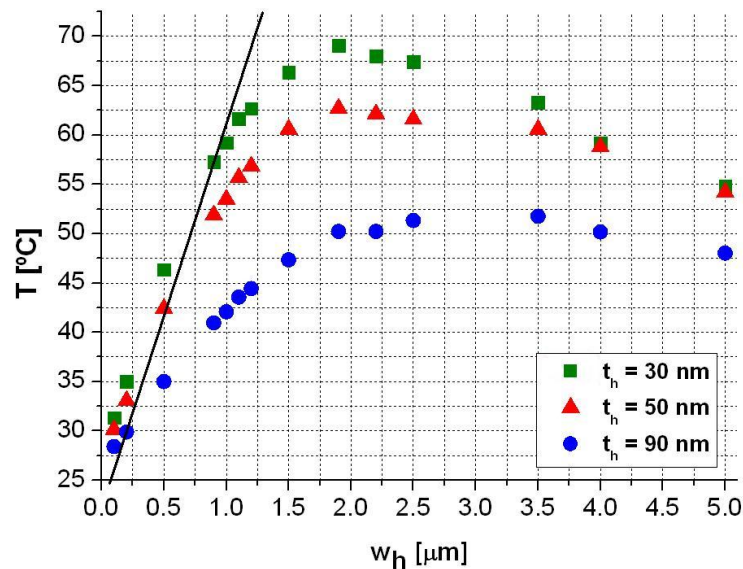


FIGURE 4.5: Temperature dependence for different values of heater thickness (a), and heater width (b). In blue the corresponding values imposed, by technological issues, on the thickness and the relative limits on the waveguide width to prevent melting of the device.

The simulations were performed by varying the heater width for three different values of the heater thickness ($t_h = 30, 50, 90 \text{ nm}$). For small values of w_h , the temperature changes marginally with the thickness – due to the small power level delivered at the silicon core. As the value of the width increases, a higher value of temperature is registered in the core. In this regime, the temperature is inversely proportional to the heater thickness.

There is a value of the width beyond which the temperature transfer into the core slowly decreases, because for a wide heater, the heat flow is no longer as the one generated from a point source but becomes diffusive. The heat transfer in this regime will be great on the side of the silicon waveguide core, where there is a smaller value of the thermal resistance associated with an increased surface area.

The black line corresponds to the value of the product $w_h t_h$. The values of thickness/width to the left of this line represent configurations where melting of the device occurs.

A heater structure wider than $1 \mu\text{m}$ could be used with a thickness of 30 nm . However this solution is technologically challenging due to the uniformity reasons of the deposited metal film. Working with thicknesses of 50 nm requires values of the width bigger than 500 nm . To obtain a higher temperature at the core, wider structures could be used, at the cost of efficiency.

A value of $1.8 \mu\text{m}$ could be chosen for the width of the heater. However in this situation, even with a bigger transfer of temperature to the core of the waveguide, there would be a decrease by a factor of 2, in the efficiency ratio $(\Delta\lambda/\Delta P)$, when compared to the configuration chosen.

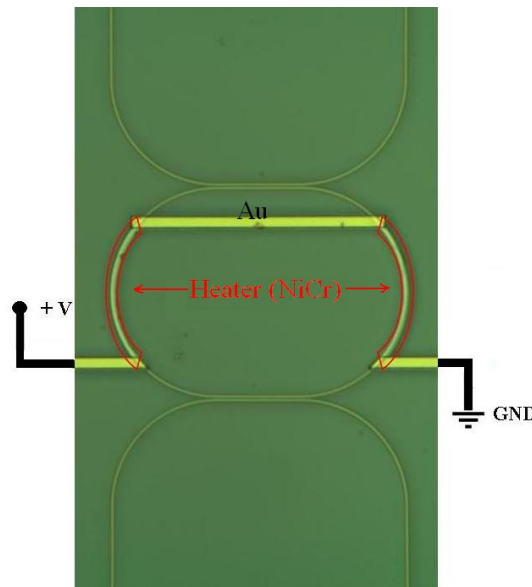


FIGURE 4.6: Optical Microscope Image of the micro heater. In red colour are indicated the high resistivity areas where the heat is generated by the Joule heating effect.

Figure 4.6 shows an optical microscope photograph of a fabricated heating structure on a ring resonator. From this picture is possible to identify the high resistivity area (NiCr), marked in red, and the gold metal wires (yellow).

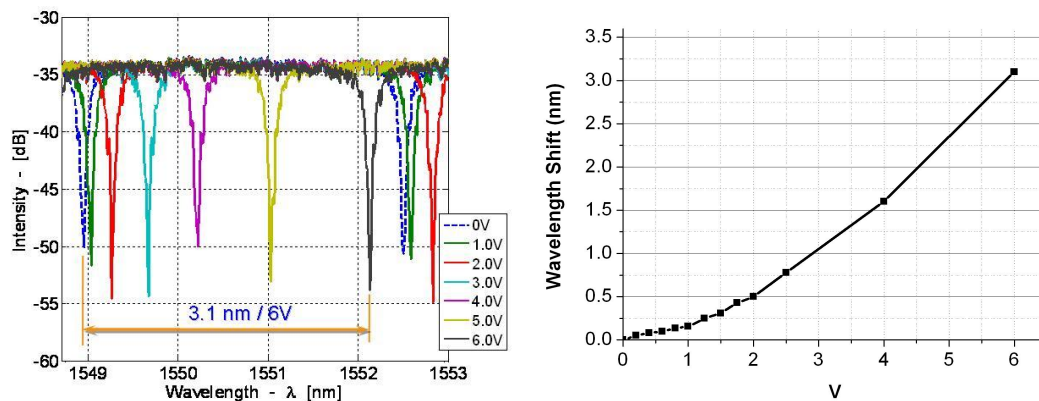
The final configuration for the metal heaters is a 900 nm wide, 50 nm thick and $62 \mu\text{m}$ long electrode for a ring resonator with a radius of $R = 20 \mu\text{m}$ and a total length of $L_r = 172 \mu\text{m}$ ($FSR = 3.1 \text{ nm}$). For the defined structure, the estimated power consumption per nanometer of tuning is 6.45 mW/nm

The fabricated devices show a mean value of resistance $R_h = 1.8 K\Omega$, in good agreement with the designed values; the resistance difference between devices is limited to only 5 %. The resistance of the 1-mm-long *NiCr/Au* contact strip is around 5Ω and the Pad Resistance (*Ti-Au*) is 1Ω , i.e. negligible when compared to the heating element.

4.4 Single Ring Tuning

The wavelength shift of the resonance for a single ring was measured for different values of applied voltage – and the results are shown in Figure 4.7(a). The notch in the transmitted intensity at the through port exhibits a progressive red shift when the voltage is increased, up to $\Delta\lambda = 3.1 \text{ nm}$ when 6 V are applied (a full *FSR*). The wavelength shift has a quadratic behaviour, in good agreement with equation 4.4.

The power consumption for typical resistances used ($R_h = 1.8 \text{ k}\Omega$) was found to be 6.45 mW/nm (equivalent to $52 \mu\text{W/GHz}$); a shift of an entire *FSR* (3.6 nm) would require 23.4 mW . These values are comparable with, if not better than the best thermo-optical controllers reported in the literature [118, 122, 126, 127].



(a) Resonance peak tuning for different values of applied voltage, 6 V for the tuning of an entire *FSR* (3.1 nm). (b) Wavelength Shift versus Voltage applied on the electrode.

FIGURE 4.7: Tuning of the resonance peak for different values of the voltage applied and correspondent Wavelength - Voltage characteristic.

In the design of a single ring or more complex coupled-ring geometries, it is important to evaluate the response speed of the devices and their thermal cross-talk (i.e. how a heated device influences the behavior of other devices). In the next two

subsections, the main results, obtained in collaboration of Politecnico di Milano, about the thermal cross talk and the tuning speed are analyzed.

4.4.1 Thermal Cross Talk

The thermal cross talk between adjacent rings has been evaluated on a device composed of two coupled ring resonators that are independently tuned.

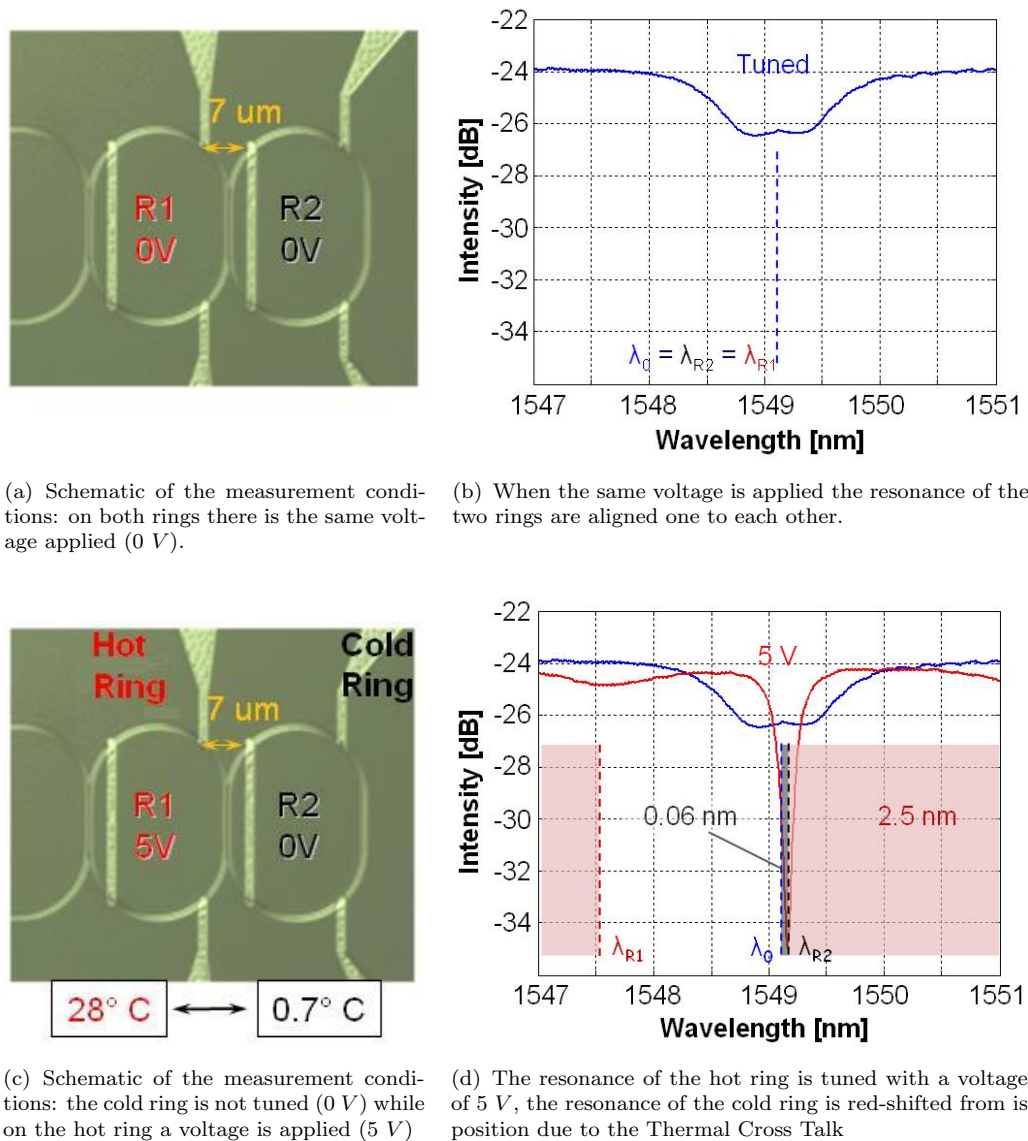


FIGURE 4.8: Schematic of the measurements and results for the evaluation of the Thermal Cross Talk of adjacent rings with metal conductor spaced $7 \mu\text{m}$.

In a static situation when there is no current flowing in the electrodes, the two rings have the same resonant wavelength ($\lambda_0 = \lambda_{R_1} = \lambda_{R_2}$). If one electrode is

biased, the resonant wavelength of the corresponding ring starts to red-shift. The wavelength shift of the untuned ring gives information on the thermal cross talk. Figure 4.8 shows the results for two rings, one of which is tuned with a voltage that progressively increases up to 5 V (labeled the *Hot Ring*). For this value of voltage the tuned ring exhibits a shift of 2.5 nm. Analyzing the transmission spectra it is possible to evaluate the resonant wavelength shift of the untuned ring (labeled the *cold ring*)– and a value equal to 0.07 nm is obtained. From these values, it can be found that the temperature variation of the waveguide ring R_1 , due to the applied voltage, is about $\Delta T = 27.76\text{ }^\circ\text{C}$, while the temperature variation of the waveguide ring R_2 , due to thermal cross talk, is only $\Delta T = 0.728\text{ }^\circ\text{C}$, and it is therefore negligible.

4.4.2 Tuning Speed

To measure the time response of the devices, a square-wave signal voltage was applied to the metal heater of a single ring as shown in Figure 4.9.

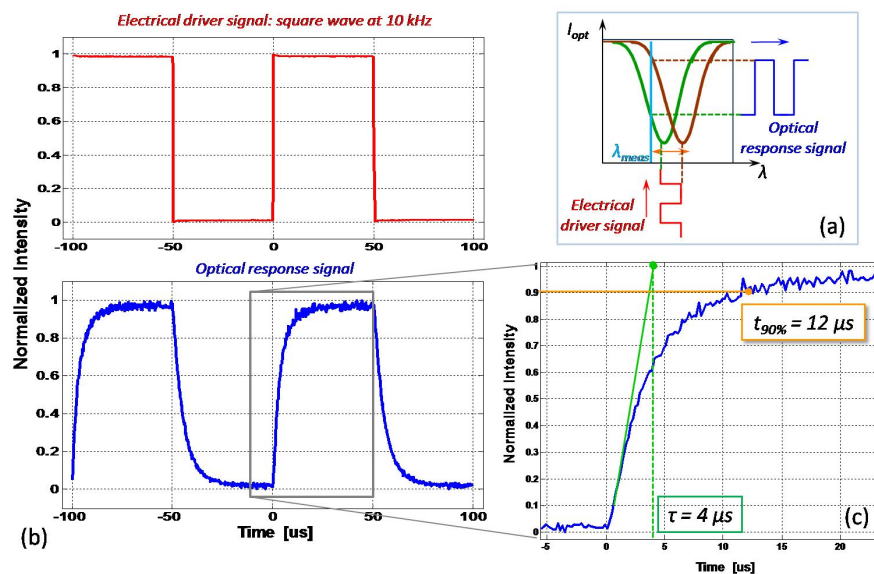


FIGURE 4.9: a) Sketch of the measurement; b) Time traces of a driving electrical square wave at 10 KHz (red line) and the corresponding optical power (blue line) at the output port of an all pass filter; c) Detail of the optical power transient.

Ideally the optical intensity acquired at the output of the device should have a square characteristic, with a period equal to the driving signal – but, due to the finite time response of the heating element there is a transient period in the rising and falling regions. Measurement of this transient gives information on the time

response. In our experiments the electrical signal applied had a frequency of 10 *KHz*. By measuring the derivative of the optical output envelope (τ) we obtain a value of $\tau=4 \mu s$ and the time for the optical output to get to 90 % (3τ) is equal to 12 μs . These values are amongst the best ever reported [118, 122, 126, 127].

4.5 Conclusions

The thermo-optic effect represents an efficient and low power tuning approach for the devices under consideration and the particular waveguide geometry chosen. The heat Transfer equation, in appendix C, and the FEM method have been used to model the electrode structure in terms of heater distance from the waveguide and geometry. All the aforementioned parameters were chosen to guarantee negligible absorption of the optical beam due to the presence of the metal and high power versus wavelength efficiency ($52 \mu W/GHz$) – avoiding the critical melting condition for the device. Figures of Merit such as thermal-cross-talk and tuning-speed were evaluated showing negligible cross-talk and high tuning-speed (12 μs). This time response is suitable for the tuning of optical devices, for an adaptive compensation of slow drifts (thermal, for example), for the occasional reconfiguration of delay lines with a fixed delay, or for off-line processing of the optical signal. However a device for communication systems would require a switching time comparable with (if not lower than) the pulse width of the optical signal. For adaptive reconfiguration and real-time processing of signal with bit-rate from 10 *Gbit/s* to 100 *Gbit/s*, a time response at least between 10 *ps* and 100 *ps* is required. Thermal effects are too slow to provide this speed – which could be obtained instead with p-i-n junctions [130]. In this case, however, as already stated, the configuration of the waveguide and all the basic building blocks should be redesigned, ex novo. Thermo-optical heaters represent, however, a unique way to demonstrate the principles of operation of delay-lines, as will be discussed in Chapter 6, which represent the fastest reconfigurable delay lines presented so far in the literature.

Chapter 5

Variability, Uniformity and Consistency in the Fabrication of Ring Resonator cavities

In this chapter, process variability, uniformity and consistency are discussed. A precise evaluation of these parameters is essential for the creation of structures with a designed working behaviour. The fabricated devices may contain photonic structures with an arbitrary complexity, in addition to waveguides. In all cases the dimensional repeatability of the structures is critical to obtaining device consistency.

In principle, it is possible to observe the differences in several realizations of the same device [131] to obtain a statistical behavior of all the possible values. If the fabrication parameters are fixed (standardized fabrication process), it is important to evaluate the maximum intra-chip and chip-to-chip device performance variability.

Ideally, nominally identical structures should have the same transmission characteristics but, due to the large index contrast of silicon, even a sub-nanometer variation of the waveguide dimension is translated into an unacceptably large variation in the resonant wavelength [132]. This effect poses a serious challenge when fabricating coupled ring resonators – where the resonances require very accurate control. The variation in the resonance peak position is a consequence of the variation in the effective index of the waveguide caused by different waveguide widths in the fabricated devices.

Despite all the positive features of HSQ, several papers have shown that HSQ suffers from significant delay effects. In particular, the dose changes with the age of the dilution, even when kept in a fridge [70, 131]. A change in the dose implies a change in the dimension of the patterned structure – and thereby a change in the effective index of propagation and a consequent variation in the resonance position.

The extremely high sensitivity of the resonance can be used to evaluate the process variability.

Several established methods for linewidth metrology are given in the literature [133–136]– and these can be subdivided into two main groups: those that measure a single point on a line – and those that inherently give an average over a given region. The first group comprises microscopy methods, such as scanning electron microscopes (SEM) [133, 135] and atomic force microscopes (AFM) [134, 135], with a typical precision of around 1 *nm*. The second group includes electrical linewidth measurements (ELM) and scatterometry [136]. Scatterometry averages the linewidth over a measured region and can have excellent repeatability: 3σ values of 0.15 *nm* have been reported for 35 *nm* lithography [136]. Drawbacks include the need for large areas of measurement, the need for a calibration sample and an accurate model. The resonance method is similar to the electrical linewidth measurement technique in as much as it measures the average width of a single test structure. Together the use of on-wafer probing, it provides an excellent method for measuring process variability – and allows an understanding of the limitations in realizations of long chains of rings.

5.1 HSQ Process Variability

To analyze the process variability, single ring resonator structures were fabricated using electron beam lithography with HSQ as the resist. Each chip under test contained several ring resonators with a radius of $R = 20 \mu\text{m}$ and a coupling region L_c with a length varying between 0 and 15 μm . The gap between the bus waveguide and the coupling region was kept constant at 260 *nm* to eliminate the uncertainty in the fitting of couplers with different gaps (section 3.5).

All the devices were written on small, $1 \times 1 \text{ cm}^2$, sized, samples cleaved from the same small area of a 200 *mm* wafer, so as to minimize the effect of any silicon core

thickness variation that might occur across the wafer. Intra-chip consistency was measured on multiple resonators with the same characteristics, spaced by about 1.5 mm. The HSQ was diluted at 50 % in MIBK and spun at a speed of 3000 rpm – to give a thickness of 240 nm. The fabrication and characterization methods were the same as those previously discussed in Chapter 2 and section 3.1, respectively. The stability of HSQ processing was monitored over a period of 70 days using two different methods for preparing the HSQ films [131]:

- Fresh Dilution: with methyl isobutyl ketone (MIBK) made up each time prior to the spinning.
- Single Dilution: with MIBK made up on the first day of the experiment – and then kept in a refrigerator over the whole period of testing.

Wafer-to-wafer consistency and long term delay effects were measured by fabricating samples over a period of 70 days for the fresh dilutions of HSQ – and over 104 days for the single dilution.

The position of the resonance peaks of the ring resonators are placed at $\lambda_r = n_{eff}L_r/m$, where n_{eff} is the effective index of the mode, L_r is the ring length and m an integer that represents the mode order number. For waveguides with $w = 500$ nm and $t = 220$ nm, the modelling software (Rsoft) showed that $n_{eff} = 2.503$ at a wavelength of 1.523 μ m. In addition, the variation of the effective index of the guided mode with the waveguide width (w), thickness (t) and wavelength (λ) has been evaluated – resulting in $\partial n_{eff}/\partial w = 0.001357$ nm⁻¹, $\partial n_{eff}/\partial t = 0.003598$ nm⁻¹ and $\partial n_{eff}/\partial \lambda = -0.0010054$ nm⁻¹ (at a fixed width and thickness).

After some algebraical manipulation it can be shown that the width varies with the resonant wavelength and thickness according to

$$\Delta w = 1.12\Delta\lambda - 2.65\Delta t \tag{5.1}$$

where $\Delta\lambda$, Δw and Δt are the changes in λ , w and t , respectively. Equation 5.1 shows that if the waveguide width is varied, the wavelength and thickness for the waveguide must be changed to obtain the same value of n_{eff} .

5.1.1 Pattern Variation results for Phase Shifter Ring Resonator Structures

Wafer to wafer consistency and long term delay effects were measured by fabricating wafers on days 1, 3, 4, 10, 17, 70 for the fresh dilutions of HSQ and days 1, 3, 10, 17, 70 and 104 for the single dilution of HSQ. The repeatability of the measurements was determined by measuring a resonance peak for a single device, multiple times. Between each measurement the substrate was removed from the optical test rig and the laser turned off. The measurements on the same device gave resonant wavelengths (in nm) with a standard deviation of 0.0025 nm .

We calculated the waveguide widths by taking an initial estimate for the refractive index of $n_{eff} = 2.5037$ from the designed size of the waveguide. Hence, from the resonance condition relation we found the value of m ; rounding m to an integer gave us an exact value for n_{eff} , which then enabled us to extract the actual value of $\partial n/\partial w$.

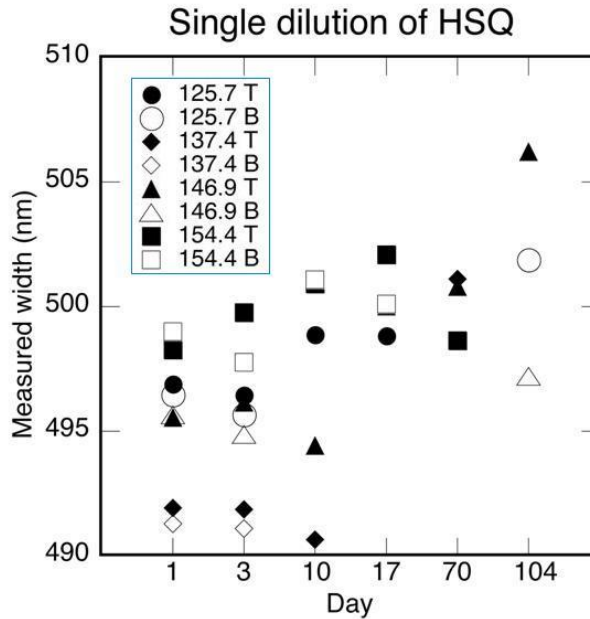


FIGURE 5.1: Calculated variation of waveguide width for several realization of fabricated devices using a Single dilution of HSQ. The inset shows the length of the ring resonator, B (bottom) and T (top) represent the position of the structure on the sample with size $1 \times 1\text{ cm}^2$.

Figure 5.1 shows the calculated variations of waveguide width for the samples fabricated using a single dilution of HSQ. The following consideration can be made by analyzing the graphs:

- The variations over the waveguide width increase to about 20 nm after a ten days period.
- A single dilution rapidly ages, and after 3 days, a noticeable decrease in reproducibility is observed.
- The device yield with the single HSQ solution also decreases significantly over time – and we observed that the as-spun films became increasingly speckled. Eventually, the single solution solidifies in the bottle after a period of 120 days. It is evident that a dilution of HSQ with MIBK has a limited lifetime, possibly caused by impurities in the MIBK.

Figure 5.2 shows the calculated variation of waveguide widths for the samples fabricated using a fresh dilution of HSQ.

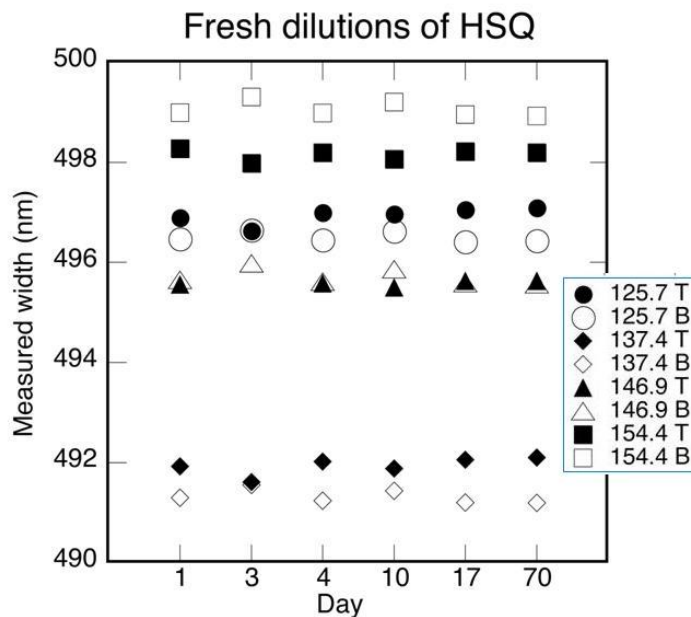


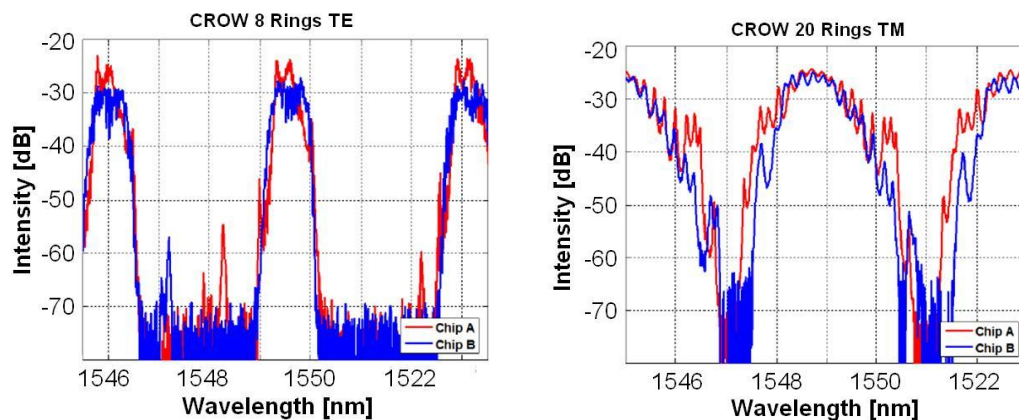
FIGURE 5.2: Calculated variation of waveguide width for several realization of fabricated devices using a Fresh dilution of HSQ. The inset shows the length of the ring resonator, B (bottom) and T (top) represent the position of the structure on the sample.

- First, there is a remarkable consistency in the waveguide width over time. There is a clear distinction between the sizes of nominally identical structures in the top and bottom groups, which is probably caused by variations in the position of the structures on the writing field of the e-beam tool. The standard deviation for variation, of the width, taking each of the eight devices separately, is 0.14 nm.

- Secondly, there is a significant change in width between the different ring lengths. This can be ascribed to the parallel section between the resonator and the bus waveguide which affects the e-beam dose and the proximity effects.
- Thirdly, the silicon across the wafer is extremely uniform. Equation 5.1 predicts that the thickness variation should be nearly three times greater.
- Finally, note that there is a strong correlation in the results from day-to-day. A slight variation in processing conditions would be expected to affect all waveguides similarly. This is indeed found for the two groups, B and T , separately. However there is an anomaly in as much as the B and T groups are strongly anti-correlated, so that as one group widens the other narrows. No explanation has yet been found for this.

5.1.2 Pattern Variation results for Coupled Ring Resonator Structures

After the assessment on a single ring resonator, coupled structures were analyzed. Design and performance of these structures are described in detail in Chapter 6; in this section measured characteristics are reported in order to illustrate the effects of process variability on the spectrum.



(a) Intensity response for 8 Coupled ring resonators in CROW configuration for TE polarization

(b) Intensity response for 20 Coupled ring resonators in CROW configuration for TM polarization

FIGURE 5.3: Intensity spectral response at drop port of Coupled Ring Resonators realized in two different fabrication runs (Chip A and Chip B) (measurements performed in Milano.)

Figure 5.3(a) shows the intensity transfer function at the drop port for two CROWs with 8 coupled rings for TE polarization, while Figure 5.3(b) shows the same measurement for two CROWs with 20 rings for TM polarization. In both cases, the transfer functions obtained on the two different fabrication runs are very similar, suggesting high repeatability of the process, and indeed, very accurate control on the alignment of the resonance frequencies of the ring resonators (8 and 20 rings can be considered a significant number).

While the observation of a CROW transfer function is useful as a qualitative evaluation of the resonance frequency dispersion, a more accurate quantitative estimation is not feasible – because, in these devices, all the resonances are coupled together. The bandwidth enlargement is a combined effect of the variation in the wavelength resonant positions of the individual resonators and the interaction of the resonator with each other.

All Pass Filters (APF) are, on the contrary, more suitable for this analysis. In fact, for identical devices, all the resonances should be perfectly aligned and the total bandwidth of the whole chain should be equal to that of a single ring. As a result of the dispersion in the resonance frequencies, a broadening of the bandwidth of the chain arises. A set of APF chains up to 64 rings was fabricated (Figure 5.4(a)) and characterized (Figure 5.4(b)).

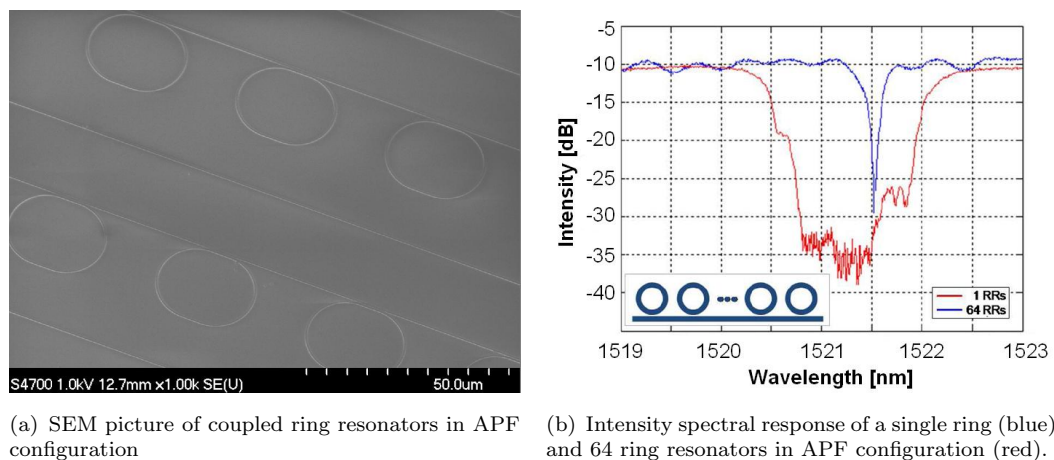


FIGURE 5.4: Measurement of the band broadening of a chain of 64 ring resonators in APF configuration.

From Figure 5.4(b) a clear broadening of the bandwidth can be seen – from 0.1 nm (single ring) to about 1.2 nm, calculated as the width of the notch at -10

dB from the maximum transmission. We can therefore estimate a maximum resonance shift of $max(\Delta\lambda_r) = \pm 0.6$ – and a relative error on the resonant wavelength of $\Delta\lambda_r/\lambda_r = 0.04$ %. Translating this into the maximum variation of the waveguide width over the entire chain, a value of $max(\Delta_w) = \pm 0.56$ nm is found – and, a variation of $max(\Delta n_{eff}) = \pm 9 \cdot 10^{-4}$ (calculated, considering that $\Delta\lambda/\lambda = \Delta n_{eff}/n_{eff}$). These results indicate the very low degree of disorder, thanks to the sub-nanometric accuracy of the technological processes and are comparable with the best reported results, e.g. those by workers at IBM [31].

5.2 Conclusions

Fresh dilution of HSQ proved to be a reliable fabrication procedure to realize device structures with good chip-to-chip consistency. The variation is as low as 0.14 nm on the total waveguide width for single ring resonators. Chains of up to 64 rings, arranged in an APF structure, showed an average variation of the waveguide width over the entire chain as low as 0.5 nm. This sub-nanometer variation is an important result in view of realizing silicon-on-insulator devices in good agreement with the designed ones.

Chapter 6

Silicon On Insulator Coupled Microring Resonator Optical Waveguides

6.1 Introduction

This chapter reports several measurements performed by our project partners in Milano on the slow-light devices developed during this thesis.

This chapter starts with some considerations in order to identify the best configuration for the realization of a delay-line. For the chosen configuration, the main figures of merit are firstly introduced. The fabrication process developments together with the the process variability and the resonance dispersion control, presented in Chapter 5, make of silicon photonic a solid technological platform. In addition, the analysis of the basic building blocks, their impairments and criticality, considered in Chapter 3, allowed the development of a robust design for the slow-light structures under consideration. These considerations are confirmed from the excellent device performances and the perfect agreement with the design specifications. Moreover, the availability of a reconfigurable behavior, obtained by means of refractive index variation by thermo-optical effect (discussed in Chapter 4) allows the possibility to access to different delay in an efficient and easy way – and dispersion compensation for devices with small bandwidths.

6.2 Slow Light Structures

There are two main configurations for cascading ring racetrack optical resonators, in order to realize a slow light structure, as shown in Figure 6.1: the all pass filters (APF) [137] and coupled ring optical waveguides (CROW) [31, 138].

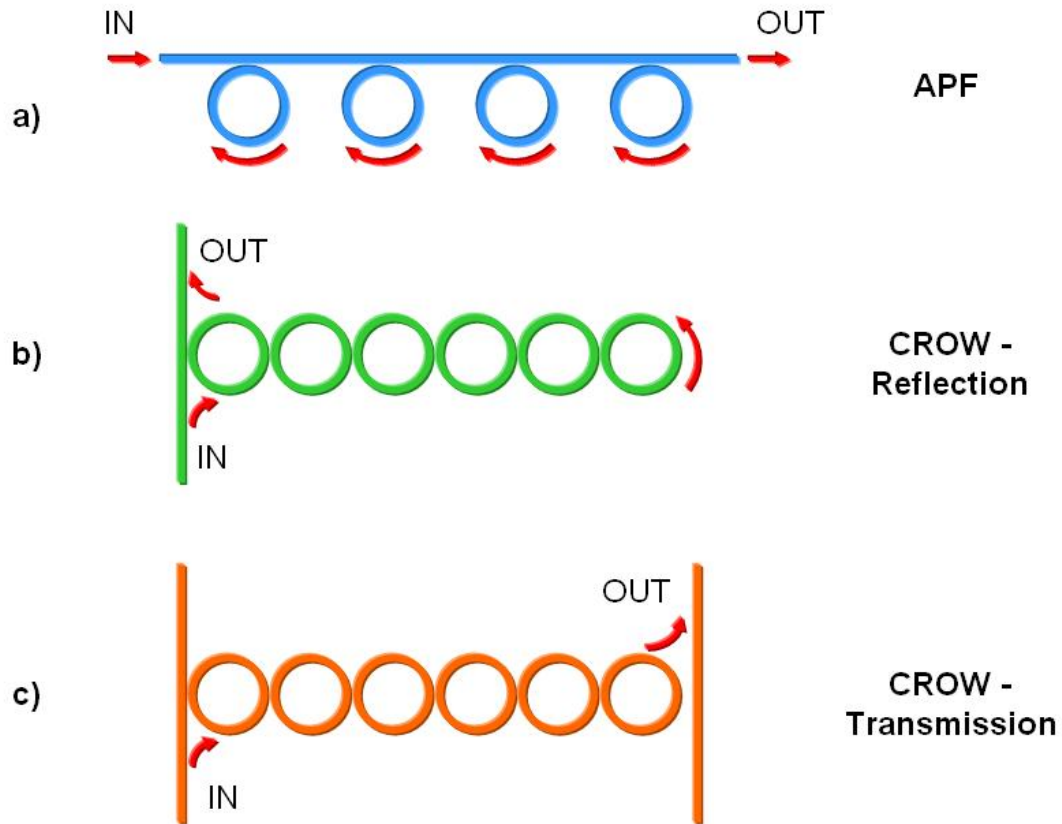


FIGURE 6.1: Ring-resonator-based slow light architectures realized in (a) all pass filters (APF), (b) coupled resonator optical waveguides (CROW) in Reflection configuration and (c) coupled resonator optical waveguides (CROW) in Transmission configuration.

- In the APF scheme, each ring is individually side-coupled to a common waveguide.

- The spectral bandwidth is defined, in the ideal case, by the quality factor of the individual resonators. In real devices, due to tolerances and errors in the fabrication process, the resulting bandwidth is broader – and the transfer function is obtained as the overlap of transfer functions of rings that resonate at different wavelengths (see Chapter 5).

- The total group delay results from a summation of the delays of all individual resonators, because there is, practically, no interaction between them [31]. Fine control of the resonance wavelengths and engineered bandwidth are achievable by slightly changing the coupling factor for each individual ring. However this approach provides poor flexibility in the design (in particular, in the width and the flatness of the band).
 - The independent behavior of each ring implies inefficient reconfigurability: to obtain a determined delay, it is necessary to tune a number of cavities proportional to the delay variation – with a resulting increase in the power consumption.
- In the CROW scheme the ring resonators are side-coupled one to another. For certain applications, the drop waveguide is removed – in which case the light traveling inside the structure is reflected at the last interface and forced to travel back again. The port where the output signal is acquired allows the categorization into Reflection and Transmission configurations, as shown in Figure 6.1(b) and Figure 6.1(c), respectively. Although, theoretically, the two configurations may be regarded as having a measure of equivalence, each one is characterized by distinct figures of merit.
- The spectral bandwidth, for both the configurations in transmission and reflection, depends on the coupling coefficient profile between the resonators. This dependence confers on the CROW based configuration a larger bandwidth in comparison with the APF.
 - The total group delay is proportional to the number of cavities. Considering two CROWs having the same number of ring resonators in the two different architectures, the total delay introduced in the Reflection configuration is double when compared to the Transmission configuration – due to a double transit into the structure.
 - The reconfiguration scheme is easily implemented and efficient for the case of the Reflection configuration: only a limited number of rings need to be activated, to achieve a designed delay. The transmission configuration would need a reconfigurable variation of the coupling coefficient between different resonators and moreover it is less robust: the change of the coupling coefficients has the effect of a bandwidth variation difficult to control.

The choice of CROW structures is motivated by their ability to provide slow-light effects and to allow, at the same time, a large and flat passband [139]. Moreover the configuration in Reflection provides a simple, flexible and efficient reconfigurability [140], that minimize the number of activated rings required for a desired delay, with a relatively easy control scheme and a lower power consumption than the previous state-of-art slow-light delay-lines [141]. More details about the reconfiguration scheme for the Reflection topology are reported in appendix D.1

6.3 Coupled Optical Resonator Waveguides

In this section, the main figures of merit for CROW structures are presented.

The dispersion equation for the propagation constant β of the Bloch wave [6] is

$$\cos(\beta d) = \frac{1}{t} \sin(\kappa L_{cav}) \quad (6.1)$$

where t is the field transmission coupling coefficient between the resonators, κ is the wave vector inside each resonator and L_{cav} is the length of the resonator cavity. From this eigenvalue equation, all the linear properties of Slow Wave Structure and their most relevant spectral characteristics may be analytically derived. Equation 6.1 states that the slow light structure consists of a periodic series of pass bands and stop bands [142, 143] centered around the resonance frequencies of the slow light structure. Similar to a single cavity $f_0 = Q \cdot FSR$, with Q integer.

The bandwidth, B , of the periodic slow light structure [6] is expressed as:

$$B = \frac{2FSR}{\pi} \sin^{-1}(t) \quad (6.2)$$

and FSR is the free spectra range, $FSR = c/n_g L_{cav}$. Equation 6.2 is a good approximation for a slow-light structure with a sufficiently high number of cells. Figure 6.2 shows the spectral response of a CROW slow-light structure for an increasing number of cells.

In the example shown, with Finesse $F = FSR/B = 5$ and $t = 0.31$, the approximation is already valid for chains of more than ten resonators.

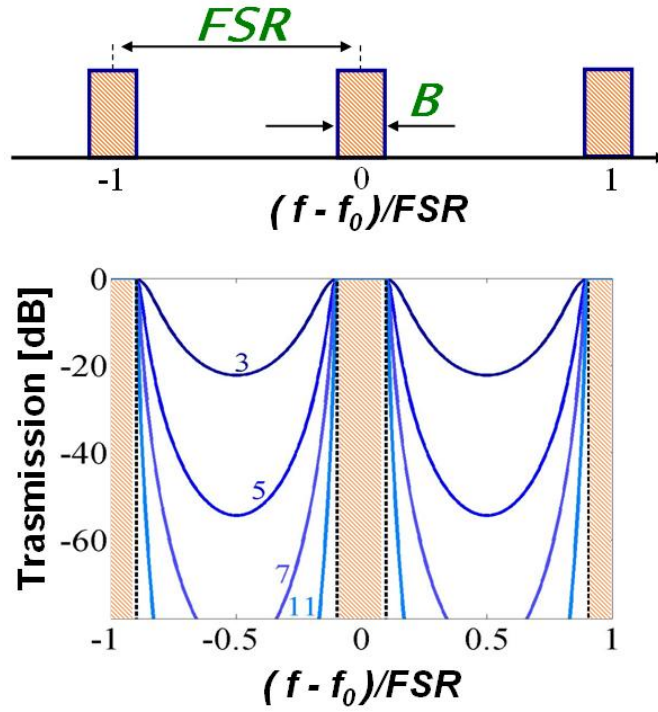


FIGURE 6.2: Spectral response for an increasing number N of resonators. Dotted lines show the theoretical response of the infinitely long Slow Light structure (courtesy of Prof. A. Melloni, Politecnico di Milano).

The finite size of the structure and the coupling to the bus waveguides result in an impedance mismatch which causes ripples in the pass-band due to reflections of the incident wave at the interface. The undesired behavior can be removed by realizing an impedance matching condition [6, 139, 144] using of a suitable apodization of the reflectivity profile along the periodical structure as described in Appendix D.2.3.

The total field propagating through a periodic structure consists of an infinite set of spatial harmonics that travel with different phase velocities, but with the same group velocity.

One can derive [140] that the group-velocity v_g of the wave propagating inside a Slow light structure is reduced, with respect to the phase velocity $v_p = c/n_{eff}$ in the same but unloaded structure ($t = 1$), by a factor S

$$S = \frac{v_p}{v_g} = \frac{\cos(kL_{cav})}{\sqrt{t^2 - \sin^2(kL_{cav})}} \quad (6.3)$$

called the *Slowing Ratio*. The factor S is shown in Figure 6.3 for different values

of coupling coefficient t . At each resonance frequency f_0 , the identity $kd = Q\pi$ holds and $S(f_0)$ simply reduces to the value:

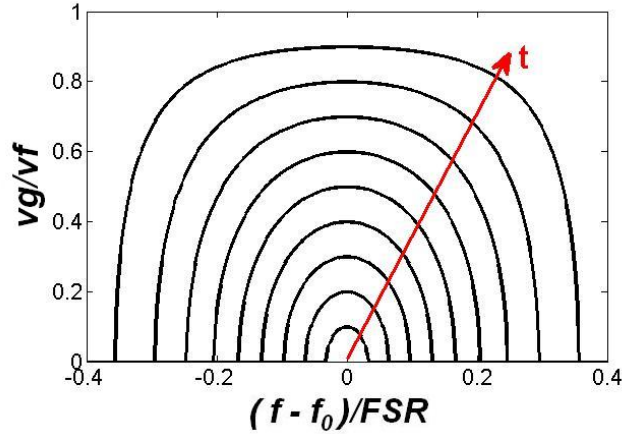


FIGURE 6.3: Inverse of the Slowing Ratio S for different value of the cross-coupling field coefficient t .

The slowing ratio S increases moving towards the band edges, where v_g ideally drops to zero. Both v_g and the bandwidth B reduce by reducing the coupling coefficient t or, equivalently, by increasing the finesse ($F = FSR/B$).

$$S = \frac{1}{t} = \frac{2}{\pi}F \quad (6.4)$$

Finally, the total group delay introduced by a CROW with N resonators is:

$$\tau_g = \frac{NSL_{cav}n_g}{c} = N\tau_r = \frac{N}{\pi B} \quad (6.5)$$

where τ_r is the unitary delay associated with each resonator – and is only dependent on the bandwidth B .

It is worth noting that, while dispersion represents the ultimate theoretical limitation, experimental results show that the dominant contribution to pulse distortion, and so the main practical limitation are the losses and disorder effects. By disorder I mean the fabrication tolerances on the coupling coefficients, inaccuracies in the resonance frequencies and roughness-induced backscattering, all of which affect the transfer function of the slow-light structures. These issues are discussed in Appendix D.2

6.4 Design of a Delay line with N resonators

Interest centres on the realization of delay-lines for optical signal processing. The main requirements are: large delay, τ_g , and large bandwidth B .

In slow-light structures, the delay is proportional to the slow-down factor, S , which is in turn proportional to the finesse F .

However, the value of F is upper-limited by two factors:

- backscattering: in ring resonators increases with the square of group index, n_g , and therefore with the square of Finesse – so that $F = 20$ is sufficient to produce an un-acceptable level of backscattering [1].
- criticality and complexity: the higher the value of F , the narrower is B compared with FSR , the smaller the phase shift required to drive the ring resonators out of resonance. This means greater sensitivity to fabrication tolerances and a need of higher accuracy and resolution in tuning and re-configuration.

Moreover, with finesse being the ratio between FSR and B ($F = FSR/B$), and since we desire a large bandwidth, to have high values of F , large FSR is needed – and so small ring resonators. However, the smaller the ring resonator, the higher the bending losses and the sensitivity to technological tolerances. A conservative trade off between F , B and ring size has therefore to be found. By large bandwidth is meant a value that capitalizes on the potential of silicon, not achievable by lower index-contrast technologies. We can therefore assume $B \geq 50GHz$. By using relatively big ring resonators with a $FSR = 450 GHz$, we are able to obtain finesse values $F = 4 - 8$, which assure significant slow-down factors $S = 2.55 - 5.10$ with acceptable bandwidth $B = 112.5 - 56.25 GHz$, respectively.

To meet all the previous requirements, coupled ring resonators structure were designed with $R = 20 \mu m$ and $L_c = 16.12 \mu m$ (purple line in Figure 3.19), ensuring the availability of a large range of K values. The desired $FSR = 450 GHz$ and the footprint of the coupled structure is equal to $N \cdot 40 \times 56 \mu m^2$, where N is the number of rings. These resonators are the same as analyzed in details in Section 3.6 and are realized with the single-mode SOI waveguides described in Section 3.2,

which have cross-section of $480 \times 220 \text{ nm}^2$, effective index $n_{eff} = 2.4925$, group index $n_g = 4.22$ and typical propagation losses $\alpha = 1.2 \div 0.2 \text{ dB/cm}$.

The design specifications of ring-based delay line, together with the measurements of the fabricated devices, are summarized in Table 6.1. In this table a chain of 20 rings was designed and realized in SOI technology, in both transmissive (Tx) and reflective (Rx) configurations. Excellent agreement between measurements and design is present confirming the good control of the process parameters on the coupler and the waveguide dimensions.

6.5 Measurement of a Delay line with N resonators

6.5.1 Static Behaviour

To compare the experimental spectral response H with its design specifications, the coupled ring structure is measured in the frequency domain and in the static regime (without tuning and reconfiguration). In this way it is possible to obtain the transmission characteristics of the fabricated device – and estimate the fabrication tolerances and variability obtained for the particular device.

Figure 6.4(c) shows the experimental results obtained for a cascade of 6 Rings, with Finesse $F = 4$ performed from colleagues at Politecnico di Milano. The Intensity transfer function $|H|^2$ is shown in Figure 6.4 b) for the through (red line) and drop (blue line) ports over a spectrum range of 10 nm . The characteristic exhibit Fabry-Perot fringes (about 5 dB peak-to-peak), due to the refractive-index contrast at the chip end facets (at the moment of the acquisition of this transfer function inverse tapers were still under development).

Figure 6.4 shows a comparison between the pass-band of the experimental response $|H|^2$ (solid lines) and the designed one (dashed lines). The great accuracy of the fabrication processes developed is clearly visible from the fact that, despite the high number of rings and the fact that the device is not tuned, there is a good agreement between the acquired signal and the designed one. The pass-band shape of the filter is well defined, the measured FSR (3.58 nm , i.e. 447 GHz) matches perfectly with the design and the extinction ratio is very high ($ER > 50 \text{ dB}$). The

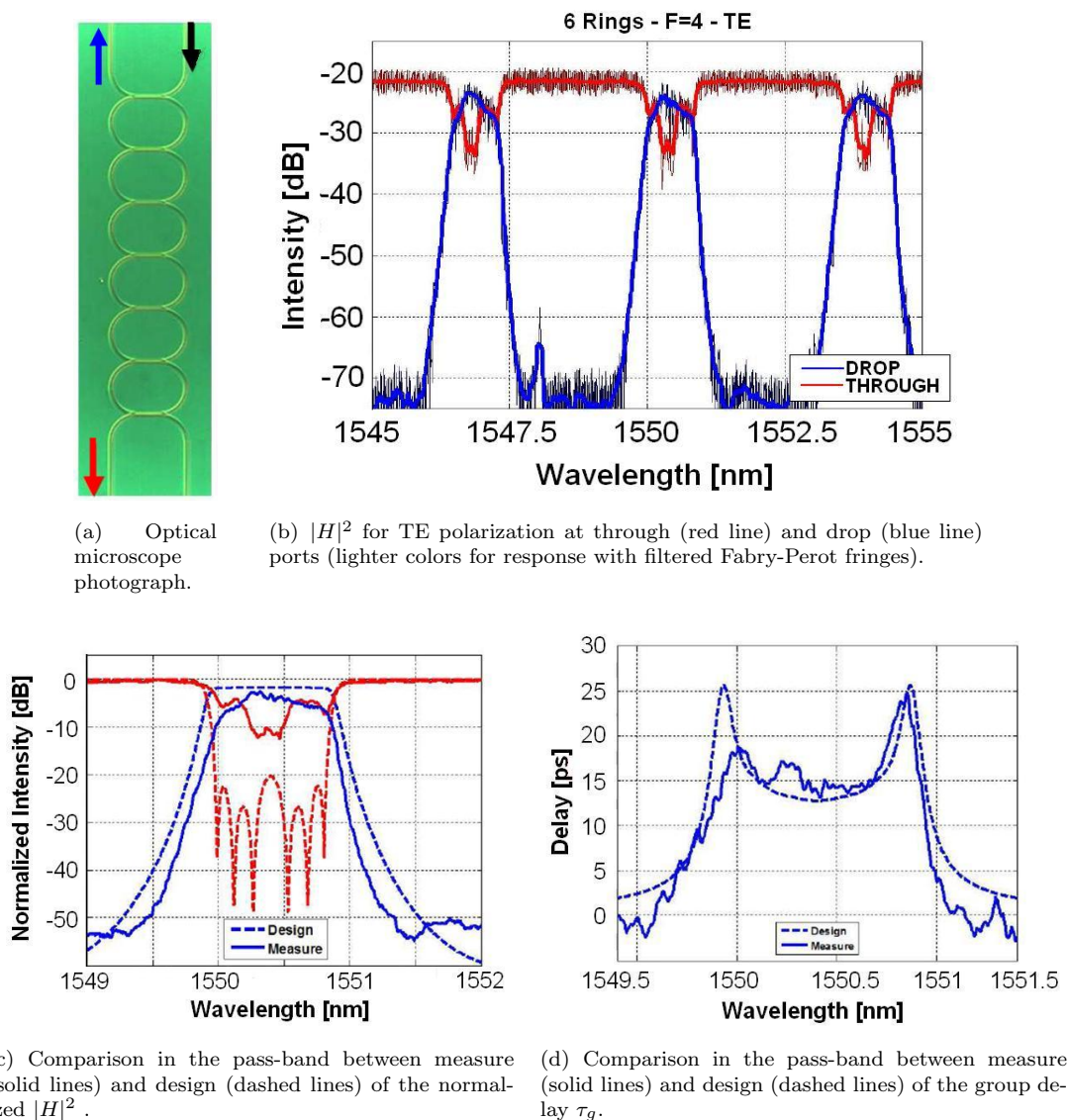


FIGURE 6.4: Measurements of a CROW structure with 6 rings and $F = 4$ in Transmission configuration .

measured bandwidth (0.82 nm , i.e. 102 GHz) is slightly lower (about 10 %) than expected, probably due to a slight under-coupling between rings. The Finesse is therefore $F = 4.38$.

Considering the high number of the variables that need be controlled for the realization of the couplers, the fair flatness of the pass-band at the drop port suggests, at least from a qualitative point of view, the good control of the fabrication process and the quality of the apodization design. The insertion losses, calculated from the difference between the through and drop output power, are about 4 dB : the propagation losses contribution is about $(L_{ring})/2\alpha NS = 0.24 \text{ dB}$, bending

losses are negligible for $R = 20 \mu m$ – and so the main contribution to the losses is due to disorder effects. Figure 6.4(d) shows, the group delay τ_g in the passband, comparing measurement (solid line) with design (dashed lines) – resulting in very good agreement. Group delay was extracted from the intensity spectral response by means of Hilbert transform [145] to recover the phase information from the amplitude spectra.

At the center of the stop-band, $\tau_g = 14 ps$, matching well with the expected value $\tau_g = 13 ps$. Analogous remarks can be made for observations on 8 rings structures with $F = 4$ – and 4 ring structures with $F = 8$. All the experimental results, compared with corresponding design specifications, are summarized in Table 6.1.

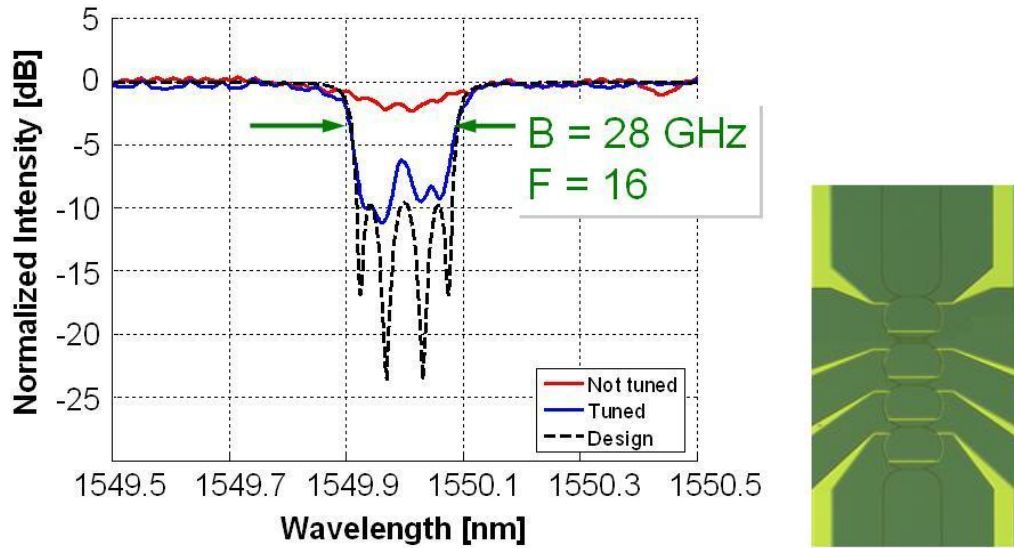
Parameter	$F = 4$; 6 rings		$F = 4$; 8 rings		$F = 8$; 4 rings	
	Measure	Design	Measure	Design	Measure	Design
$FSR [GHz]$	447.2	450	449.2	450	449.2	450
(nm)	3.58	3.61	3.6	3.61	3.6	3.61
$B [GHz]$	102	112.5	98.2	112.5	51.2	56.25
(nm)	0.82	0.9	0.8	0.9	0.41	0.45
$IL [dB]$	4	> 0.3	5	> 0.4	3	> 0.2
$ER [dB]$	> 50	-	> 45	-	> 45	-

TABLE 6.1: Comparison between design specifications and measured parameters for three different configurations of Coupled Optical Resonators.

6.5.2 Reconfigurable Behaviour

The resonances of devices with a bandwidth smaller than $50 GHz$ ($0.4 nm$) are more critical to align. In fact, the small but not absent variability in the fabrication process, chapter 5, have proved that a change in the device dimension as small as $\pm 0.56 nm$ is able to produce a dispersion in the resonance wavelengths position as big as $\pm 1.2 nm$. Long chains of ring resonators with bandwidths smaller than $50 GHz$ could suffer of a sensible dispersion. If this is the case, the developed thermo-controllers can be used to slightly change the effect of the phase disorder (i.e. shift of the resonance frequencies).

Figure 6.5 shows, as an example, a structure comprising 4 Rings with a Bandwidth of $28 GHz$ and a Finesse of $F = 16$. From the transmission spectra of the *as-fabricated* devices (red line) it is possible to improve further the shape of the transmission characteristic (blue line) in order to match it with the designed one (black dashed line).



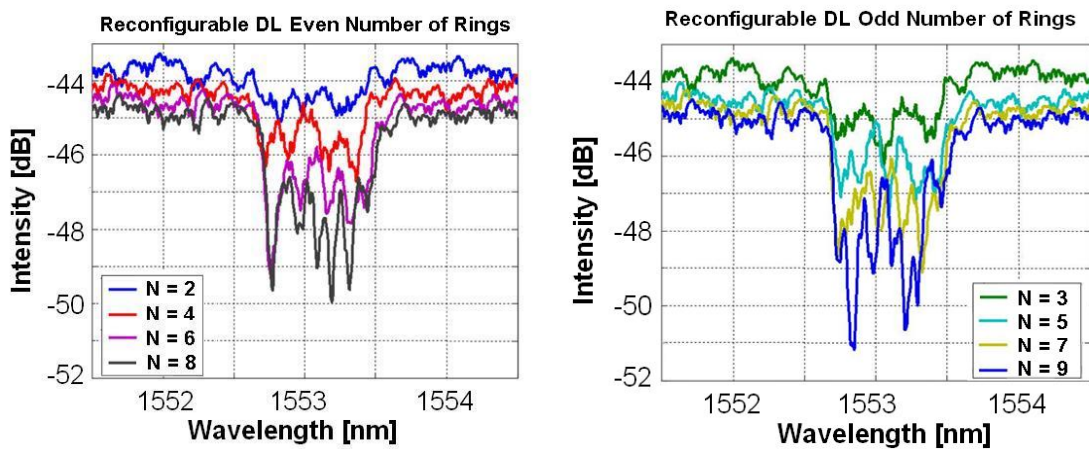
(a) From the *as fabricated* device (red line) it is possible to further improve the shape of the Bandwidth (blue line), by means of thermal tuning wavelength shift, in order to match with the designed one (black dashed line). (b) Optical microscope photograph of the tuned device.

FIGURE 6.5: Fine tuning and phase disorder adjustment for a CROW with 4 Rings, a Bandwidth of 28 GHz and a Finesse $F = 16$.

Further improvement is limited by the physics of the device related to the variation of the couplers from the designed ones – and the presence of roughness and backscattering. Once the required transmission spectra has been obtained, it is possible to achieve a delay-line functionality.

The architecture used is the Reflection configuration, which has been previously realized on SION platform from colleagues of Politecnico di Milano [140] and is discussed more in details in section D.1.

Tuning across a chain of ring resonators may be used to introduce a discrete (digital) delay that corresponds to the time spend in a double transit across each of the elementary ring resonators of the structure (τ_r). Once all the (M) rings in the chain are perfectly tuned according to transfer function design, a delay equal to $N\tau_r$ is obtained shifting the ($N + 1$)-th ring resonator out of resonance. This property means that all the possible values of delays achievable required the activation of only a limited number of thermo-controller (two, to increase the rejection). A continuous analogue delay is possible by fine tuning the position of the ($N + 1$)-th ring resonator around any working point of the structure, thereby changing its contribution to the total delay – from zero to the maximum value achievable from the single ring (τ_r).



(a) Intensity spectra for an even number of rings tuned on resonance. (b) Intensity spectra for an odd number of rings tuned on resonance.



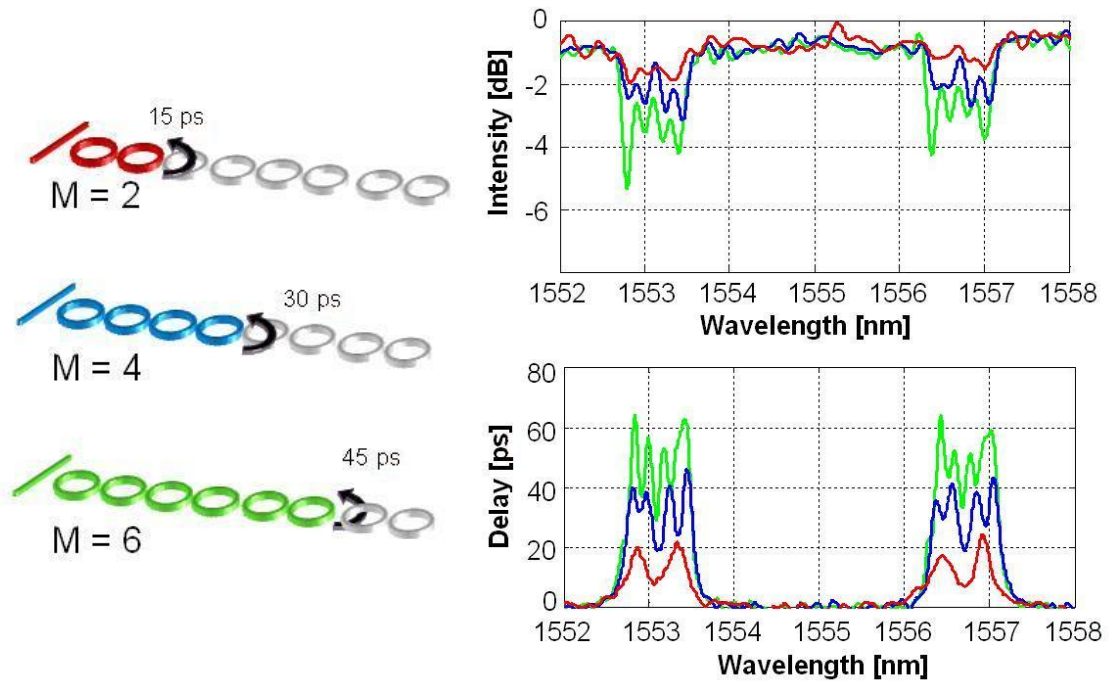
(c) Schematic representation of the ring on resonance (green) and off resonance (red).

FIGURE 6.6: Experimental intensity spectra of a CROW with $M = 20$: by controlling the resonance of two ring resonators (red rings in (c)), the length of the delay line (green rings in (c)) was discretely changed from $N = 2$ to $N = 9$.

Figure 6.6 shows the measured intensity spectra of coupled ring resonators with $M = 20$ rings and a Finesse $F = 4$ as specified in Table D.1. By controlling the resonance of two ring resonators, the length of the delay line was discretely changed from $N = 2$ to $N = 9$. Results for even (a) and odd values (b) of N are shown separately, in Figure 6.6, only to improve the readability of the curves.

The number of peaks in the pass band corresponds to the number of rings tuned on resonance N (at least for small values of N) and the depth of the in-band notch increases linearly with the number N of tuned resonators. This result establishes the capability of realizing an efficient and accurate full reconfiguration of SOI slow wave structure with a significantly large number of ring resonators.

Figure ?? shows the measured intensity spectra (top image) and the corresponding delay (bottom image) that correspond to the activation of N different numbers of rings of the same coupled ring resonators structure. The measured values of $FSR = 450 \text{ GHz}$ and $B = 87 \text{ GHz}$ with finesse $F = 5.17$ and slow-down factor $S = 3.3$.



(a) Schematic representation of the activation of different number of rings to achieve different delays.

(b) Experimental Intensity and corresponding Delay.

FIGURE 6.7: Intensity measurements and delay of a CROW structure with $M = 20$, for N varying from 2 to 6.

Higher attenuation is observed at the band-edges, where the group delay of coupled-resonator structures exhibit sharp transmission/reflection peaks, which increase in magnitude as the number of tuned resonators increases.

According to the expression for the delay in CROWs, i.e. $\tau = N\tau_r$, the delay increases linearly with the number of ring resonators driven at resonance. For $N = 2, 4$ and 6 , the corresponding delay is $\tau = 15, 30$ and 45 ps. The unitary delay is therefore $\tau_r = 7.5$ ps/RR, in near-perfect agreement with the theoretical value: $\tau_r = 2/\pi B = 7.3$ ps/RR. The maximum delay achievable with this device, for $N = 20$, is therefore $\tau = N\tau_r = 150$ ps. The fabricated devices are therefore demonstrated to be able to impose a continuously variable delay on an optical signal.

The reported results constitute the first demonstration of a continuously tunable delay line in silicon photonics. Measurements of the devices in real telecommunication systems performed by our project partners in Milano are presented in appendix E of this thesis.

6.6 Conclusions

The characterization of the realized silicon-on-insulator reconfigurable slow-light structure that have been fabricated provides very interesting figures for performance, demonstrating the powerful capabilities of these structures for use as delay applications.

The fabrication development performed during this thesis enables the control of the dispersion of the resonances position within 0.2-0.3 *nm* and allows the realization of a CROW delay-line of 8 ring resonators with a bandwidth of 100 *GHz* and $F = 4$ with all the resonances already aligned in the bandwidth. This result was consistent between different realizations of the same fabricated device. The robustness and repeatability is the result of the high control of all the variables involved in the fabrication process (e.g. waveguides dimension, coupler geometry, coupler filling which are all dependent from fabrication conditions: temperature, gases, umidity etc..). More critical devices with higher Finesse and smaller bandwidths required a post- fabrication phase-disorder compensation. This was achieved by a fine tuning of the ring refractive indeces by means of the thermo-optic effect. The possibility of dynamical tuning of the devices was used to demonstrate continuous tuning of the delay from 0 to 150 *ps* on the same geometry (Reflection CROW configuration). Moreover, for the particular geometry chosen, only a limited number of ring resonators needs to be tuned, thereby minimizing the power consumption per delay.

The system performance for both amplitude and phase-modulation formats, from 10 to 100 *Gbit/s*, are reported in Appendix E, showing a considerable potential for optical signal processing, especially for large bandwidth and high bit-rate applications [26, 141].

Chapter 7

Conclusions and Future Work

In this work we have demonstrated that reconfigurable slow light delay lines made with micro-ring-based CROW (coupled resonator optical waveguide) structures have a great potential for advanced, high performance, large-bandwidth optical signal processing applications. The dynamic operation of our devices is enabled by an efficient tuning scheme that is flexible and continuously reconfigurable. Moreover, a large operating bandwidth (up to 100 GHz and beyond) and an ultra-small footprint are allowed by exploitation of the high index contrast technology. These are the main features that make silicon waveguide delay-lines a unique solution in the slow-light scenario.

The reconfigurability of slow-light delay-lines is efficiently realized by controlling only 2 rings – and providing the very low power consumption value of $P = 20 \text{ mW}$. The thermo-optical control that has been developed enables high thermal efficiency ($52 \mu\text{W}/\text{GHz}$), with negligible cross-talk and with a response time of 12 μs . Moreover, phase-preserving and error-free transmission up to 100 Gbit/s has been demonstrated, proving the compatibility of these devices with advanced modulation formats and high bit-rate transmission systems, as discussed in appendix E.

The excellent performances of the slow-light device functionality are a direct consequence of a number of achievements that were produced in this work.

The extensive optimisation on ebeam lithography and dry etching of SOI devices provided the robustness and reliability required for the fabrication of long chains of ring resonators. This result is made achievable due to a high control of all the variables involved in the fabrication process. Waveguide losses as low as

1 - 1.5 dB/cm is not anymore a *best result* but can be consistently reproduced on all the fabricated devices. The outcomes of the experiments on the stability of the HSQ resist ensure a high level of patterning uniformity over large samples and repeatability of the process over time. The buffering of the silicon waveguides by a combination of HSQ and PECVD silica provides a complete and uniform filling of gaps as small as 50 nm and therefore largely improves the control over the couplers between the ring resonators.

The optimum design and fabrication of the thermo-optical controllers made it possible the access to tuning functionalities of the devices with figures of merit comparable if not better than the state-of-the-art in silicon photonics. The development of the inverse taper coupler has increased the power coupling efficiency and filtered out almost all of the spurious Fabry Perot effects present in the measurement set up yielding to a better estimation of the device performances.

Another important point has been the investigations that produced a clear understanding on the technological limitations of SOI devices and their impact on the device performance in simple waveguides, in single ring resonators and in CROW structures - through a collaborative work with partners in the Politecnico di Milano. One result has been the experimental demonstration that resonance dispersion between ring resonators is in the order of 30-50 GHz. These figures were obtained with state-of-the-art technology and correspond to dispersion over the device dimensions comparable to the crystal lattice (i.e. a few Angstrom). We believe this is a fundamental technological limit with available lithographic and etching technologies. It was also found that backscattering adds coherently in resonators - and scales as the square of n_g . It can therefore dramatically modify the spectral response of ring resonators even at moderate Q values. Backscattering emerges as one of the most severe limiting factors for the performance of high index-contrast resonators - and must be carefully evaluated in slow light structure design.

All these results made it possible the realization of a continuously tunable delay up of to 1 Byte, over a very large bandwidth (about 100 GHz), by tuning 11 Ring Resonators and with a footprint of only $56 \times 440 \mu m^2$. The main figures of merit for optical delay lines, such as storage efficiency, fractional delay and fractional losses, are comparable with the-state-of-the-art in the field, realized in SiON technology. The SOI devices provide, however a bandwidth that is one order of magnitude larger - and a footprint that is several order of magnitude smaller.

The obtained evidence shows that multiple ring-resonators slow light structures provide an optimum trade off between conversion efficiency and bandwidth, overcoming the limitations of both simple waveguides and single ring-resonators – and, representing, therefore, the-state-of-the-art in the field.

Considering the future activities that could follow from the present research, I believe that proposed silicon ring-based slow-light delay-lines still have a large margin for improvement, but also several critical aspects that must be addressed. Taking into account the performance of the technology developed and the backscattering constraints, a factor of 4 can be reasonably gained in the FSR (up to $2 THz$), finesse (up to 16) and S (up to 10) – while assuring, at the same time, more than $100 GHz$ bandwidth. This combination will produce a considerable improvement, proportional to S , in the delay-line performance.

The main limitations on the proposed structures are, however, the losses and thermo-optic activation time. The results reported in this thesis suggest indeed that the maximum achievable delay is limited, rather than by dispersion issues, by the round trip losses of the resonators, which quickly impair the signal quality when the light is trapped inside the slow light structures.

Reduction of the sidewall roughness losses is therefore an issue that require to be carefully addressed in the future. Only limited improvements can be introduced in the lithography or etching techniques [146]. However, an oxidation process could be introduced in the process sequence in order to reduce the surface roughness [58] – with a consequent reduction of the propagation losses and backscattering. The second constraint arises from the slow activation time provided by thermo-optical control. A $12 \mu s$ time response limits the possible switching frequency to only $80 KHz$ – and prevents certain developments such as long-tune scale storing and pulse trapping. The silicon platform does, however, enable the realization of p-i-n junctions with very fast time response (on the order of tens or hundreds of picoseconds), that would enable further exploitation of these concepts and geometries.

In conclusion, I believe that the results obtained in this work set new milestones - both in the field of slow-light and in optical signal processing applications, showing unique performance and also revealing interesting perspectives for future development and research. The technological developments and deep understanding on the limiting factors of SOI devices have largely improved the potential of this technology and provides a more robust and reliable technological platform for the exploitation of silicon photonics.

Appendix A

Transfer Matrix Method (TMM)

A.1 Transfer Matrix Method

The Transfer Matrix Approach allows the solution of a general complex system by matrix products of basic cells. In the following, the basic building block matrices are introduced for the analysis of systems with an increasing number of cells. The formulations of coupled ring structures are extracted for the two most common configurations: APFs (All Pass Filters) and CROWs (Coupled Resonator Optical Waveguides).

A.1.1 Waveguide

A waveguide introduces a phase shift $e^{-j\beta L_w}$. The four-port transfer-matrix associated with two parallel waveguides is:

$$\Lambda_k = \begin{bmatrix} e^{-j\beta L_w} & 0 \\ 0 & e^{j\beta L_w} \end{bmatrix} \quad (\text{A.1})$$

where β is the propagation constant and L_w is the length of the waveguide.

A.1.2 Coupler

When two waveguides are brought close together, there is coupling between the field components according to the self-coupling (r) and cross-coupling (t) coefficients. Figure A.1 shows, graphically, the field amplitudes used in the matrix representation.

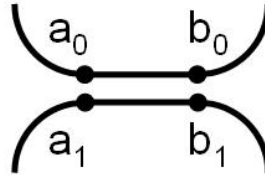


FIGURE A.1: Graphical representation of the coupler with the amplitudes of the fields at the four ports.

The matrix representation of a coupler is:

$$\begin{bmatrix} a_1 \\ b_1 \end{bmatrix} = \frac{1}{it} \begin{bmatrix} -r & e^{-j\beta L_c} \\ -e^{j\beta L_c} & r \end{bmatrix} \begin{bmatrix} a_0 \\ b_0 \end{bmatrix} = P \begin{bmatrix} a_0 \\ b_0 \end{bmatrix} \quad (\text{A.2})$$

where L_c is the total length of the coupling region and β is the propagation constant.

A.1.3 Ring Resonator Filter

A ring resonator can be considered as a combination of couplers and curved waveguides. The curved waveguides, in the configuration of Figure A.2, introduce a phase shift $e^{j\beta 2\pi R/2}$

$$\begin{bmatrix} a'_1 \\ b'_1 \end{bmatrix} = \begin{bmatrix} 0 & \gamma e^{j\beta 2\pi R/2} \\ \gamma e^{-j\beta 2\pi R/2} & 0 \end{bmatrix} \begin{bmatrix} a_1 \\ b_1 \end{bmatrix} = Q \begin{bmatrix} a_1 \\ b_1 \end{bmatrix} \quad (\text{A.3})$$

where $\gamma = \exp(-\alpha_r L_r/2)$ represents the attenuation of the field per round trip. The relation between the input and output fields, for a single ring resonator structure, is simply obtained as the matrix product of the basic cells describing the

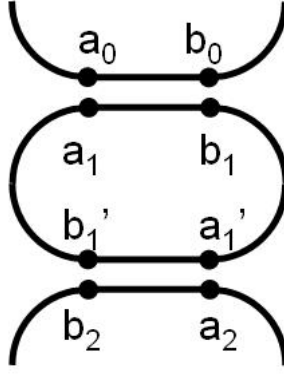


FIGURE A.2: Graphical representation of a ring resonator structure coupled to two bus waveguides, with the complex amplitudes of the fields in the different sections of the ring.

couplers and the propagation section inside the ring.

$$\begin{bmatrix} a_2 \\ b_2 \end{bmatrix} = -\frac{1}{t^2} \begin{bmatrix} -r & e^{-j\beta L_c} \\ -e^{j\beta L_c} & r \end{bmatrix} \begin{bmatrix} 0 & \gamma e^{j\beta 2\pi R/2} \\ \gamma e^{-j\beta 2\pi R/2} & 0 \end{bmatrix} \begin{bmatrix} -r & e^{-j\beta L_c} \\ -e^{j\beta L_c} & r \end{bmatrix} \begin{bmatrix} a_0 \\ b_0 \end{bmatrix} \quad (\text{A.4})$$

$$\begin{bmatrix} a_2 \\ b_2 \end{bmatrix} = PQP \begin{bmatrix} a_0 \\ b_0 \end{bmatrix} = R \begin{bmatrix} a_0 \\ b_0 \end{bmatrix} \quad (\text{A.5})$$

where the two matrices P represent each of the two couplers.

The general formulation make it possible to change, in an easy way, the coupling coefficients, the lengths of the couplers and the guiding sections during the design process. To obtain couplers with different lengths and coupling coefficients, it is sufficient to change the matrix elements according to the particular geometry. This feature make this method flexible and the design optimization can be easily and quickly performed. The compact matrix form for the system is:

$$\begin{bmatrix} a_2 \\ b_2 \end{bmatrix} = R \begin{bmatrix} a_0 \\ b_0 \end{bmatrix} = \begin{bmatrix} A & B \\ C & D \end{bmatrix} \begin{bmatrix} a_0 \\ b_0 \end{bmatrix} \quad (\text{A.6})$$

If we assume that the input $a_0 = 1$ and no added signal at the other end, $a_2 = 0$, we obtain:

$$b_0 = -\frac{A}{B} \quad (\text{A.7})$$

$$b_2 = C - \frac{DA}{B} \quad (\text{A.8})$$

Although the solution of a single ring resonator is easily achievable by solving the matrices products, a software implementation simplifies the computational difficulties and reduces the time required.

A.2 Coupled Optical Resonators

Under the assumption of resonators that all have identical characteristics (i.e. lengths and coupling gap), it is possible to analyze the behavior of the structure as a periodic spatial repetition of identical cells. The tight-binding analysis has been used extensively to study optical propagation in CROWs [147–149] – and the electric field of an eigenmode E_K of the CROW may be described as a Bloch wave superposition of the individual resonator modes E_Ω [25]. Even if mathematically rigorous, the tight-binding method is not always a convenient approach to describe physical systems. Some of the major limitations, for example, are that it does not take into account the finite length of the resonator chain and other factors such as losses, differences in resonator size, input and output coupling and variation in the coupling strengths that radically modify the response of the structure.

The Transfer Matrix formalism is a powerful approach that overcomes the limitations of the tight-binding model and can be applied to the analysis of arbitrarily shaped geometries.

In the case of a one-dimensional repetition of cells, two different topologies can be analyzed: one with periodicity along the bus waveguide (APF) and one with periodicity perpendicular to the bus waveguide (CROW).

- APF is a repetition of basic cells (e.g. ring resonators) individually coupled to a single bus waveguide. The transfer function of a ring based APF structure of K elements is simply obtained as the matrix product of N matrices associated with the single ring resonators and the $K - 1$ waveguides with length L_k that take into account the spatial separation of the devices along the bus waveguide. With reference to the formalism shown in Figure A.3, the matrix representation is:

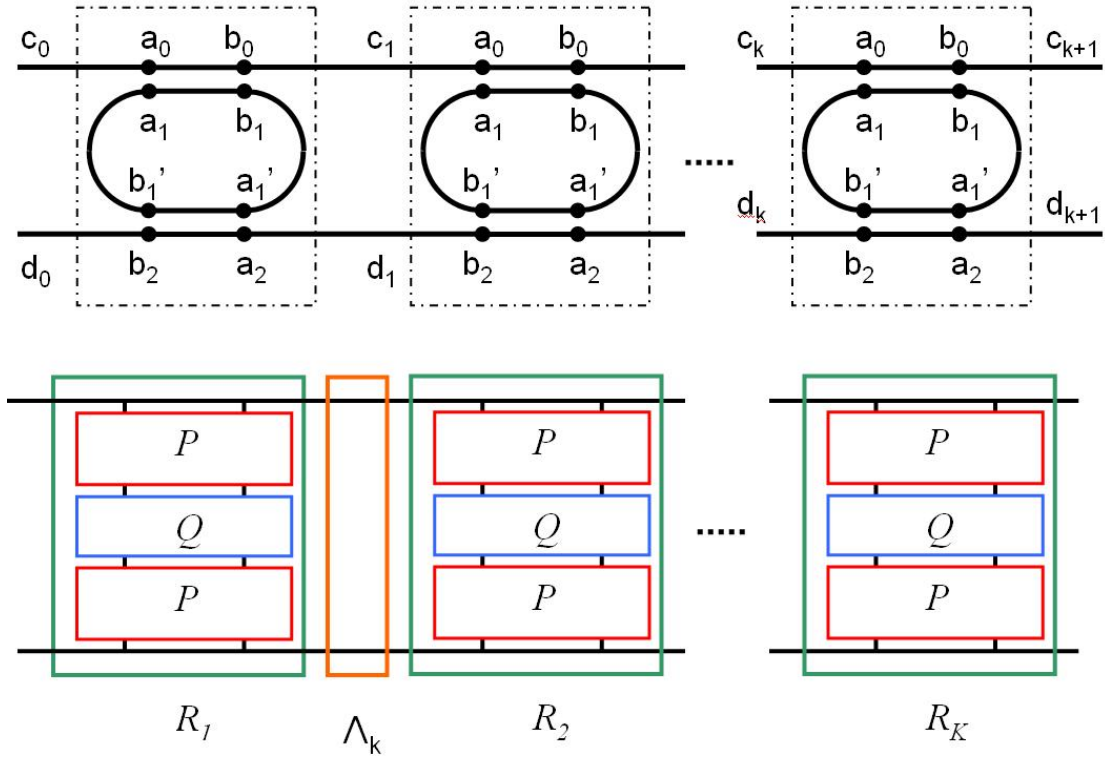


FIGURE A.3: Schematic representation of an APF system. Starting from a basic level, it is possible to analyze systems with an increasing complexity where the Ring cell (green square) is obtained as a combination (matrix product) of sub-building blocks (couplers and waveguides - red and blue, respectively) and the cascade is a product of the matrix of each ring resonator multiplied by the waveguide phase shift matrix (orange).

$$\begin{bmatrix} c_{k+1} \\ d_{k+1} \end{bmatrix} = R_k \begin{bmatrix} c_k \\ d_k \end{bmatrix} \quad (\text{A.9})$$

where each ring and waveguide shift can be different one from each other.

$$\begin{bmatrix} c_{k+1} \\ d_{k+1} \end{bmatrix} = \prod_{k=0}^{K-1} (R_k \Lambda_k) R_K \begin{bmatrix} c_0 \\ d_0 \end{bmatrix} \quad (\text{A.10})$$

For the special case of 'nominally' identical rings, equally spaced, the system becomes that shown in Figure A.3 and can be described as

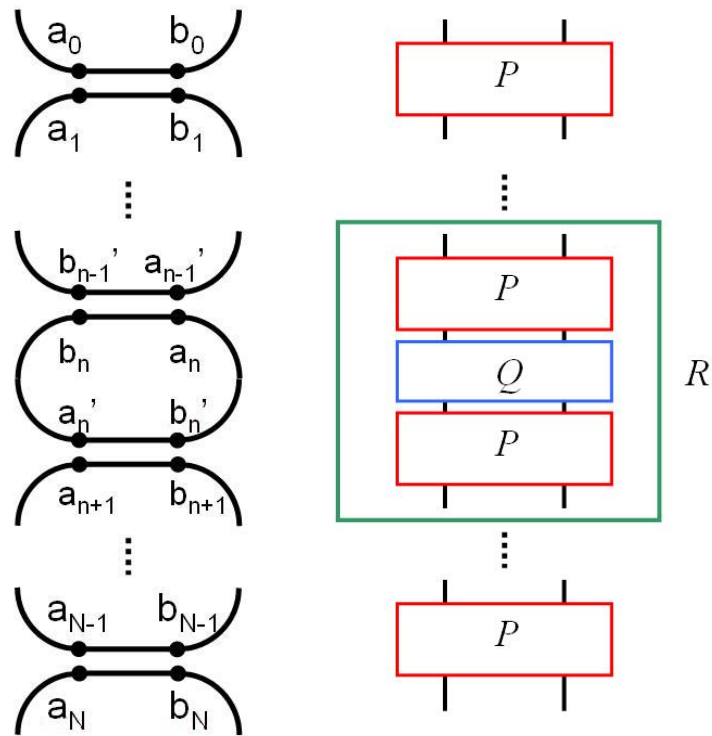
$$\begin{bmatrix} c_{k+1} \\ d_{k+1} \end{bmatrix} = (R\Lambda)^{K-1} R \begin{bmatrix} c_0 \\ d_0 \end{bmatrix} = \begin{bmatrix} A & B \\ C & D \end{bmatrix} \begin{bmatrix} c_0 \\ d_0 \end{bmatrix} \quad (\text{A.11})$$

For this system, if we assume an input $c_0 = 1$ and no added signal on (i.e. $d_{k+1} = 0$), the value of c_{k+1} directly gives the transmission, while d_0 gives the *dropped* signal.

$$c_{k+1} = -\frac{C}{D} \quad (\text{A.12})$$

$$d_0 = A - \frac{BC}{D} \quad (\text{A.13})$$

- CROW: In this case each ring resonator is coupled sequentially to the next and only the first and the last cells are coupled to the bus waveguides as shown in Figure A.4. The matrix representation is



(a) Schematic representation of CROW system, the fields are considered in correspondence of the dots.

(b) Schematic representation of coupled system, the single elements are substituted by matrices.

FIGURE A.4: Schematic representation of a CROW system. Starting from a basic level, with the consideration of fields (left) it is possible to analyze systems with an increasing complexity (right), where a basic building block (ring - green square) is obtained as combination (matrices product) of sub building blocks (couplers and waveguides - red and blue, respectively).

$$\begin{bmatrix} a_N \\ b_N \end{bmatrix} = P_N Q_{N-1} P_{N-1} \dots P_2 Q_1 P_1 \begin{bmatrix} a_0 \\ b_0 \end{bmatrix} \quad (\text{A.14})$$

$$\begin{bmatrix} a_N \\ b_N \end{bmatrix} = (PQ)^N P \begin{bmatrix} a_0 \\ b_0 \end{bmatrix} = \begin{bmatrix} A & B \\ C & D \end{bmatrix} \begin{bmatrix} a_0 \\ b_0 \end{bmatrix} \quad (\text{A.15})$$

For this system, if we assume that $a_0 = 1$ and $a_N = 0$ (no added signal), we obtain:

$$b_0 = -\frac{A}{B} \quad (\text{A.16})$$

$$b_N = C - \frac{AD}{B} \quad (\text{A.17})$$

A.3 Conclusions

A general system can be considered as a combination of basic building blocks that are in principle easy to design and characterize. The solution of the complete system in terms of transfer function (amplitude and phase) is simply obtained as matrix products. The methodology presented is only based on the determination of the field amplitude at the ports of the devices and does not require the analysis of the internal behavior of the devices.

The Transfer Matrix Method allows for a fast and efficient optimization of the single building blocks. The developed technique is much faster and less memory consuming when compared to simulation methods based on FDTD, Beam Propagation and FEM – then it is more suited for the simulation of large circuits and makes it possible to concentrate on a higher system level, and allows to extract precious information for the design of the circuit. Moreover, for periodic systems, it takes into account the boundary conditions related to the finite length of the device and the presence of input and output waveguides and the possibility to have sub-blocks with different geometries.

Appendix B

Origin and Extraction of the propagation losses

B.1 The origin of propagation losses

In order to perform any optimization in both the design and the fabrication process, it is necessary to identify the origin of the losses. Losses in an optical waveguide can be classified into three main categories, depending on the physical phenomena from which they originate: scattering (α_{sc}), absorption (α_{ab}) and radiation (α_{rad}).

$$\frac{\ln(\mathcal{A})}{L_w} = \alpha_{tot} = \alpha_{sc} + \alpha_{ab} + \alpha_{rad} \quad (\text{B.1})$$

- The scattering in an optical waveguide can be of two types:
 - a) Volume scattering: caused by imperfections in the bulk waveguide material, such as dislocations, voids and contaminant atoms, their size with respect to the propagation wavelength and their position inside the waveguide. The high quality level of the SOI fabrication process make this contribution to the total losses negligible, typically.
 - b) Interface scattering: originates from surface scattering of the propagating optical beam, due to interaction with the roughness at the interface between the core and the cladding of the waveguide. This

constitutes a non-negligible contribution to the total losses; a formula that approximates the scattering losses is [55]

$$\alpha_{sc} = \frac{\sigma^2 k_0^2 h}{\beta} \frac{E_s^2}{\int E^2 dx} \Delta n^2 \quad (\text{B.2})$$

where σ is the interface roughness, k_0 is the free space wavenumber, β is the modal propagation constant, Δn is the difference between the refractive indices of the core and the cladding, while h is the transverse propagation constants in the core and $E_s^2 / \int E^2 dx$ is the normalized electric field intensity at the core/cladding interface. The losses are proportional to the modal confinement, the square of the interface sidewall roughness σ and the index contrast Δn . In order to reduce the propagation losses for a large index contrast material it is crucial to reduce the sidewall roughness (σ), realizing ultra-smooth waveguide edges and surfaces by specific optimized processing steps.

- The two main potential sources of absorption loss for semiconductor waveguides are:
 - a) Band edge absorption (or interband absorption): occurs when photons with energy greater than the band gap are absorbed to excite electrons from the valence band to the conduction band. The band edge wavelength of silicon is approximately $1.1 \mu m$, and the interband absorption is very small at the wavelengths under examination ($1.55 \mu m$), typically providing a contribution of only $0.004 dB/cm$ [150] to the total losses. Two photon absorption (TPA) becomes relevant only for power levels exceeding several tens of milliWatts.
 - b) Free carrier absorption: this affects both the real and imaginary parts of the refractive index. Changes in absorption in semiconductors can be described by the DrudeLorenz equation [151]:

$$\Delta\alpha = \frac{e^3 \lambda_0^2}{4\pi^2 c^3 \epsilon_0 n} \left(\frac{N_e}{\mu_e (m_{ce}^*)^2} + \frac{N_h}{\mu_h (m_{ch}^*)^2} \right) \quad (\text{B.3})$$

where e is the electronic charge; c is the velocity of light in vacuum; μ_e and μ_h are the electron and hole mobility respectively, m_{ce} and m_{ch} are the effective masses of electrons and holes respectively; N_e is

the free-electron concentration; N_h is the free-hole concentration, ϵ_0 is the permittivity of free space; and λ_0 is the free space wavelength. This contribution to total losses is negligible for the substrate under consideration due to its low value of doping (see section 2.1). Care must be taken when doping the material to create p-n junctions for electrical tuning.

- Radiation loss is related to the leakage of the waveguide into the surrounding media, typically the upper or lower claddings. If the waveguide is well designed, this loss will not normally be significant – although unwanted perturbations in the waveguide due, for example, to a slightly damaged fabrication mask may cause power conversion from the fundamental mode to higher-order modes. The second mode may, in turn, be affected by some radiative loss if that mode is leaky. Curvature and micro-bending of the waveguide may also result in some radiative loss. As discussed in section 3.2 a deeply etched geometry in the waveguide has been chosen in order to guarantee a negligible contribution to the losses above a certain radius of curvature.

For a multilayer waveguide structure such as the SOI rib waveguide, the possibility of radiative loss exists if the lower waveguide cladding is not thick enough. In the case of SOI, the buried oxide layer is, usually, sufficiently thick to prevent optical modes from penetrating the oxide layer and coupling to the silicon substrate. Clearly the required thickness will vary from mode-to-mode since each mode penetrates the cladding to a different depth. Furthermore, the penetration depth also varies with the waveguide dimensions and the wavelength of operation. As the waveguide dimensions reduce, the mode tails extend proportionately further into the cladding. The buried oxide thickness in the wafer under consideration is $2\ \mu\text{m}$ – and a waveguide width of $480\ \text{nm}$ guarantees a loss into the substrate of less than $0.001\ \text{dB/cm}$ [152].

After a detailed analysis of the various sources of loss we can conclude that scattering losses represent the major contribution to the total losses ($\alpha_{tot} = \alpha_{sc}$). In this thesis, for simplicity of notation, we shall refer to the loss contribution through the symbol α .

The fabrication process developed is able to guarantee a very low value of sidewall roughness – of the order of a nanometre.

B.2 The extraction of the propagation losses

B.2.1 The properties of the sample cavity

The most common method for extracting the value of the propagation losses is the cut-back method. A sample containing straight waveguides is measured and cleaved several times to obtain a value of the transmittivity for different lengths [153]. The main problem with single crystal silicon is related to the cleaving due to its hardness, the complexity of the SOI and the availability of multiple sets of cleavage planes. These properties can result in bad facet quality, which could entail a reduction of the transmitted power and a bad estimation of the propagation losses.

Instead of directly measuring the power, it is possible to use the properties of Fabry-Perot (FP) cavities [154]. One particularly important result of the measurement setup is the effect on the measured transmission spectrum of oscillations produced by the facet reflectivity of the device.

Light propagating in the waveguides is reflected at the cleaved facets, which act as partial mirrors – and circulates back and forth in the waveguide. When the optical round-trip length is a whole number of wavelengths, all components of the field will interfere constructively and a transmission peak will occur at this wavelength. This effect is stronger when the losses inside the cavity are low. The cavity formed has a characteristic transmission spectrum which, for a simple waveguide, is dependent on the facet reflectivity, waveguide loss and total propagation length. For more complex structures, the transmission spectrum is a complex product the transfer functions of each of the constitutive blocks inside the cavity [155].

For transmission loss measurements purpose, the presence of FP oscillation allows a good alternative to the multiple cleaving of the cut back method and moreover is not a destructive technique.

Figure B.1 represents a one-dimensional cavity consisting of a single-mode waveguide with effective refractive index n_{eff} , enclosed between two identical mirrors (cleaved facets) with a modal reflectivity R , spaced by a distance L .

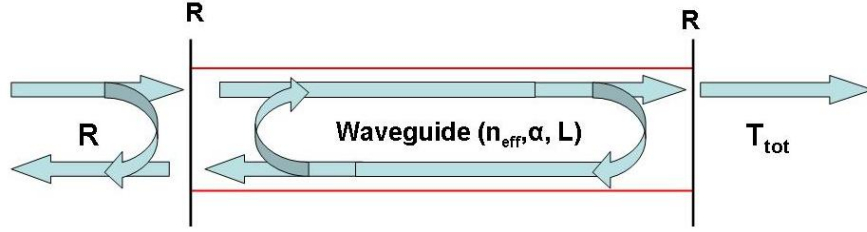


FIGURE B.1: Schematic of Fabry Perot Cavity

It is possible to calculate the transmittance T_{tot} as a superposition of multiple reflections of a wave traveling through the mirrors. The modal field attenuation constant is α and the total transmittance is expressed by equation B.4:

$$T_{tot} = \frac{(1 - R)^2 e^{-2\alpha L}}{(1 - Re^{-2\alpha L})^2 + 4Re^{-2\alpha L} \sin^2(kn_{eff}L)} \quad (\text{B.4})$$

where $k = \frac{2\pi}{\lambda_0}$ is the free-space wave-number and λ_0 is the free-space wavelength. The transmittance is a periodic function in the k -space domain with a period $k_0 = \pi/n_{eff}L$ and can be expressed by Fourier Transform [156] as:

$$\mathcal{F}[T_{tot}](l) = \frac{(1 - R)^2 e^{-2\alpha L}}{(1 - Re^{-2\alpha L})^2} \sum_m e^{-\Gamma\pi l} \delta(l - ml_0) \quad (\text{B.5})$$

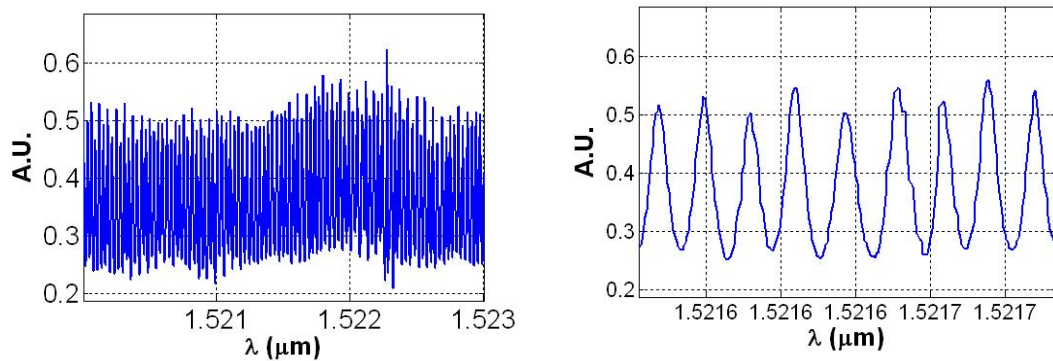
where $\Gamma = \frac{2\alpha L - \ln(R)}{nL}$ [154].

The two expressions for the transmittance in the wavenumber domain (equation B.4) and its Fourier Transform space (equation B.5) allow the extraction of the round-trip attenuation \mathcal{A}_{rt} independently from the input power coupled into the system.

B.2.2 Fabry-Perot measurements using Fringe Contrast

From the contrast of the periodic fringes in the FP oscillations, it is possible to extract the loss in the whole cavity very accurately [156]. Considering the FP cavity transmission characteristic, the fringe contrast \mathcal{C} , defined as the ratio between the local maxima and minima of $T(k)$ [157] – as, for example, in Figure B.2. The value of \mathcal{C} does not depend on the input conditions and can be expressed by

$$C = \frac{T_{max}}{T_{min}} = \frac{(1 + \mathcal{A}_{rt})^2}{(1 - \mathcal{A}_{rt})^2} \quad (\text{B.6})$$



(a) Typical transmission spectra acquired. In the picture the Fabry-Perot oscillation of the cleaved facets are visible. (b) Expanded section of the transmission spectra of the picture reported on the left. Due to imperfections the amplitude of the FP oscillation is not constant.

FIGURE B.2: Transmission spectra of a waveguide under consideration.

Where \mathcal{A}_{rt} in equation B.6 represents the amplitude loss per round trip. Equation B.6 can alternatively be rewritten as:

$$\mathcal{A}_{rt} = \frac{\sqrt{C} - 1}{\sqrt{C} + 1} \quad (\text{B.7})$$

which can be used for the experimental evaluation of \mathcal{A}_{rt} .

To better estimate the value of the losses, it is possible to fit the data obtained from the measurements of waveguides with different lengths, by using for example the geometry shown in Figure B.3.

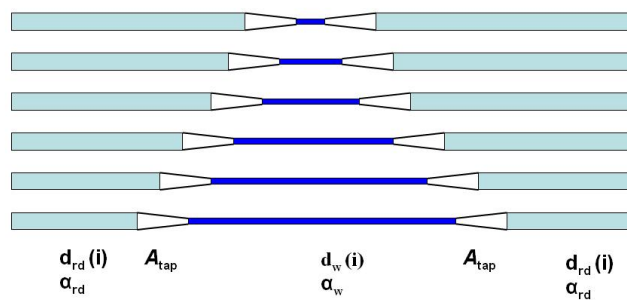


FIGURE B.3: Waveguide Configuration for the estimation of the losses.

It consists of three main blocks: a large $2 \mu m$ access waveguide (pale blue) at the edges of the sample, a photonic wire in the middle (navy blue) and two $300 \mu m$ long tapers (white).

The round trip attenuation inside the cavity is the product of the loss factors of the individual elements:

$$\mathcal{A}_{rt} = Re^{-2\alpha_w d_w} e^{-2\alpha_{rd} d_{rd}} \mathcal{A}_{tap}^2 \quad (\text{B.8})$$

where R is the reflectance of the facets, α_w and α_{rd} are the field attenuation of the photonic wire and large input-output coupling waveguides, respectively; d_w and d_{rd} are the propagation lengths of the wire and the ridge, and finally \mathcal{A}_{tap} is the power attenuation coefficient for the tapered section.

The tapers are designed to provide an adiabatic transition between two sections – and their contribution to the total loss can be neglected; moreover α_{rd} can be considered a small fraction of the total losses: the main source of attenuation being related to the propagation in the narrow wire (α_w).

The slope of the fitted data for wires of different lengths in equation B.8 gives a good estimation of the attenuation constant α , independently from the input-output power coupling. The fitted data is a linear function of the wire length and, from the intercept with the ordinate axis, it is possible to extract graphically the value of reflectivity R .

$$\mathcal{A}_{rt} = Re^{-2\alpha_w d_w} \quad (\text{B.9})$$

Although this method is simple, its accuracy is limited by a number of factors. First of all, the photonic wire should be single-mode. If not, the interference between two or more modes gives rise to an additional modulation of the spectrum (as in Figure B.2). In this case the maxima and minima are only local – and an unique value for \mathcal{A}_{rt} can not be extracted.

Moreover, this method works well only when the system is formed by a single cavity (a photonic wire with its cleaved facets). When the structure contains reflecting interfaces inside the cavity, a multi-cavity structure is formed, which may originate from misalignment during the writing process between different layers and from stitching errors. Even if the system could be represented by a single waveguide, a shift of only few nanometres in between two writing fields could cause a major change in the FP oscillations and a consequently poor estimation of the losses [154].

B.2.3 Fourier Analysis of Transmission Losses

A more accurate technique relies on Fourier Analysis to separate the contributions of the various cavities. From the expression for T_{TOT} of equation B.5, the attenuation can be evaluated by measuring the height of the peaks. In Figure B.4 is shown the Fourier Transform of the transmission spectra of the device shown in Figure B.2 – evaluated by using equation B.5. The first peak at $L = 0$ is the most prominent, and has a peak height of amplitude P_0 .

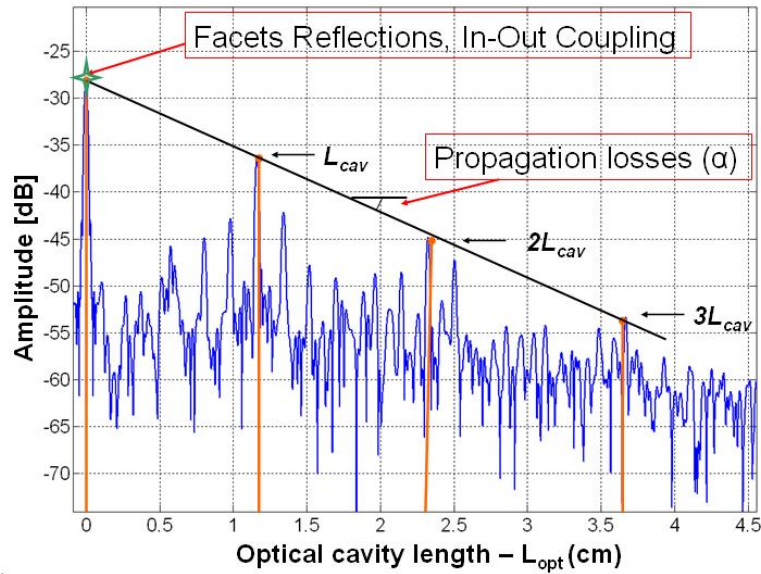


FIGURE B.4: Fourier Transform of the transmission spectra of the device shown in Figure B.2. The oscillations in the transmission spectra are clearly visible from the presence of the peaks in the FT. For a good estimation of the Transmission losses, it is necessary to have a FT with clearly isolated peaks.

If the value of R is known in advance from simulations or evaluated by other measurements, it is possible to extract the value of the attenuation constant. For a single cavity system this approach gives a good estimation of the propagation losses but, in the general case, the presence of additional cavities has the effect of reducing the maximum amplitude of the peaks associated to each cavity length. The first peak of the Fourier Transform, at $L = L_{cav}$, however, can in most cases be isolated. We can also use the height of this peak to extract the internal cavity loss $e^{-\alpha L}$. The height of the first peak is equal to

$$P_0 = \frac{(1 - R)^2 e^{-2\alpha L}}{(1 - R e^{-2\alpha L})^2} \quad (\text{B.10})$$

The peak at $L = 0$ represents the light passing once through the cavity. Each subsequent peak represents light that has made an additional round-trip in the cavity. In low-loss cavities the peaks will only slowly diminish while, in a lossy cavity, the peaks will rapidly tend to zero – as most of the light is lost in the first few round-trips through the cavity.

$$P_1 = Re^{-2\alpha L} \frac{(1 - R)^2 e^{-2\alpha L}}{(1 - Re^{-2\alpha L})^2} \quad (\text{B.11})$$

Instead of using a single peak to evaluate the value of the losses, it is more accurate to measure the ratio between two subsequent peaks. For a single Fabry-Perot cavity, the ratio between two adjacent peaks in the Fourier transform is $Re^{-2\alpha L}$, and therefore provides a direct measure for the losses. As with the fringe-contrast method, we can use the values of $Re^{-2\alpha L}$ for different waveguide lengths to have a more accurate measurement, irrespective of the in-coupling efficiency. Moreover the presence of any defects and extra cavities is highlighted in the Fourier Transform analysis by the presence of isolated defects and extra peaks in the Fourier Transform space.

Both the Fringe-Contrast method and the Fourier-Transform method have been used in the course of this Thesis to analyze the transmission losses for different waveguide configurations. These methods have been used to control periodically the quality of the fabricated devices or to check a new batch of electron-beam resist and developer – or to analyze the losses for samples undergoing different thermal treatments, or with different over-cladding materials. In section 3.3 are shown the propagation losses, evaluated with both

Appendix C

Thermal Model

C.1 Thermal Model

In order to calculate the temperature profile inside a structure, the thermal resistance concept can be used. This general concept makes it possible, at least from a qualitative point of view, to identify the thermal distribution in an intuitive way. The formalism used is similar to that of an electrical network where the electrical resistances, the Voltage (V) and the Current (I) are substituted by the thermal resistances, the Temperature (T) and the Heat flow (Q). In Figure C.1 is shown a schematic where Q , T and R_T are displayed graphically.

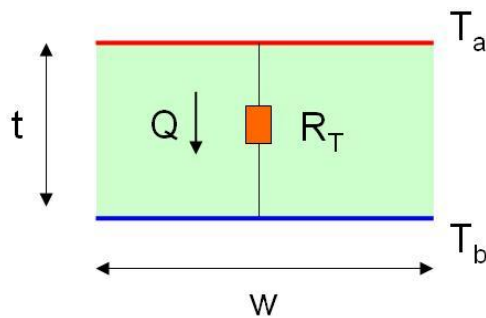


FIGURE C.1: Schematic of the Thermal Resistance. The difference in temperature on the two surface will produce an heat flow proportional to the Thermal resistance of the layer.

Considering the heat flow (\dot{Q}_{cond} [W]) through a section of area A and length t with a thermal conductivity k [W/mK] the heat conduction through that plane is

$$\dot{Q}_{cond} = \frac{T_a - T_b}{R_T} \quad (\text{C.1})$$

where T_a and T_b are the values of the temperatures [K] at the two side of the section of the medium.

The value of R_T [K/W] in equation C.1 is

$$R_T = \frac{t}{kA} \quad (\text{C.2})$$

In a similar fashion to that for electrical networks, it is possible to extend this concept to a network of general complexity, where the thermal resistances are arranged in series and parallel. The heat transfer is constant for series of thermal resistances while the temperature is the same for points on the same surface. The transfer of heat in a multi-layered structure is described by the relative thermal conductivity of each layer. The geometry of the electrodes and the distance between the heating element and the waveguide play an important role in terms of the tuning efficiency of the device.

Even if this concept is fast and intuitive, a deeper understanding of the heat transfer process requires the definition of a model. As the dimensions are reduced, two dimensional heat propagation arises and the analysis with lumped elements must be modified. For these geometries it is necessary to analyze the structure in terms of partial derivatives in the Heat Transfer equation.

C.1.1 Heat transfer equation

The temperature profile of a generic structure depends upon the rate of its internally-generated heat, its capacity to store some of this heat, and its thermal conduction rate at the boundaries (where the heat is transferred to the surrounding environment). The mathematical representation of heat transfer by conduction is the heat equation [129]

$$DC \frac{\partial T}{\partial t} + \nabla(-k\nabla T) = \dot{g} \quad (\text{C.3})$$

where T is the temperature [K], \dot{g} is the rate of heat generation or sinking per unit volume [W/m^3], D is the density [kg/m^3], C is the heat capacity [J/kgK] and k is the thermal conductivity [W/mK] of the medium. The last three thermo-physical properties determine the thermal diffusivity α [m^2/s], which gives information on how rapidly a temperature variation at the medium surface propagates through the medium itself. In stationary state problems, the temperature does not change with time – and so the first term of the equation C.3 disappears. If there is no production or consumption of heat in the medium, \dot{g} can be set to zero. With the presence of a heat source and solving the partial derivatives, equation C.3 become

$$\frac{\partial}{\partial x} \left(k_x \frac{\partial T}{\partial x} \right) + \frac{\partial}{\partial y} \left(k_y \frac{\partial T}{\partial y} \right) + \frac{\partial}{\partial z} \left(k_z \frac{\partial T}{\partial z} \right) + \dot{g} = 0 \quad (C.4)$$

In our analysis the structure is assumed to be invariant along the direction normal to the cross section, so its derivative is equal to zero, i.e. $\partial/\partial z = 0$. The rate of heat conduction through a medium in a specified direction is proportional to the temperature difference across the medium and the area normal to the direction of the heat transfer. In a generic direction

$$\dot{Q}_i = -k_i A_i \frac{\partial T}{\partial i} \quad (C.5)$$

The heat conduction vector can be expressed in terms of its components:

$$\vec{\dot{Q}}_n = \dot{Q}_x \vec{x} + \dot{Q}_y \vec{y} + \dot{Q}_z \vec{z} \quad (C.6)$$

The rate of heat transfer per unit of area normal to the direction of the heat transfer is defined as the heat flux and is expressed as:

$$\dot{q}_i = \frac{\dot{Q}_i}{A_i} = -k_i \frac{\partial T}{\partial i} \quad (C.7)$$

Substituting equation C.7 in equation C.4 and applying all the symmetry conditions, it is possible to obtain a more compact form for the heat flow equation:

$$\frac{\partial}{\partial x} \dot{q}_x + \frac{\partial}{\partial y} \dot{q}_y + \dot{g} = 0 \quad (C.8)$$

The temperature distribution inside a particular geometry can be calculated after the thermo-physical properties and the boundary conditions are defined. These conditions are essentially of two types: Dirichlet or Neumann. In the first type, a temperature is imposed on the medium surface as

$$T = T_0 \quad (\text{C.9})$$

while the second type sets the heat flux \dot{q}_n on a boundary as

$$\vec{n} \cdot \vec{\dot{q}}_n = q_0 \quad (\text{C.10})$$

The values of thermal conductivity (k) and electrical resistivity (ρ) for the materials under consideration are given in Table C.1.

Material	k [W/mK]	ρ [Ωm]
Si	163	$3.2 \cdot 10^3$
SiO ₂	1.38	10^{14}
Si ₃ N ₄	30	10^{14}
Air @ 30 °C	0.026	10^{20}

TABLE C.1: Thermal conductivity and electrical resistivity of the materials under interest.

C.1.2 Joule Heating

In this work resistive metal electrodes have been used as a source of heat to tune the waveguide refractive index by exploiting the thermo-optic effect. The temperature of a metal resistance wire rises rapidly when an electric current passes through it as a result of the electrical energy being converted to heat; the heat produced via this mechanism is proportional to the electric resistance of the metal layer (R_h) and the square of the current inside the conductor (I) according to:

$$Q \propto R_h I^2 = V^2 / R_h \quad (\text{C.11})$$

In particular, in the section where the heat is generated:

$$\dot{g} = \sigma \nabla_{\tau}^2 V \quad (\text{C.12})$$

where σ is the electrical conductivity (S/m), the subscript τ stands for the tangential components of the gradient, and V is the electric potential applied to the electrode (V). On the internal boundaries, the continuity of the electric field must be satisfied.

A Finite Element Method (FEM) based software, from Comsol, has been used for the analysis of the propagation of the heat and the temperature profile inside the structure. The results obtained are presented in chapter 4.

Appendix D

CROW structures

In this appendix considerations relative to the design of CROW structures are presented, which arise from fruitful discussion with the project partners in Politecnico di Milano during project meetings. An exhaustive explanation of each of these concepts can be found in [1].

D.1 Reconfigurable Slow Light Delay Lines Architectures

It is possible to design structures that allow, at the same time, both a digital and analogue delay. The structure shown in Figure D.1 has been previously realized on SION [140] platform. The realization of the structure in Silicon-on-Insulator technology allows a reduction of the physical dimensions of the structure and higher delays.

As shown in Figure D.1, the structure comprises two cascaded all-pass structures, namely $S1$ and $S2$, coupled with the same bus waveguide. The structure $S1$ is a slow-light structure made of M directly coupled ring resonators, while the structure $S2$ simply consists of a single ring resonator phase-shifter. All the rings of the two structures have the same physical dimensions. This ring-based delay-line can be used to provide a continuously tunable and frequency dependent time delay by controlling the individual resonances of the ring resonators. In particular, the delay line $S1$ provides a discrete (or digital) delay, while the structure $S2$ is used to add a small continuous (or analogue) delay.

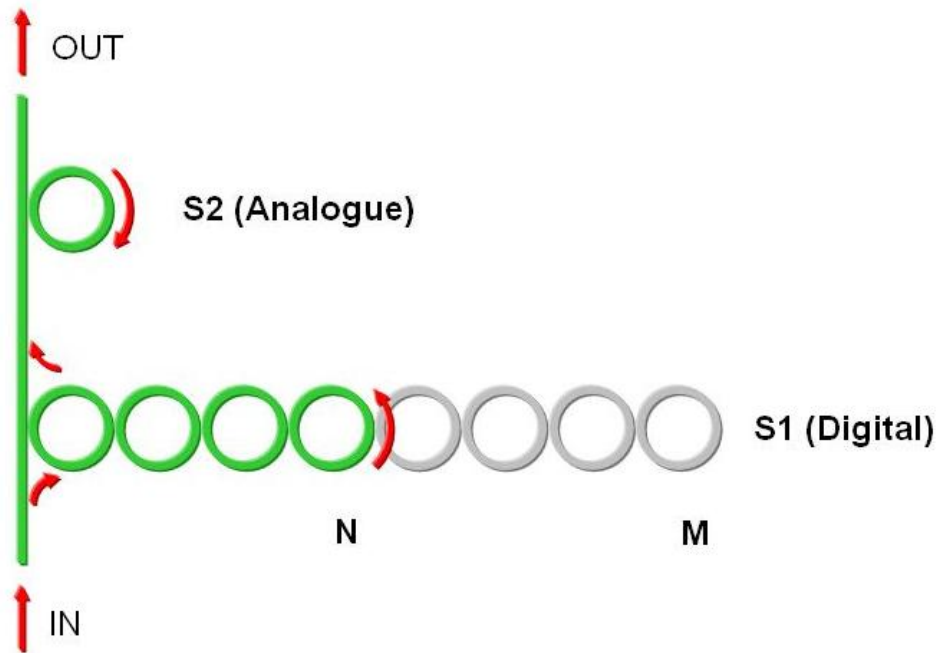


FIGURE D.1: Scheme of a continuously tunable Ring based delay line: the coupled-resonator Slow light structure $S1$ provides a digital tunable delay and the all-pass ring $S2$ gives an additional analog tunable delay.

D.1.1 Digital Delay

Starting from the structure $S1$, an optical signal, incoming from the In port, can propagate along the chain of resonators only if its spectrum is entirely contained within the passband B , given formally by equation 6.2.

If the signal spectrum lies outside B , the signal is directly transferred to the output port without entering $S1$ – and experiences only the propagation delay of the bus waveguide.

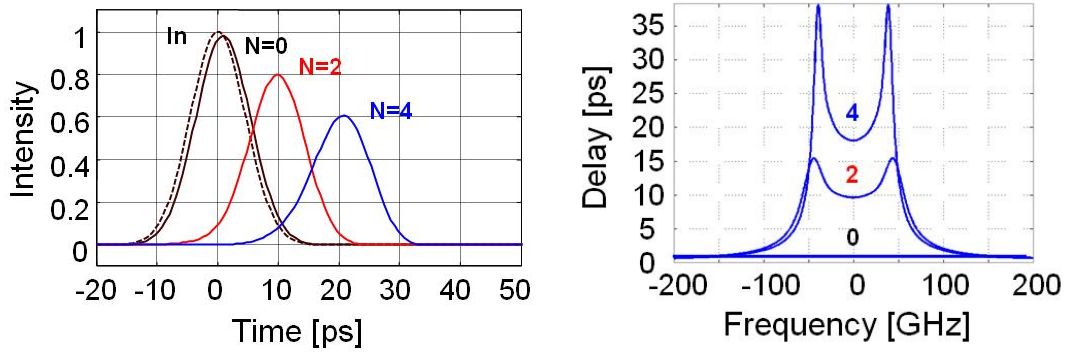
When the pulse is inside the slow-light structure, its propagation is effectively slowed down by the slowing factor S , defined in equation 6.3, which is characteristic of the structure.

If a reconfiguration scheme is present, it is possible to tune the number of rings on resonance for both $S1$ and $S2$. With this tuning option, it may be assumed that the first N rings have been set to the same resonant frequency f_0 ($N = 4$ in Figure D.1). The optical signal can propagate along the chain of rings only up to the N^{th} ring, because all the $N + n^{th}$ rings, ($n > 1$), are off-resonance. Once it

has arrived at the N^{th} ring, the signal is reflected backward to the bus waveguide. The delay experienced by the signal is $\tau_d = 2N/\pi B = N\tau_r$, where τ_r given by:

$$\tau_r = \frac{2}{\pi B} \quad (\text{D.1})$$

is the group delay produced by the double transit through every elementary resonator of the folded structure. The number of rings resonating at f_0 , and hence the overall delay, can be arbitrarily selected by controlling the round-trip phase-shift of the rings of $S1$. Depending on the waveguide technology, the required control can be conveniently obtained by thermo-optic [141], electro-optic [130] or even all-optic control [14, 158]. By selecting N , a discrete tunable delay between zero and $\tau_{dmax} = N\tau_r = 2N/\pi B$ – and with a minimum time-step equal to τ_r can be achieved.



(a) Simulated 10-ps-long Gaussian pulses at the output of the structure $S1$ of Figure D.1, with $B = 125 \text{ GHz}$ and $FSR = 500 \text{ GHz}$, for different values of N . (b) Time delay versus frequency of the structure for increasing N .

FIGURE D.2: Time domain simulations for a Gaussian pulse traveling inside the coupled ring resonator structures while varying the number of on-resonance ring resonators [1].

Figure D.2(b) shows the group delay of the structure $S1$ of Figure D.1 when an increasing number N of ring resonators is tuned to resonance. The structure, with $B = 125 \text{ GHz}$ and $FSR = 500 \text{ GHz}$, exhibits a slowing ratio at resonance of $S(f_0) = 2.5$, in agreement with the theoretical result shown in Figure 6.3 for $t = 0.4$ ($FSR/B = 4$). The unitary delay per additional ring resonator is $\tau_r = 5 \text{ ps}$.

One remarkable advantage of the proposed architecture is that the ring-based slow-light delay-line bandwidth does not change with N .

The shape of the pulses at the output of the structure is shown in Figure D.2(a) for different values of N , when the input pulse (dashed line), with carrier frequency

f_0 , has a 10 ps long Gaussian envelope. Pulse attenuation, increasing with the time delay, is clearly visible; broadening and distortion due to the dispersion are only slightly noticeable.

D.1.2 Analogue Delay

Continuously tunable delay, from 0 to $\tau_{dmax} = 2N/\pi B$, can be achieved by adding a small analogue delay, covering the range from 0 to τ_r , to the discrete delay provided by the S1 structure of Figure D.1. Two different strategies can be followed to obtain this result.

The first approach, shown in the architecture of Figure D.1, exploits a Ring Resonator phase-shifter cascaded to the slow-light structure S1. The delay of the phase-shifter S2 is selected by simply detuning its resonant frequency with respect to the signal carrier frequency. In this way, it is possible to make the optical signal experience any delay between [102]:

$$\tau_{2max} = \frac{1 + r_2}{1 - r_2} \frac{1}{FSR} \quad (D.2)$$

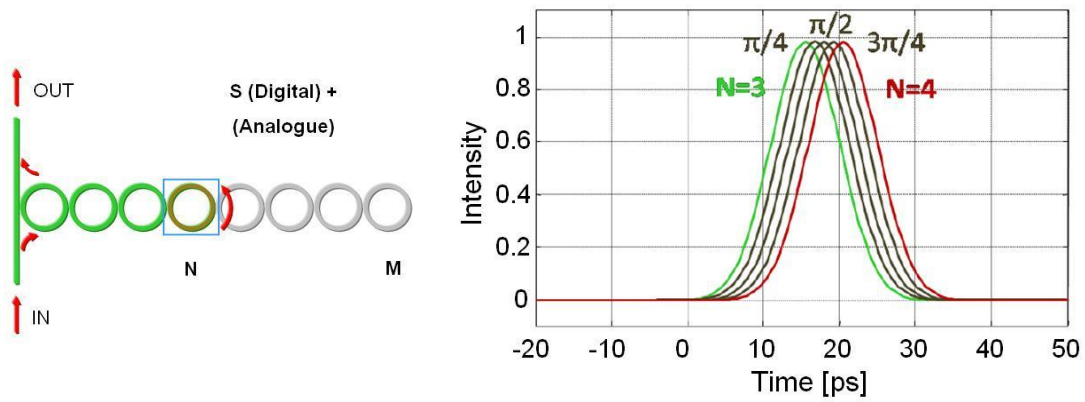
at the phase-shifter resonance and

$$\tau_{2max} = \frac{1 - r_2}{1 + r_2} \frac{1}{FSR} \quad (D.3)$$

at the phase-shifter anti-resonance frequency, where r_2 is the through-port field coupling coefficient of the ring S2. Straightforwardly, the condition to guarantee a continuously variable delay by the combination of the two cascaded structures, S1 and S2 is $\tau_{2max} - \tau_{2max} > \tau_r$.

The second approach requires no additional structures cascaded to the structure S1. In fact, by slightly detuning the resonance of a given number of ring resonators of the structure S1, the delay induced by S1 can be adjusted conveniently. In this way, an arbitrarily small delay variation between 0 and τ_r is achieved.

In most cases the fine tuning can be managed by acting only on the last $N - th$ ring of the chain, as shown in Figure D.3(a). Figure D.3(b) shows the delay experienced by the pulse at the output of S1 in Figure D.1 – when a small frequency detuning



(a) Scheme of the analogue and digital delay integrated in the same chain of rings. (b) Delay experienced by the pulse at the output and correspondent values of the additional round-trip phase shifts.

FIGURE D.3: Fine tuning of the delay by slightly changing the resonance wavelength of the last resonator (number 4 in the Figure) [1].

is induced on the last ($N = 4$) ring, while all the first 3 ring resonators remain resonant at the same frequency.

Although the last ring of the chain does not resonate at the same frequency as all the other $N - 1$ rings, the change in the pulse delay is not accompanied by noticeable distortion. Note that, as the slow-light pass band is 125 GHz , a frequency detuning in excess of 125 GHz is sufficient to completely remove the delay contribution of the forth ring-resonator.

Since the slowing ratio, S , depends strictly on the coupling coefficient t , the time delay could also be varied by means of tunable couplers between ring resonators. However, controlling the delay by tuning rings resonances is more flexible and robust against tolerances and imperfections in the tuning process.

Moreover, if the $N - th$ ring is detuned after the forward transit of the optical pulse, the pulse can be trapped inside the structure and released after an integer number of round trips along $N - M$ resonators, so as to realize an optical memory or buffer. This scheme requires, however, a very fast switching time, at least lower than the round trip time along $N - M$ rings.

D.2 CROW impairments

D.2.1 Dispersion limits

Dispersion is a fundamental issue in slow-light propagation. The group velocity reduction arises from large first order dispersion due to optical resonances within materials or structures.

At the same time, however, there are high-order dispersion terms, that severely distort the optical signals. An optical pulse may propagate through a coupled resonator structure only if its spectrum B_p is narrower than B or, in other words, if its full width at half maximum $T_{FWHM} = 1/B_p$ is larger than the inverse of B . Since the group velocity inside the SLS is strongly frequency dependent pulse propagation is significantly affected by chromatic dispersion.

- β_2 is negative for $f < f_0$ (anomalous dispersion) - and positive for $f > f_0$ (normal dispersion)
- At resonance, $\beta_2 = 0$, while $\beta_3 \neq 0$.

It can be shown [6] that, for small values of the field coupling coefficient t , the number of cavities beyond which the dispersion become evident is:

$$N_{max} \cong 6.7 \left(\frac{B}{B_p} \right)^3 \quad (\text{D.4})$$

In the case of a lossless structure, chromatic dispersion is the main factor limiting the maximum delay $T_{d,max}$ achievable in a slow-light structure [159]. The slow-light structure dispersion scales with both the number of cascaded resonators, i.e. the effective length of the structure, and the ratio B_p/B between the pulse and the structure bandwidth. The maximum delay $T_{d,max}$ sets also the maximum number of storable pulses (i.e. bits) D_{max} inside the device. Since the number of cavities occupied by a single Gaussian pulse is approximately

$$N_{1b} = \pi \frac{B}{B_p} \quad (\text{D.5})$$

Equation D.5 states that the maximum number of bits that can be accommodated in the structure is:

$$D_{max} = 2.1 \left(\frac{B}{B_p} \right)^2 \quad (\text{D.6})$$

Note that all these results are independent of the *FSR* and by the technology of the slow-light structure. Equations D.4, D.5 and D.6 show that the performance of the slow-light structure is severely dispersion limited: for a pulse with $B_p = B$, dispersion-induced distortion already becomes significant for 7 resonators and 2 stored bits. To increase the number of undistorted stored bits, the slow light structure bandwidth B must be increased with respect to the pulse bandwidth B_p .

In other words, for a given number of stored bits, the length of the structure can be shortened by narrowing the bandwidth, but at the price of more pulse distortion.

To minimize the group velocity dispersion close to the edges of the passband, CROWs can be designed by exploiting the techniques for the synthesis of Bessel filters, that maximize the flatness of the group delay response.

Moreover, while dispersion represents the ultimate theoretical limitation, experimental results show that the dominant contribution to pulse distortion, and so the main practical limitation are the losses and disorder effects.

By *disorder* I mean the fabrication tolerances on the coupling coefficients, inaccuracies in the resonance frequencies and roughness-induced backscattering, all of which affect the transfer function of the slow-light structures. These issues are analyzed in the next section.

D.2.2 Limits on propagation losses, disorder and backscattering

The total losses associated with the propagation in a slow-light structure with N resonators and slow down factor S can be expressed as:

$$IL = NS\gamma \quad (\text{D.7})$$

where γ represents the round trip losses inside the cavity. As the light is trapped inside the structure to recirculate several times for each passage, it experiences losses proportional to S . If we consider only the contribution of the propagation losses we obtain:

$$\alpha_{tot} = NS\alpha L_r = \frac{c\alpha}{n_g}\tau_g \quad (\text{D.8})$$

For a defined structure, IL is only dependent on the product $\alpha\tau_g$, where τ_g is the absolute delay introduced.

The value of τ_g constitutes a key parameter in storage applications.

The available bandwidth, and the number of bits stored, are key parameters of coupled resonator structures used for signal processing applications. The losses per bit result from the ratio between the losses per resonator (IL_r) and the number of bits per resonator (i.e. the spectral efficiency η_s):

$$\alpha_{bit} = \frac{L_r}{\eta_s} = \frac{S\alpha L_r}{\eta_s} = \frac{c}{\pi n_g} \frac{\alpha}{B\eta_s} \quad (\text{D.9})$$

If we now compare slow-light structure with the same S and efficiency (η_s), the IL_{bit} values are dependent on the ratio $\alpha/n_g B$

If high index contrast technologies pay one order of magnitude on α , they gain, however, at least a factor 50 in bandwidth and n_g , revealing them to be advantageous for high-bit rate applications (for instance $B = 200 \text{ GHz}$ and $n_g = 4$ for silicon, compared to $B = 10 \text{ GHz}$ and $n_g = 1.5$ for *SiON*).

Unfortunately, in real devices, it is not only propagation losses that affect the transmission, but also several other contributions, first of all, coupling and bending losses, then the round trip loss expression becomes $\gamma = IL_{coup} + \alpha L_r$.

Other sources of losses and back reflection can significantly affect the transfer function and originate from three different causes:

- perfect impedance matching between two generic structures cannot be achieved over an arbitrarily wide bandwidth;

- the so-called *disorder* in the structure, i.e. fabrication tolerances on coupling coefficients, inaccuracies in resonance frequencies and waveguide sidewall roughness, all of which generate backscattering and losses;
- when the pulse bandwidth exceeds the CROW bandwidth, the high frequency components of the signal spectrum do not enter the CROW and are reflected.

These three contributions have different origins; the first one is a theoretical limit, since off-band back reflection depends on the design and the management of the CROW. The disorder is related to the fabrication quality and tuning accuracy: for this reason disorder is the most uncontrollable contribution and therefore the main issue. The dependence of disorder on other slow light structure parameters, especially n_g and S , is therefore a hot topic in this field [5, 160, 161].

The disorder itself can be classified, depending on its origin:

- Coupling disorder: due to a random variation in the coupling coefficient between resonators,
- phase disorder: due to random variation in the optical lengths of the resonators,
- roughness-induced backscatter: random perturbation of the waveguide sidewall and isolated defects.

The first two contributions produce back reflection at the BAR port, introducing losses and significantly affecting the pulse shape in the reflection configuration. Only recently has it been demonstrated that both coupling [161] and phase [162] disorder-induced back reflections are proportional to $(\sigma S)^2$, where σ is the standard deviation of the random disorder. The roughness induced back reflection, instead, creates counter-propagating waves that destroy the directionality of the structure and reflecting the signal to the input port, as already shown in the case of single ring resonators in section 3.6.

D.2.3 Apodisation of the structure

As already highlighted previously in Section 3.6 the apodization can be realized:

- by varying the coupling length L_c of the couplers. However, since in CROWs all resonators must have the same optical length, a variation of L_c requires a consequent variation in the shape of the ring resonator, in order to keep the total length L_r constant – and so, also, the FSR.
- by varying the gap width G between ring resonators. The value of L_c must enable the realization of a large set of K for a defined value of G , but allows an easier design procedures – since all the ring resonators are identical.

The general transfer function of the system is obtained as matrix products of each building block – and the resulting transfer function consists in a polynomial ratio. The coefficients (i.e. the coupling coefficients) can be chosen accordingly to the standard polynomials used, in signal processing, for the design of filters – as described in [144].

The major drawback of this method is related to its poor flexibility, since the coefficients do not take into account the frequency dependent variations.

Another approach [139] based on the synthesis of filters for microwave circuits allows a direct connection between the components of the optical structure and the physical parameters of the filter. This feature has a fundamental importance since it removes the idealised behaviour of the filters – and allows the correction of the optical components for real systems.

The synthesis consists in two different steps:

- 1 First, an equivalent prototype filter, made up from ideal resonators is calculated. This procedure is exact, uses only closed-form formulae – and can be applied to a large number of filter structures and frequency responses.
- 2 Then, each element of the prototype is substituted with suitable optical components.

Once the specifications of the filter in terms of frequency response (i.e bandwidth, maximum reflection in-band, out-of-band attenuation, free spectral range (FSR), and group delay), the order of the filter (that is, the number of resonators) and the type of filter (e.g., Butterworth, Chebyshev, elliptic, Bessel) are chosen, it is possible to design a bandpass filter with connected resonators that are all of the same type – by means of suitable coupling elements called impedance inverters.

A coupled-resonators filter of N ring-resonators is constituted by $N + 1$ impedance inverters, indicated by K_q . An impedance inverter is an ideal quarter-wave transformer. A load impedance Z_L connected at one end is seen as an impedance Z_i that has been inverted with respect to the real coefficient K , as $Z_i = K^2/Z_L$. Each impedance inverter introduces a phase shift of $\pi/2$. The parameters K_q are calculated using the procedure detailed in [142], with the modification introduced in [139] to take into account the different $FSRs$.

An example of apodization is shown in Figure D.4 for $N = 8$ rings and finesse $F = 4$. The beneficial effects of apodization are clearly visible in the intensity transfer function (Figure D.4(a)) for both transmission, where in-band ripples are removed – and, in reflection, where the return loss is dramatically reduced. Moreover, the apodization has a fundamental impact also on the group delay profile, as shown in Figure D.4(b), where sharp ripple is smoothed, producing an almost flat region at the center of the pass-band.

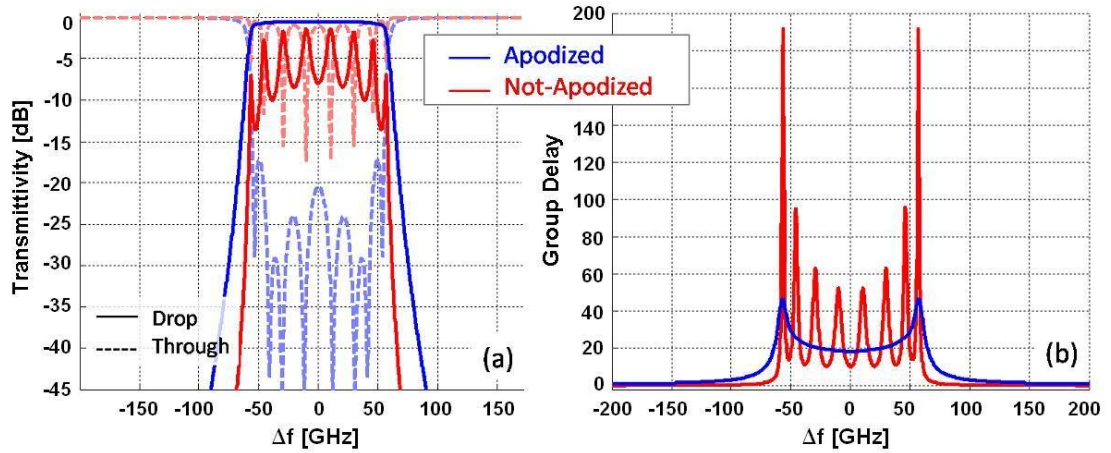


FIGURE D.4: a) Intensity transfer function in the Transmission (drop port: solid lines) and Reflection (through port: dashed lines). b) Group delay of a CROW structure with $N = 8$ rings and finesse $F = 4$ for apodized (blue lines) and non-apodized (red lines) structures.

Table D.1 shows, as an example, the K values and the corresponding gap widths required to realize an apodized structure with 20 Rings.

D.2.4 Back scattering in CROW structures

Experimental analysis of ring resonators has demonstrated that backscattering must be carefully taken into consideration (section 3.6) since it distorts the optical

F		1	2	3	4	5	6	7	8-11	12-20
4	K	0.794	0.327	0.184	0.161	0.153	0.150	0.148	0.146	0.144
	G [nm]	182	250	287	295	298	299	300	301	302
8	K	0.532	0.094	0.049	0.043	0.041	0.040	0.039	0.038	0.038
	G [nm]	215	328	367	376	379	380	381	382	383

TABLE D.1: Apodization of 20 rings coupled ring resonator in Reflection configuration with Finesse values of 4 and 8: the values of the coupling coefficients required and the corresponding values of the gap dimension (G).

device frequency response even for moderate values of Finesse. In applications such as coupled ring resonators, where the group delay $\tau_g = Nn_gL_r/c$ must be maximized, the problem of roughness-induced backscatter is even more a critical issue.

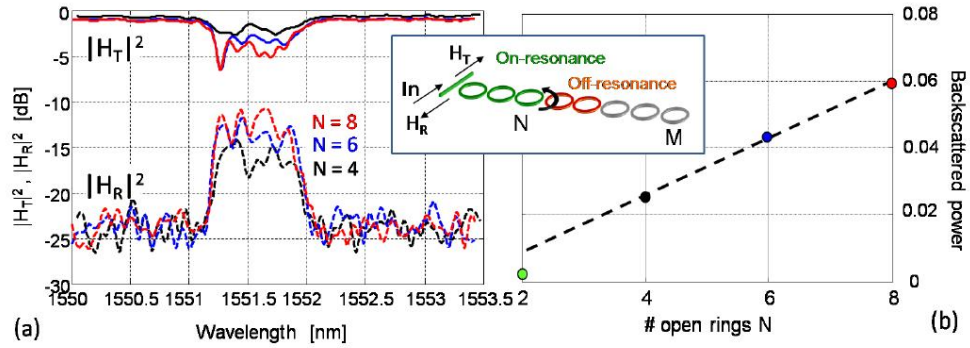


FIGURE D.5: Measured transmission ($|H_T|^2$) and backreflection ($|H_R|^2$) spectra of a reconfigurable coupled optical resonator structure with $N = 4$ (black solid curves), $N = 6$ (blue dotted curves) and $N = 8$ (red dashed curve) on-resonance Ring Resonators. Experimental data are averaged over 16 $FSRs$ (1520 nm - 1580 nm wavelength range). (b) Backscattering of SOI (averaged over 87 GHz bandwidth of the device), versus the number N of coupled Ring Resonators.

The cavity-enhanced backscattering scales up according to the square of the group index n_g . To limit backreflection effects, rather than greatly increasing n_g (and so F and S), it is preferable to increase L_r , even there is a penalty in terms of FSR and the footprint that have to be paid. Figure D.5(a) shows the transmission ($|H_T|^2$) and backreflection ($|H_R|^2$) spectra of a silicon reconfigurable coupled optical resonator structure with $M = 20$ rings, when the number of Ring resonators driven at resonance is $N = 4$ (black solid curves), $N = 6$ (blue dotted curves) and $N = 8$ (red dashed curve). In the inset is provided a sketch of the operational principle. It can be seen that the out-of-band back reflection is almost entirely due to the bus waveguide only and it is independent of N . As shown in Figure D.5(b), the average in-band reflection increases linearly with N , because the power

backscattered by each Ring Resonators is uncorrelated with the backscattering of the other Ring Resonators. The number of N acts exactly in the same way as L_r , with both adding uncorrelated contributions to backscattering, which exhibit a linear dependence on both N and L_r . The back-reflected power level, instead, increases with the square of n_g (and therefore on F and S), since it gives coherent contributions to backscattering. From the point of view of backscattering, therefore, optical delay lines with a greater number of large ring resonators are preferable to coupled structure with high finesse.

Appendix E

System measurements for CROW structures

E.1 Time domain characterization

The potential of delay lines and the characteristics of their spectral response have been presented in the chapter 6. In this appendix, the characterization of these devices in telecommunications systems, carried out from our project partners in Politecnico di Milano, is discussed [26, 141].

A key feature of the present devices is the large operation bandwidth, in addition to amplitude modulation *OOK* at 10 *Gbit/s*, also phase modulation formats and 100 *Gbit/s* encoding are also presented and discussed, showing great potential for optical signal processing – mainly at high bit-rate.

E.1.1 10 Gbit/s OOK transmission

The device under consideration consists of a chain of $M = 20$ ring resonators with a designed finesse of $F = 4$.

A 100 *ps* long Gaussian probe pulses, generated by means of 10 *Gbit/s* intensity modulation in non-return to-zero (*OOK – NRZ*) format were applied as input to the delay line – and the time delay and the distortion of the injected pulses were evaluated at the output of the sample using an oscilloscope – for several different values of delay (i.e. different number of tuned ring-resonators).

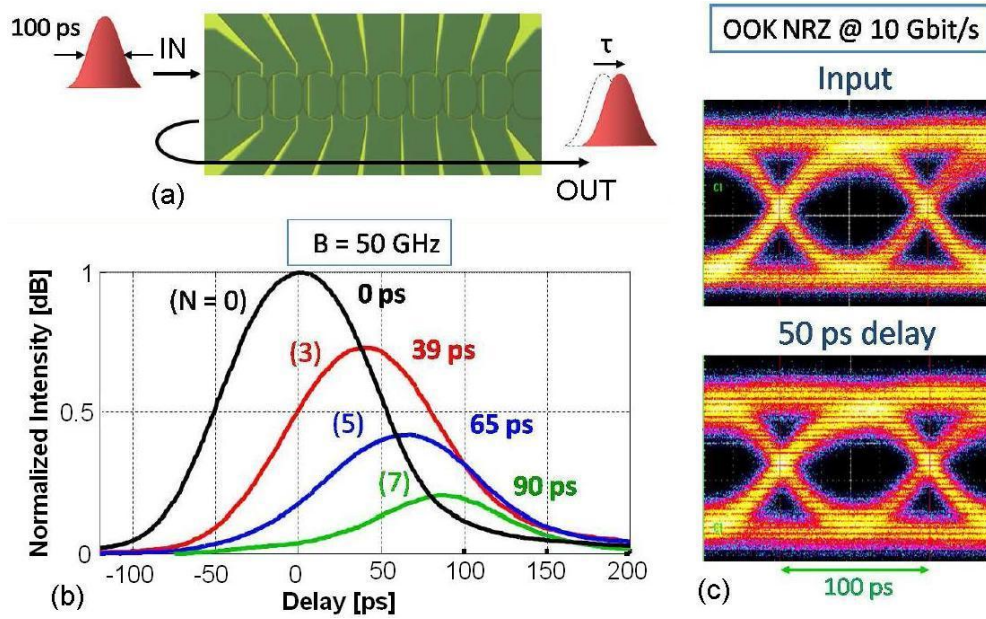


FIGURE E.1: Time-domain measurements at 10 *Gbits/s* of the tunable delay of a Slow Wave Delay line with bandwidth $B = 50 \text{ GHz}$. (a) 100-ps-long Gaussian probe pulses with carrier λ_r are employed. (b) Reference trace (black) corresponding to propagation in the bus waveguide only ($N = 0$); delay of 39 *ps* (red) 69 *ps* (blue) and 90 *ps* (green) with negligible pulse distortion are obtained when 3, 5 and 7 Ring Resonators are tuned at resonance, respectively. (c) Experimental eye diagram for 10 *Gbits/s* NRZ transmission: input optical signal (upper image) and output optical signal delayed by 50 *ps* (lower image)

A sketch of the measurement principle is shown in Figure E.1(a) and the experimental time traces are shown in E.1(b). When all the rings were off-resonance ($N = 0$, black trace), the signal propagated along the bus waveguide without entering into the delay line: the resulting delay is the reference minimum due to the propagation in the waveguide alone. Increasing the number of tuned ring resonators, for $N = 3, 5$, and 7 rings, a delay of 39 *ps* (red trace) 69 *ps* (blue trace) and 90 *ps* (green trace), respectively, were introduced.

The measured device bandwidth was 50 *GHz*, with a fairly flat response. This was a combination that was able to accommodate the 10 *GHz* signal spectrum entirely. Figure E.1(c) shows the eye diagrams for the 10 *Gbits/s* OOK – NRZ optical signal, observed at the input port of the device (top image) and at the output port, when a 50 *ps* delay is introduced by the slow-light delay-line (bottom image).

The Intersymbolic Interference (*ISI*) is negligible since there is not any significant distortions in the eye shape and aperture. Every Ring Resonator provides a unitary delay of $\tau_r = 12.7 \text{ ps}$ and therefore a storage efficiency of $\eta_s = \tau_r/\tau_b = 0.13 \text{ bit/RR}$,

where τ_b , is the pulse width (i.e. 100 ps). The absolute losses were $IL_{abs} = 70$ dB/ns and the fractional losses $IL_{frac} = 7$ dB/bit, far from the theoretical limit $min(IL_{frac}) = \alpha c/B_b/n_g = 1.4$ dB/bit, determined by the waveguide losses α (where n_g is the waveguide group index, c is the speed of the light in the vacuum and $B_b = 1/\tau_b$ is the Bandwidth of the signal).

This performances appears to be fairly poor when compared to devices based on low-loss glasses [163]. The behavior observed is attributable to the large pulse width τ_b compared with the unitary delay τ_r , (i.e. the small bandwidth of the signal B_b in comparison with the device bandwidth B). By increasing the value of B_b (i.e. increasing the bit-rate), the unitary delay per ring τ_r and absolute losses ($IL_{abs} = 70$ dB/ns) remains unchanged, but the storage efficiency η_s and fractional losses IL_{frac} increase – because a lower absolute delay is required to store the same number of bits. This suggests that SOI Slow light delay-lines become competitive and gives more useful performances at high bit-rates. If we indeed suppose a 50 Gbit/s modulation rate, the same device provides $\eta_d = 0.65$ bit/RR and $IL_{abs} = 1.4$ dB/bit: so a 1 Byte delay can be obtained with only 13 Ring Resonators, with a penalty of 11 dB.

E.1.2 Phase modulation formats

The large device bandwidth does not introduce any distortion to the optical signal. In this situation the phase information in the signal is preserved and this behaviour makes the structure compatible with phase modulation formats [164, 165]. To verify this feature, a Differential Phase Shift Keying (DPSK) signal was generated by phase modulating a distributed feedback (DFB) laser using a commercially available phase modulator at a bit rate of 10 Gbit/s and applied as input to the device.

After propagation through the tunable delay lines, the signal was detected using an integrated MachZehnder interferometer realized in high index contrast silicon oxynitride technology [166] by project partners in Milan. A schematic of the system used for measurement is shown in Figure E.2(a). The eye diagrams of the input DPSK signal and the signal received at the output are shown in Figure E.2(b).

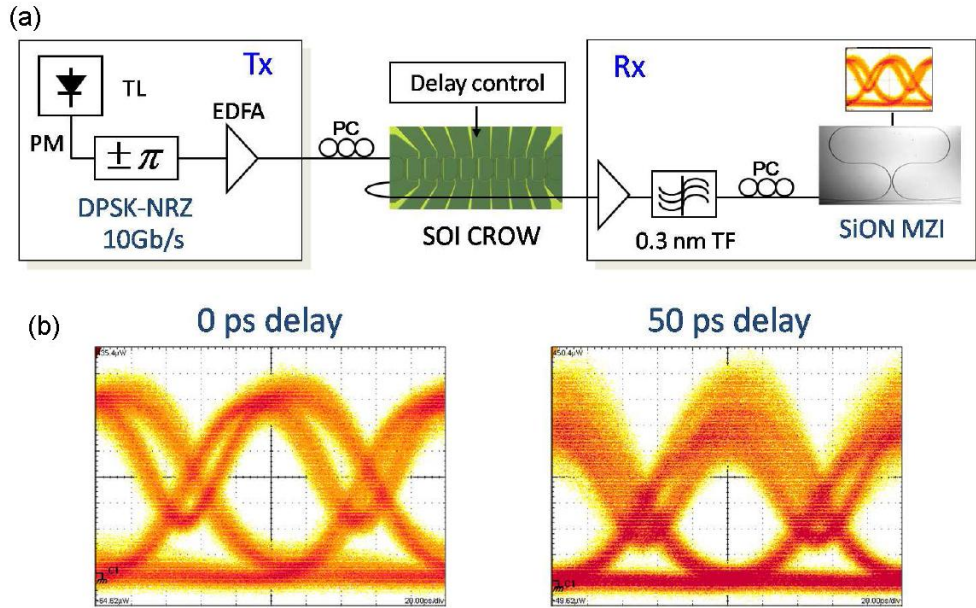


FIGURE E.2: Transmission of 10 *Gbits/s* DPSK - NRZ data stream through a reconfigurable Slow Wave Delay line with bandwidth $B = 50$ *GHz*: (a) setup scheme; (b) eye diagrams of the input DPSK signal (left side) and of the DPSK signal transmitted through the device with a delay of 50 *ps* (right side).

Analyzing these eye diagrams of the data pulses can be extracted that after the propagation through the device, it is observed that the eye is still open and well-preserved, suggesting a low level of inter-symbolic interference (ISI), and small signal distortion – being attributable to the moderate amount of ripples present in the in-band group delay response of the CROW.

The results of this experiment clearly show that the CROW structure does not significantly affect the phase information encoded in a wide-band optical signal.

E.1.3 1 Byte delay at 100 Gbit/s OOK

A 10 *ps* long Gaussian probe pulses, corresponding to a 100 *Gbit/s* OOK NRZ modulation, were generated and transmitted through a delay line having bandwidth $B = 87$ *GHz*, $F = 5.17$ and $M = 20$. A schematic of the measurement principle is shown in Figure E.3(a), while Figure E.3(b) shows the experimental time traces.

The $N = 0$ (black trace) is the minimum reference delay. By increasing the numbers of rings tuned to resonance, for $N = 4$, 8, and 12 rings, a delay of 29 *ps* (red trace) 59 *ps* (green trace) and 88 *ps* (blue trace), respectively, were

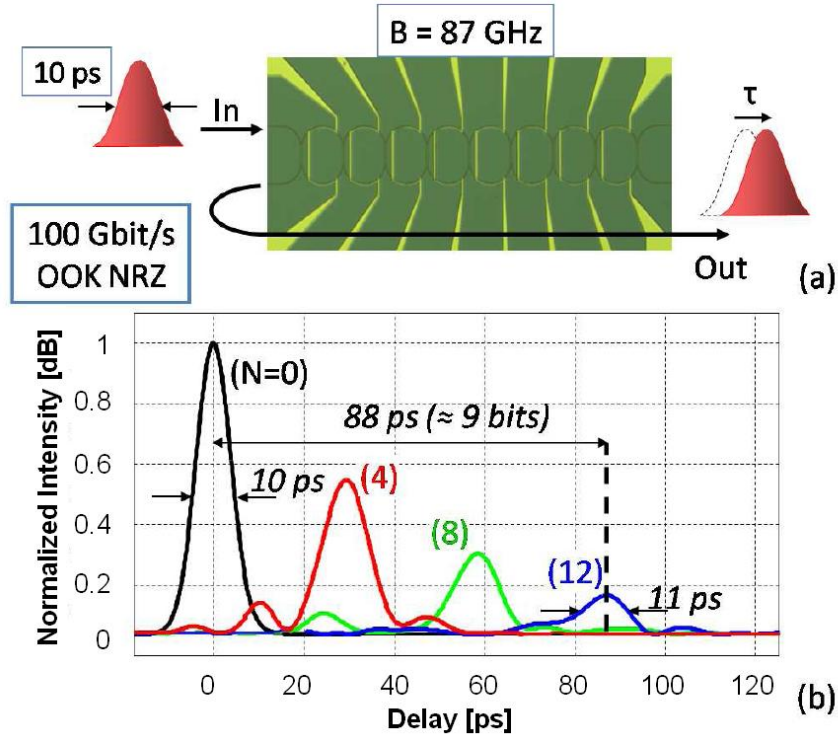


FIGURE E.3: Schematic of the time-domain characterization principle, exploiting 10 ps long Gaussian probe pulses, equivalent to 100 Gbit/s OOK-NRZ transmission; b) measured optical pulses at the output port of SOI Delay Line with bandwidth $B = 87 \text{ GHz}$, $F = 5.17$ and $M = 20$: delay and attenuation is observed when 0 (black), 4 (red), 8 (green) and 12 (blue) Ring Resonators are tuned at resonance; only a slight broadening and distortion of the pulse is noticeable for highest delay.

introduced. It is appropriate to highlight how, for $N = 12$, more than 1 Byte delay is provided. A small broadening of about 1 ps, due to chromatic dispersion, and a slight distortion of the tail of the pulse, due to third order dispersion, becomes noticeable only for the largest delay, providing clear evidence that the fairly flatness of pass-band is able to accommodate the 100 GHz signal spectrum with negligible pulse distortion [6, 165].

The main features and performances of the structure are:

- Large bandwidth ($B = 87 \text{ GHz}$), finesse $F = 5.17$ and so slow down factor $S = 3.3$;
- unitary delay $\tau_r = 7.3 \text{ ps/RR}$, as expected from theory ($\tau_r = 2/\pi B$) and confirming frequency domain measurements;
- maximum delay achievable, for $N = 20$, is $\tau = N\tau_r = 147 \text{ ps}$;

- storage efficiency for 100 *Gbit/s* transmission is $\eta_s = \tau_r/\tau_b = 0.73 \text{ bit}/RR$;
- measured absolute losses are $IL_{abs} = 85 \text{ dB}/ns$;
- fractional losses are only $IL_{frac} = 0.85 \text{ dB}/bit$;
- footprint is only $56 \times 40 \mu m^2$ for each ring resonator.

E.2 Comparison with the-State-of-Art

The main results obtained can be summarized as:

- A simple and flexible scheme to realize fully reconfigurable integrated optical delay lines, based on slow-wave propagation in coupled ring resonators, has been successfully realized in SOI technology.
- The first experimental demonstration of continuously-tunable delay in silicon photonics has been provided by independently control the resonance of each Ring Resonator using the thermo-optic effect.
- A continuously variable absolute delay up to 146 *ps* can be achieved by tuning 20 Ring Resonators, over the very large bandwidth of about 90 *GHz* – and with a very small footprint of $56 \times 800 \mu m^2$, paying an absolute loss penalty of $IL_{abs} = 85 \text{ dB}/ns$.
- System characterization demonstrated error free transmission (10^{-9}) up to 100 *Gbit/s* and compatibility with advanced modulation formats.
- At 100 *Gbit/s* transmission rate, a variable delay of up to 1 Byte was demonstrated with 11 Ring Resonators, providing a storage efficiency of $\eta = 0.73 \text{ bit}/RR$ and fractional losses of only $IL_{frac} = 0.85 \text{ dB}/bit$.

The figures of merit of the devices described in this work can be compared with the state-of-the-art for integrated optical buffers [1], summarized in Table E.1.

To date, the most interesting result on ring based delay lines, realized on Silicon-on-Insulator platform, is constituted by the one realized by workers at IBM T.J. Watson Research Center [31]. This consists of 56 ring resonators in APF configuration coupled to a common bus waveguide. The small foot-print obtained

Device	IBM [31]	PoliMi [163]	This work
Technology	SOI APF	SiON CROW	SOI CROW
N	56	8	11
Footprint [mm^2]	0.09	7	0.025
B [GHz]	50	6.25	90
Delay [ps]	510	800	80
Error Free [$Gbit/s$]	10	5	100
N_b [bit]	5^\diamond	8^\diamond	8^\perp
IL_{frac} [dB/bit]	4.4^\diamond	1^\diamond	0.85^\perp
η [bit/RR]	0.09^\diamond	$> 1^\diamond$	0.73^\perp
Tunability	NO	easy	<i>efficient</i>

$^\diamond$ for 10 Gbit/s transmission

$^\perp$ for 100 Gbit/s transmission

TABLE E.1: Figures of merit for the state-of-the-art integrated ring resonators delay lines.

was achieved by using a ring radius as small as $R = 6.5 \mu m$ and the waveguides having a $510 \times 226 nm^2$ cross-sectional dimensions with propagation losses of $\alpha = 1.7 \pm 0.1 dB/cm$. Compared the structures realized, these delay lines exhibits a larger FSR of $1375 GHz$ ($11 nm$) and a bandwidth of $50 GHz$ ($0.4 nm$). A higher absolute delay of $510 \pm 10 ps$ was therefore observed at the center of the bandwidth, where attenuation was $22 dB$.

Despite the large bandwidth, the system performances of the device was poor even for moderate bit-rates. Error free propagation is indeed guaranteed only up to $5 Gbit/s$, while at $10 Gbit/s$ transmission rate, the fractional delay is only $N_b = 5 bits$, the fractional losses are $IL_{frac} = 4.4 dB/bit$ and the storage efficiency is very low: $\eta_s = 0.09 bit/RR$).

Apart from the absolute delay, the performances discussed remains lower than in the present work, due to the intrinsic disadvantages of APF chains.

Moreover, reconfiguration of the has structure has not been provided, precluding any possibilities of dynamically change the induced delay – and moreover a thermo-optical control would be more difficult to realise and more inefficient in APF configuration.

A configuration to realize an all optical switch on SOI devices has been proposed recently by the same group [158], but over CROW structures using a femtosecond laser source operating at $850 nm$ to illuminate the surface of the structure using a fibre orientated at the right angle with respect to the surface of the chip. The very high optical power required (> 350), the out-of-plane illumination and the

reduced selectivity of the control constitute the main disadvantages that make this solution of limited interest for our purpose.

The devices presented in the present work are therefore the state of the art in SOI delay lines, providing the best figures of merit and the first demonstration of continuously tunable delay.

Since suitable reconfigurable integrated optical buffers are not yet reported in high index contrast technology, comparison may be made between our results and SiON reconfigurable delay lines realized at Politecnico di Milano [163], formed by 8 Ring Resonators in CROW configuration. The reduced index contrast for this platform implies the need for ring radius of $570 \mu m$ – so bigger footprint and a lower FSR ($50 GHz$). An interesting value for the propagation losses of only $\alpha = 0.35 dB/cm$ has been measured. This device provides the largest absolute delay ($800 ps$), but a significant comparison needs to be carried out that takes account of the performance at the maximum bit-rate allowed by the available bandwidth.

SiON buffer at $10 Gbit/s$ and SOI buffer of this work at $100 Gbit/s$, achieve the same fractional delay of 1 Byte, enabling error-free operation, with comparable figures in terms of storage efficiency and fractional losses. However the foot-print area is about 280 times bigger in comparison with silicon on insulator devices. We can conclude that, while silica-on-silicon based devices may have the best performances at low bit-rate, they can not provide bandwidth higher than 20 – 40 GHz. Moreover, comparing the two structures in terms of the thermo-optical control, SOI structures have been shown to have higher efficiency, faster response and lower cross-talk with respect to their counterparts in SiON.

Finally, we remark also that, although dispersion has often been addressed as the main theoretical limitation for this kind of devices, the results obtained suggest that, in a reflective CROW, the losses constitute the main limiting factor that has to be addressed in order to improve their performance [1].

Bibliography

- [1] A. Canciamilla. *Slow light structures for optical signal processing*. 2010.
- [2] K. Okamoto. *Fundamentals of Optical Waveguides*. Academic Press, 2006.
- [3] N. Shaw and W.J. Stewart and J. Heaton and D.R. Wight. Optical slow-wave resonant modulation in electro-optic gaas/algaas modulators. *Electronics Letters*, 35(18):1557–1558, 1999.
- [4] F. Morichetti A. Melloni and M. Martinelli. Optical slow wave structures. *Optics Photonics News*, 14:44–48, 2003.
- [5] T. F. Krauss. Why do we need slow light? *Nature Photonics*, (2):448–450, 2008.
- [6] M. Martinelli A. Melloni, F. Morichetti. Linear and nonlinear pulse propagation in coupled resonator slow-wave optical structures. *Journal of Optical and Quantum Electronics*, 35(4):365–379, 2003.
- [7] Z. Dutton C. H. Behroozi L. Vestergaard Hau, S. E. Harris. Light speed reduction to 17 metres per second in an ultracold atomic gas. *Nature*, 397: 594–598, 1999.
- [8] M. D. Lukin M. Bajcsy, A. S. Zibrov. Stationary pulses of light in an atomic medium. *Nature*, 426:638–641, Dec 2003.
- [9] Ryan M. Camacho, Michael V. Pack, John C. Howell, Aaron Schweinsberg, and Robert W. Boyd. Wide-bandwidth, tunable, multiple-pulse-width optical delays using slow light in cesium vapor. *Phys. Rev. Lett.*, 98(15):153601, Apr 2007.
- [10] Kijoon Lee and Nabil M. Lawandy. Optically induced pulse delay in a solid-state raman amplifier. *Applied Physics Letters*, 78(6):703–705, 2001.

-
- [11] Yoshitomo Okawachi, Matthew S. Bigelow, Jay E. Sharping, Zhaoming Zhu, Aaron Schweinsberg, Daniel J. Gauthier, Robert W. Boyd, and Alexander L. Gaeta. Tunable all-optical delays via brillouin slow light in an optical fiber. *Phys. Rev. Lett.*, 94(15):153902, Apr 2005.
- [12] Michael D. Stenner, Mark A. Neifeld, Zhaoming Zhu, Andrew M.C. Dawes, and Daniel J. Gauthier. Distortion management in slow-light pulse delay. *Opt. Express*, 13(25):9995–10002, 2005.
- [13] Jay Sharping, Yoshitomo Okawachi, and Alexander Gaeta. Wide bandwidth slow light using a raman fiber amplifier. *Opt. Express*, 13(16):6092–6098, 2005.
- [14] Yoshitomo Okawachi, Mark Foster, Jay Sharping, Alexander Gaeta, Qianfan Xu, and Michal Lipson. All-optical slow-light on a photonic chip. *Opt. Express*, 14(6):2317–2322, 2006.
- [15] Jay Sharping, Yoshitomo Okawachi, James van Howe, Chris Xu, Yan Wang, Alan Willner, and Alexander Gaeta. All-optical, wavelength and bandwidth preserving, pulse delay based on parametric wavelength conversion and dispersion. *Opt. Express*, 13(20):7872–7877, 2005.
- [16] Yoshitomo Okawachi, Jay E. Sharping, Chris Xu, and Alexander L. Gaeta. Large tunable optical delays via self-phase modulation and dispersion. *Opt. Express*, 14(25):12022–12027, 2006.
- [17] Y. Wang, C. Yu, L. Yan, A.E. Willner, R. Roussev, C. Langrock, and M.M. Fejer. Continuously-tunable dispersionless 44-ns all optical delay element using a two-pump ppln, dcf, and a dispersion compensator. *IEE Conference Publications*, 2005(CP502):v4–793–v4–793, 2005.
- [18] Mohammad Soltani, Siva Yegnanarayanan, and Ali Adibi. Ultra-high q planar silicon microdisk resonators for chip-scale silicon photonics. *Opt. Express*, 15(8):4694–4704, 2007.
- [19] Jin Yao, D. Leuenberger, M.-C.M. Lee, and M.C. Wu. Silicon microtoroidal resonators with integrated mems tunable optical coupler. pages 17–18, Aug. 2006.
- [20] M. Ghulinyan, M. Galli, C. Toninelli, J. Bertolotti, S. Gottardo, F. Marabelli, D. S. Wiersma, L. Pavesi, and L. C. Andreani. Wide-band transmission

- of nondistorted slow waves in one-dimensional optical superlattices. *Applied Physics Letters*, 88(24):241103–241103–3, jun 2006.
- [21] J. Cp J. Petreck P. Bienstman G. Priem B. Maes M. Lauritano G. Bellanca F. Morichetti, A. Melloni. Self-phase modulation in slow-wave structures: A comparative numerical analysis. *Journal of Optical and Quantum Electronics*, 38(9):761–780, 2006.
- [22] P. Velha, E. Picard, T. Charvolin, E. Hadji, J.C. Rodier, P. Lalanne, and D. Peyrade. Ultra-high q/v fabry-perot microcavity on soi substrate. *Opt. Express*, 15(24):16090–16096, 2007.
- [23] Antonio Samarelli, Ahmad R. Md Zain, Marco Gnan, Harold Chong, Marc Sorel, Richard M. De La Rue, Paola Frascella, Caterina Ciminelli, and Mario N. Armenise. Single row soi-based photonic crystal/photonic wire micro-cavities with medium q-factor and high transmission. In *Integrated Photonics and Nanophotonics Research and Applications*, page IWD5. Optical Society of America, 2007.
- [24] A.R.M. Zain, N.P. Johnson, M. Sorel, and R.M. De La Rue. Coupling strength control in photonic crystal/photonic wire multiple cavity devices. *Electronics Letters*, 45(5):283–284, february 2009.
- [25] Amnon Yariv, Yong Xu, Reginald K. Lee, and Axel Scherer. Coupled-resonator optical waveguide: a proposal and analysis. *Opt. Lett.*, 24(11):711–713, 1999.
- [26] Francesco Morichetti, Carlo Ferrari, Antonio Canciamilla, Matteo Torregiani, Andrea Melloni, Antonio Samarelli, Richard De La Rue, and Marc Sorel. Processing light in coupled ring resonators. In *Integrated Photonics and Nanophotonics Research and Applications*, page JMA2. Optical Society of America, 2009.
- [27] H. F. Hamann A. Yurii, M O’Boyle and S. J. McNab. Active control of slow light on a chip with photonic crystal waveguides. *Nature*, 438(2):65–69, November 2005.
- [28] E. Kuramochi M. Notomi and T. Tanabe. Large-scale arrays of ultrahigh-q coupled nanocavities. *Nature Photonics*, (2):741–747, 2008.

- [29] B.E. Little, S.T. Chu, P.P. Absil, J.V. Hryniewicz, F.G. Johnson, F. Seiferth, D. Gill, V. Van, O. King, and M. Trakalo. Very high-order microring resonator filters for wdm applications. *Photonics Technology Letters, IEEE*, 16(10):2263–2265, oct. 2004.
- [30] Joyce K. Poon, Lin Zhu, Guy A. DeRose, and Amnon Yariv. Transmission and group delay of microring coupled-resonator optical waveguides. *Opt. Lett.*, 31(4):456–458, 2006.
- [31] Fengnian Xia, Lidija Sekaric, and Yurii Vlasov. Ultracompact optical buffers on a silicon chip. *Nature Photonics*, 1(1):65–71, December 2006.
- [32] C. Ferrari F. Morichetti L. OFaolain T. F. Krauss R. De La Rue A. Samarelli M. Sorel A. Melloni, A. Canciamilla. Tunable delay lines in silicon photonics: Coupled resonators and photonic crystals, a comparison. *IEEE Photonics Journal (invited)*, Volume 2(Number 2):181–194, April 2010.
- [33] L Pavesi. Will silicon be the photonic material of the third millenium? *Journal of Physics: Condensed Matter*, 15(26):R1169.
- [34] J. D. Meindl, J. A. Davis, P. Zarkesh-Ha, C. S. Patel, K. P. Martin, and P. A. Kohl. Interconnect opportunities for gigascale integration. *IBM Journal of Research and Development*, 46(2.3):245–263, march 2002.
- [35] Bahram Jalali, Sasan Fathpour, and Kevin Tsia. Green silicon photonics. *Opt. Photon. News*, 20(6):18–23, 2009.
- [36] Worlds first 2-billion transistor microprocessor. URL <http://www.intel.com/technology/architecturesilicon/2billion.htm>.
- [37] Assia Barkai, Yoel Chetrit, Oded Cohen, Rami Cohen, Nomi Elek, Eyal Ginsburg, Stas Litski, Albert Michaeli, Omri Raday, Doron Rubin, Gadi Sarid, Nahum Izhaky, Mike Morse, Olufemi Dosunmu, Ansheng Liu, Ling Liao, Haisheng Rong, Ying hao Kuo, Shengbo Xu, Drew Alduino, Jeffrey Tseng, Hai-Feng Liu, and Mario Paniccia. Integrated silicon photonics for optical networks. *J. Opt. Netw.*, 6(1):25–47, 2007.
- [38] L. C. Kimerling. Photons to the rescue: Microelectronic becomes microphotonics. *The Electrochemical Society Interface*, 9(2):28–31, 2000.

- [39] A. Melloni, R. Costa, G. Cusmai, F. Morichetti, and M. Martinelli. Waveguide index contrast: implications for passive integrated optical components. In *Fibres and Optical Passive Components, 2005. Proceedings of 2005 IEEE/LEOS Workshop on*, pages 246 – 253, 22-24 2005.
- [40] Haiyan Ou. Different index contrast silica-on-silicon waveguides by pecvd. *Electronics Letters*, 39(2):212 – 213, 23 2003.
- [41] Andrea Melloni, Raffaella Costa, Paolo Monguzzi, and Mario Martinelli. Ring-resonator filters in silicon oxynitride technology for dense wavelength-division multiplexing systems. *Opt. Lett.*, 28(17):1567–1569, 2003.
- [42] Shiang-Ping Cheng Yuan-Kuang Tu, Jung-Chuan Chou. Single-mode sion/sio₂/si optical waveguides prepared by plasma-enhanced chemical vapor deposition. *Journal of Fiber and Integrated Optics*, Volume 14(Number 2):133, April 1995.
- [43] H. Wong, B.L. Yang, and Y.C. Cheng.
- [44] W. Stutius and W. Streifer. Silicon nitride films on silicon for optical waveguides. *Appl. Opt.*, 16(12):3218–3222, 1977.
- [45] Tzyy-Jiann Wang, Yen-Hao Huang, and Hsuen-Li Chen. Resonant-wavelength tuning of microring filters by oxygen plasma treatment. *Photonics Technology Letters, IEEE*, 17(3):582 –584, march 2005.
- [46] Michael J. Shaw, Junpeng Guo, Gregory A. Vawter, Scott Habermehl, and Charles T. Sullivan. Fabrication techniques for low-loss silicon nitride waveguides. volume 5720, pages 109–118. SPIE, 2005.
- [47] Nicola Daldosso, Mirko Melchiorri, Francesco Riboli, Manuel Girardini, Georg Pucker, Michele Crivellari, Pierluigi Bellutti, Alberto Lui, and Lorenzo Pavesi. Comparison among various si₃n₄ waveguide geometries grown within a cmos fabrication pilot line. *J. Lightwave Technol.*, 22(7): 1734, 2004.
- [48] K. Tsuzuki, Y. Shibata, N. Kikuchi, M. Ishikawa, T. Yasui, H. Ishii, and H. Yasaka. Full c-band tunable dfb laser array copackaged with inp mach x2013;zehnder modulator for dwdm optical communication systems. *Selected Topics in Quantum Electronics, IEEE Journal of*, 15(3):521 –527, may-june 2009.

- [49] Andreas Beling and Joe C. Campbell. Inp-based high-speed photodetectors. *J. Lightwave Technol.*, 27(3):343–355, 2009.
- [50] Michal Lipson. Guiding, modulating, and emitting light on silicon-challenges and opportunities. *J. Lightwave Technol.*, 23(12):4222, 2005.
- [51] Bahram Jalali and Sasan Fathpour. Silicon photonics. *J. Lightwave Technol.*, 24(12):4600–4615, 2006.
- [52] Photonics research group mission, . URL <http://photonics.intec.ugent.be>.
- [53] R. Soref and J. Lorenzo. All-silicon active and passive guided-wave components for $\lambda = 1.3$ and 1.6 microns. *Quantum Electronics, IEEE Journal of*, 22(6):873 – 879, jun 1986.
- [54] Toshifumi Watanabe Jun-Ichi Takahashi Hiroshi Fukuda Mitsutoshi Takahashi Tetsufumi Shoji Shingo Uchiyama Emi Tamechika Sei-Ichi Itabashi Hirofumi Morita Koji Yamada, Tai Tsuchizawa. Silicon wire waveguiding system: Fundamental characteristics and applications. *Electronics and Communications in Japan (Part II: Electronics)*, 89(3):42–55, 2006.
- [55] Yurii Vlasov and Sharee McNab. Losses in single-mode silicon-on-insulator strip waveguides and bends. *Opt. Express*, 12(8):1622–1631, 2004.
- [56] C. G. Poulton, C. Koos, M. Fujii, A. Pfrang, T. Schimmel, J. Leuthold, and W. Freude. Radiation modes and roughness loss in high index-contrast waveguides. *Selected Topics in Quantum Electronics, IEEE Journal of*, 12(6):1306 –1321, nov.-dec. 2006.
- [57] M. Gnan, S. Thorns, D.S. Macintyre, R.M. De La Rue, and M. Sorel. Fabrication of low-loss photonic wires in silicon-on-insulator using hydrogen silsesquioxane electron-beam resist. *Electronics Letters*, 44(2):115 –116, january 2008.
- [58] Jaime Cardenas, Carl B. Poitras, Jacob T. Robinson, Kyle Preston, Long Chen, and Michal Lipson. Low loss etchless silicon photonic waveguides. *Opt. Express*, 17(6):4752–4757, 2009.
- [59] Vilson R. Almeida, Roberto R. Panepucci, and Michal Lipson. Nanotaper for compact mode conversion. *Opt. Lett.*, 28(15):1302–1304, 2003.

- [60] D. Taillaert, W. Bogaerts, P. Bienstman, T.F. Krauss, P. Van Daele, I. Moerman, S. Verstuyft, K. De Mesel, and R. Baets. An out-of-plane grating coupler for efficient butt-coupling between compact planar waveguides and single-mode fibers. *Quantum Electronics, IEEE Journal of*, 38(7):949–955, jul 2002.
- [61] Silicon photonics. URL <http://techresearch.intel.com/articles/Tera-Scale/1419.htm>.
- [62] Silicon integrated photonics. URL <http://www.research.ibm.com/index.shtml>.
- [63] Soitec. URL <http://www.soitec.com>.
- [64] M. Bruel, B. Aspar, and A.J. Auberton-Hervé. Smart-cut: A new silicon on insulator material technology based on hydrogen implantation and wafer bonding. *Japanese Journal of Applied Physics*, 36(Part 1, No. 3B):pp 1636–1641, 1997.
- [65] Mechanics of smart-cut technology. *International Journal of Solids and Structures*, 41(16-17):4299 – 4320, 2004. ISSN 0020-7683.
- [66] W. R. Thurber, R. L. Mattis, Y. M. Liu, and J. J. Filliben. Resistivity-dopant density relationship for phosphorus-doped silicon. *Journal of The Electrochemical Society*, 127(8):1807–1812, 1980.
- [67] Lithography resolution imec. URL http://www2.imec.be/be_en/research/scaling-driven-nanoelectronics/lithography.html.
- [68] L. O’Faolain, M. V. Kotlyar, N. Tripathi, R. Wilson, and T. F. Krauss. Fabrication of photonic crystals using a spin-coated hydrogen silsesquioxane hard mask. *Journal of Vacuum Science & Technology B: Microelectronics and Nanometer Structures*, 24(1):336–339, 2006.
- [69] H. Namatsu, T. Yamaguchi, M. Nagase, K. Yamazaki, and K. Kurihara. Nano-patterning of a hydrogen silsesquioxane resist with reduced linewidth fluctuations. *Microelectron. Eng.*, 41-42:331–334, 1998.
- [70] Falco C. M. J. M. van Delft. Delay-time and aging effects on contrast and sensitivity of hydrogen silsesquioxane. *Papers from the 46th International Conference on Electron, Ion, and Photon Beam Technology and Nanofabrication*, 20(6):2932–2936, 2002.

- [71] W. Henschel, Y. M. Georgiev, and H. Kurz. Study of a high contrast process for hydrogen silsesquioxane as a negative tone electron beam resist. *Journal of Vacuum : Microelectronics and Nanometer Structures*, 21(5):2018–2025, 2003.
- [72] Hideo Namatsu, Yasuo Takahashi, Kenji Yamazaki, Toru Yamaguchi, Masao Nagase, and Kenji Kurihara. Three-dimensional siloxane resist for the formation of nanopatterns with minimum linewidth fluctuations. *Journal of Vacuum Science & Technology B: Microelectronics and Nanometer Structures*, 16(1):69–76, 1998.
- [73] Y.M. Georgiev, W. Henschel, A. Fuchs, and H. Kurz. Surface roughness of hydrogen silsesquioxane as a negative tone electron beam resist. *Vacuum Science & Technology B*, 77(2):117 – 123, 2005.
- [74] M. Sugawara. *Plasma Etching: Fundamentals and Applications*. Oxford Science Publications, 1998.
- [75] Z. Cui. *Nanofabrication: Principles, Capabilities and Limits*. Springer, 2008.
- [76] Oxford plasma instrument. URL <http://www.oxford-instruments.com/products/Pages/products.aspx>.
- [77] Sts, surface technology systems. URL <http://www.stsystems.com>.
- [78] R. F. Figueroa, S. Spiesshoefer, S. L. Burkett, and L. Schaper. Control of sidewall slope in silicon vias using sf_6/o_2 plasma etching in a conventional reactive ion etching tool. volume 23, pages 2226–2231. AVS, 2005.
- [79] R Legtenberg H Jansen, M de Boer and M Elwenspoek. The black silicon method: a universal method for determining the parameter setting of a fluorine-based reactive ion etcher in deep silicon trench etching with profile control. *Journal of Micromechanics and Microengineering*, 5(2):115–120, dec. 1995.
- [80] Oxford instruments, surface technology systems, . URL <http://www.oxinst.com/products/etching-deposition-growth/processes-techniques/plasma-deposition/pecvd/Pages/pecvd.aspx>.
- [81] Plassys meb 400 s e-beam evaporator jwnc. URL <http://www.jwnc.gla.ac.uk/facility-metallisation.htm>.

- [82] S. Thoms and D. S. MacIntyre. Electron beam lithography course. URL <http://www.elec.gla.ac.uk/jwnc/index.php>.
- [83] Qianfan Xu, Vilson R. Almeida, Roberto R. Panepucci, and Michal Lipson. Experimental demonstration of guiding and confining light in nanometer-size low-refractive-index material. *Opt. Lett.*, 29(14):1626–1628, 2004.
- [84] Yuan X. McIntyre D. Thoms-S. Chong H. De La Rue R.M. Krauss T.F. Ofaolain, L. Low-loss propagation in photonic crystal waveguides. *Electronics Letters*, 42(25):1454–1455, 7 2006.
- [85] Fmm, film mode matching, . URL http://www.photond.com/products/fimmwave/fimmwave_features_21.htm.
- [86] W. Hellmich and P.P. Deimel. Optimal ar-coating for optical waveguide devices. *Lightwave Technology, Journal of*, 10(4):469–476, apr 1992.
- [87] Jaromir Krepelka. Maximally flat antireflection coatings. *Jemna Mechanika A Optika*, pages 3–5, 1992. ISSN 0030-4018.
- [88] W. Bogaerts, D. Taillaert, B. Luyssaert, P. Dumon, J. Van Campenhout, P. Bienstman, D. Van Thourhout, R. Baets, V. Wiaux, and S. Beckx. Basic structures for photonic integrated circuits in silicon-on-insulator. *Opt. Express*, 12(8):1583–1591, 2004.
- [89] T. Shoji, T. Tsuchizawa, T. Watanabe, K. Yamada, and H. Morita. Low loss mode size converter from 0.3[emsp4 1/4-em space] μm square si wire waveguides to singlemode fibres. *Electronics Letters*, 38(25):1669–1670, 2002.
- [90] Kevin K. Lee, Desmond R. Lim, Dong Pan, Christian Hoepfner, Wang-Yuhl Oh, Kazumi Wada, Lionel C. Kimerling, Kuan Pei Yap, and My The Doan. Mode transformer for miniaturized optical circuits. *Opt. Lett.*, 30(5):498–500, 2005.
- [91] Yan Liu, Yan Li, Zhongchao Fan, Bo Xing, Yude Yu, and Jinzhong Yu. Fabrication and optical optimization of spot-size converters with strong cladding layers. *Journal of Optics A: Pure and Applied Optics*, 11(8):085002, 2009.
- [92] Thorsten Wahlbrink, Wan Shao Tsai, Michael Waldow, Michael Frst, Jens Bolten, Thomas Mollenhauer, and Heinrich Kurz. Fabrication of high efficiency soi taper structures. *Microelectronic Engineering*, 86(4-6):1117 –

- 1119, 2009. MNE '08 - The 34th International Conference on Micro- and Nano-Engineering (MNE).
- [93] G. Hugh Song and W. J. Tomlinson. Fourier analysis and synthesis of adiabatic tapers in integrated optics. *J. Opt. Soc. Am. A*, 9(8):1289–1300, 1992.
- [94] Francesco Morichetti, Antonio Canciamilla, Carlo Ferrari, Matteo Torregiani, Andrea Melloni, and Mario Martinelli. Roughness induced backscattering in optical silicon waveguides. *Phys. Rev. Lett.*, 104(3):033902, Jan 2010.
- [95] Measurements of modal birefringence and polarimetric sensitivity of the birefringent holey fiber to hydrostatic pressure and strain. *Optics Communications*, 241(4-6):339 – 348, 2004.
- [96] P.D. Trinh, S. Yegnanarayanan, and B. Jalali. Integrated optical directional couplers in silicon-on-insulator. *Electronics Letters*, 31(24):2097 –2098, nov 1995.
- [97] Pennings E.C.M. Soldano, L.B. Optical multi-mode interference devices based on self-imaging: principles and applications. *Lightwave Technology, Journal of*, 13(4):615 –627, Apr 1995.
- [98] T.-T. Le and L.W. Cahill. The design of soi-mmi couplers with arbitrary power splitting ratios using slotted waveguide structures. In *LEOS Annual Meeting Conference Proceedings, 2009. LEOS '09. IEEE*, pages 246 –247, 2009.
- [99] Gini E. Bachmann M. Melchior-H. Besse, P.A. New 2 times;2 and 1 times;3 multimode interference couplers with free selection of power splitting ratios. *Lightwave Technology, Journal of*, 14(10):2286 –2293, Oct 1996.
- [100] Juerg Leuthold and Charles H. Joyner. Multimode interference couplers with tunable power splitting ratios. *J. Lightwave Technol.*, 19(5):700, 2001.
- [101] Shanjo Xu, S.T. Peng, and F.K. Schwing. Effect of transition waveguides on dielectric waveguide directional couplers. *Microwave Theory and Techniques, IEEE Transactions on*, 37(4):686–690, Apr 1989.
- [102] C. K. Madsen and J. H. Zhao. *Optical filter design and analysis: a signal processing approach*. John Wiley, New York, 1999.

- [103] Otto Schwelb. Transmission, group delay, and dispersion in single-ring optical resonators and add/drop filters - a tutorial overview. *J. Lightwave Technol.*, 22(5):1380, 2004.
- [104] Jan Niehusmann, Andreas Vorckel, Peter Haring Bolivar, Thorsten Wahlbrink, Wolfgang Henschel, and Heinrich Kurz. Ultrahigh-quality-factor silicon-on-insulator microringresonator. *Opt. Lett.*, 29(24):2861–2863, 2004.
- [105] Eric Dulkeith, Fengnian Xia, Laurent Schares, William M. J Green, and Yurii A. Vlasov. Group index and group velocity dispersion in silicon-on-insulator photonic wires. *Opt. Express*, 14(9):3853–3863, May 2006.
- [106] Amy C. Turner, Christina Manolatou, Bradley S. Schmidt, Michal Lipson, Mark A. Foster, Jay E. Sharping, and Alexander L. Gaeta. Tailored anomalous group-velocity dispersion in silicon channel waveguides. *Opt. Express*, 14(10):4357–4362, May 2006.
- [107] F. Morichetti, A. Canciamilla, M. Martinelli, A. Samarelli, R. M. De La Rue, M. Sorel, and A. Melloni. Coherent backscattering in optical microring resonators. *Applied Physics Letters*, 96(8):081112, 2010.
- [108] Brent E. Little, Juha-Pekka Laine, and Sai T. Chu. Surface-roughness-induced contradirectional coupling in ring and disk resonators. *Opt. Lett.*, 22(1):4–6, 1997.
- [109] T. J. Kippenberg, S. M. Spillane, and K. J. Vahala. Modal coupling in traveling-wave resonators. *Opt. Lett.*, 27(19):1669–1671, 2002.
- [110] Matthew Borselli, Thomas Johnson, and Oskar Painter. Beyond the rayleigh scattering limit in high-q silicon microdisks: theory and experiment. *Opt. Express*, 13(5):1515–1530, 2005.
- [111] A. Melloni, M. Martinelli, Giuseppe Cusmai, and R. Siano. Experimental evaluation of ring resonator filters impact on the bit error rate in non return to zero transmission systems. *Optics Communications*, 234(1-6):211 – 216, 2004.
- [112] R. Soref and B. Bennett. Electrooptical effects in silicon. *Quantum Electronics, IEEE Journal of*, 23(1):123–129, Jan 1987.

- [113] J. A. McCaulley, V. M. Donnelly, M. Vernon, and I. Taha. Temperature dependence of the near-infrared refractive index of silicon, gallium arsenide, and indium phosphide. *Phys. Rev. B*, 49(11):7408–7417, Mar 1994.
- [114] D. Van Thourhout I. Christiaens and R. Baets. Low power thermo-optic tuning of vertically coupled microring resonators. In *International Conference on Indium Phosphide and Related Materials*. IEEE, 2004.
- [115] R. Amatya, C. W. Holzwarth, H. I. Smith, and R. J. Ram. Efficient thermal tuning for second-order silicon nitride microring resonators. In *Conference on Photonics in Switching (San Francisco, CA, 2007)*, pages 149–150. IEEE, 2007.
- [116] Y. Hida, H. Onose, and S. Imamura. Polymer waveguide thermo-optic switch with low electric power consumption at $1.3 \mu\text{m}$. *Photonics Technology Letters, IEEE*, 5(7):782–784, jul 1993.
- [117] M.P. Earnshaw, M.A. Cappuzzo, E. Chen, L. Gomez, and A. Wong-Foy. Ultra-low power thermo-optic silica-on-silicon waveguide membrane switch. *Electronics Letters*, 43(7):393–394, march 2007.
- [118] R.L. Espinola, M.C. Tsai, J.T. Yardley, and Jr. R.M. Osgood. Fast and low-power thermo-optic switch on thin silicon-on-insulator. *Photonics Technology Letters, IEEE*, 15(10):1366–1368, oct. 2003.
- [119] Adam Densmore, Siegfried Janz, Rubin Ma, Jens H. Schmid, Dan-Xia Xu, André Delâge, Jean Lapointe, Martin Vachon, and Pavel Cheben. Compact and low power thermo-optic switch using folded silicon waveguides. *Opt. Express*, 17(13):10457–10465, 2009.
- [120] M.W. Geis, S.J. Spector, R.C. Williamson, and T.M. Lyszczarz. Submicrosecond submilliwatt silicon-on-insulator thermo-optic switch. *Photonics Technology Letters, IEEE*, 16(11):2514–2516, nov. 2004.
- [121] Tao Chu, Hirohito Yamada, Satomi Ishida, and Yasuhiko Arakawa. Compact 1 μm thermo-optic switches based on silicon photonic wire waveguides. *Opt. Express*, 13(25):10109–10114, 2005.
- [122] Tao Chu, H. Yamada, A. Gomyo, J. Ushida, S. Ishida, and Y. Arakawa. Tunable optical notch filter realized by shifting the photonic bandgap in a

- silicon photonic crystal line-defect waveguide. *Photonics Technology Letters, IEEE*, 18(24):2614–2616, dec.15, 2006.
- [123] Marcel W. Pruessner, Todd H. Stievater, Mike S. Ferraro, and William S. Rabinovich. Thermo-optic tuning and switching in soi waveguide fabry-perot microcavities. *Opt. Express*, 15(12):7557–7563, 2007.
- [124] H.M.H. Chong and R.M. De La Rue. Tuning of photonic crystal waveguide microcavity by thermo-optic effect. *Photonics Technology Letters, IEEE*, 16(6):1528–1530, june 2004.
- [125] G. Cocorullo and I. Rendina. Thermo-optical modulation at 1.5 μm in silicon etalon. *Electronics Letters*, 28(1):83–85, 1992.
- [126] M. A. Popovic-M. S. Dahlem C. W. Holzwarth P. T. Rakich H. I. Smith E. P. Ippen F. Gan, T. Barwicz and F. X. Krtner. Maximizing the thermo-optic tuning range of silicon photonic structures. In *Conference on Photonics in Switching (San Francisco, CA, 2007)*, pages 67–68. IEEE, 2007.
- [127] Po Dong, Wei Qian, Hong Liang, Roshanak Shafiiha, Ning-Ning Feng, Dazeng Feng, Xuezhe Zheng, Ashok V. Krishnamoorthy, and Mehdi Asghari. Low power and compact reconfigurable multiplexing devices based on silicon microring resonators. *Opt. Express*, 18(10):9852–9858, 2010.
- [128] G. Ghosh. *Handbook of thermo-optic coefficient of optical material with applications*. Academic Press, 1998.
- [129] Allan D. Kraus Adrian Bejan. *HEAT TRANSFER HANDBOOK*. JOHN WILEY SONS, INC., 2003.
- [130] S. Pradhan Q. Xu, B. Schmidt and M.Lipson. Micrometre-scale silicon electro-optic modulator. *Nature*, 435:325–327, 2005.
- [131] A. Samarelli, D. S. Macintyre, M. J. Strain, R. M. De La Rue, M. Sorel, and S. Thoms. Optical characterization of a hydrogen silsesquioxane lithography process. *Journal of Vacuum Science Technology B: Microelectronics and Nanometer Structures*, 26(6):2290–2294, nov 2008.
- [132] Peter Debackere, Dirk Taillaert, Katrien De Vos, Stijn Scheerlinck, Peter Bienstman, and Roel Baets. Si based waveguide and surface plasmon sensors. volume 6477, page 647719. SPIE, 2007.

- [133] Zhigang Wang, Kock Khuen Seet, Ritsuo Fukaya, Yasuhiro Kadowaki, Noriaki Arai, Makoto Ezumi, and Hidetoshi Satoh. Long-term critical dimension measurement performance for a new mask cd-sem, s-9380m. volume 6730, page 67304T. SPIE, 2007.
- [134] Baw-Ching Perng, Jyu-Horng Shieh, S.-M. Jang, M.-S. Liang, Renee Huang, Li-Chien Chen, Ruey-Lian Hwang, Joe Hsu, and David Fong. Accurate in-line cd metrology for nanometer semiconductor manufacturing. volume 6152, page 61520Q. SPIE, 2006.
- [135] J. Foucher, A. L. Fabre, and P. Gautier. Cd-afm versus cd-sem for resist ler and lwr measurements. volume 6152, page 61520V. SPIE, 2006.
- [136] Gary Jiang, Michael Kotelyanskii, and Fei Shen. Characterization of the poly gate aci structure with laser based angle resolved multiple wavelength scatterometry. volume 6922, page 69223Q. SPIE, 2008.
- [137] R. Grover, V. Van, T. A. Ibrahim, P. P. Absil, L. C. Calhoun, F. G. Johnson, J. V. Hryniewicz, and P.-T. Ho. Parallel-cascaded semiconductor microring resonators for high-order and wide-fsr filters. *J. Lightwave Technol.*, 20(5):872, 2002.
- [138] Joyce K. S. Poon, Jacob Scheuer, Yong Xu, and Amnon Yariv. Designing coupled-resonator optical waveguide delay lines. *J. Opt. Soc. Am. B*, 21(9):1665–1673, 2004.
- [139] A. Melloni and M. Martinelli. Synthesis of direct-coupled-resonators band-pass filters for wdm systems. *Lightwave Technology, Journal of*, 20(2):296–303, feb 2002.
- [140] F. Morichetti, A. Melloni, A. Breda, A. Canciamilla, C. Ferrari, and M. Martinelli. A reconfigurable architecture for continuously variable optical slow-wave delay lines. *Opt. Express*, 15(25):17273–17282, 2007.
- [141] A. Canciamilla, C. Ferrari, A. Melloni, M. Torregiani, F. Morichetti, A. Samarelli, M. Sorel, and R. De La Rue. Reconfigurable crow delay lines on a silicon platform. In *CLEO/Europe and EQEC 2009 Conference Digest*, page CK64. Optical Society of America, 2009.
- [142] R. E. Collin. *Foundations for microwave engineering*. McGraw-Hill, 1992.

- [143] Pochi Yeh, Amnon Yariv, and Chi-Shain Hong. Electromagnetic propagation in periodic stratified media. i. general theory. *J. Opt. Soc. Am.*, 67(4):423–438, 1977.
- [144] R. Orta, P. Savi, R. Tascone, and D. Trincherro. Synthesis of multiple-ring-resonator filters for optical systems. *Photonics Technology Letters, IEEE*, 7(12):1447–1449, dec. 1995.
- [145] Ronald W. Schafer Englewood Cliffs Alan V. Oppenheim. *Digital signal processing*. Prentice-Hall, 1975.
- [146] Oxford instruments cryogenic, . URL <http://www.oxford-instruments.com/products/cryogenic-systems/Pages/cryogenic-systems.aspx>.
- [147] Mehmet Bayindir, B. Temelkuran, and E. Ozbay. Tight-binding description of the coupled defect modes in three-dimensional photonic crystals. *Phys. Rev. Lett.*, 84(10):2140–2143, Mar 2000.
- [148] Shayan Mookherjea and Amnon Yariv. Optical pulse propagation in the tight-binding approximation. *Opt. Express*, 9(2):91–96, 2001.
- [149] Shayan Mookherjea and Amnon Yariv. Pulse propagation in a coupled resonator optical waveguide to all orders of dispersion. *Phys. Rev. E*, 65(5):056601, Apr 2002.
- [150] Emis Data Review Series no 4. *Properties of Silicon*. INSPEC IEE, 1988.
- [151] G J Burell T S Moss and B Ellis. *Semiconductor Opto-electronics*. Butterworth, London, 1973.
- [152] B L Weiss et al. G T Reed, A G Rickman. Optical characteristics of planar waveguides in simox structures. *Proc. Mater. Res. Soc.*, (244):387393, 1992.
- [153] A. Rickman, G.T. Reed, B.L. Weiss, and F. Namavar. Low-loss planar optical waveguides fabricated in simox material. *Photonics Technology Letters, IEEE*, 4(6):633–635, jun 1992.
- [154] M. Gnan. *Photonic Wire Devices in Silicon-on-Insulator*. 2007.
- [155] Marco Gnan, Gaetano Bellanca, and Richard M. DeLa Rue. Post-process removal of spurious fabry-perot oscillations caused by cleaved waveguide-ends. *J. Lightwave Technol.*, 27(5):500–510, 2009.

- [156] Daniel Hofstetter and Robert L. Thornton. Theory of loss measurements of fabry perot resonators by fourier analysis of the transmission spectra. *Opt. Lett.*, 22(24):1831–1833, 1997.
- [157] R.G. Walker. Simple and accurate loss measurement technique for semiconductor optical waveguides. *Electronics Letters*, 21(13):581–583, 1985.
- [158] Fengnian Xia Yurii Vlasov, William M. J. Green. High-throughput silicon nanophotonic wavelength-insensitive switch for on-chip optical networks. *Nature Photonics*, 2:242 – 246, 2008.
- [159] Jacob B Khurgin. Dispersion and loss limitations on the performance of optical delay lines based on coupled resonant structures. *Opt. Lett.*, 32(2): 133–135, 2007.
- [160] R. J. P. Engelen, D. Mori, T. Baba, and L. Kuipers. Two regimes of slow-light losses revealed by adiabatic reduction of group velocity. *Phys. Rev. Lett.*, 101(10):103901, Sep 2008.
- [161] Shayan Mookherjea and Andrew Oh. Effect of disorder on slow light velocity in optical slow-wave structures. *Opt. Lett.*, 32(3):289–291, 2007.
- [162] Carlo Ferrari, Francesco Morichetti, and Andrea Melloni. Disorder in coupled-resonator optical waveguides. *J. Opt. Soc. Am. B*, 26(4):858–866, 2009.
- [163] Andrea Melloni, Francesco Morichetti, Carlo Ferrari, and Mario Martinelli. Continuously tunable 1 byte delay in coupled-resonator optical waveguides. *Opt. Lett.*, 33(20):2389–2391, 2008.
- [164] P. Boffi, M. Ferrario, L. Marazzi, P. Martelli, P. Parolari, A. Righetti, R. Siano, and M. Martinelli. Stable 100-gb/s polmux-dqpsk transmission with automatic polarization stabilization. *Photonics Technology Letters, IEEE*, 21(11):745 –747, june1, 2009.
- [165] C. Ferrari M. Torregiani M. Ferrario R. Siano P. Boffi L. Marazzi P. Martelli P. Parolari A. Samarelli M. Sorel R. M. De La Rue L. OFaolain D. M. Beggs A. Melloni T. F. Krauss F. Morichetti, A. Canciamilla and M. Martinelli. Silicon photonics for 100 gb/s systems. *to be submitted*.

-
- [166] Francesco Morichetti, Raffaella Costa, Giuseppe Cusmai, Alessandro Cabas, Massimo Ferè, Maria Chiara Ubaldi, Andrea Melloni, and Mario Martinelli. Integrated optical receiver for rz-dqpsk transmission systems. In *Optical Fiber Communication Conference*, page FC8. Optical Society of America, 2004.